Compressible Flow Exfoliation of 2D Nanomaterials

SAEED ARABHA

A DISSERTATION SUBMITTED TO THE FACULTY OF GRADUATE STUDIES IN PARTIAL FULFILLMENT OF THE REQUIREMENTS FOR THE DEGREE OF DOCTOR OF PHILOSOPHY

GRADUATE PROGRAM IN MECHANICAL ENGINEERING
YORK UNIVERSITY
TORONTO, ONTARIO

September 2026

© Saeed Arabha, 2026

Abstract

Two-dimensional (2D) nanomaterials such as graphene, hexagonal boron nitride (h-BN), and molybdenum disulfide (MoS_2) have exceptional properties, but scalable production remains challenging. This dissertation investigates Compressible Flow Exfoliation (CFE), which combines carrier-gas expansion, particle acceleration, aerodynamic shear, momentum transfer, and thermally assisted interlayer weakening to separate layered precursors into nanosheets.

A multiscale framework connects continuum flow analysis, molecular dynamics, and exfoliation energetics. Continuum results identify high-velocity acceleration regions as major contributors to exfoliation, rather than attributing the process solely to shock waves. Atomistic simulations show that increased gas velocity, pressure, and temperature promote layer fluctuations and separation. Helium is effective because of its high attainable velocity. Potential of mean force analysis identifies sliding and edge-peeling pathways, with peeling generally facing lower energetic resistance. Heating reduces separation barriers and supports the use of nitrogen and air.

Experiments demonstrate that gas preheating substantially improves recovered product concentrations. Optimization of nitrogen-based h-BN processing increased concentration from approximately 0.003 to 0.155 $g \cdot L^{-1}$, an approximately 52-fold increase. Compressed-air processing initially yielded approximately 0.21, 0.15, and 0.14 $g \cdot L^{-1}$ for h-BN, graphene, and MoS_2, respectively. Repeated sediment re-dispersion and recovery increased these concentrations to approximately 0.53, 0.43, and 0.34 $g \cdot L^{-1}$. Centrifugation separated MoS_2 fractions with different nanosheet sizes and thicknesses, while smaller precursor particles improved recovered concentration. Graphene sediment re-exfoliation achieved approximately 316 mg cumulative recovery from a 1 g feed, corresponding to 31.6%.

Electron microscopy shows nanosheet morphologies with preserved lattice features. X-ray photoelectron spectroscopy indicates retention of the dominant bonding frameworks, with moderate gas-dependent surface or edge modification. Raman spectroscopy supports thickness reduction and preservation of graphitic, h-BN, and predominantly 2H-MoS_2 structural fingerprints. The results establish heated CFE as a tunable gas-driven platform for producing multiple 2D materials with recyclable sediment recovery. They provide a basis for continuous feeding, multi-nozzle scale-up, integrated recovery, and application development.

Acknowledgements

I am sincerely grateful to Professor Reza Rizvi, my supervisor, for his invaluable guidance, support, and encouragement throughout this research. His mentorship, insight, and trust have played an essential role in shaping this work and my development as a researcher.

I would also like to express my sincere appreciation to Professor Cuiying Jian, my co-supervisor, for her thoughtful feedback, valuable advice, and continued support during this journey. Her guidance has greatly contributed to the progress and completion of this thesis.

My thanks also extend to Professors Pisana and O'Brien, members of my examination committee, for their time, careful evaluation, constructive comments, and helpful suggestions.

I am deeply grateful to my family and friends for their unwavering love, patience, and support. Their encouragement gave me strength throughout the challenges of this PhD journey. Finally, I would like to acknowledge the Iranian people, who have endured an exceptionally difficult year with resilience, courage, and hope. Their strength has been a profound source of inspiration for me.

Table of Contents

Abstract ii

Acknowledgements iii

Table of Contents iv

List of Tables ix

List of Figures xi

List of Symbols xxiii

List of Abbreviations xxvii

Chapter 1: Introduction 1

1.1 Background and Motivation 1

1.2 Two-Dimensional (2D) Nanomaterials: Overview 2

1.3 Current Exfoliation Techniques and Their Limitations 2

1.4 Compressible Flow Exfoliation (CFE): Introduction and Principles 3

1.5 Research Objectives, Original Contributions, and Thesis Outline 4

1.5.1 Research Objectives 4

1.5.2 Original Contributions of This Thesis 5

1.5.3 Thesis Outline 6

Chapter 2: Literature Review 8

2.1 Fundamentals of Two-Dimensional (2D) Nanomaterials 8

2.1.1 Graphene 9

2.1.2 Molybdenum Disulfide (MoS_2) 12

2.1.3 Hexagonal Boron Nitride (h-BN) 13

2.1.4 Other Emerging 2D Materials 15

2.2 Production Techniques: A Comparative Analysis 16

2.2.1 Overview of Exfoliation Strategies 16
2.2.2 Mechanics of Exfoliation 17
2.2.3 Micromechanical Cleavage 18
2.2.4 Ball Milling 21
2.2.5 Ultrasonication 24
2.2.6 Shear Exfoliation 27
2.2.7 Electrochemical Exfoliation 30
2.2.8 Other Notable Exfoliation Techniques 33
2.2.9 Summary of Production Techniques 34
2.3 Compressible Flow Exfoliation (CFE) 38
2.3.1 Methodology and Experimental Configuration 39
2.3.2 Exfoliation Results and Material Characterization 40
2.3.3 Parametric Optimization of the CFE Process 42
2.3.4 Application Case Study: PET Nanocomposite 45
2.3.5 Conclusions and Remaining Knowledge Gaps in CFE 47
Chapter 3: Continuum Perspective Analysis of CFE 50
Introduction to CFE Modeling and Multiscale Simulation Approaches 50
3.1 Multiscale Modelling Strategy for CFE 51
3.2 Continuum Flow Model and Computational Details 54
3.3 Results and Discussion 56
3.3.1 Flow Acceleration, Mach Number, and Shock Structure 56
3.3.2 Relative Velocity, Drag Force, and Effective Work 59
3.4 Chapter Summary and Bridge to Atomistic Modelling 66
Chapter 4: Atomistic Perspective Simulation of CFE 69

4.1 Introduction 70
4.2 Computational Details 71
4.3 Results and Discussion 74
4.4 Conclusion 83
Chapter 5: Energy-Based Analysis of CFE 85
5.1 Introduction 85
5.2 Computational Details 86
5.3 Steered Molecular Dynamics (SMD) 89
5.4 Results and Discussion 91
5.4.1 Reaction Coordinate and Validation 91
5.4.2 PMF and Free Energy of CFE 93
5.4.3 Effect of Flow Characteristic on CFE 95
5.4.4 Effect of Gas Type 99
5.4.5 Effect of Graphene Specifications 103
5.4.6 Effect of Structural Defects on Exfoliation Energetics 108
5.5 Conclusion 110
Chapter 6: Experimental Optimization of CFE 113
6.1 Introduction 113
6.2 Methodology and Experimental Configuration 114
6.2.1 Precursor Materials and Carrier Gases 114
6.2.2 Collection Solvent and Dispersion Medium 115
6.2.3 CFE Apparatus and Operating Protocol 116
6.2.4 Gas Preheating Design and Heat-Transfer Estimate 118
6.2.5 Post-Exfoliation Recovery and Centrifugation Protocols 121

6.2.6 Concentration Determination and UV–Vis Calibration 122
6.3 Experimental Validation of the Reconstructed CFE System 123
6.4 Parameter Optimization of CFE Process 128
6.5 Extension of Optimized CFE to Multiple 2D Materials 132
6.6 Recovery of Entrapped Nanosheets by Re-Dispersion and Re-Centrifugation 136
6.7 UV–Vis Extinction Analysis of MoS_2 Nanosheet Dispersions 140
6.8 Solution Stability of CFE-Produced Nanosheet Dispersions 145
6.9 Effect of Starting Particle Size on CFE Output 149
6.10 Yield Enhancement by Re-Exfoliating Graphene Sediment 152
6.11 Chapter Summary 154
Chapter 7: Material Characterization of Optimized CFE 156
7.1 Introduction 156
7.2 Material Characterization Techniques 157
7.2.1 X-ray Photoelectron Spectroscopy (XPS) 157
7.2.2 Transmission Electron Microscopy (TEM) 158
7.2.3 Raman Spectroscopy 158
7.3 Qualitative Morphological Analysis (TEM, STEM) 159
7.4 Surface Chemistry and Chemical State Analysis (XPS) 163
7.4.1 Graphene 164
7.4.2 Hexagonal Boron Nitride (h-BN) 169
7.4.3 Molybdenum Disulfide (MoS_2) 177
7.4.4 Overall XPS Conclusion 183
7.5 Structural Integrity and Exfoliation Quality (Raman) 185
7.5.1 Graphene 186

7.5.2 Hexagonal Boron Nitride (h-BN) 190
7.5.3 Molybdenum Disulfide (MoS_2) 194
7.6 Integrated Characterization Summary 199
Chapter 8: Conclusion and Future Work 201
8.1 Summary of Research Objectives 201
8.2 Major Contributions of the Thesis 202
8.3 Current Limitations of the Present Study 209
8.4 Future Work Connected to Current Limitations 211
8.4.1 Automated Precursor Feeding 211
8.4.2 Parallelized Multi-Nozzle CFE Architecture for Throughput Enhancement 214
8.4.3 Moisture- and Agent-Conditioned Precursor Feeding for Yield Enhancement 215
8.4.4 Continuous Recovery and Concentration Using Tangential Flow Filtration 217
8.4.5 Expansion of CFE toward MXenes and Other Emerging 2D Materials 220
8.4.6 Application-Oriented Demonstration in Composite System 222
8.5 Final Remarks 225
References 228

List of Tables

Table 2.1: *Summary of Graphene Properties* *11*

Table 2.2: *Comparison of Key 2D Materials* *15*

Table 2.3. *Summary of Exfoliation Techniques* *35*

Table 3.1: *UV–Vis absorbance ratios at 300 nm for h-BN dispersions produced under different gas and pressure conditions.* *65*

Table 3.2: *Work ratios calculated at different cut-off forces for helium and nitrogen CFE conditions.* *65*

Table 4.1. *Lennard-Jones interaction parameters used for gas–Graphene and interlayer molecular dynamics simulations [118, 119].* *74*

Table 4.2: *Mean lateral sliding distance (D_{xy}) and vertical separation distance (D_z) between Graphene nanosheets under different helium flow velocities.* *80*

Table 5.1: *$|\Delta G_{CFE}|$ in vacuum and helium gas at static and V=800 $m \cdot s^{-1}$ conditions for RC I and RC II.* *94*

Table 6.1: *UV–Vis-derived lateral size and estimated layer number of MoS_2 nanosheets produced from different starting particle sizes after CFE and repeated recovery at 1500 rpm.* *151*

Table 7.1: *Representative projected dimensions and aspect ratios of CFE-produced Graphene, h-BN, and MoS_2 nanosheets measured from TEM images.* *162*

Table 7.2: *High-resolution C 1s deconvolution of reference and CFE-processed Graphene samples.* *165*

Table 7.3: *High-resolution C 1s peak parameters for reference and CFE-processed Graphene samples.* *166*

Table 7.4: *High-resolution B 1s deconvolution of reference and CFE-processed h-BN samples.* *170*

Table 7.5: *High-resolution N 1s deconvolution of reference and CFE-processed h-BN samples. 172*

Table 7.6: *High-resolution C 1s deconvolution of reference and CFE-processed h-BN samples. 174*

Table 7.7: *High-resolution S 2s–Mo 3d deconvolution of reference and CFE-processed MoS_2 samples..... 178*

Table 7.8: *High-resolution S 2p deconvolution of reference and CFE-processed MoS_2 samples. 180*

Table 7.9: *Raman metrics for the cascade centrifugation series of air-exfoliated Graphene. .. 188*

Table 7.10: *Raman metrics for Graphene exfoliated using different carrier gases..... 189*

Table 7.11: *Raman metrics for the cascade centrifugation series of air-exfoliated h-BN..... 191*

Table 7.12: *Raman metrics for h-BN exfoliated using different carrier gases. 192*

Table 7.13: *Raman metrics for the cascade centrifugation series of air-exfoliated MoS_2..... 195*

Table 7.14: *Raman metrics for MoS_2 exfoliated using different carrier gases. 197*

List of Figures

Figure 2.1: *Selected 2D materials arranged by bandgap, with perspective views of their crystal structures. Bars show the range from bulk to monolayer; black and red bars distinguish the direction of the bandgap change. The grey box contains metallic or near-zero-bandgap materials [21]. Copyright © The Author(s) 2020. Licensed under CC BY 4.0 ..... 9*

Figure 2.2: *Graphene Derivatives, a) Few-layer Graphene, b) single-layer Graphene, c) Graphene-oxide (GO) and d) Reduced Graphene-oxide (rGO) [22]. Copyright © 2020 Acta Materialia Inc. Published by Elsevier B.V..... 10*

Figure 2.3: *Different polymorphs or phases of MoS_2: (a) 1H phase, (b) 1T phase, (c) 2H phase, and (d) 3R phase [28]. Copyright © 2015 The Royal Society of Chemistry. 12*

Figure 2.4: *Lattice structure of monolayer h-BN. The parallelogram denotes a primitive unit cell containing one boron atom (B) and one nitrogen atom (N). The armchair and zigzag crystallographic directions are indicated [34]. Copyright © 2020 Higher Education Press and Springer-Verlag GmbH Germany, part of Springer Nature..... 14*

Figure 2.5: *The five most common exfoliation processes. 2D materials are most commonly exfoliated using micromechanical, ball milling, ultrasonication, shear, and electrochemical processes to separate layers of 2D materials. 17*

Figure 2.6: *Micromechanical cleavage techniques using scotch tape. (a) A schematic representation of the micromechanical cleavage method for exfoliating 2D material. (b) Partially exfoliated Graphene on scotch tape [51]. Copyright © 2015 American Chemical Society. (c) Optical microscope image of an exfoliated single layer, bilayer, and multilayer Graphene flakes [52]. Copyright © 2012 Elsevier Ltd. (d) Schematic representation of performing oxygen plasma treatment to remove organic residues from the substrate, annealing the substrate containing graphite on adhesive tape to enhance the adhesion between the substrate and the boundary graphite layers, and cooling the substrate to reduce the pressure at the interface between graphite and the substrate [51]. Copyright © 2015 American Chemical Society. (e) Schematic of the metal-*

assisted exfoliation process of 2D monolayers [53]. © 2020 The Author(s), licensed under CC BY 4.0..... 20

***Figure 2.7:** Ball milling exfoliation mechanisms of 2D materials. (a) Schematic diagram and corresponding SEM images of the exfoliation mechanism of h-BN [56]. Copyright © 2015 American Chemical Society. (b) XRD and (c) variation of interplanar spacing with milling time of ball-milled Graphene [57]..... 23*

***Figure 2.8:** Liquid sonication exfoliation mechanisms of 2D materials. (a) A schematic of liquid sonication demonstrating how bulk material is fragmented into 2D nanosheets using ultrasonication [67], (b) high-speed sequence of frames illustrating the ultrasonication exfoliation of a Graphene flake [71], (c) schematic of surfactant-assisted ultrasonic exfoliation of Graphene nanosheets [72], Copyright © 2012 American Chemical Society. (d) ultrasonicated WS_2, $MoTe_2$, $MoSe_2$, $NbSe_2$, $TaSe_2$, and h-BN stabilized in water using sodium cholate [73]. Copyright © 2011 WILEY-VCH Verlag GmbH & Co. KGaA, Weinheim. 26*

***Figure 2.9:** Liquid Shear exfoliation mechanisms of 2D materials. Shear exfoliation technique. (a) Schematic of a high shear mixer and mechanisms facilitating exfoliation of layer materials in shear mixture. (b) Schematic representation of the exfoliation of few-layer Graphene from bulk graphite using the wet jet milling method. (c)–(e) MoS_2, WS2, and h-BN produced by wet jet milling [9]. Copyright © 2022 AIP Publishing LLC..... 29*

***Figure 2.10:** (a) Schematic illustration of ion intercalation and exfoliation of 2D sheets in the electrochemical method. (b) Schematic of a micro electrochemical cell under a microscope. (c) Illustration of intercalation and expansion of a black phosphorous cathode in organic DMSO electrolyte. (d) False color SEM image of black phosphorous before expansion, (e) after applying a voltage of 3.5 V (double arrow shows expansion gap), and (f) 5 V [9]. Copyright © 2022 AIP Publishing LLC. 32*

***Figure 2.11:** a) Process schematic of the compressible flow exfoliation setup including a description of the critical components and the initial and final structures of the BN powder. b) Still images of the collection vessel before, during, and after the CFE process for BN powder. c)*

Exfoliated suspensions of various 2D layered nanomaterials after centrifugation [18]. Copyright © 2018 WILEY-VCH Verlag GmbH & Co. KGaA, Weinheim. 40

Figure 2.12: *a) UV–Vis and b) Raman spectra for h-BN produced using CFE and the comparable liquid-phase exfoliation technique. c) The AFM scan image of a BN flake isolated after CFE with insets showing the height profile of the flake and the thickness distribution of several flakes. d) The TEM images (scale bar: 800 nm) for various 2D materials produced by CFE along with their diffraction patterns (inset) at the marked spot, shown here are h-BN (left), Graphene (middle), and MoS_2 (right) [18]. Copyright © 2018 WILEY-VCH Verlag GmbH & Co. KGaA, Weinheim.... 41*

Figure 2.13: *a–d) Plots showing the effects of initial BN concentration (a), upstream gas pressure (b), flow geometry (tube diameter) (c), and carrier gas type (d) on the final BN concentration and yield in CFE. All error bars represent the standard deviation (n=3) [18]. Copyright © 2018 WILEY-VCH Verlag GmbH & Co. KGaA, Weinheim. 44*

Figure 2.14: *PET-BN nanocomposites prepared using CFE exfoliated and bulk BN at 0.017 and 0.15 vol% of BN. (a) Visual light transmittance. (b) Tensile Young's modulus. (c) Oxygen permeation rate (OPR) at 0.15 vol% BN. (d) A tilted view of a freeze-fractured cross-section of PET-CFE-BN 0.15 vol% showing the protruded BN particles (scale bar: 10 µm). All error bars represent the standard deviation (n=3) [18]. Copyright © 2018 WILEY-VCH Verlag GmbH & Co. KGaA, Weinheim. 46*

Figure 3.1: *Geometry of the converging-diverging nozzle used for the continuum CFE flow analysis [100]. © 2026 The Author(s). Advanced Engineering Materials published by Wiley-VCH GmbH. 54*

Figure 3.2: *(a) Comparison of axial flow velocity profiles at 5.6 MPa obtained from COMSOL Multiphysics and the quasi-1D Euler model using the same CD-nozzle geometry. (b) Corresponding Mach number distributions for both methods [100]. © 2026 The Author(s). Advanced Engineering Materials published by Wiley-VCH GmbH. 57*

Figure 3.3: *(a) Axial velocity and (b) Mach number profiles predicted by the quasi-1D Euler model for helium and nitrogen at different upstream pressure [100]. © 2026 The Author(s). Advanced Engineering Materials published by Wiley-VCH GmbH. 58*

Figure 3.4: *(a) Particle Reynold's number obtained using helium and (b) nitrogen at different upstream pressures [100]. © 2026 The Author(s). Advanced Engineering Materials published by Wiley-VCH GmbH. 59*

Figure 3.5: *(a) Relative velocity and (b) density variations through the axial distance of the CD nozzle for different upstream pressures of He:5.6 and 1.4 MPa, and N_2: 5.6 and 1.4 MPa [100]. © 2026 The Author(s). Advanced Engineering Materials published by Wiley-VCH GmbH..... 61*

Figure 3.6: *Drag force acting on an h-BN particle travelling through the converging-diverging nozzle under helium and nitrogen flow at different upstream pressures [100]. © 2026 The Author(s). Advanced Engineering Materials published by Wiley-VCH GmbH..... 62*

Figure 3.7: *(a) Cumulative work done on a nanoparticle at different upstream pressures using helium and nitrogen gas (a1) without cut-off force and (a2) at cut-off force=30 μN. (b) Work done on the particle at different cut-off forces compared across helium and nitrogen flow conditions [100]. © 2026 The Author(s). Advanced Engineering Materials published by Wiley-VCH GmbH. 63*

Figure 4.1: *(a) System setup, a 10×40×10 nm^3box is considered with 5 nm entrance to apply velocity to gas particles (b) top view and side view of Graphene nanosheet of 6 × 4 nm^2 with 0.33 nm interlayer separation distance [116] Copyright © 2022 American Chemical Society..... 73*

Figure 4.2: *RMSD plot of exfoliating Graphene layer at five different temperatures ranging from 273K to 2000K (a) Graphene bilayer without any gaseous medium (b) Graphene bilayer with helium gas particle [116] Copyright © 2022 American Chemical Society..... 76*

Figure 4.3: *Effect of flow velocity of helium gas ranging from 1000 ms^{-1} to 2000 ms^{-1} on Graphene exfoliation (a) temperature and (b) RMSD of bilayer Graphene. (c) The correlation of temperature and RMSD [116] Copyright © 2022 American Chemical Society. 77*

Figure 4.4: *The energy transferred from Helium gas to bilayer Graphene at different Helium velocities ranging from 1000 ms^{-1} to 2000 ms^{-1} [116] Copyright © 2022 American Chemical Society. 78*

Figure 4.5: *Structural properties of Graphene bilayer at 1000 - 2000 ms^{-1} velocities of helium gas (a) definition of sliding and vertical direction of exfoliation. Normalized probability distribution of (b) sliding distance Dxy, and (c) vertical distance Dz of Graphene bilayer [116] Copyright © 2022 American Chemical Society.* *79*

Figure 4.6: *Effect of supply pressure of gas on Graphene exfoliation (a) temperature of Graphene (b) the energy transferred from Helium gas to bilayer Graphene at different Helium at 1.4 and 5.5 MPa [116] Copyright © 2022 American Chemical Society.* *81*

Figure 4.7: *Simulated exfoliation phenomena of Graphene bilayer in two different gas medium (a) RMSD of exfoliating layer of Graphene (b) Normalized interlayer interaction energy between Graphene layers in helium and argon gas [116] Copyright © 2022 American Chemical Society.* *82*

Figure 5.1: *(a) Simulation domain (20 × 80 × 20 nm^3) with 10 nm inlet slab for velocity assignment; (b) Graphene bilayer (7 × 7 nm^2) with (c) 0.33 nm spacing (3D/side views) [127] Copyright © 2026 American Chemical Society.* *87*

Figure 5.2: *Instantaneous gas velocity tracking during a molecular dynamics simulation (target velocity $V = 800\ m \cdot s^{-1}$ for Helium) [127] Copyright © 2026 American Chemical Society.*..... *89*

Figure 5.3: *Illustrates the three reaction coordinates (RCs) explored for the separation of two Graphene nanosheets. (a), RC I: depicts the distance between the COMs of the two nanosheets in the lateral (parallel) direction. (b) RC II: shows the distance between the edge atoms of the two sheets in the normal direction. Finally, (c) RC III: the distance between the center of mass (COM) of the two sheets is measured along the normal (vertical) direction [127] Copyright © 2026 American Chemical Society.* *90*

Figure 5.4: *Effect of SMD pulling velocity on the calculated potential of mean force for Graphene separation along RC I and RC II [127] Copyright © 2026 American Chemical Society.* *91*

Figure 5.5: *Force–displacement curves for two initially stacked Graphene nanosheets in vacuum condition, pulled apart along the three reaction coordinates: RC I (lateral sliding), (b) RC II (edge peeling), and (c) RC III (normal) [127] Copyright © 2026 American Chemical Society.*..... *92*

Figure 5.6: *(a) snapshots and (b) PMF of exfoliation of bilayer 7nm Graphene sheets as a function of time [127] Copyright © 2026 American Chemical Society..... 93*

Figure 5.7: *Potential of mean force curves for bilayer Graphene nanosheet separation under vacuum and helium gas environments [127] Copyright © 2026 American Chemical Society. .. 95*

Figure 5.8: *Effects of gas characteristics on the PMF-Factor: (a) velocity, (b) density, and (c) temperature. The PMF-Factor is defined as the ratio of the PMF to the PMF under vacuum conditions. In each study, one gas characteristic varies while keeping the others constant. (d) Sensitivity Analysis: This metric compares how different flow characteristics affect the PMF required for exfoliation. A larger vertical range indicates that the exfoliation energy barrier is highly sensitive to that specific gas characteristic [127] Copyright © 2026 American Chemical Society..... 98*

Figure 5.9: *Variations in density and relative velocity* $(vfluid - vparticle)$ *along the axial distance of the CD nozzle for different gases: helium, argon, and nitrogen. (b) Energy transferred from gas to Graphene sheets under static conditions (no velocity) and for flowing gas in reaction coordinates (RC) I and II [127] Copyright © 2026 American Chemical Society. 101*

Figure 5.10: *Average energy transferred to Graphene particles using gas mixtures of helium with argon and nitrogen at varying helium concentrations (0%, 25%, 50%, 75%, and 100%) [127] Copyright © 2026 American Chemical Society..... 102*

Figure 5.11: *PMF required for the exfoliation of four-layer Graphene under vacuum and helium gas conditions. Panels (a) and (b) show the PMF profiles for the separation of the first and second layers, respectively, along the sliding pathway (RC I). Panels (c), (d), and (e) depict the PMF profiles for the separation of the first, second, and third layers, respectively, along the peeling pathway (RC II) [127] Copyright © 2026 American Chemical Society..... 105*

Figure 5.12: *Interlayer center-of-mass (COM) trajectories along the lateral sliding pathway (RC I) during steered molecular dynamics simulations. (a) Under vacuum conditions, the applied pulling force on the top layer results in sequential separation, as evidenced by the diverging layer-wise velocities and distinct decoupling events. (b) Under high-speed helium flow (V = 800 m·s⁻¹), continuous kinetic momentum transfer from gas atoms bombarding the exposed leading edges*

provides a supplemental driving force. This gas-dynamic assistance overcomes interlayer slip, synchronizing the layer velocities and resulting in the simultaneous block-sliding of all three unconstrained upper layers [127] Copyright © 2026 American Chemical Society..... 106

Figure 5.13: *PMF required for the exfoliation of Graphene for, (a) PMF for bi-layer Graphene at varying lengths. (b) PMF as a function of the number of Graphene layers at a fixed length of L=7 nm, under vacuum and helium gas environments [127] Copyright © 2026 American Chemical Society..... 108*

Figure 5.14: *The effect of structural defect concentration (1%, 3%, and 5% random vacancies) on the PMF-Factor for lateral sliding (RC I) and edge peeling (RC II) under a helium gas flow (V = 800 $m \cdot s^{-1}$, D = 6 $g \cdot L^{-1}$). The increasingly negative Factor (%) indicates that gas dynamics become significantly more effective at lowering the exfoliation barrier as structural imperfections increase [127] Copyright © 2026 American Chemical Society. 109*

Figure 6.1: *Schematic illustration of the Compressible Flow Exfoliation (CFE) Process for gas-phase exfoliation and liquid-phase collection of two-dimensional (2D) nanomaterials. The system consists of a high-pressure carrier-gas source, pressure regulation and isolation valves, an in-line gas-heating section, a powder entrainment chamber, an adjustable Swagelok nozzle/orifice, and a downstream collection vessel containing 200 mL of DI/IPA co-solvent. The apparatus enables rapid fluidization, gas-phase acceleration, and shear-driven exfoliation of bulk layered materials, followed by immediate liquid-phase capture and stabilization of the exfoliated nanosheets..... 117*

Figure 6.2*: Experimental validation workflow for the reconstructed CFE system. The reference valve-based CFE condition was first reproduced using h-BN and helium/nitrogen carrier gases. 125*

Figure 6.3*: UV–Vis validation of h-BN exfoliation using the reconstructed CFE system. He-CFE and N_2-CFE h-BN suspensions were compared with the reference gas-dependent CFE trend. The reconstructed system produced approximately 0.23 $g \cdot L^{-1}$ using helium and 0.04 $g \cdot L^{-1}$ using nitrogen, reproducing the reference gas-dependent trend in which helium produces a higher h-BN concentration than nitrogen under comparable valve-based CFE conditions..... 127*

***Figure 6.4**: Optimization of the modified CFE process for h-BN exfoliation using nitrogen. Effect of (a) starting h-BN particle size, (b) stagnation temperature, (c) initial raw-material loading, and (d) upstream pressure on the final h-BN concentration. The optimized condition increased the concentration from 0.003 g·L⁻¹ to 0.155 g·L⁻¹ using a 200 mL collection volume, showing improved exfoliation and material recovery in the modified CFE system.* *130*

***Figure 6.5**: Extension of the optimized heated CFE process to h-BN, few-layer Graphene, and MoS_2 using compressed air and nitrogen carrier gases.* *134*

***Figure 6.6**: Concentration analysis of various 2D nanomaterials produced using compressed air. (a) Cumulative concentration of h-BN, MoS_2, and Graphene dispersions plotted against the number of centrifugation cycles. (b) Comparison of the total final concentrations achieved for h-BN, MoS_2, and Graphene. A reference value for h-BN processed with helium from previous literature is included for comparison [18].* *137*

***Figure 6.7**: Beer–Lambert calibration curves for the determination of extinction coefficients. Optical absorbance plotted as a function of concentration for h-BN, MoS_2, and Graphene dispersions. The calculated extinction coefficients are 1804 $L\,g-1m-1$ at 300 nm for h-BN, 1541 $L\,g-1m-1$ at 672 nm for MoS_2 , and 1282 $L\,g-1m-1$ at 600 nm for Graphene.* ... *139*

***Figure 6.8**: Effect of centrifugation speed and repeated sediment re-dispersion on MoS_2 recovery and nanosheet dimensions. (a) Photographs of MoS_2 supernatants collected from successive re-dispersion/centrifugation cycles, showing a gradual decrease in suspension darkness as the recoverable nanosheet content decreases with repeated cycles. The visible laser path confirms light scattering from dispersed MoS_2 nanosheets. (b) Cumulative concentration plotted over 10 cycles for centrifugation speeds of 1500, 3000, and 4500 rpm. A clear inverse relationship is observed where higher speeds result in lower cumulative yields. (c) Analysis of the total concentration yields reveals the mass distribution of the exfoliated material and (d) UV–Vis-derived nanosheet dimensions at different centrifugation speeds.* *144*

Figure 6.9**: Solution stability and nanosheet-dimension analysis of CFE and LPE dispersions over a 350h storage period.* ***(a) *UV–Vis spectra of CFE dispersions collected at different times.* ***(b)*** *UV–*

Vis spectra of LPE dispersions collected at different times. ***(c)*** *Flake-length evolution over time for CFE and LPE samples.* ***(d)*** *Layer-number evolution over time for CFE and LPE samples. 147*

Figure 6.10*: (a) UV–Vis spectra of MoS_2 suspensions recovered from different starting bulk particle sizes of 12.5 µm, 4.5 µm, and 1.5 µm after repeated re-dispersion/centrifugation cycles. (b) Recovered MoS_2 concentration as a function of centrifugation cycle at a fixed centrifugation speed of 1500 rpm, showing that smaller starting particles produce higher final concentrations. After five cycles, the concentration increased to approximately 0.29 $g \cdot L^{-1}$, 0.77 $g \cdot L^{-1}$, and 1.38 $g \cdot L^{-1}$ for 12.5 µm, 4.5 µm, and 1.5 µm starting powders, respectively. UV–Vis-derived (c) lateral size and (d) number of layers for the recovered MoS_2 nanosheets, showing similar final nanosheet dimensions despite different starting particle sizes. The average lateral sizes were 280 ± 23 nm, 325 ± 47 nm, and 289 ± 13 nm, while the estimated layer numbers were 22 ± 2.1, 24 ± 2.3, and 23 ± 2.2 for 12.5 µm, 4.5 µm, and 1.5 µm starting powders, respectively. 150*

Figure 6.11*: Sediment recycling for Graphene yield enhancement. (a) Workflow showing CFE exfoliation, centrifugation/re-dispersion, sediment freeze-drying, and reuse of the sediment for the next exfoliation pass. (b) Final cumulative Graphene concentration after five recovery cycles for three successive exfoliation passes, increasing from 0.431 to 0.538 and 0.611 $g \cdot L^{-1}$. 153*

Figure 7.1*: Morphological characterization of CFE-exfoliated Graphene: (a) STEM image, (b) TEM image, and (c) HRTEM image with corresponding diffraction/FFT pattern. 160*

Figure 7.2*: Morphological characterization of CFE-exfoliated MoS_2: (a) STEM image, (b) TEM image, and (c) HRTEM image with corresponding diffraction/FFT pattern. 160*

Figure 7.3*: Morphological characterization of CFE-exfoliated h-BN: (a) STEM image, (b) TEM image, and (c) HRTEM image with corresponding diffraction/FFT pattern. The h-BN nanosheet shows an elongated morphology, local thickness variation, and preserved crystalline lattice features. 161*

Figure 7.4*: TEM-based representative dimensional analysis of CFE-exfoliated (a) Graphene, (b) h-BN, and (c) MoS_2 nanosheets. Representative dimensional analysis of CFE-exfoliated nanosheets. 163*

***Figure 7.5**: XPS survey spectra of (a) reference graphite, (b) Air-CFE Graphene, and (c) He-CFE Graphene, together with high-resolution C 1s spectra of (d) reference graphite, (e) Air-CFE Graphene, and (f) He-CFE Graphene. The survey spectra confirm carbon as the main element and show minor surface oxygen and trace fluorine in the processed samples. The C 1s spectra were used to evaluate changes in sp² carbon, sp³ carbon, and oxygen-containing surface species after CFE.* *165*

***Figure 7.6**: Relative distribution of oxygenated C 1s components in reference graphite, Air-CFE Graphene, and He-CFE Graphene. Both CFE conditions increase oxygen-containing surface species relative to the reference sample, while helium preserves a slightly higher sp² carbon contribution.* *168*

***Figure 7.7:** XPS survey spectra of (a) reference h-BN, (b) He-CFE h-BN, and (c) Air-CFE h-BN. The spectra confirm B and N as the main components of the h-BN structure, together with smaller C and O surface contributions attributed to adventitious carbon, adsorbed oxygen-containing species, and CFE-induced surface/edge functionalization.* *170*

***Figure 7.8:** High-resolution B 1s XPS spectra and fitted components of (a) reference h-BN, (b) He-CFE h-BN, and (c) Air-CFE h-BN. The dominant B–N contribution confirms preservation of the h-BN framework, while the stronger B–O component in Air-CFE h-BN indicates enhanced oxygen-containing boron surface environments.* *172*

***Figure 7.9:** High-resolution N 1s XPS spectra and fitted components of (a) reference h-BN, (b) He-CFE h-BN, and (c) Air-CFE h-BN. The spectra are dominated by N–B bonding, confirming that the nitrogen environment of h-BN is largely preserved after CFE. The small N–C contribution in Air-CFE h-BN suggests slightly higher defect- or surface-associated bonding in the air-processed sample.* *173*

***Figure 7.10:** High-resolution C 1s XPS spectra and fitted components of (a) reference h-BN, (b) He-CFE h-BN, and (c) Air-CFE h-BN. The spectra are dominated by C–C/C–H carbon. The broad high-binding-energy component near 288.6 eV is assigned to mixed C–N/C–N–B/oxygenated carbon surface species and is most pronounced in Air-CFE h-BN.* *175*

Figure 7.11: *High-resolution O 1s XPS spectra of (a) reference h-BN, (b) He-CFE h-BN, and (c) Air-CFE h-BN. The broad O 1s envelope is assigned to overlapping O–B/O–H/oxygen-containing surface species rather than to a single pure oxygen bonding environment..... 176*

Figure 7.12: *XPS survey spectra of (a) reference MoS_2, (b) He-CFE MoS_2, and (c) Air-CFE MoS_2. The spectra confirm Mo and S as the primary elements of the MoS_2 samples. Minor surface signals are treated as extrinsic surface species and are not used as the main evidence for intrinsic MoS_2 structure. 178*

Figure 7.13: *High-resolution S 2s–Mo 3d XPS spectra and fitted components of (a) reference MoS_2, (b) He-CFE MoS_2, and (c) Air-CFE MoS_2. ..... 180*

Figure 7.14: *High-resolution S 2p XPS spectra and fitted components of (a) reference MoS_2, (b) He-CFE MoS_2, and (c) Air-CFE MoS_2. ..... 181*

Figure 7.15: *Raman spectra of graphite and CFE-exfoliated Graphene. (a) Raman spectra of graphite and air-exfoliated Graphene fractions obtained after cascade centrifugation at 1500, 3000, and 4500 rpm. (b) Raman spectra of graphite and Graphene exfoliated using air, nitrogen, and helium carrier gases. Spectra are normalized to the G band and vertically offset for clarity. Dashed guide lines indicate the D, G, and 2D bands..... 187*

Figure 7.16: *Raman spectra of bulk h-BN and CFE-exfoliated h-BN. (a) Raman spectra of bulk h-BN and air-exfoliated h-BN fractions obtained at different centrifugation speed of 1500, 3000, and 4500 rpm. (b) Raman spectra of bulk h-BN and h-BN exfoliated using air, nitrogen, and helium carrier gases. Spectra are vertically offset for clarity. The dashed guide line identifies the E_{2g} Raman mode of h-BN near 1366–1368 cm^{-1}..... 191*

Figure 7.17: *Raman spectra of bulk MoS_2 and CFE-exfoliated MoS_2. (a) Air-exfoliated MoS_2 fractions obtained after cascade centrifugation at 1500, 3000, and 4500 rpm. (b) MoS_2 exfoliated using air, nitrogen, and helium carrier gases. The arrows show $\Delta = A_1g - E_2g^1$, which decreases after CFE and provides evidence of layer reduction or enrichment of few-layer MoS_2 nanosheets. 195*

Figure 8.1*: Conceptual schematic of an automated precursor-feeding system for continuous CFE operation..... 213*

***Figure 8.2**: Conceptual schematic of tangential flow filtration for future CFE product recovery and concentration. 220*

List of Symbols

Symbol	Definition
A	Absorbance; cross-sectional area, depending on context
$A(x)$	Nozzle cross-sectional area as a function of axial position
A_p	Projected particle area
A_{tube}	Cross-sectional area of the heating tube
A_H	Hamaker constant
a	Speed of sound
C	Concentration
C_0	Initial concentration
C_D	Drag coefficient
C_p	Specific heat capacity at constant pressure
C_v	Specific heat capacity at constant volume
D	Gas density/concentration parameter used in molecular dynamics sensitivity studies; characteristic diameter or distance where explicitly defined
D_{xy}	Lateral sliding distance between two nanosheets
D_z	Vertical separation distance between two nanosheets
d	Distance, diameter, or interlayer spacing, depending on context
d_p	Particle diameter
d_{in}	Inlet diameter
d_{out}	Outlet diameter
E	Energy
E_t	Total energy
F	Force
F_c	Cut-off force used in effective-work analysis
F_D	Drag force acting on a particle
F_{ad}	Adhesion force per unit area between adjacent layers
F_{peel}	Peeling force per unit area during edge-peeling exfoliation
H	Total enthalpy
h	Convective heat-transfer coefficient
I_D/I_G	Raman intensity ratio of the D band to the G band

Symbol	Definition
I_{2D}/I_G	Raman intensity ratio of the 2D band to the G band
I_{CFE}	CFE production intensity
J	Flux
k	Thermal conductivity or force constant, depending on context
k_B	Boltzmann constant
L	Length, nanosheet length, or characteristic length
L_{min}	Minimum required heating-tube length
l	Optical path length in the Beer–Lambert relationship
M	Mach number
m	Mass
m_{rec}	Recovered mass of exfoliated material
$\dot{m}$	Mass flow rate
N	Number of atoms, molecules, cycles, layers, or data points, depending on context
n	Number of layers, number of samples, or amount of substance, depending on context
Nu	Nusselt number
P	Pressure
p	Static pressure
P_0	Stagnation pressure / total pressure
P_u	Upstream pressure
Pr	Prandtl number
Q	Heat transfer
$\dot{Q}$	Heat-transfer rate / thermal power
R	Gas constant; radius; or fitting coefficient, depending on context
R^2	Coefficient of determination
Re	Reynolds number
Re_p	Particle Reynolds number
T	Temperature
T_{in}	Inlet temperature
T_{out}	Outlet temperature
T_s	Surface temperature of the heating section

Symbol	Definition
t	Time
t_{burst}	Active gas-discharge or CFE burst time
u	Gas velocity
u_p	Particle velocity
u_r	Relative velocity between gas and particle
V	Velocity or volume, depending on context
v	Particle or molecular velocity, depending on context
W	Mechanical work
W_{F_c}	Effective work above a selected cut-off force
x	Axial coordinate / distance along the nozzle
y	Lateral coordinate
z	Vertical coordinate / out-of-plane coordinate
α	Absorption coefficient or proportionality coefficient, depending on context
γ	Ratio of specific heats, C_p/C_v
Δ	Raman peak separation, especially $A_1g - E_2g^1$ for MoS_2; change in a quantity
ΔG	Change in free energy
ΔG_{CFE}	CFE-induced change in free-energy barrier
ΔT	Temperature difference
ΔT_{lm}	Log mean temperature difference
ε	Molar absorptivity in the Beer–Lambert relationship; Lennard-Jones energy parameter, depending on context
λ	Wavelength
μ	Dynamic viscosity
ν	Frequency or kinematic viscosity, depending on context
ρ	Density
ρ_g	Gas density
ρ_p	Particle density
σ	Lennard-Jones size parameter; stress or surface density, depending on context
τ	Shear stress
ω	Phonon frequency / Raman peak position
A_1g	Out-of-plane Raman vibrational mode of MoS_2

Symbol	Definition
E_2g	In-plane Raman vibrational mode of h-BN
E_2g^1	In-plane Raman vibrational mode of MoS_2

List of Abbreviations

Abbreviation / Notation	Full Term
1T-MoS_2	Metallic octahedral phase of molybdenum disulfide
2D	Two-dimensional
2D band	Second-order Raman band of graphitic materials
2H-MoS_2	Semiconducting trigonal-prismatic phase of molybdenum disulfide
3R-MoS_2	Rhombohedral phase of molybdenum disulfide
AFM	Atomic force microscopy
Air-CFE	Compressible Flow Exfoliation using compressed air as the carrier gas
AIREBO	Adaptive intermolecular reactive empirical bond order
AIREBO–M	Adaptive intermolecular reactive empirical bond order-Morse
Ar	Argon
BET	Brunauer–Emmett–Teller surface-area analysis
BN	Boron nitride
BNNS	Boron nitride nanosheet
CD	Converging–diverging
CFE	Compressible Flow Exfoliation
CFF	Cross-flow filtration
CFD	Computational fluid dynamics
COM	Center of mass
CVD	Chemical vapor deposition
D band	Defect-activated Raman band of graphitic materials
DI	Deionized
DI/IPA	Deionized water/isopropyl alcohol co-solvent
DMF	N,N-dimethylformamide
DMSO	Dimethyl sulfoxide
DUV	Deep ultraviolet
EMI	Electromagnetic interference
FET	Field-effect transistor
FFT	Fast Fourier transform
FLG	Few-layer graphene

Abbreviation / Notation	Full Term
FWHM	Full width at half maximum
G band	In-plane graphitic Raman band
GNP	Graphene nanoplatelet
GO	Graphene oxide
He	Helium
He-CFE	Compressible Flow Exfoliation using helium as the carrier gas
HER	Hydrogen evolution reaction
h-BN	Hexagonal boron nitride
HPP	Hyperbolic phonon polariton
HRTEM	High-resolution transmission electron microscopy
IPA	Isopropyl alcohol / isopropanol
ITO	Indium tin oxide
LAMMPS	Large-scale Atomic/Molecular Massively Parallel Simulator
LED	Light-emitting diode
LJ	Lennard-Jones
LMTD	Log mean temperature difference
LPE	Liquid-phase exfoliation
MAX	MAX phase layered carbide/nitride precursor for MXenes
MBE	Molecular beam epitaxy
MD	Molecular dynamics
MoS_2	Molybdenum disulfide
MoO_x	Molybdenum oxide species
MXene	Transition metal carbide, nitride, or carbonitride two-dimensional material
N_2	Nitrogen gas
N_2-CFE	Compressible Flow Exfoliation using nitrogen as the carrier gas
NIR	Near infrared
NMP	N-methyl-2-pyrrolidone
NVE	Constant number, volume, and energy ensemble
NVT	Constant number, volume, and temperature ensemble
OPR	Oxygen permeation rate
PET	Polyethylene terephthalate

Abbreviation / Notation	Full Term
PLD	Pulsed laser deposition
PMF	Potential of mean force
PVD	Physical vapor deposition
RANS	Reynolds-averaged Navier–Stokes
RC	Reaction coordinate
RC I	Lateral sliding reaction coordinate
RC II	Edge-peeling reaction coordinate
RC III	Normal / vertical separation reaction coordinate
rGO	Reduced graphene oxide
RF	Radio frequency
RMSD	Root mean square displacement
rpm	Revolutions per minute
SEM	Scanning electron microscopy
SMD	Steered molecular dynamics
SO_x	Sulfur oxide species
STEM	Scanning transmission electron microscopy
TEM	Transmission electron microscopy
TFF	Tangential flow filtration
TMD	Transition metal dichalcogenide
UHP	Ultra-high purity
UV	Ultraviolet
UV–Vis	Ultraviolet–visible spectroscopy
vdW	van der Waals
XPS	X-ray photoelectron spectroscopy
XRD	X-ray diffraction
B 1s	Boron 1s XPS core-level region
C 1s	Carbon 1s XPS core-level region
Mo 3d	Molybdenum 3d XPS core-level region
N 1s	Nitrogen 1s XPS core-level region
O 1s	Oxygen 1s XPS core-level region
S 2p	Sulfur 2p XPS core-level region

Abbreviation / Notation	Full Term
S 2s	Sulfur 2s XPS core-level region
C–B	Carbon–boron bonding environment
C–C	Carbon–carbon bonding environment
C–H	Carbon–hydrogen bonding environment
C–N	Carbon–nitrogen bonding environment
C–N–B	Mixed carbon–nitrogen–boron bonding environment
C–O	Carbon–oxygen bonding environment
C=O	Carbonyl bonding environment
N–B	Nitrogen–boron bonding environment
N–C	Nitrogen–carbon bonding environment
O–B	Oxygen–boron bonding environment
O–H	Hydroxyl bonding environment

Chapter 1: Introduction

1.1 Background and Motivation

The isolation of Graphene in 2004 marked a fundamental paradigm shift in condensed matter physics, demonstrating for the first time that thermodynamically stable, two-dimensional (2D) atomic crystals could exist at room temperature [1]. Before this discovery, theoretical frameworks such as the Mermin-Wagner theorem suggested that thermal fluctuations would destroy the long-range order of strictly 2D lattices. However, the successful extraction of a single atomic layer of carbon demonstrated the stability of atomically thin crystals under experimental conditions and unveiled a new class of materials with extraordinary physical properties [1, 2]. Graphene exhibits massless Dirac fermions, exceptional mechanical strength (~1 TPa), and superior thermal conductivity, immediately positioning it as a transformative material for next-generation electronics, composites, and energy storage [2, 3, 4].

This breakthrough catalyzed a global research effort to identify other bulk crystals that could be exfoliated into atomically thin layers. Today, the family of 2D van der Waals (vdW) materials has expanded into a vast library, each offering distinct electronic, optical, and chemical behaviors [5, 6]. Despite this progress, a significant gap remains between laboratory-scale research and commercial application. The primary bottleneck is the lack of scalable, cost-effective manufacturing techniques. While high-quality flakes can be obtained via mechanical exfoliation, this process is inherently unscalable. Conversely, existing top-down approaches also suffer from critical drawbacks, mechanical exfoliation is inherently unscalable, while liquid-phase and shear-assisted techniques are often plagued by low single-pass efficiency, extended processing times, and a reliance on hazardous solvents that degrade material quality [7]. Consequently, there is an urgent industrial need for novel exfoliation strategies that can achieve high-throughput production of high-quality nanosheets without the limitations of current batch processing or toxic chemical environments [7].

1.2 Two-Dimensional (2D) Nanomaterials: Overview

The definition of 2D materials extends far beyond Graphene, encompassing a diverse spectrum of crystals that share a common structural motif: strong covalent or ionic bonding within the atomic plane and weak van der Waals interactions between adjacent layers [8, 9]. This extreme geometric anisotropy allows bulk crystals to be delaminated, or "exfoliated", into single or few-layer sheets that retain their structural integrity. The field now includes materials covering the entire range of electronic properties, from semimetals and semiconductors to insulators and superconductors.

At the forefront of this family is Graphene, which serves as the prototype semimetal with zero-bandgap behavior and ultra-high electron mobility. Following its success, researchers have synthesized other elemental monolayers, collectively known as "Xenes," such as phosphorene (black phosphorus) and Borophene [8, 10]. Unlike Graphene, phosphorene offers a tunable direct bandgap, bridging the gap between Graphene and silicon technologies, though it often requires passivation to prevent degradation. Complementing these are the transition metal dichalcogenides (TMDs), such as molybdenum disulfide (MoS_2). These materials are critical for optoelectronics because they transition from an indirect bandgap in their bulk form to a direct bandgap at the monolayer limit, enabling efficient light emission and absorption [11, 12]. The library of materials also includes essential insulators like hexagonal boron nitride (h-BN), often referred to as "white Graphene." Due to its wide bandgap, atomic smoothness, and chemical inertness, h-BN acts as an ideal dielectric substrate and encapsulation layer for high-performance devices [13]. More recently, the field has expanded to include complex families such as MXenes (transition metal carbides and nitrides), which combine metallic conductivity with hydrophilic surface terminations, making them highly effective for electromagnetic shielding and electrochemical energy storage [14]. This vast diversity allows for the creation of van der Waals heterostructures, where different 2D layers are stacked to engineer entirely new artificial materials with tailored properties.

1.3 Current Exfoliation Techniques and Their Limitations

The field of 2D material synthesis began with micromechanical cleavage, famously known as the "Scotch tape" method. This top-down technique, used by Novoselov and Geim to isolate Graphene for the first time, involves peeling atomic layers from a bulk crystal using adhesive tape [1]. It

remains the gold standard for producing crystals of the highest structural quality and cleanliness, serving as the benchmark for fundamental physics research. However, despite its simplicity and ability to yield pristine flakes, the process is inherently stochastic, labor-intensive, and produces negligible yields, rendering it strictly a laboratory-scale technique unsuitable for industrial manufacturing [1, 7].

To address the inability of mechanical cleavage to produce large-area films, researchers developed bottom-up growth strategies such as Chemical Vapor Deposition (CVD), Molecular Beam Epitaxy (MBE), and Pulsed Laser Deposition (PLD). CVD, in particular, is the primary route for growing wafer-scale films of Graphene and Transition Metal Dichalcogenides (TMDs) on catalytic substrates [5]. While effective for electronics, these bottom-up methods face significant barriers to broad commercial adoption: they are energy-intensive, require expensive substrates, and often necessitate complex "transfer processes" to move the grown films to functional surfaces, a step that frequently introduces wrinkles, cracks, and impurities [6, 7].

For applications requiring bulk quantities of nanosheets, such as composites, inks, and energy storage, scalable top-down approaches are preferred. Ball milling is one such method, utilizing shear and impact forces from grinding media to delaminate layers. While scalable, it is often destructive; the high-energy collisions tend to pulverize the material, resulting in small, defective flakes with low aspect ratios [7]. A more widely adopted compromise is Liquid-Phase Exfoliation (LPE), which disperses bulk crystals in a solvent and applies energy via ultrasonication. The resulting cavitation bubbles collapse and create shockwaves that fragment the bulk material [15, 16]. Although versatile, sonication is a time-consuming batch process that often requires hazardous high-boiling-point solvents (e.g., NMP) to prevent re-aggregation, complicating post-processing and environmental compliance [15, 16]. Similarly, emerging shear-assisted methods (e.g., high-shear mixing) improve throughput but often still rely on multiple recycling passes and specific chemical environments, limiting their integration into fully continuous production lines [17].

1.4 Compressible Flow Exfoliation (CFE): Introduction and Principles

To overcome the limitations of batch processing and solvent dependency, this research investigates CFE. This novel approach leverages the thermodynamics of high-pressure gas expansion to drive exfoliation. In CFE, bulk layered materials are suspended in a high-pressure carrier gas (e.g.,

helium, nitrogen) and forced through a converging-diverging nozzle or critical orifice. As the gas expands, it accelerates to supersonic velocities, creating a flow regime defined by rapid pressure drops and extreme turbulence [18].

The primary mechanism driving exfoliation in this process is the generation of massive strain rates and wall shear stresses within the nozzle. These hydrodynamic forces are sufficient to overcome the weak van der Waals binding energy between layers, effectively peeling the material apart in a single pass [18]. Unlike liquid-based methods, CFE operates continuously, driven by pressure differentials. Additionally, the exfoliation occurs primarily in the gas phase, allowing for the use of inert carrier gases. This minimizes chemical oxidation and removes the need for harsh solvents, offering a cleaner and more efficient pathway for producing high-quality 2D nanomaterials [18].

1.5 Research Objectives, Original Contributions, and Thesis Outline

1.5.1 Research Objectives

The overarching goal of this doctoral research is to develop a mechanistic and experimental understanding of Compressible Flow Exfoliation as a scalable gas-driven route for producing two-dimensional nanomaterials. Rather than treating CFE as a purely empirical process, this thesis connects nozzle-scale compressible flow, atomistic gas–solid interactions, exfoliation energetics, experimental optimization, and material characterization. The specific objectives are as follows:

Objective 1 – Establish the multiscale mechanisms behind compressible flow exfoliation

The first objective is to determine how compressible gas expansion contributes to the exfoliation of layered materials. This objective is addressed using continuum flow analysis, molecular dynamics simulations, and energy-based exfoliation calculations. The focus is on identifying the roles of gas velocity, pressure, density, shock location, drag force, mechanical work, gas type, temperature, and exfoliation pathway. The outcome of this objective is a mechanistic framework describing CFE as a coupled thermo-kinetic gas-driven exfoliation process rather than a shock-wave-only or wall-shear-only process.

Objective 2 – Experimentally develop, validate, and optimize a modified CFE process

The second objective is to experimentally evaluate the process variables that control recovered nanosheet concentration and material recovery. This includes validation of the reconstructed CFE

apparatus, optimization of gas preheating, carrier gas selection, pressure, precursor particle size, raw-material loading, centrifugation speed, repeated sediment re-dispersion, and sediment re-exfoliation. The outcome of this objective is the identification of operating conditions that improve recovered concentration for h-BN, Graphene, and MoS_2, especially using practical carrier gases such as nitrogen and compressed air.

Objective 3 – Characterize the structure, chemistry, and quality of CFE-produced 2D materials.

The third objective is to determine whether the improved CFE output is achieved while preserving the key structural and chemical features of the exfoliated materials. This objective is addressed through electron microscopy, Raman spectroscopy, and X-ray photoelectron spectroscopy. The focus is on nanosheet morphology, representative lateral dimensions, lattice preservation, defect-related Raman features, chemical bonding states, oxidation or surface modification, and phase retention in MoS_2. The outcome of this objective is an assessment of the quality and application readiness of CFE-produced Graphene, h-BN, and MoS_2, while leaving full device- or composite-level validation as a future development step.

1.5.2 Original Contributions of This Thesis

- It establishes a multiscale mechanistic interpretation of CFE by connecting continuum compressible-flow analysis, atomistic molecular dynamics simulations, and energy-based exfoliation calculations.
- It shows that CFE should not be interpreted as a shock-wave-only exfoliation method. Instead, the process is described as a coupled thermo-kinetic gas-driven mechanism involving particle acceleration, gas–particle momentum transfer, drag-induced work, aerodynamic shear, and thermal assistance.
- It identifies gas preheating as a key experimental modification that enables practical exfoliation using nitrogen and compressed air, reducing dependence on helium while improving recovered nanosheet concentration.
- It demonstrates that optimized CFE can be extended beyond a single material system by producing nanosheet-rich dispersions of h-BN, Graphene, and MoS_2.

- It evaluates post-exfoliation recovery strategies, including repeated sediment re-dispersion, centrifugation-based fractionation, precursor particle-size control, and Graphene sediment re-exfoliation, showing that product recovery is a critical part of CFE performance.
- It verifies through TEM, STEM, HRTEM, XPS, and Raman spectroscopy that the optimized process produces sheet-like nanomaterials while largely preserving the main structural and chemical fingerprints of Graphene, h-BN, and predominantly 2H-MoS_2.
- It provides a scientific foundation for future CFE scale-up through continuous precursor feeding, parallel multi-nozzle operation, integrated filtration-based recovery, and application-oriented testing.

1.5.3 Thesis Outline

The thesis is organized to move from the general production challenge to mechanism, optimization, product validation, and future development. Chapter 2 reviews the fundamentals of 2D materials and compares existing exfoliation techniques, establishing the limitations that motivate the development of CFE. Chapter 3 then examines CFE from a continuum compressible-flow perspective, identifying the nozzle-scale flow features, gas velocity, Mach number, density variation, drag force, and mechanical work that define the macroscopic exfoliation environment. Chapter 4 moves from the nozzle scale to the atomistic scale by using molecular dynamics simulations to evaluate how gas velocity, pressure, temperature, and gas type affect Graphene layer motion, energy transfer, sliding, and separation. Chapter 5 extends this atomistic analysis using energy-based simulations and potential of mean force calculations to compare exfoliation pathways and identify how gas flow can reduce the energetic resistance to lateral sliding and edge peeling.

The experimental part of the thesis begins in Chapter 6, where the reconstructed CFE system is validated and optimized. This chapter tests whether the mechanistic insights from Chapters 3–5 can be translated into improved recovered concentration using gas preheating, practical carrier gases, precursor-size control, centrifugation strategies, repeated recovery, and sediment re-exfoliation. Chapter 7 then evaluates whether the optimized process preserves material quality by characterizing the morphology, lattice structure, surface chemistry, and Raman signatures of CFE-

produced Graphene, h-BN, and MoS_2. Finally, Chapter 8 summarizes the findings, limitations, and directions for CFE scale-up.

Chapter 2: Literature Review

2.1 Fundamentals of Two-Dimensional (2D) Nanomaterials

Two-dimensional (2D) nanomaterials are atomically thin crystalline materials with strong in-plane bonding and weak out-of-plane van der Waals interactions between adjacent layers [8, 9]. This structural anisotropy gives 2D materials properties that differ from their bulk counterparts and, more importantly for this thesis, allows layered crystals to be separated into single- or few-layer nanosheets through exfoliation [8, 9]. In materials such as Graphene, hexagonal boron nitride (h-BN), and molybdenum disulfide (MoS_2), the strong in-plane bonds preserve the basal-plane structure, while the weaker interlayer interactions provide a pathway for delamination when sufficient mechanical, shear, or flow-induced forces are applied [9, 19]. Therefore, the production of 2D nanomaterials depends not only on the intrinsic properties of the layered material, but also on the ability of the exfoliation process to overcome interlayer attraction without causing excessive fragmentation or structural damage.

2D nanomaterials are defined by extreme anisotropy. Their mechanical, thermal, and electrical properties differ by orders of magnitude between the in-plane and out-of-plane directions [8, 9]. For instance, while Graphene exhibits the highest known in-plane thermal conductivity, its out-of-plane conductivity is limited by weak phonon coupling between layers [20]. This anisotropy extends to mechanical strength; the in-plane covalent bonds are among the strongest in nature, while the out-of-plane vdW interactions are weak, allowing for the sliding of layers that facilitates exfoliation [19]. The family of 2D materials encompasses the entire spectrum of electronic behaviors: from the superconducting and metallic (e.g., MXenes) to the semi-metallic (Graphene), semiconducting (Transition Metal Dichalcogenides, Black Phosphorus), and insulating (Hexagonal Boron Nitride) [8]. ***Figure 2.1*** illustrates the broad diversity of 2D materials and shows how their electronic bandgaps vary across metallic, semiconducting, and insulating material classes.

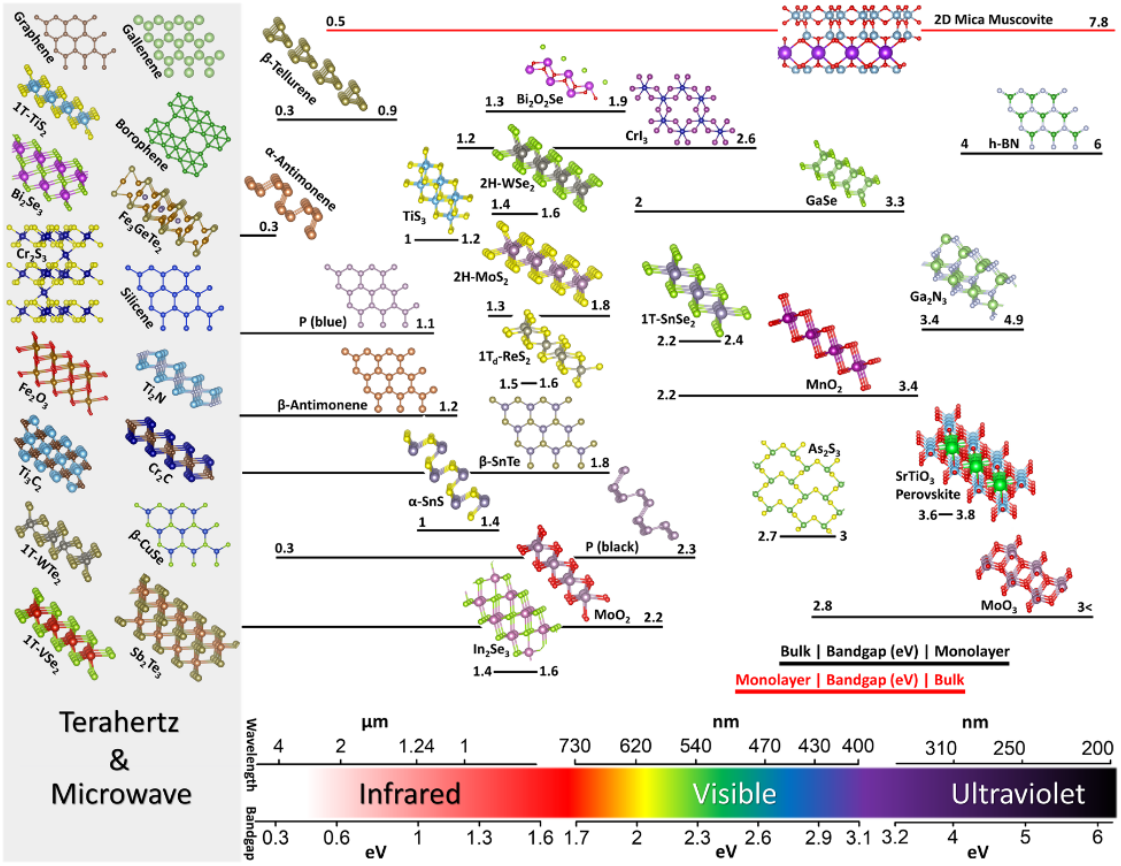

Figure 2.1: *Selected 2D materials arranged by bandgap, with perspective views of their crystal structures. Bars show the range from bulk to monolayer; black and red bars distinguish the direction of the bandgap change. The grey box contains metallic or near-zero-bandgap materials [21]. Copyright © The Author(s) 2020. Licensed under CC BY 4.0*

2.1.1 Graphene

Structure

Graphene, the first 2D material to be isolated and characterized, serves as the foundational archetype for the entire field. Isolated in 2004, Graphene consists of a single planar sheet of carbon atoms arranged in a hexagonal honeycomb lattice [20]. The atomic structure is defined by sp^2 hybridized carbon atoms, where each atom forms three strong σ-bonds with its nearest neighbors in the plane, separated by an interatomic distance of approximately 1.42 Å. These covalent bonds are responsible for the lattice's extraordinary mechanical integrity. The fourth valence electron

occupies a p_z orbital oriented perpendicular to the planar sheet. These orbitals overlap to form a delocalized π-electron system that governs the electronic transport properties of Graphene [2].
The common Graphene-derived structures discussed in this section, including few-layer Graphene, single-layer Graphene, Graphene oxide, and reduced Graphene oxide, are summarized schematically in ***Figure 2.2***.

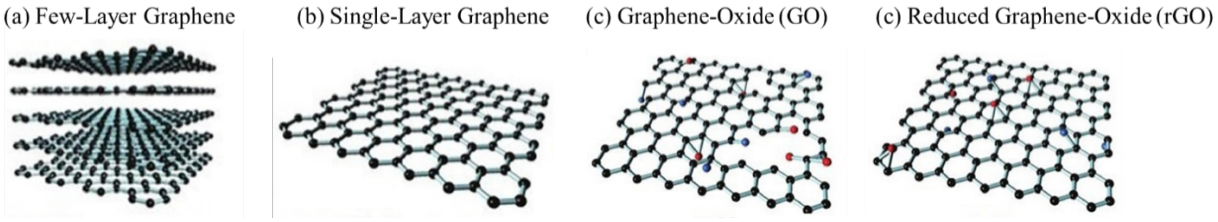

Figure 2.2: *Graphene Derivatives, a) Few-layer Graphene, b) single-layer Graphene, c) Graphene-oxide (GO) and d) Reduced Graphene-oxide (rGO) [22]. Copyright © 2020 Acta Materialia Inc. Published by Elsevier B.V.*

Properties

Graphene exhibits a suite of properties that often exceed those of any other known material, earning it the title of a "wonder material." Electronically, charge carriers in its lattice behave as massless Dirac fermions, allowing them to travel with extraordinary mobility. Theoretical values exceed 200,000 $cm^2V^{-1}s^{-1}$, and even at room temperature, experimental films routinely demonstrate mobilities of ~10,000 $cm^2V^{-1}s^{-1}$, an order of magnitude higher than silicon [2]. Graphene is classified as a zero-bandgap semimetal; while this unique band structure facilitates high conductivity and ambipolar transport (allowing carrier tuning between electrons and holes up to concentrations of 10^{13} cm^{-2}), the lack of a bandgap prevents the material from being effectively switched off, which poses a significant challenge for digital logic applications [2, 23].
Mechanically, Graphene is the strongest material ever tested, boasting an intrinsic tensile strength of approximately 130 GPa and a Young's modulus of roughly 1 TPa, far surpassing structural steel, which has a tensile strength of only ~0.4 GPa [3]. Despite this extreme stiffness, it remains highly elastic and can withstand stretching of up to 20% without brittle fracture. In terms of optical and thermal behavior, a single layer absorbs only ~2.3% of incident white light, resulting in a transparency of over 97% [24]. Furthermore, it exhibits superior thermal conductivity ranging

from 3000 to 5000 $Wm^{-1}K^{-1}$, making it highly efficient at dissipating heat [4, 20]. The key mechanical, optical, thermal, and electronic properties of Graphene are summarized in ***Table 2.1***.

Table 2.1: *Summary of Graphene Properties*

Property	Value/Characteristic	Comparison	Source
Electron Mobility	>200,000 cm^2/Vs (suspended)	>100x Silicon	[2]
Tensile Strength	~130 GPa	>200x Steel	[3]
Young's Modulus	~1 TPa	~5x Steel	[3]
Optical Absorption	2.3% per layer	Highly Transparent	[24]
Thermal Conductivity	3000–5000 $W \cdot m^{-1} \cdot K^{-1}$	> Copper (~400 $W \cdot m^{-1} \cdot K^{-1}$)	[4]
Bandgap	0 eV (Zero gap)	Logic Limitation	[2]

Applications

In the biomedical field, Graphene's high surface-to-volume ratio makes it a prime candidate for nanomedicine. Graphene oxide (GO) serves as a nanocarrier, where its π-conjugated structure allows for the loading of aromatic drug molecules via π-π stacking interactions. In photothermal therapy, Graphene nanoparticles absorb near-infrared (NIR) light to ablate tumor cells, though biocompatibility remains a critical hurdle [25]. In electronics, its combination of high conductivity and transparency positions it as a potential replacement for Indium Tin Oxide (ITO) in touchscreens and solar cells [20]. While digital logic is challenged by the zero bandgap, Graphene excels in analog radio-frequency (RF) transistors where high mobility translates to high operational frequencies [20]. Additionally, in energy storage, Graphene electrodes offer immense

surface area for supercapacitors and improve the conductivity of battery cathodes [20]. Finally, its sensitivity to surface adsorbates enables gas sensors capable of detecting single molecules (NO_2, NH_3) with ppb-level precision [26].

2.1.2 Molybdenum Disulfide (MoS_2)

Structure

Molybdenum Disulfide (MoS_2) represents the transition metal dichalcogenide (TMD) family. Structurally, it consists of a hexagonal lattice where a single layer is formed by a plane of molybdenum (Mo) atoms sandwiched between two planes of sulfur (S) atoms (S-Mo-S structure). The interaction between these atomic planes is covalent, but adjacent layers in the bulk crystal are stacked via weak van der Waals interactions, allowing for exfoliation [12]. The material exhibits polymorphism; the thermodynamically stable 2H phase is semiconducting with trigonal prismatic coordination, while the metastable 1T phase is metallic and catalytically active, featuring octahedral coordination often induced by chemical intercalation [12, 27]. The main MoS_2 polymorphs, including 1H, 1T, 2H, and 3R structures, are shown in ***Figure 2.3***.

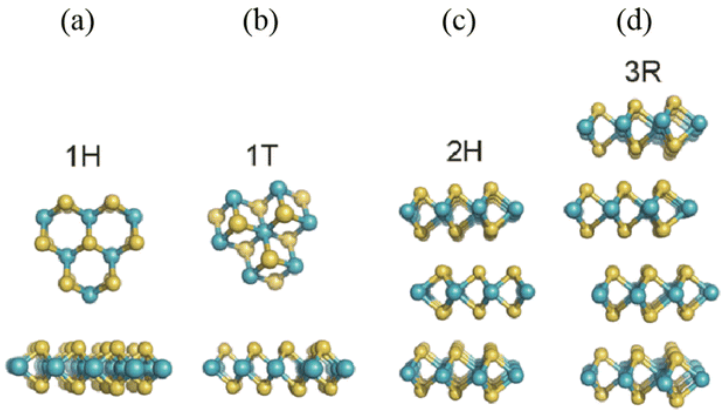

Figure 2.3: *Different polymorphs or phases of MoS_2: (a) 1H phase, (b) 1T phase, (c) 2H phase, and (d) 3R phase [28]. Copyright © 2015 The Royal Society of Chemistry.*

Properties

The most striking property of MoS_2 is the crossover from an indirect to a direct bandgap due to quantum confinement. Bulk MoS_2 possesses an indirect gap of ~1.29 eV, whereas monolayer MoS_2

exhibits a direct bandgap of ~1.90 eV. This transition enhances the photoluminescence quantum yield by a factor of $>10^4$ compared to the bulk, making the monolayer an efficient light emitter [11, 29]. Additionally, the heavy Mo atoms induce strong spin-orbit coupling, which splits the valence band at the K point. In the 2H phase, the lack of inversion symmetry combined with this coupling allowing for the selective excitation of carriers in specific valleys (K or K') using circularly polarized light [30]. Mechanically, MoS_2 is robust, though less stiff than Graphene, with the 2H phase being stiffer than the metallic 1T phase [12].

Applications

In next-generation electronics, MoS_2 Field Effect Transistors (FETs) exhibit high on/off current ratios (up to 10^8) and steep subthreshold swings, making them excellent candidates for low-power digital logic where Graphene fails [31]. In electrocatalysis, MoS_2 is a leading earth-abundant catalyst for the Hydrogen Evolution Reaction (HER), particularly when phase-engineered to the conductive 1T phase or defect-engineered at edge sites [32]. Furthermore, its direct bandgap in the visible spectrum makes it highly suitable for optoelectronic devices such as photodetectors and ultrasensitive sensors [29].

2.1.3 Hexagonal Boron Nitride (h-BN)

Structure

Hexagonal Boron Nitride (h-BN), commonly known as "white Graphene," shares the honeycomb lattice structure of Graphene with a very similar lattice constant (~2.50 Å vs 2.46 Å). This 1.7% lattice mismatch makes h-BN an ideal substrate for the epitaxial growth of Graphene and for encapsulation in heterostructures. The atoms are bonded by strong covalent sp^2 bonds within the plane, but unlike Graphene, the B-N bonds possess ionic character due to the electronegativity difference between boron and nitrogen [13, 33]. The monolayer h-BN lattice structure, consisting of alternating boron and nitrogen atoms in a honeycomb arrangement, is shown in ***Figure 2.4***.

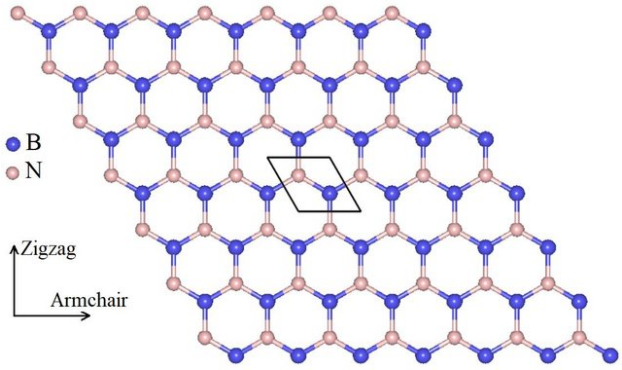

Figure 2.4: *Lattice structure of monolayer h-BN. The parallelogram denotes a primitive unit cell containing one boron atom (B) and one nitrogen atom (N). The armchair and zigzag crystallographic directions are indicated [34]. Copyright © 2020 Higher Education Press and Springer-Verlag GmbH Germany, part of Springer Nature.*

Properties

Electronically, h-BN distinguishes itself as a wide-bandgap insulator with a gap of ~5.9 eV, rendering it optically transparent and electrically insulating [35]. It features a high dielectric breakdown voltage and an atomically smooth surface free of dangling bonds [13]. Optically, it supports Hyperbolic Phonon Polaritons (HPPs) in the mid-infrared region, allowing it to confine light to volumes far below the diffraction limit [33, 36, 37]. It also possesses a direct bandgap in the deep ultraviolet (DUV) range. Thermally and chemically, h-BN is exceptionally stable, resisting oxidation up to ~1000°C in air and exhibiting high in-plane thermal conductivity [33, 36, 37].

Applications

The most critical application of h-BN is as a substrate for high-performance 2D electronics. Unlike rough SiO_2 substrates with charged impurities, atomically flat h-BN reduces electron scattering, improving the mobility of overlying Graphene devices by an order of magnitude [13]. In nanophotonics, its ability to support HPPs enables the creation of hyperlenses for sub-diffraction imaging and infrared absorbers for radiative cooling [33]. Additionally, h-BN p-n junctions are being developed for high-efficiency deep UV LEDs and photodetectors, which are crucial for sterilization technologies [35].

2.1.4 Other Emerging 2D Materials

Beyond Graphene, h-BN, and MoS_2, the family of 2D materials also includes emerging systems such as MXenes, phosphorene, silicene, and other layered or quasi-layered materials. Among these, MXenes are particularly relevant to future CFE development because they are transition metal carbides, nitrides, or carbonitrides with high electrical conductivity, hydrophilic surface terminations, and strong potential in energy storage, electromagnetic shielding, and membrane-related applications [14, 38, 39]. Phosphorene and silicene further demonstrate the broad property range of 2D materials, including tunable electronic behavior and compatibility with advanced device concepts [10, 40, 41, 42]. **Table 2.2** compares representative 2D materials in terms of structure, electronic character, key properties, and typical applications.

Table 2.2: *Comparison of Key 2D Materials*

Material	Class	Bandgap	Key Feature	Primary Application
Graphene	Semi-metal	0 eV	High Mobility, Strength	RF Electronics, Composites
MoS_2	Semiconductor	1.2-1.9 eV	Direct Gap (Monolayer)	Digital Logic, LEDs
h-BN	Insulator	~5.9 eV	Atomically Flat Surface	Substrate, UV Photonics
Phosphorene	Semiconductor	0.3-1.5 eV	Anisotropic, Tunable	Gas Sensors, IR Optics
MXene	Metal	Metallic	Hydrophilic, Conductive	EMI Shielding, Batteries

Material	Class	Bandgap	Key Feature	Primary Application
Silicene	Semi-metal	Tunable	Silicon Compatibility	Topological Devices

2.2 Production Techniques: A Comparative Analysis

2.2.1 Overview of Exfoliation Strategies

The transition of 2D materials from laboratory demonstrations to industrial implementation hinges on synthesis methods that balance material quality, yield, and cost-effectiveness. Bottom-up processes such as chemical vapor deposition (CVD) and physical vapor deposition (PVD) can produce high-quality, large-area films with monolayer precision; however, their reliance on specific growth substrates, high temperatures, and complex transfer processes limits their scalability for many bulk applications [43]. Consequently, top-down exfoliation methodologies have emerged as the primary vehicle for high-throughput production, particularly for applications such as energy storage, functional coatings, conductive inks, and composite reinforcements [9]. Exfoliation techniques are generally categorized based on the physical or chemical mechanism used to overcome interlayer adhesion. ***Figure 2.5*** illustrates the five predominant methodologies explored in this review: micromechanical cleavage, ball milling, ultrasonication, shear exfoliation, and electrochemical exfoliation. Each technique presents a unique trade-off between the density of defects introduced and the throughput achievable. For instance, micromechanical cleavage yields the highest crystallinity but remains restricted to micro-scale laboratory research, whereas liquid-phase techniques like shear exfoliation and ultrasonication offer continuous processing capabilities at the expense of reduced lateral sheet dimensions [9, 17, 44].

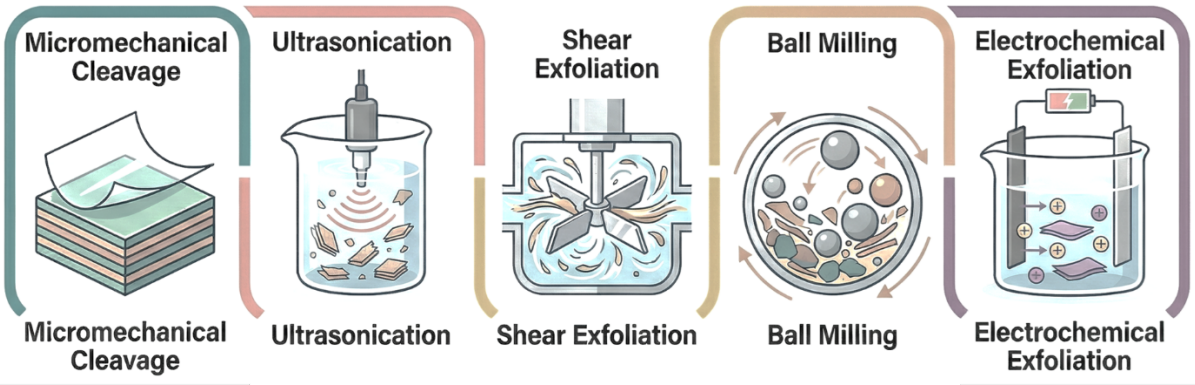

Figure 2.5: *The five most common exfoliation processes. 2D materials are most commonly exfoliated using micromechanical, ball milling, ultrasonication, shear, and electrochemical processes to separate layers of 2D materials.*

Beyond these established methods, the research landscape has expanded to include robotic automation and the exfoliation of non-van der Waals (non-vdW) crystals, which lack traditional layered analogues in their bulk form [45, 46, 47]. The following sections provide an exhaustive analysis of the mechanics governing these processes, the mathematical models used to predict their efficiency, and the resulting material properties that dictate their end-use applications.

2.2.2 Mechanics of Exfoliation

The successful exfoliation of layered 2D materials requires overcoming the weak interlayer van der Waals adhesion while preserving the stronger in-plane bonding of the nanosheet [15, 48]. The interaction between two adjacent layers can be described by the van der Waals interaction energy per unit area, which depends on the interlayer distance and the Hamaker constant [48]:

$$W = -\frac{A}{12\pi D^2} \qquad 2.1$$

where (W) is the interaction energy per unit area, (A) is the Hamaker constant, and (D) is the separation distance between the two surfaces. The corresponding adhesion force per unit area can be estimated by differentiating the interaction energy with respect to the separation distance:

$$F_{ad} = -\frac{\partial W}{\partial D} = -\frac{A}{6\pi D^3} \qquad 2.2$$

However, exfoliation does not always occur by direct normal separation of two perfectly parallel layers. The required force depends strongly on the separation pathway. In particular, peeling or

lateral sliding can reduce the effective force required for exfoliation compared with direct layer separation. For a peeling pathway, the force per unit area can be approximated as [48]:

$$F_{peel} = \frac{A}{12\pi D^2 d} \approx F_{ad}\frac{D}{2d} \quad 2.3$$

where (d) is the lateral peeling distance. Because the interlayer distance (D) is much smaller than the lateral length scale (d), the peeling force is considerably lower than the direct adhesion force. This mechanical advantage explains why layered materials can be exfoliated more effectively through shear, sliding, or edge-peeling pathways than by complete normal separation of entire layers.

In summary, the modeling of exfoliation spans from fundamental physicochemical theories regarding van der Waals forces to advanced simulation techniques and data-driven machine learning tools. These models provide the theoretical framework necessary to understand the specific mechanical, chemical, and electrochemical processes detailed in subsequent sections on specific exfoliation techniques.

2.2.3 Micromechanical Cleavage

The first exfoliation of 2D atomic layers from bulk crystals was performed using the Scotch tape method. In this process, a graphite flake is placed on a piece of tape, stuck against itself, and then peeled repeatedly. The graphite flakes become thinner on each subsequent peel, and then, the tape is pressed on a substrate to leave behind an assortment of 2D material thicknesses. The first-ever isolation of a single layer of 2D material was similarly reported by Novoselov et al. by mechanical exfoliation, also referred to as micromechanical cleavage. In their study, a fresh surface of a graphite was rubbed against another surface, which left a variety of flakes on it and was later determined by transmission electron microscopy (TEM) and atomic force microscopy (AFM) to contain monolayers [1].

Micromechanical cleavage, commonly known as the Scotch tape method, was the first successful route used to isolate Graphene and remains an important benchmark for producing high-quality 2D flakes [1]. In this method, repeated peeling mechanically separates thin layers from a bulk layered crystal, allowing single- or few-layer flakes to be transferred onto a substrate. Because the process does not require harsh chemical treatment, the resulting flakes can retain excellent

crystallinity, low defect density, and large lateral dimensions compared with many other exfoliation methods.

This method has also been applied to other layered materials, including h-BN and MoS_2, demonstrating that adhesive-based cleavage can isolate thin flakes from different van der Waals solids [49, 50]. However, the process is highly dependent on crystal quality, substrate interaction, and repeated manual peeling. As a result, the amount of recovered material is extremely small, the flake distribution is inconsistent, and the method is not suitable for high-throughput production. Repeated mechanical peeling can also fracture flakes and reduce lateral size, further limiting its usefulness for applications that require bulk quantities of nanosheets [7].

Therefore, micromechanical cleavage is best understood as a laboratory-scale benchmark rather than a scalable production method. It is valuable for fundamental studies where pristine flakes are required, but it cannot meet the material quantity, reproducibility, and throughput requirements needed for industrial applications such as composites, coatings, inks, or energy materials. This limitation motivates the development of scalable exfoliation methods that can produce useful quantities of 2D nanosheets while maintaining acceptable structural quality. The main steps and representative outputs of micromechanical cleavage are shown in ***Figure 2.6***.

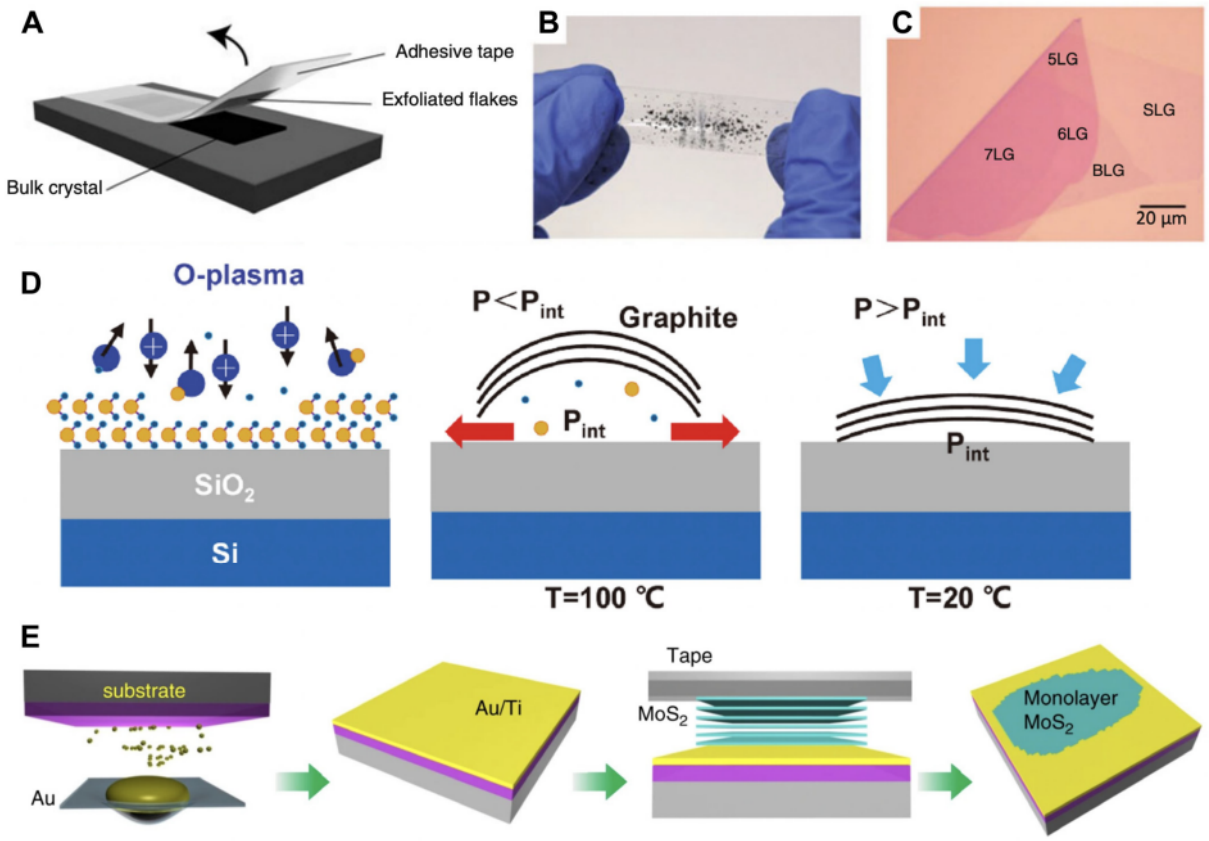

Figure 2.6: *Micromechanical cleavage techniques using scotch tape. (a) A schematic representation of the micromechanical cleavage method for exfoliating 2D material. (b) Partially exfoliated Graphene on scotch tape [51]. Copyright © 2015 American Chemical Society. (c) Optical microscope image of an exfoliated single layer, bilayer, and multilayer Graphene flakes [52]. Copyright © 2012 Elsevier Ltd. (d) Schematic representation of performing oxygen plasma treatment to remove organic residues from the substrate, annealing the substrate containing graphite on adhesive tape to enhance the adhesion between the substrate and the boundary graphite layers, and cooling the substrate to reduce the pressure at the interface between graphite and the substrate [51]. Copyright © 2015 American Chemical Society. (e) Schematic of the metal-assisted exfoliation process of 2D monolayers [53]. © 2020 The Author(s), licensed under CC BY 4.0.*

Although micromechanical cleavage is a well-known technique capable of producing 2D materials with high crystallinity and was used to exfoliate Graphene for the first time, this method remains mostly relevant for laboratory-scale studies due to low throughput and consistency. In this regard, micromechanical cleavage has been most successfully used to investigate the benchmark

properties of high-quality 2D materials for many fundamental studies. For example, in 2008 the Young's modulus and intrinsic strength of defect-free exfoliated monolayer Graphene was measured to be 1.0 TPa and 130 GPa, respectively, making it one of the strongest materials available [3]. This mechanical cleavage method has also been used to exfoliate pristine 2D sheets of MoS_2, h-BN, and Graphene oxide proving their exceptional mechanical strength and fracture behavior [36, 54, 55]. The ultrahigh strength and stiffness values of these 2D materials are attributed to the pristine nature of 2D materials when produced by exfoliation, including a structure free of point defects and without out-of-plane bonding (i.e., only covalent sp^2 bonding in Graphene sheets).

Micromechanically exfoliated 2D materials are valuable because they can retain near-pristine crystal quality, making them useful for fundamental studies of intrinsic mechanical and electronic properties. For example, mechanically exfoliated Graphene and h-BN have been used to evaluate layer-dependent mechanical behavior, while exfoliated Graphene and MoS_2 have enabled high-performance electronic device studies [7, 31]. However, these examples mainly demonstrate the quality of flakes produced by micromechanical cleavage rather than the scalability of the method. Because the process produces only small quantities of material with limited reproducibility, it remains unsuitable for applications requiring bulk nanosheet production.

Micromechanical exfoliation was the first technique to isolate 2D materials from their bulk forms owing to the ease of mechanically overcoming the vdW forces in the material to split apart the layers. This technique can repeatably produce 2D materials with minimal defects and large lateral sizes, making it ideal for identifying and evaluating the fundamental properties of the materials and creating proof-of-concept designs such as 2D material FETs. However, as mechanically separating layers of 2D materials is a tedious process with low throughput, this technique has been largely limited to bench-scale applications [7].

2.2.4 Ball Milling

While adhesive tape-based micromechanical exfoliation was the first to demonstrate successful isolation of 2D materials, ball milling employs a similar mechanical exfoliation technique but is more suitable for batch scalability. Conventionally, ball milling is used for fragmentation and mixing metallic powder to fabricate alloys, but recently, researchers have employed this method

to exfoliate layered 2D materials in bulk quantities. As the balls roll and bounce in the mill along with the 2D material, they exhibit shear, rolling, and impact forces on the 2D material, which can overcome the vdW bonding and separate 2D layers. For example, Lee et al. demonstrated a technique to ball mill BN in the presence of sodium hydroxide (NaOH) [56]. Synergistic shear and hydroxylation enable cutting into the h-BN plane, which induces minimal structural damage while yielding a high percentage of flakes up to 1.5 μm in width with a yield of 18%. However, ball milling alone is very aggressive and has been shown to induce basal plane and edge defects in layered materials [57]. This is because two significant mechanisms are in play during the ball mill exfoliation process; shear forces by rolling of the balls allow for large area exfoliation of 2D materials, while the impact forces of bouncing balls break the agglomerated particles into smaller ones. The impact forces can additionally fragment the 2D sheets, which can lower yield, reduce lateral size, and induce defects in the exfoliated sheets. Despite this disadvantage, ball milling produces a significantly higher yield of layered materials compared to other 2D material synthesis techniques and is easily scalable to industrial volumes.

Ball milling is a widely employed technique used to exfoliate a variety of 2D materials including MoS_2 [58], Graphene [59], and h-BN [60]. These high-yield processes have successfully produced exfoliated 2D materials for use in lubrication oil, electrochemical energy storage, conductive polymers, and Li-ion batteries [61]. Part of this success can be attributed to milling-generated defects, which are actually beneficial in engineering the properties of 2D materials for applications such as energy storage where the defects provide more active adsorption sites, allow faster diffusion, and enhance storage capacity [62]. One major consideration for ball milling is that different milling parameters are vital in determining product quality and yield. Deepika et al. systemically studied milling parameters such as milling speed, ball-to-powder ratio, and ball size to optimize the system for the highest efficiency and product yield. Smaller balls (0.1–0.2 mm), intermediate speeds of approximately 800 rpm, and a ball-to-powder ratio of 10:1 exfoliated layered h-BN most efficiently. Under this optimum condition, they reported a yield as high as 13.8%, and the h-BN were 0.5-1.5 μm in diameter and a few nanometers thick [63]. The impact- and shear-assisted exfoliation mechanisms involved in ball milling are illustrated in ***Figure 2.7***.

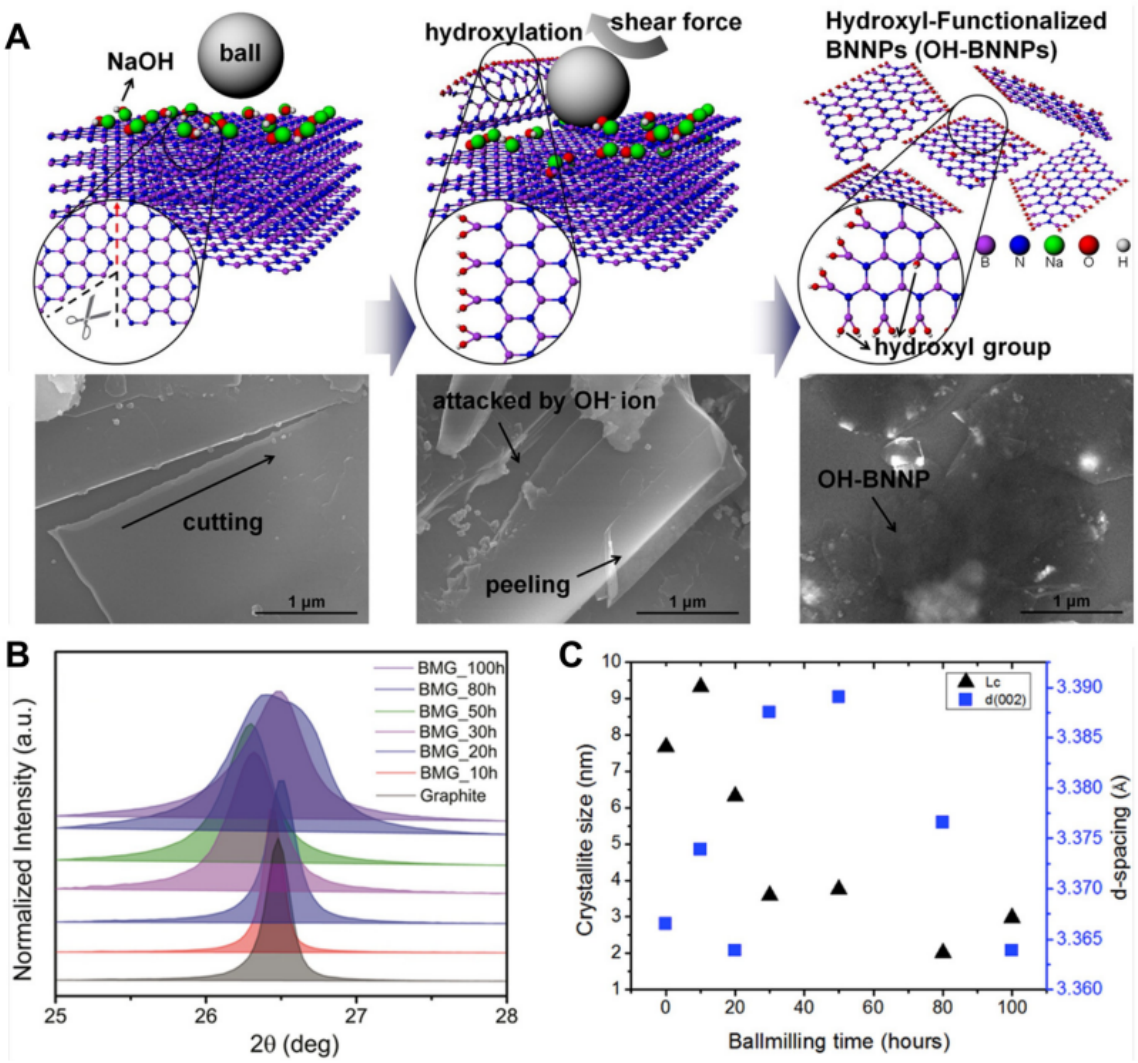

Figure 2.7: *Ball milling exfoliation mechanisms of 2D materials. (a) Schematic diagram and corresponding SEM images of the exfoliation mechanism of h-BN [56]. Copyright © 2015 American Chemical Society. (b) XRD and (c) variation of interplanar spacing with milling time of ball-milled Graphene [57].*

Ball milling can also be modified using plasma-, salt-, hydrothermal-, or additive-assisted conditions to improve exfoliation efficiency, reduce restacking, or enable one-step functionalization. These assisted approaches are useful because ball milling can generate both impact and shear forces while processing relatively large quantities of material [59, 64, 65]. However, detailed energy-transfer models and extended composite examples are not necessary here. For this thesis, the key point is that ball milling is scalable and versatile, but the repeated

high-energy collisions can also fragment flakes, introduce defects, reduce lateral size, and produce broad thickness distributions [7, 60, 63]. Therefore, ball milling is suitable for applications that can tolerate thicker or more defective nanosheets, but it remains limited when large, highly crystalline, few-layer materials are required.

The mechanical exfoliation of 2D materials by ball milling is a batch-scalable process that has demonstrated extremely high yields of many types of 2D materials. However, the aggressive nature of the technique leads to high defect densities and smaller lateral sizes, which is restrictive for some of the end applications of these materials. As the result, one of the best applications for ball-milled 2D materials is the production of polymer composites, including mechanical reinforcement and thermal and electrical conductivity enhancement for multifunctional applications [66].

2.2.5 Ultrasonication

While micromechanical cleavage and ball milling induce exfoliation by physically separating layers, many materials can be solution-processed and exfoliated through the relatively gentler process of ultrasonication. During ultrasonication, a solution containing dispersed bulk materials is exposed to a transducer that emits ultrasonic waves throughout the material. These ultrasonic waves generate vast swarms of unstable cavitation bubbles that, upon their inward collapse, emit high temperature, pressure, and velocity jets of liquid in the local environment. This creates a hydrodynamic shear force that leads to deagglomeration of the bulk materials and is strong enough to overcome the weak vdW forces between layers to exfoliate relatively small 2D layers from the bulk material [15]. 2D materials exfoliated via ultrasonication tend to have lateral sizes of a few micrometers, and with thicknesses no more than a few layers. Yields of ~1 wt.% are routinely achievable, which can be improved to 7–12 wt.% with further processing.

Liquid-phase exfoliation is a chemical process assisted by mechanical mechanisms, and vice versa. Therefore, the choice of medium for ultrasonication is a governing parameter and different solvents can help achieve different production objectives [67]. A study of over 40 different solvents identified surface tension as one of the most important solvent parameters and characterized solubility parameters for highly efficient exfoliation [68]. A common mechanism in which a solvent assists the exfoliation process is through interfacial tension by reduction of the potential energy within layers to overcome vdW forces of the layered material. The greater the

difference between the surface tension of the solvent and the 2D material, the greater heterogeneity of the exfoliated sheets. Solvents with surface tensions close to that of the 2D material, such as ortho-dichlorobenzene in the case of Graphene, have shown to produce relatively large and highly homogenous dispersions without a noticeable Raman D band, indicating low defect concentration [69]. Exfoliated Graphene using sonication in N-methyl-2-pyrrolidone (NMP) and N,N-dimethylformamide (DMF) showed that the defect population of Graphene exfoliated in NMP was significantly lower than that in DMF due to the lower energy cost for creating new surface areas in NMP, which is a result of similar surface energies [70]. The cavitation-driven mechanism and representative liquid-phase exfoliation products produced by ultrasonication are summarized in ***Figure 2.8***.

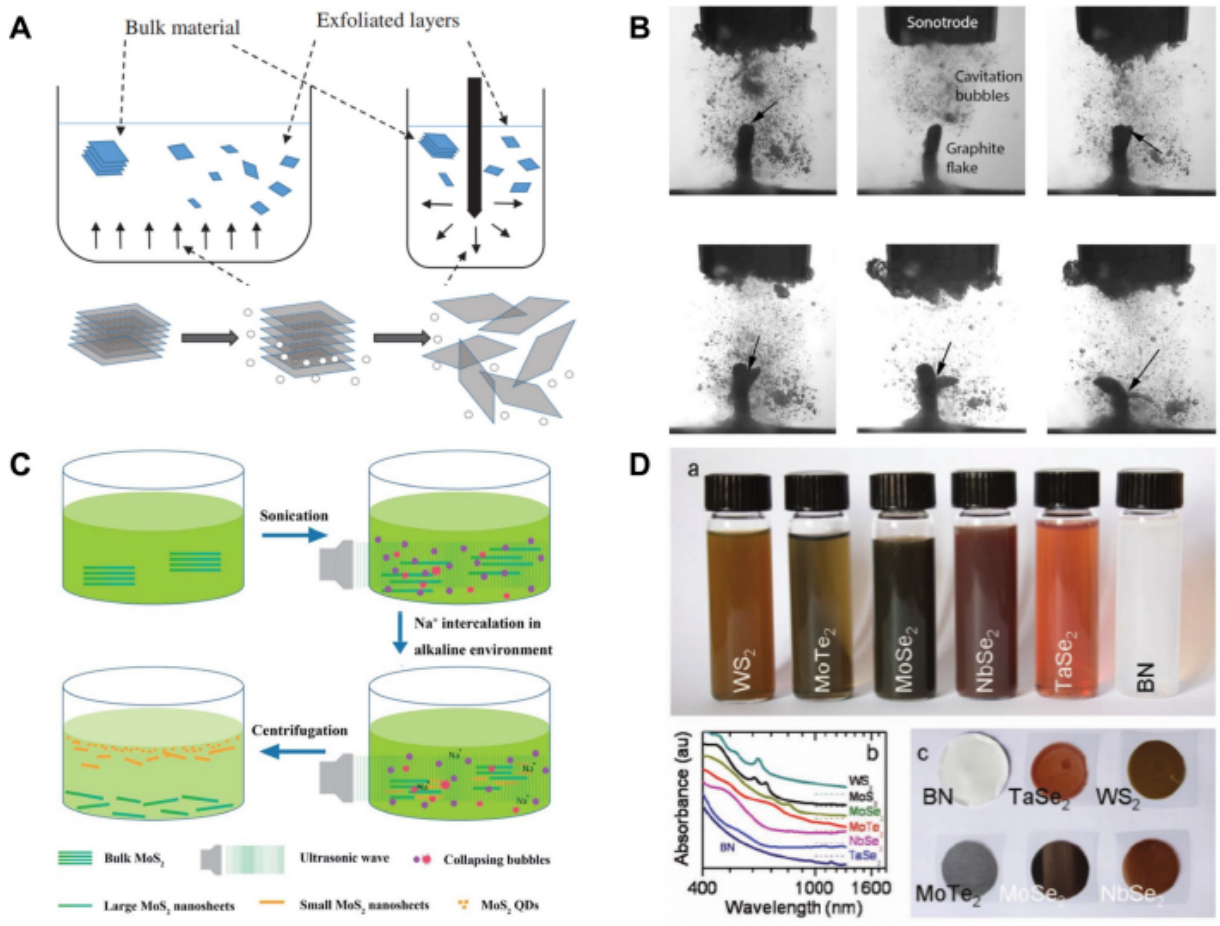

Figure 2.8: *Liquid sonication exfoliation mechanisms of 2D materials. (a) A schematic of liquid sonication demonstrating how bulk material is fragmented into 2D nanosheets using ultrasonication [67], (b) high-speed sequence of frames illustrating the ultrasonication exfoliation of a Graphene flake [71], (c) schematic of surfactant-assisted ultrasonic exfoliation of Graphene nanosheets [72], Copyright © 2012 American Chemical Society. (d) ultrasonicated WS_2, $MoTe_2$, $MoSe_2$, $NbSe_2$, $TaSe_2$, and h-BN stabilized in water using sodium cholate [73]. Copyright © 2011 WILEY-VCH Verlag GmbH & Co. KGaA, Weinheim.*

Ultrasonication, commonly used as part of liquid-phase exfoliation (LPE), separates layered materials through acoustic cavitation in a liquid medium. During sonication, cavitation bubbles form, grow, oscillate, and collapse, producing localized shock waves, microjets, and shear forces that can overcome interlayer van der Waals attraction and separate bulk layered crystals into nanosheets [9, 67, 71]. The exfoliation efficiency depends strongly on the solvent, sonication

power, sonication time, and the ability of the liquid medium to stabilize newly exposed nanosheet surfaces.

Solvent and additive selection is central to LPE because exfoliated nanosheets tend to reaggregate after separation. Suitable solvents can reduce the surface-energy mismatch between the liquid and the nanosheet surface, while surfactants, polymers, and ions can stabilize dispersions through electrostatic or steric repulsion [44]. For example, surfactant-stabilized aqueous exfoliation has been used to produce dispersions of Graphene, h-BN, and transition metal dichalcogenides, while organic solvents such as N-methyl-2-pyrrolidone have been used to disperse Graphene by improving solvent–Graphene compatibility [44]. After sonication, centrifugation is typically required to remove unexfoliated bulk particles and isolate the nanosheet-rich supernatant.

Despite its versatility, ultrasonication/LPE has several limitations. The process often requires long sonication times, careful solvent or surfactant selection, and additional post-processing to remove excess solvent, surfactant, or unexfoliated material. Increasing sonication time or amplitude can improve exfoliation yield, but it can also fragment flakes, reduce lateral size, and increase defect density, especially in Graphene-based materials [74]. Cavitation conditions therefore need to be controlled carefully: strong collapse events can enhance exfoliation but may also damage nanosheets, whereas more stable cavitation can provide gentler repeated forces with reduced defect formation [75]. Overall, ultrasonication/LPE is a widely used and adaptable exfoliation route, but it remains limited by processing time, solvent handling, post-processing requirements, and the trade-off between exfoliation yield and nanosheet quality.

2.2.6 Shear Exfoliation

An alternative method for solution exfoliation of 2D materials, which is also highly scalable, is high shear mixing. This technique involves exfoliating nanoparticle agglomerates in a solution by the viscous forces that flow through a narrow channel with very high velocity. The viscous forces in the channel cause the solvent to exert high shear forces across the 2D particles, which, when combined with the weakening of vdW forces by the solvent solution, break the vdW bonds producing thinner sheets. Additionally, the shear forces in the solvent mechanically enhance the degree of intercalation for molecules between 2D layers, which further decreases vdW forces in a synergistic effect [76, 77]. This results in 2D sheets with a low defect content as the forces required

are much weaker than other exfoliation methods. Nonetheless, this process requires a balance of forces to ensure efficient exfoliation without breaking the exfoliated 2D sheets.

Paton et al. first demonstrated a rotary mixing process where a critical shear rate of $\sim 10^4 s^{-1}$was necessary for the shear exfoliation of Graphene in NMP [17]. The rotor-stator gap was maintained on the order of 100 μm to create high shear rates in the narrow channel. However, due to the breaking of the nanosheets, high-defect contents were recorded in 2D Graphene exfoliated at high rotor speed. To address this issue, Liu et al. used a high shear mixer to exfoliate relatively low-defect density Graphene nanosheets [78]. The shear mixer consisted of a high-speed rotor and a stator where the rotor's blades spin at high speed, expelling the solvents into the surrounding space and resulting in high-speed fluid flows in the tight space between the stator and rotor. The fluid's velocity gradient generates an enormous shear force across the 2D material, which separates the weakly bonded 2D nanosheets from the bulk material. Moreover, jet cavitation due to the high-pressure difference and collision between the particles also facilitates the exfoliation of layered materials. ***Figure 2.9*** summarizes representative shear-exfoliation configurations, including high-shear mixing and wet-jet milling approaches.

Shear exfoliation separates layered materials by applying viscous shear forces in a liquid medium. When the local shear rate exceeds a critical value, the hydrodynamic stress can overcome the interlayer adhesion between adjacent sheets and promote delamination. This critical shear condition depends on the liquid viscosity, particle size, nanosheet bending rigidity, interlayer adhesion energy, and defect or flaw size within the starting particles [17]. Therefore, shear exfoliation is controlled not only by the applied mixing speed, but also by the fluid properties and the mechanical response of the layered material.

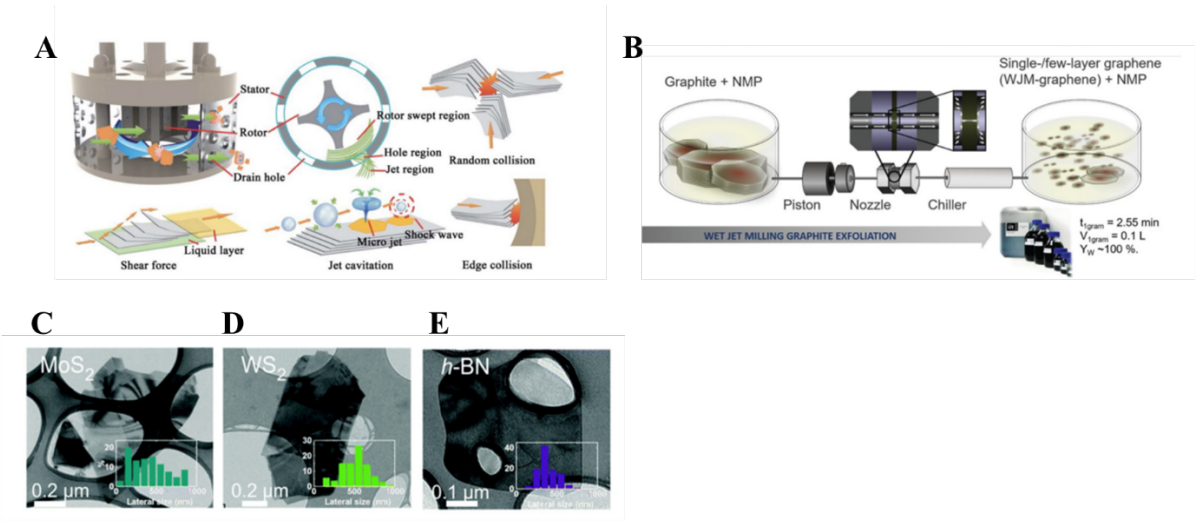

Figure 2.9: *Liquid Shear exfoliation mechanisms of 2D materials. Shear exfoliation technique. (a) Schematic of a high shear mixer and mechanisms facilitating exfoliation of layer materials in shear mixture. (b) Schematic representation of the exfoliation of few-layer Graphene from bulk graphite using the wet jet milling method. (c)–(e) MoS_2, WS2, and h-BN produced by wet jet milling [9]. Copyright © 2022 AIP Publishing LLC.*

Compared with micromechanical cleavage and conventional ultrasonication, shear exfoliation is more attractive for scalable liquid processing because it can operate in larger volumes and can be implemented using rotor–stator mixers, Taylor–Couette flow, microfluidizers, high-shear mixers, and wet-jet milling systems [17, 79] . These approaches generate strong velocity gradients or high-speed liquid flow through narrow gaps or channels, allowing exfoliation and dispersion to occur in the same processing step. Wet-jet milling is particularly relevant as a continuous shear-based method, where a pressurized liquid–particle suspension is forced through small nozzles or perforated disks to generate intense shear and homogenization [80].

Despite these advantages, shear exfoliation still relies on liquid-phase processing and therefore requires careful solvent, surfactant, or stabilizer selection to prevent restacking. It may also require multiple passes, centrifugation, or additional post-processing to separate exfoliated nanosheets from unexfoliated particles. The product quality depends strongly on the balance between applying enough shear to exfoliate the material and avoiding excessive fragmentation or lateral-size reduction. Therefore, shear exfoliation represents an important scalable route for producing 2D

nanosheets, but it still involves trade-offs among processing volume, solvent handling, yield, flake size, and post-processing complexity.

Shear exfoliation is a truly continuous process where the constant flow of material through the rotor or nozzle can produce bulk quantities of material in a liquid solution, making it an ideal synthesis method for applications requiring significant amounts of material when specific defect concentrations and monolayer precision are not required. Several different techniques can be used to produce continuous shear forces within the supernatant solution, including wet-jet milling. As shear exfoliation provides a scalable, facile, and concurrent method for synthesizing 2D material in a liquid medium, cement composites are quickly produced in a two-step process, enhancing the dispersion, mixing, and curing processes. As the most used material globally, cement reinforcement and enhancement are of utmost concern for structural applications, and cement-2D material composites have demonstrated vastly enhanced structural properties.

2.2.7 Electrochemical Exfoliation

Electrochemical exfoliation is a scalable method capable of producing a large quantity of 2D nanosheets in a liquid solution (electrolyte) using an electrical current either by cathodic reduction or anodic oxidation. The electrical current introduces ions within the electrolyte that are attracted to the bulk 2D material and intercalate between layers. This intercalation thereby weakens vdW bonds and separates layers through a one-step rate-controlled exfoliation process. Electrochemical exfoliation methods are relatively simple to design, assemble, and operate under ambient conditions. In 2014, Liu et al. first demonstrated a mechanism for anodic exfoliation of MoS_2 in an aqueous Na_2SO_4 solution [81]. The $\dot{OH}$ and $\dot{O}$ radicals are created by oxidation of water and intercalate into MoS_2 layers when a positive voltage is applied to the bulk MoS_2 electrodes. As a result of the oxidation of the radicals and anions, O_2 and/or SO_2 gas is produced, which considerably extends the interlayer distance of MoS_2 and accumulates enough to separate MoS_2 flakes from the bulk MoS_2 crystals. However, because the electrooxidation reaction takes place on the surface of the bulk material electrode, the products are oxidized quickly, which affects the quality and degree of the exfoliated MoS_2.

Parvez et al. demonstrated efficient electrochemical exfoliation of graphite using ammonium sulfate $[(NH_4)_2SO_4]$, sodium sulfate (Na_2SO_4), and potassium sulfate (K_2SO_4) [82]. They

reported that ~85% of the exfoliated nanosheets were three or fewer layers thick. The suggested mechanism of exfoliation for this system was as follows: Applying a bias voltage results in a reduction of water at the cathode, creating hydroxyl ions that act as a strong nucleophile in the electrolyte. The nucleophilic attack of graphite initially occurs at the edge sites and grain boundaries, which leads to depolarization and expansion of the graphite layers, thereby facilitating the intercalation of sulfate ions (SO_4^{2-}) within the graphitic layers. During this stage, water molecules may also intercalate with the SO_4^{2-} anions. Reduction of SO_4^{2-} anions and self-oxidation of water produce gaseous species such as SO_2 and O_2, as evidenced by the vigorous gas evolution during the electrochemical process, which separates the 2D layers. There have also been numerous other reports on the electrochemical exfoliation of Graphene using ions of H_2SO_4, Bu_4NBF_4, and other electrolytes with good yields [83, 84, 85]. The ion-intercalation and expansion mechanism responsible for electrochemical exfoliation is illustrated in ***Figure 2.10***.

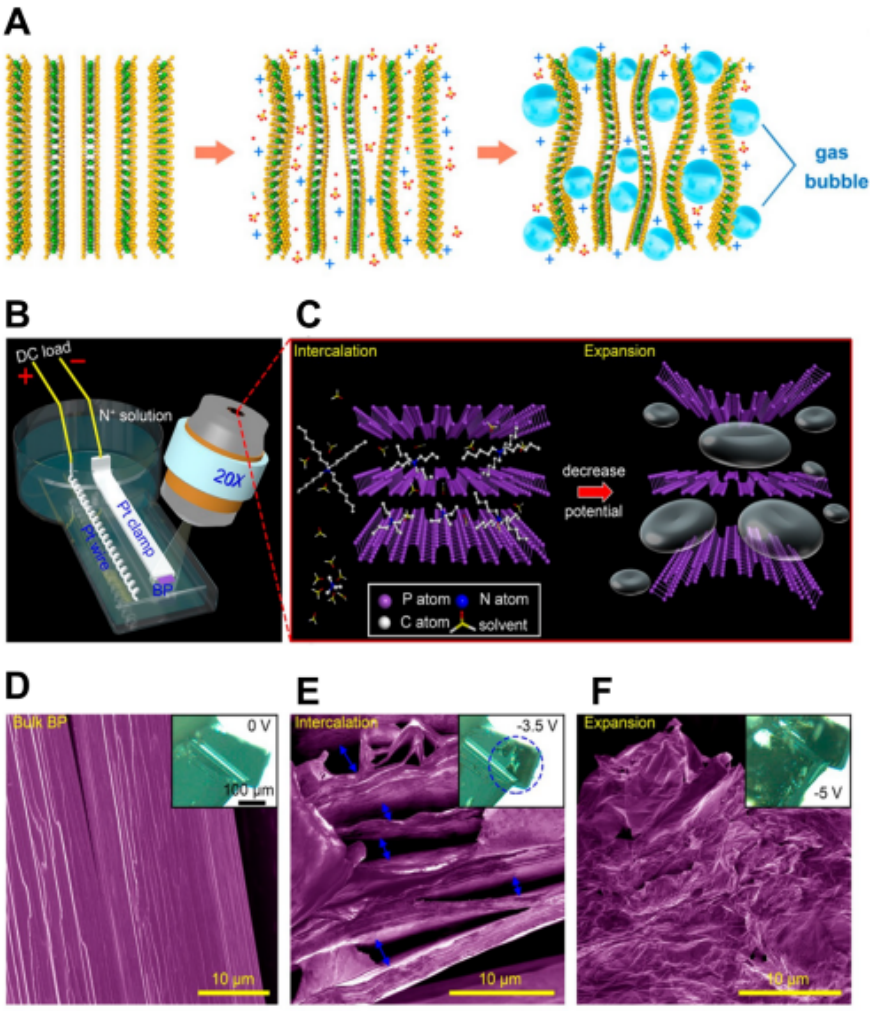

Figure 2.10: *(a) Schematic illustration of ion intercalation and exfoliation of 2D sheets in the electrochemical method. (b) Schematic of a micro electrochemical cell under a microscope. (c) Illustration of intercalation and expansion of a black phosphorous cathode in organic DMSO electrolyte. (d) False color SEM image of black phosphorous before expansion, (e) after applying a voltage of 3.5 V (double arrow shows expansion gap), and (f) 5 V [9]. Copyright © 2022 AIP Publishing LLC.*

Electrochemical exfoliation separates layered materials through ion intercalation driven by an applied electrical potential. In a typical process, ions from the electrolyte migrate into the interlayer galleries of a bulk layered material. This intercalation expands the spacing between adjacent layers and weakens the van der Waals interactions. Depending on the electrolyte and applied potential, gas evolution or electrochemical reactions can further assist layer separation, producing exfoliated nanosheets in solution [82, 83].

Compared with purely mechanical methods, electrochemical exfoliation can offer relatively high yield, shorter processing time, and better control over exfoliation conditions. The applied voltage, electrolyte composition, electrode polarity, and processing time can be adjusted to influence the extent of intercalation, flake thickness, and degree of exfoliation [86]. This makes electrochemical exfoliation attractive for producing Graphene, phosphorene, MoS_2, and other layered materials with tunable layer number and solution processability [86, 87].

However, the same electrochemical reactions that promote exfoliation can also modify the material chemically. Oxidation, functionalization, edge damage, residual ions, electrolyte contamination, and phase changes may occur depending on the operating conditions and electrolyte chemistry [82, 86]. These effects can be useful for some applications, but they are undesirable when the goal is to preserve the intrinsic structure and chemistry of the parent layered material. Therefore, electrochemical exfoliation is a powerful and controllable route for producing 2D nanosheets, but its use requires careful control of electrolyte chemistry and applied potential to balance yield, layer control, and chemical integrity.

Electrochemical exfoliation provides relatively direct control over the exfoliation environment through the applied potential or current, electrolyte composition, ion species, electrode polarity, and processing time. These parameters can influence the degree of intercalation, layer thickness, flake size, surface chemistry, and defect density of the resulting nanosheets.

Such control can be advantageous for energy-storage electrode materials, where interlayer spacing, accessible surface area, defect density, and ion-transport pathways can strongly affect electrochemical performance. Ion intercalation may expand the interlayer spacing and improve electrolyte accessibility; however, these benefits must be balanced against possible oxidation, structural damage, electrolyte residues, and undesired phase changes. Although electrochemical exfoliation can offer relatively high yield and short processing times, practical scale-up requires addressing limitations associated with electrode area, current distribution, electrolyte handling, washing, and post-processing.

2.2.8 Other Notable Exfoliation Techniques

Apart from the five well-studied exfoliation processes previously mentioned, there are reports of other interesting and unique methods to exfoliate layered materials. Some emerging methods that

present potential but have not been widely explored and adopted have been included here for discussion. Tang et al. used the interaction between polymer chains and different surfaces of MoS_2 (edge and basal plane surfaces) by a functionalized atomic force microscope cantilever to initiate polymer-based exfoliation of thin layers of MoS_2 by creating shear forces with the AFM tip [88]. Another interesting technique uses plasma-assisted exfoliation of GO by Wang et al. using a magnetically enhanced dielectric barrier discharge system to produce the plasma [89]. This was employed to exfoliate N-doped Graphene from polyaniline-modified GO to fabricate high-performance solid-state flexible supercapacitors.

MXenes are an interesting unique class of 2D material, which are synthesized by selective etching (chemical exfoliation) of MAX phases, in which the A atoms are attacked by an acid, leaving a 2D MX structure behind. This has been widely employed for various MXene materials, such as $Ti_3C_2T_x$ and Nb_2CT_x, and has unlocked a new 2D material class since the first synthesis of a stable MXene in 2011 [39]. Finally, a novel and fast method (~10 min) to exfoliate ultrathin 2D materials, including Graphene, h-BN, and BP, using liquid nitrogen and microwave treatment, was demonstrated by Zhu et al. The bulk material is first soaked in liquid N_2 and then exposed to pulsed microwaves (~700 W) to produce 2D materials of <5 nm thickness [90]. Liquid N_2 pretreatment weakens the vdW force between the layers of 2D materials before the microwaves add energy to overcome the bonds. While these techniques are indeed nonstandard, they employ the same mechanical, ultrasonic, or electrochemical approaches of the more common methods to accomplish similar outcomes through a unique methodology.

2.2.9 Summary of Production Techniques

The isolation of two-dimensional (2D) materials from their bulk counterparts has unlocked a new era of materials science, offering unprecedented electrical, mechanical, and thermal properties. Since the initial isolation of Graphene in 2005, the field has expanded to include a vast library of materials such as Graphene, TMDs, h-BN, and MXene. However, the transition from laboratory-scale discovery to commercial application hinges critically on the manufacturing process. No single synthesis method is universally superior; rather, the best technique is dictated entirely by the specific requirements of the end application, whether it be the pristine quality needed for high-speed electronics or the bulk volume required for composite reinforcement.

Top-down exfoliation methods, which separate layers from bulk crystals by overcoming weak van der Waals forces, remain the most accessible and scalable routes for production. These methods range from mechanical approaches like micromechanical cleavage and ball milling to fluid-dynamic processes like ultrasonication and shear exfoliation, as well as electrochemical intercalation. Each method involves distinct trade-offs between yield, lateral flake size, thickness control, defect density, and processing cost. For instance, while micromechanical cleavage yields the highest quality crystals suitable for fundamental research, it is inherently unscalable. Conversely, methods like shear exfoliation and ball milling offer industrial scalability but often at the cost of reduced lateral size or increased defect density.

Table 2.3 provides a comparative summary of these five primary exfoliation techniques. It details the specific materials compatible with each method, the typical dimensions of the resulting nanosheets, and a critical analysis of their respective advantages and disadvantages to guide selection for specific engineering and research needs.

Table 2.3. *Summary of Exfoliation Techniques*

Technique	Materials and Sizes	Advantages	Disadvantages
Micromechanical Cleavage	**Materials:** Graphene, h-BN, MoS_2, WS_2, WSe_2. **Sizes:** From few layers to cm thick; 10–100 nm graphite crystallites; typically, between a few and ten atomic layers; micron lateral dimensions.	• Simple and low-cost. • High-quality single-crystalline mono- and few-layer nanosheets. • Strong conductance modulation. • Electron transport properties are not degraded. • Can integrate with etching to achieve desired shapes.	• Small-scale production; not suitable for large-scale continuous monolayers. • Difficult to control flake lateral size and thickness. • Adhesive tape may leave residues. • Efficiency depends on interfacial adhesion between substrate and material.

Technique	Materials and Sizes	Advantages	Disadvantages
Ball Milling	**Materials:** Graphene, h-BN, MoS_2, sandwiched MoS_2/rGO. **Sizes:** 0.5–1.5 µm diameter; few nm thick (1–5 layers); often produces few-layered nanosheets with reduced lateral size.	• Highly scalable (batch production). • High yield (~98% reported for h-BN). • Capable of producing highly concentrated suspensions. • Low-energy milling can preserve crystal structure (tearing vs. impact).	• Difficult to obtain high yield of monolayers. • High-energy milling can fracture particles and destroy crystallinity. • Chemical species from milling agents can contaminate nanosheets. • Requires optimization of many parameters (speed, ball-to-powder ratio, etc.).
Ultrasonication	**Materials:** Graphene, h-BN, MoS_2, $MoSe_2$, $MoTe_2$, TaS_2, $TaSe_2$, $NiTe_2$, $NbSe_2$, Bi_2Te_3, WS_2. **Sizes:** Few nm to hundreds of µm laterally; mono- to few-layer (avg. ~3–10 nm thickness).	• Versatile and upscalable. • Low cost and uses standard lab equipment. • Low defect concentration and high quality. • Stable dispersions (can last >6 months). • Can deposit on various substrates.	• Uncontrollable number of layers. • Relatively low yield of single-layer sheets. • Requires long sonication times. • Potential for chemical residues from solvents. • Irregular lateral flake sizes.

Technique	Materials and Sizes	Advantages	Disadvantages
Shear Exfoliation	**Materials:** Graphene, h-BN, MoS_2, WS_2, Phosphorene. **Sizes:** Mono- and few-layer (0.3–15 nm thick); lateral sizes from 500 nm to 1.5 μm.	• Mature, scalable technology (hundreds of liters). • Flakes can be unoxidized and free of basal-plane defects. • Higher production rate than sonication. • Tunable "soft energy" source. • Concentration decays weakly with volume increase.	• Not ideal for high volume of monolayers. • Irregularities in lateral flake size. • Requires a minimum (threshold) shear rate. • Solvent matching required to balance energy. • May require assistance mechanisms (turbulence, temperature) adding complexity.

Technique	Materials and Sizes	Advantages	Disadvantages
Electrochemical Exfoliation	**Materials:** Graphene, MoS_2, WS_2, Phosphorene, Arsene, **Sizes:** Monolayer or few layers; lateral sizes up to 20 µm (large sheets 5–30 µm possible).	• Mass production capable. • High efficiency and yield. • Excellent conductivity and low defect content ($I_D/I_G < 0.1$). • Single-stage method (often no ultrasonication needed) • Can be eco-friendly in organic solutions.	• Lateral size is smaller compared to mechanical cleavage. • Surfactants/solvents may leave difficult-to-wash residues. • Cation diameter is a key factor. • Risk of structural damage (scrolling, wrinkling, fracture) and oxidation. • Wide distribution of thickness.

2.3 Compressible Flow Exfoliation (CFE)

The rapid integration of 2D nanomaterials, such as Graphene, hexagonal boron nitride, and transition metal dichalcogenides, into next-generation electronics, consumer goods, energy generation and storage, and healthcare is currently hindered by the lack of scalable production methods. This report details the development of CFE, a novel methodology utilizing the fluid dynamics of high-pressure compressible gases undergoing supersonic expansion to generate massive shear forces exceeding 10^5 s^{-1}. The study demonstrates that CFE can continuously exfoliate bulk layered materials into nanosheets with yields up to 10% in a matter of seconds. The resulting materials exhibit high quality with minimal defects, distinct from the damaged structures often produced by traditional high-energy sonication. The method's utility is validated through the fabrication of Polyethylene terephthalate (PET) nanocomposites, which showed significant mechanical and barrier improvements without compromising optical transparency, thereby offering a viable path for industrial-scale nanomanufacturing.

2.3.1 Methodology and Experimental Configuration

The fundamental principle driving the CFE technique is the utilization of stored potential energy in high-pressure gases to generate kinetic energy and shear. In comparable liquid-phase methods, shear rates of approximately ~10^4 s^{-1} are identified as critical for overcoming the Van der Waals forces holding 2D layers together [17]; however, liquids are incompressible, and achieving these rates often risks cavitation. By using compressible gases, the expansion process converts potential energy into supersonic velocities almost instantaneously. The physics is governed by the behavior of compressible fluids flowing through variable cross-sections, where the relationship between velocity change and area change dictates that in a converging-diverging nozzle, a gas accelerating towards the narrowest point (throat) becomes choked at Mach 1 [91]. Upon expanding into the diverging section, the velocity becomes supersonic (Mach > 1), creating a steep velocity gradient perpendicular to the flow direction. This gradient defines the shear rate, and the study targets shear rates exceeding 10^5 s^{-1}, an order of magnitude higher than critical thresholds for liquid exfoliation, ensuring sufficient force to delaminate the crystal structure.

The experimental apparatus for Compressible Flow Exfoliation is designed to create a continuous multiphase flow of 2D layered materials suspended in a high-pressure gas (***Figure 2.11***). The system comprises a standard gas cylinder supplying Helium, Nitrogen, or Carbon Dioxide at pressures ranging from 1.4 to 14 MPa, connected to a sample chamber acting as a reservoir for the bulk powder (hexagonal Boron Nitride, Graphite, or Molybdenum Disulfide). This mixture is forced through a fine expansion orifice, typically a Swagelok needle valve opened approximately one-quarter turn to create a 0.1 mm annular gap, or alternatively, fixed-diameter tubes. The expanding supersonic jet containing the sheared particles sprays directly into a collection vessel containing a suitable solvent, such as isopropanol. The process is characterized by its rapidity; upon opening the valve, the clear solvent transforms into a milky-white suspension for Boron Nitride in less than two seconds. For comparison, control suspensions were made using the popular liquid-phase exfoliation (LPE) method by bath sonicating the same initial concentration for 3 hours. The resulting CFE dispersions exhibit the Tyndall effect [18], confirming colloidal nanoparticles, and gravimetric measurements were used to determine concentrations. Notably, the process operates without surfactants [18], ensuring pristine interfaces.

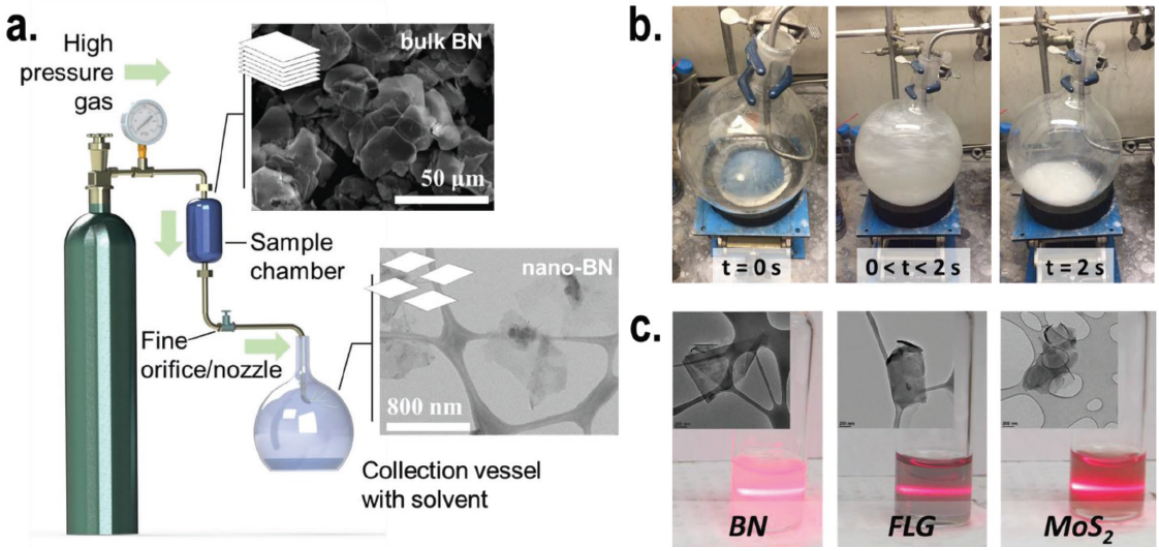

Figure 2.11: *a) Process schematic of the compressible flow exfoliation setup including a description of the critical components and the initial and final structures of the BN powder. b) Still images of the collection vessel before, during, and after the CFE process for BN powder. c) Exfoliated suspensions of various 2D layered nanomaterials after centrifugation [18]. Copyright © 2018 WILEY-VCH Verlag GmbH & Co. KGaA, Weinheim.*

2.3.2 Exfoliation Results and Material Characterization

The quality and yield were assessed using UV–Vis spectroscopy based on the Beer–Lambert law. CFE-processed Boron Nitride achieved concentrations of 0.075 $g \cdot L^{-1}$, significantly higher than the 0.004 $g \cdot L^{-1}$ obtained from LPE control samples. Graphite and Molybdenum Disulfide achieved concentrations of 0.028 and 0.026 $g \cdot L^{-1}$ respectively, compared to LPE values of 0.020 and 0.008 $g \cdot L^{-1}$. The process yield is estimated between 5% and 10% for a single pass.

Structural integrity was verified using Raman spectroscopy. For Boron Nitride, the bulk E_{2g} peak at 1366 cm^{-1} redshifted to 1362 cm^{-1} in CFE samples, while LPE controls showed no significant shift. For Graphite, bulk spectra show a G peak at 1580 cm^{-1} and a 2D peak at 2690 cm^{-1}. CFE samples showed a redshift of 8 cm^{-1} in the 2D peak and a wide symmetric peak (FWHM: 75 cm^{-1}), indicating turbostratic disorder [18]. The defect density ratio (I_D/I_G) was 0.5 for CFE, compared to 1.1 for LPE, indicating CFE is less destructive. For MoS_2, the peak separation between E^1_{2g}

and A_{1g} reduced from roughly 26 cm^{-1} (bulk) to 22.8 cm^{-1} (CFE), corresponding to 3-4 layers, whereas LPE resulted in 24 cm^{-1} (>4 layers) [18].

Atomic Force Microscopy indicated that h-BN flakes produced at 10 MPa had a mean thickness of 4.2 nm and length of 276 nm (aspect ratio 66), whereas at 5.5 MPa, thickness was 5.7 nm and length 160 nm (aspect ratio 28). At 10 MPa, 43% of flakes were less than 3.2 nm thick. Transmission Electron Microscopy confirmed electron-transparent flakes with occasional Moiré patterns indicating basal plane rearrangement. CFE flakes exhibited straight edges, while LPE flakes had rounded edges and significant debris (<50 nm) [18]. Suspensions remained stable after 6 months of storage. The UV–Vis, Raman, AFM, and TEM evidence supporting CFE-based exfoliation is summarized in ***Figure 2.12***.

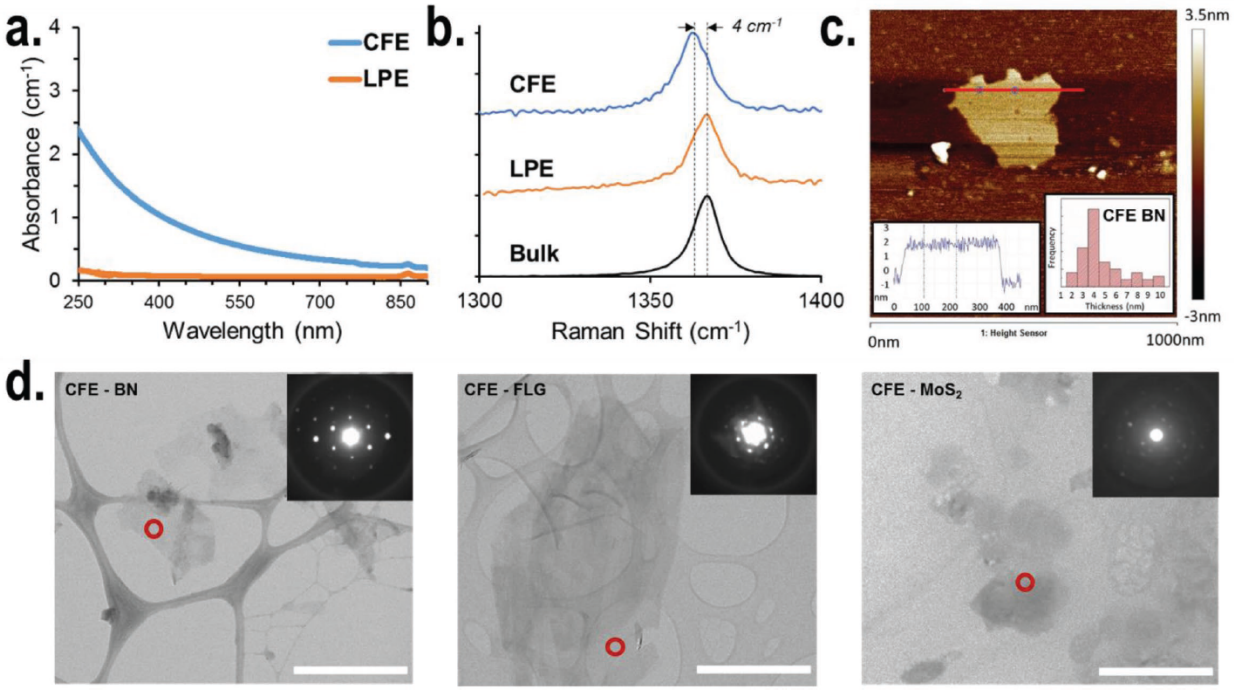

Figure 2.12: *a) UV–Vis and b) Raman spectra for h-BN produced using CFE and the comparable liquid-phase exfoliation technique. c) The AFM scan image of a BN flake isolated after CFE with insets showing the height profile of the flake and the thickness distribution of several flakes. d) The TEM images (scale bar: 800 nm) for various 2D materials produced by CFE along with their diffraction patterns (inset) at the marked spot, shown here are h-BN (left), Graphene (middle), and MoS_2 (right) [18]. Copyright © 2018 WILEY-VCH Verlag GmbH & Co. KGaA, Weinheim.*

2.3.3 Parametric Optimization of the CFE Process

The efficiency and yield of the CFE process depend heavily on the careful tuning of operational parameters, such as precursor mass loading, upstream driving pressure, flow channel geometry, and the choice of carrier gas. A series of controlled experiments using boron nitride (BN) demonstrate how these variables interact to maximize the continuous, high-throughput production of 2D layered nanomaterials.

The initial concentration is defined as the ratio of BN powder fed into the gas flow to the volume of liquid solvent it sprays into after processing. As shown in ***Figure 2.13(a)***, an increase in the initial concentration results in a concomitant rise in the final exfoliated concentration. This positive correlation holds for both variable valve (0.1 mm gap) and constant-area straight tube (2.1 mm) geometries until the mass loading becomes excessively high. At higher loadings, physical clogging restricts the flow, particularly in narrow valve geometries. Remarkably, under optimal conditions, the process yields between 5% and 10% of exfoliated material with a process run time of just 2 seconds, an efficiency highly competitive with traditional liquid-phase exfoliation methods [18].

Expansion of the compressed gas at stagnant upstream pressure through a fine orifice generates the supersonic velocities required to shear the suspended particles. The effect of driving pressure, detailed in ***Figure 2.13(b)***, varies significantly depending on the flow geometry. For a variable-area converging-diverging nozzle (a partially open needle valve), concentrations of 0.04 $g \cdot L^{-1}$ are attainable at pressures as low as 1.4 MPa (200 psi). Increasing the pressure continuously enhances the yield, reaching a maximum concentration of 0.2 $g \cdot L^{-1}$ at the maximum tested pressure of 11 MPa.

Conversely, forcing the feedstock through a constant-area straight tube results in fundamentally different fluid dynamics. The final concentration initially increases but plateaus at 0.11 $g \cdot L^{-1}$ for pressures of 5.5 MPa or greater. This plateau is governed by Fanno flow, which describes the adiabatic expansion of a compressible gas in a constant-area duct experiencing friction [91, 92]. Under Fanno flow, the expanding gas accelerates until it reaches a maximum choked velocity at the channel exit, corresponding to the local speed of sound (Mach 1). Once choked flow is achieved, further increases in upstream pressure cannot accelerate the gas further, thereby capping the applied shear rate.

The physical dimensions of the flow channels dictate the shear rate distribution. In constant-area tubes operating at 5.5 MPa, altering the inner diameter from a starting value of 4.6 mm profoundly impacts the process (***Figure 2.13(c)***). Halving the tube diameter to an optimal 2.1 mm increases the final concentration to 0.11 $g \cdot L^{-1}$, an improvement by a factor of 5.4. This enhancement occurs because a narrower channel increases the relative fraction of the high-shear near-wall zone compared to the overall flow cross-section.

However, over-constricting the channel to 1.3 mm severely deteriorates process efficiency, dropping the concentration to 0.045 $g \cdot L^{-1}$. At this diameter, the flow fails to achieve choked conditions, and exit velocities fall considerably below Mach 1. Wall friction dominates at these small diameters; for instance, reducing the tube from 2.1 mm to 1.3 mm for helium flowing at Mach 1 increases the friction factor from 0.028 to 0.035, per the Moody-Colebrook relationship [18, 92]. Additionally, this reduction lowers the Reynolds number ($Re = VD/\nu$) from 18,000 to 11,000, reducing the turbulent nature of the flow and the stochastic generation of eddies that contribute to centerline shear rates.

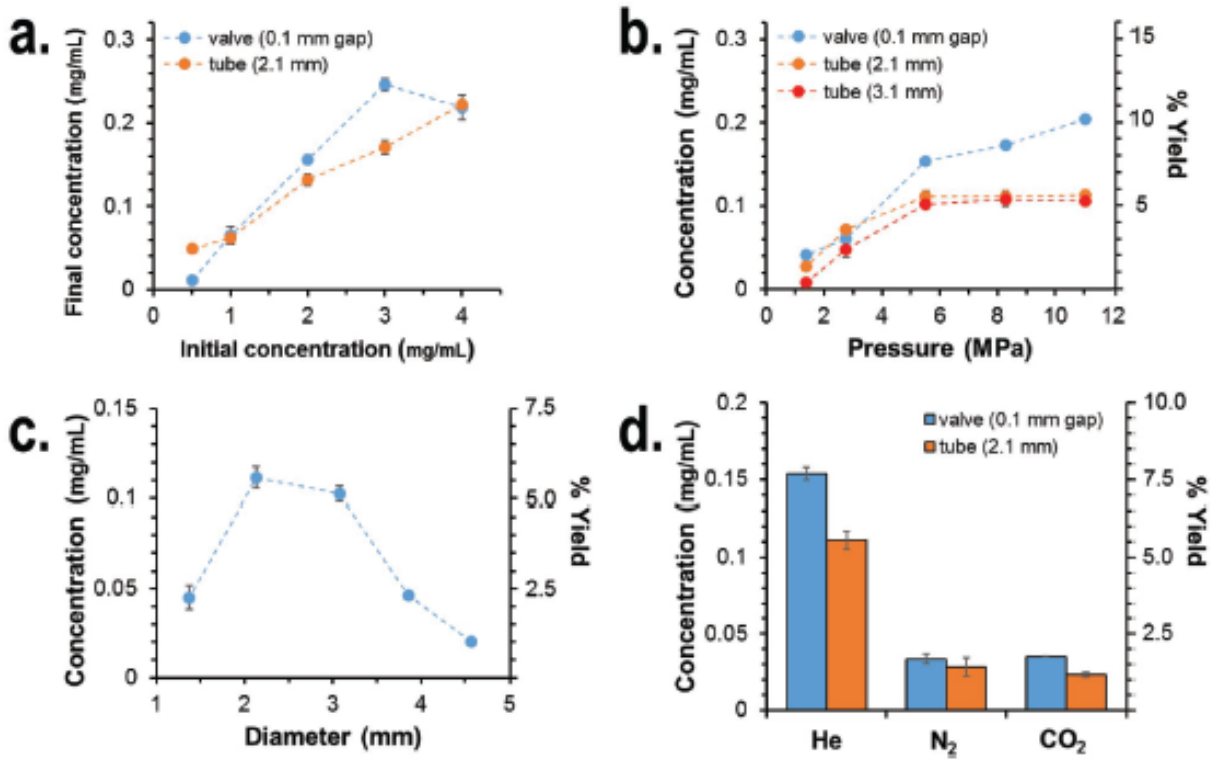

Figure 2.13: *a–d) Plots showing the effects of initial BN concentration (a), upstream gas pressure (b), flow geometry (tube diameter) (c), and carrier gas type (d) on the final BN concentration and yield in CFE. All error bars represent the standard deviation (n=3) [18]. Copyright © 2018 WILEY-VCH Verlag GmbH & Co. KGaA, Weinheim.*

The thermodynamic properties of the chosen carrier gas strictly limit the maximum achievable shear rates because choked flow velocity is bounded by the gas's speed of sound. ***Figure 2.13(d)*** demonstrates this limitation using different gases at a constant pressure of 5.5 MPa. Helium, a light monatomic gas, yields final concentrations of ~0.15 $g \cdot L^{-1}$ (in a valve configuration), nearly five times greater than heavier gases like nitrogen (~0.03 $g \cdot L^{-1}$) or carbon dioxide (~0.03 $g \cdot L^{-1}$).

This dramatic difference is tied directly to their acoustic velocities. At 293 K, the speed of sound in helium is approximately 1000 m/s, while nitrogen and carbon dioxide possess considerably lower acoustic velocities of 350 m/s and 270 m/s, respectively. Consequently, helium accelerates to much higher maximum velocities, imparting significantly higher shear rates $\dot{\gamma} > 10^5\ s^{-1}$ onto the suspended 2D particles. Although hydrogen gas possesses an even higher speed of sound (1270

m/s) and would theoretically serve as a superior exfoliating medium, safety considerations prevented its experimental evaluation.

2.3.4 Application Case Study: PET Nanocomposite

To demonstrate the practical utility of the ultrafast CFE method, exfoliated 2D layered nanomaterials were evaluated as a reinforcing phase to improve the barrier properties of poly(ethylene terephthalate) (PET). PET is widely utilized in food and beverage packaging, an application where balancing high optical transparency with strict limits on oxygen permeation has historically proven challenging [93, 94]. In this case study, highly concentrated suspensions of CFE-processed h-BN and unexfoliated bulk-BN powder were added to a powdered PET resin. Following solvent evaporation, the materials were mixed in the melt phase at 265 °C and extruded into continuous films.

Thermal analysis revealed that the fundamental melting characteristics of the PET, specifically its melting temperature (T_m) of 246 °C and enthalpy of melting (ΔH_m) of 40 $J \cdot g^{-1}$, remained statistically unchanged regardless of the type or concentration of BN added. The incorporation of BN did yield a marginal increase in the apparent glass transition temperature by approximately 1.5–2 °C. More notably, the nanocomposites exhibited distinct crystallization behaviors during cooling from the melt at a rate of 10 °C/min. The crystallization peak shifted upward from 198 °C for neat PET to 207 °C for PET containing both 0.017 and 0.15 vol% CFE-BN. In comparison, the bulk-BN composites peaked at 203 °C and 206 °C for the respective volumes. This accelerated crystallization kinetics for the CFE-BN composites is directly attributable to the potent heterogeneous nucleation effect provided by the highly dispersed exfoliated nanomaterials [18, 95].

Crucially for packaging applications, the resulting nanocomposites successfully preserved the polymer's baseline optical clarity. As detailed in ***Figure 2.14(a)***, the neat PET films exhibited an optical transmittance of 94%. The addition of either 0.017 or 0.15 vol% of CFE-BN or bulk-BN powder maintained excellent transparency, with all samples exceeding 90% transmittance. Furthermore, optical haze, defined as transmitted light subject to wide-angle scattering (>2.5° from normal), was found to be measurably lower for the films containing the exfoliated 2D nanomaterials compared to those utilizing the bulk BN aggregates.

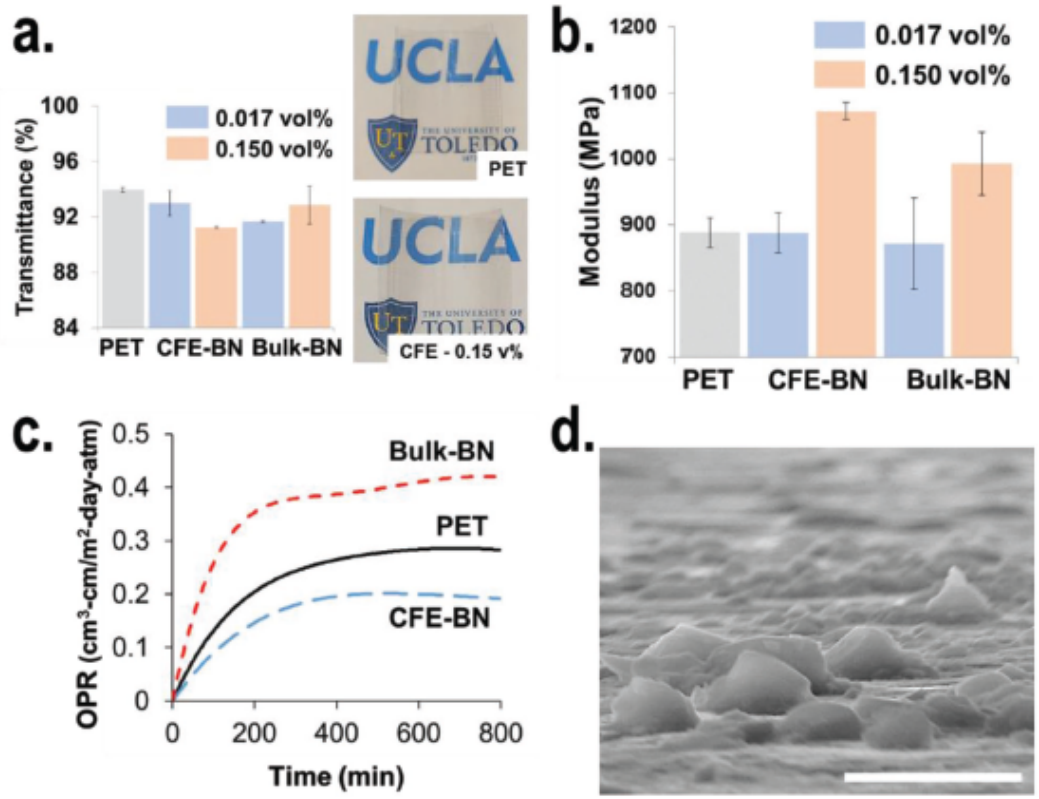

Figure 2.14: *PET-BN nanocomposites prepared using CFE exfoliated and bulk BN at 0.017 and 0.15 vol% of BN. (a) Visual light transmittance. (b) Tensile Young's modulus. (c) Oxygen permeation rate (OPR) at 0.15 vol% BN. (d) A tilted view of a freeze-fractured cross-section of PET-CFE-BN 0.15 vol% showing the protruded BN particles (scale bar: 10 µm). All error bars represent the standard deviation (n=3) [18]. Copyright © 2018 WILEY-VCH Verlag GmbH & Co. KGaA, Weinheim.*

The mechanical reinforcement of the PET matrix was highly dependent on both the volume fraction and the structural state of the additive. At a low volume content of 0.017 vol%, neither the exfoliated nanoparticles nor the bulk particles induced a noticeable difference in the tensile Young's modulus, which remained near the neat PET baseline of 888 MPa. However, increasing the loading to 0.15 vol% of CFE-BN resulted in a substantial 21% improvement in the modulus, raising it to 1072 $\pm$ 15 MPa (***Figure 2.14(b)***). Conversely, adding an equivalent 0.15 vol% of bulk-BN yielded a comparatively modest 12% improvement (993 $\pm$ 55MPa). Other mechanical parameters, including tensile strength and strain at failure, showed no significant variations regardless of the BN type or loading, likely due to the overall low volumes utilized.

The advantages of the CFE process were most pronounced in the material's barrier properties. Prior to testing, the films were biaxially stretched at low speeds and temperatures to a 20 μm thickness to prevent strain-induced crystallization. The steady-state oxygen permeation rate (OPR) of neat PET and the 0.017 vol% composites was recorded at 0.27 ± 0.01 cm³·cm/(m²·day·atm). As illustrated in ***Figure 2.14(c)***, incorporating 0.15 vol% of CFE-BN significantly enhanced the barrier, dropping the OPR by 26% to 0.20 ± 0.01 cm³·cm/(m²·day·atm). Surprisingly, incorporating the same 0.15 vol% of bulk-BN had a severely detrimental effect, increasing the OPR to 0.37 ± 0.08 cm³·cm/(m²·day·atm). This degradation likely occurred because the larger layered aggregates in the bulk-BN delaminated during the biaxial stretching phase, opening up microscopic, low-resistance pathways for oxygen transport.

Scanning electron microscopy (SEM) visually corroborated these structural differences. A tilted view of a freeze-fractured surface of the 0.15 vol% PET-CFE-BN nanocomposite (***Figure 2.14(d)***) reveals thin nanosheets protruding from the matrix, confirming the successful dispersion of the BN particles. Ultimately, the significantly improved mechanical and barrier properties of the CFE-BN nanocomposites are driven by the effective exfoliation of the layered particles into thin sheets. This morphology enables a highly efficient load transfer across the polymer-particle interface and constructs a tortuous internal labyrinth that effectively halts gas permeation.

2.3.5 Conclusions and Remaining Knowledge Gaps in CFE

Rizvi et al. [18] demonstrated CFE as a novel, continuous, and high-throughput method for producing two-dimensional layered nanomaterials. In their approach, bulk layered precursor particles were suspended in a compressible carrier gas and accelerated through fine converging-diverging nozzles to sonic or supersonic velocities. The rapid gas expansion, fluid acceleration, and strong velocity gradients generated very high shear rates, exceeding (10^5 s^{-1}), which were proposed to overcome the weak interlayer van der Waals interactions and promote exfoliation.

Using helium as the carrier gas and bulk BN as the model precursor, the study showed that CFE could produce high-quality BN nanosheet suspensions. The exfoliated BN nanosheets had an average thickness of approximately 4.2 nm and an average lateral length of approximately 276 nm, corresponding to an aspect ratio of about 65. The process also achieved suspension concentrations up to approximately 0.2 $g \cdot L^{-1}$ and reported mass recoveries of about 10% within very short

processing times. The method was further shown to be applicable beyond BN, with successful exfoliation of other layered materials such as few-layer Graphene and MoS_2 using carrier gases including helium, nitrogen, and carbon dioxide.

A key advantage highlighted in previous CFE work is the partial decoupling of the mechanical exfoliation step from the liquid-phase stabilization step. In contrast to conventional liquid-phase exfoliation, where solvent selection, sonication, exfoliation, and stabilization are strongly coupled, CFE delivers the main exfoliation energy in the gas phase and uses the liquid medium mainly for downstream capture and dispersion stabilization. This feature can reduce reliance on prolonged sonication and harsh solvent environments, potentially limiting basal-plane damage, edge degradation, and excessive fragmentation.

The practical value of CFE-produced nanosheets was also demonstrated through incorporation of CFE-BN into PET nanocomposites. Compared with composites containing bulk BN aggregates, the PET-CFE-BN nanocomposites showed improved mechanical stiffness and oxygen barrier performance while maintaining optical transparency. This application study provided evidence that CFE-produced nanosheets can retain sufficient quality for polymer nanocomposite reinforcement and packaging-related applications.

Overall, previous CFE studies established the feasibility of using compressible gas dynamics for rapid exfoliation of layered materials. They showed that CFE can produce nanosheet-rich suspensions, can be extended to more than one 2D material, and has potential advantages over conventional liquid-phase and mechanically intensive exfoliation routes. However, several important scientific and process-level questions remained unresolved.

First, the exfoliation mechanism was not fully separated into its individual gas-dynamic contributions. Previous descriptions emphasized supersonic flow, high shear rates, shock formation, and rapid expansion, but the relative roles of gas acceleration, particle–gas relative velocity, drag force, aerodynamic shear, wall interactions, shock location, and cumulative mechanical work were not clearly distinguished. Therefore, it remained unclear whether exfoliation was governed mainly by localized shock events, wall shear, or the integrated transfer of momentum and energy from the expanding gas to suspended particles.

Second, the role of carrier-gas properties required further clarification. Helium was shown to be highly effective, but its performance may result from several coupled properties, including high

speed of sound, high attainable gas velocity, low density, and strong particle–gas relative motion. For future scale-up, lower-cost and more accessible gases such as nitrogen and compressed air are more practical, but the conditions required to make these gases effective were not fully established. Third, the influence of temperature was not sufficiently connected to the CFE mechanism. If gas preheating reduces the energetic resistance to interlayer sliding or edge peeling, then temperature is not only an auxiliary process variable but a central part of the exfoliation mechanism. The relationship between gas temperature, atomistic energy transfer, interlayer weakening, and recovered nanosheet concentration therefore required systematic investigation.

Fourth, previous work did not fully resolve the role of post-exfoliation recovery. The measured product concentration depends not only on the gas-phase exfoliation event inside the nozzle, but also on particle capture, dispersion stability, centrifugation, sediment re-dispersion, and recovery of nanosheets trapped with larger particles or sediment. Therefore, recovered concentration and apparent yield must be interpreted carefully and should not be treated only as direct measures of exfoliation inside the nozzle.

These unresolved questions motivate the multiscale and experimental investigations developed in this thesis. The following chapters address CFE through continuum compressible-flow analysis, atomistic molecular dynamics simulations, energy-based exfoliation calculations, experimental optimization, and final material characterization. In this way, the thesis positions CFE as a coupled thermo-kinetic gas-driven exfoliation process rather than a purely empirical, shock-wave-only, or wall-shear-only method.

.

Chapter 3: Continuum Perspective Analysis of CFE[1]

Introduction to CFE Modeling and Multiscale Simulation Approaches

While empirical optimization has successfully demonstrated the viability of CFE as a high-throughput, continuous method for producing 2D nanomaterials [18], the highly transient and extreme conditions of the process present significant observational challenges. The fundamental mechanisms of layer separation occur within a fraction of a second, driven by supersonic gas expansion, shock wave formation, and atomic-scale momentum transfer. Because these critical fluid-solid interactions are practically inaccessible to direct in-situ experimental measurement, relying solely on empirical data limits the ability to predictably scale and optimize the process. To bridge this gap, a comprehensive multiscale computational framework is essential. By employing advanced modeling and simulation approaches, it becomes possible to elucidate the exact physical laws governing the CFE process, translating macroscopic operational parameters, such as upstream pressure, gas type, and nozzle geometry, into atomic-scale thermodynamic outcomes.

To fully capture the physics of CFE, simulation approaches must span multiple length and time scales. At the continuum scale, the rapid expansion of compressible gases through converging-diverging (CD) geometries or narrow orifices generates complex flow structures, including choked flow, Fanno flow dynamics, and normal shock waves. Computational Fluid Dynamics (CFD) and quasi-one-dimensional Euler analyses are indispensable at this macroscopic level. These tools resolve the spatial gradients of velocity, density, and pressure, allowing for the precise calculation of aerodynamic drag and thrust forces exerted on the suspended bulk nanomaterials.

However, fluid dynamics alone cannot explain the thermodynamic energy barriers of the 2D materials themselves. To understand how these macroscopic aerodynamic forces translate into

---

[1] *Publication and Author Contribution Statement. Portions of this chapter are adapted from: Islam, M. F., Arabha, S., Hixon, R., and Rizvi, R. "Compressible Flow Exfoliation of Two-Dimensional Nanomaterials: Insights Into Layer Separation Informed by Gas Dynamics."* Advanced Engineering Materials *28 (2026): e202502168.* https://doi.org/10.1002/adem.202502168.

Saeed Arabha made substantial contributions to the development and refinement of the continuum-flow analysis, data analysis and visualization, interpretation of the gas–particle dynamics, development of the mechanistic discussion, manuscript preparation, revision, and finalization of the published article. The thesis chapter expands the published work by integrating the continuum analysis into the broader multiscale framework developed in this dissertation.

actual layer separation, the analysis must transition to the atomistic scale. Classical Molecular Dynamics (MD) simulations and Potential of Mean Force (PMF) calculations provide the necessary thermodynamic and kinetic resolution at the gas-solid interface. At this molecular level, exfoliation is fundamentally a free-energy problem governed by the rigid sp^2-hybridized carbon lattice and the relatively weak interlayer van der Waals (π-π) interactions. MD simulations enable the tracking of discrete, highly energetic collisions between the high-velocity carrier gas atoms and the 2D lattice. These simulations reveal how kinetic momentum transfer from the gas amplifies the intrinsic thermal vibrations of the nanosheets, actively weakening interlayer cohesion.

Furthermore, atomistic simulations allow for the mapping of specific reaction coordinates, such as lateral sliding versus edge peeling. By calculating the potential of mean force required to physically separate the sheets under various simulated flow conditions, MD provides a quantitative measure of how macroscopic variables lower the thermodynamic barrier to exfoliation. For example, atomic-scale analysis explains why lighter, high-velocity gases like helium excel at transferring kinetic energy, and how strategic gas mixtures (such as helium entraining heavier argon atoms) can create synergistic collisional dynamics that maintain high exfoliation efficiency at a reduced economic cost.

Ultimately, this multiscale approach, integrating macroscopic fluid kinematics with atomic-scale thermodynamics, transforms CFE from an empirical black box into a predictable, designable manufacturing paradigm. The following sections of this chapter will detail these computational methodologies, presenting a rigorous analysis of flow dynamics, force generation, and the free-energy landscapes that dictate the high-volume aerodynamic production of 2D layered nanomaterials.

3.1 Multiscale Modelling Strategy for CFE

The objective of this chapter is to identify the continuum-scale gas-dynamic conditions created inside the CFE nozzle and to determine which flow features are most relevant to particle forcing and possible exfoliation. Previous descriptions of CFE often emphasized supersonic flow, shock formation, and high shear rates [18]. Although these features are important indicators of an intense compressible-flow environment, they do not by themselves explain how mechanical energy is transferred to suspended layered particles. For this reason, this chapter evaluates not only Mach

number and shock position, but also gas velocity, density variation, particle–gas relative velocity, drag force, and cumulative mechanical work.

This continuum analysis forms the first part of the multiscale framework used in this thesis. At the nozzle scale, compressible-flow modelling can show where the gas accelerates, where density and velocity gradients are strongest, and where particles experience large drag forces. These quantities are essential because exfoliation requires useful momentum and energy transfer from the carrier gas to the layered precursor particles. Therefore, the chapter treats shock waves as one feature of the flow field, rather than as the only or necessarily dominant exfoliation mechanism.

The analysis is performed using a converging-diverging nozzle geometry representative of the CFE process. The model compares helium and nitrogen at different upstream pressures in order to evaluate how gas type and stagnation pressure influence velocity, Mach number, density, relative velocity, drag force, and work done on particles. The results provide continuum-scale inputs and mechanistic guidance for the atomistic simulations in Chapters 4 and 5, where the response of layered nanosheets to gas flow, energy transfer, sliding, peeling, and separation is examined directly.

To see how these macroscopic flow phenomena translate into mechanical layer separation, a continuum perspective must be adopted. Treating the high-velocity carrier gas as a continuous medium governed by the Navier-Stokes equations for compressible flow allows for the resolution of spatial variations in velocity, pressure, and density within the exfoliation chamber [91, 92]. This macroscopic analysis is critical because relying solely on empirical trial-and-error is insufficient for scaling or optimizing a system governed by highly non-linear supersonic gas dynamics. The global system parameters, such as inlet stagnation pressure, temperature, and specific nozzle geometry, directly dictate the localized kinetic environment experienced by the suspended bulk materials [18, 96]. A continuum approach effectively maps the boundaries and intensities of this flow field, providing the deterministic mathematical foundation needed to predict the behavior of the gas phase before introducing discrete particle interactions.

The necessity and validity of adopting this continuum fluid dynamics approach are strongly supported by precedent in literature. For instance, in the context of liquid-phase shear exfoliation, Paton et al. [17] utilized computational fluid dynamics (CFD) to map the local velocity gradients within a high-shear rotor-stator mixer. By treating the liquid solvent as a continuous medium, they

successfully calculated the precise hydrodynamic shear rates imparted on suspended graphite flakes. Their analysis yielded a critical quantitative threshold: they demonstrated that when the local continuum shear rate exceeds 10^4 s^{-1} , the viscous shear forces successfully overcome the interlayer van der Waals attractions, resulting in the scalable production of defect-free Graphene.

Similarly, in the domain of high-speed gas dynamics, continuum-based CFD has been instrumental in resolving complex particle-shock wave interactions. For example, studies investigating supersonic multiphase flows [97] have simulated the precise moment a discrete particle crosses a shock front. By resolving the continuum flow field, specifically the abrupt discontinuities in gas density, pressure, and velocity, these models demonstrated that particles experience sudden, non-linear spikes in aerodynamic drag and unsteady history forces. They found that traditional incompressible drag models severely underpredict these forces, and that incorporating continuum compressibility effects is mandatory to capture the extreme transient mechanical stresses exerted on the particles. By building upon these foundational methodologies, the present analysis adapts the continuum perspective to the unique converging-diverging geometry and compressible flow regime of the CFE process.

Furthermore, analyzing the CFE process through a continuum lens is fundamentally essential for understanding the particle-laden nature of the flow. As the precursor materials traverse the steep velocity gradients and shock fronts predicted by continuum gas dynamics, they are subjected to sudden, intense aerodynamic drag and shear forces. Although the ultimate separation of 2D layers is a microscopic event dictated by intermolecular bonds, the prerequisite mechanical stresses can be accurately described by the continuum flow field [98]. Therefore, the continuum perspective serves as the necessary, indispensable bridge between controllable macroscopic gas dynamics and the resultant micro-scale exfoliation events.

Consequently, in this section, we establish the fundamental continuum mechanics framework that governs the CFE process. We will systematically define the governing equations, incorporating the conservation of mass, momentum, and energy for compressible fluids, and analyze the thermodynamic relations driving the gas expansion through the nozzle. By fully resolving the macroscopic flow field, this section provides the essential theoretical and physical baseline required to subsequently model the discrete aerodynamic forces, particle interactions, and the ultimate mechanisms of layer separation.

3.2 Continuum Flow Model and Computational Details

The exfoliation of 2D materials via CFE is driven by high-velocity gas flow interacting with layered nanomaterials. Understanding the role of gas dynamics, shock waves, and particle forces is crucial for optimizing this process and achieving higher exfoliation yields. Before delving into post-centrifuging specifics, it is essential to establish the underlying mechanisms that govern exfoliation efficiency. The effectiveness of CFE depends on the interaction between the traveling gas flow and layered materials, where forces contribute to the separation of nanosheets.

The Quasi 1D Euler equations were utilized to accurately capture the steady shock wave phenomena occurring within the nozzle [99]. The use of the Quasi 1D Euler code served as a valuable tool to confirm the accuracy and reliability of the simulation outcomes. Specifically, it facilitated the capture of the shock wave behavior and provided a comprehensive understanding of the particle-laden flow characteristics within the nozzle during the exfoliation process.

The Quasi 1D Euler analysis was based on considering the following 1D Euler equations:

$$\frac{\partial}{\partial t}\begin{bmatrix}\rho\\ \rho u\\ E_t\end{bmatrix}+\frac{\partial}{\partial x}\begin{bmatrix}\rho u\\ \rho u^2+p\\ \rho uH\end{bmatrix}=-\frac{1}{A}\frac{\partial A}{\partial x}\begin{bmatrix}\rho u\\ \rho u^2\\ \rho uH\end{bmatrix} \quad 3.1$$

where, H is total enthalpy, $H=(E_t + p)/\rho$, E_t is the total energy, $E_t=\frac{p}{\gamma-1}+\frac{\rho}{2}u^2$, p is the total pressure, ρ is the density of fluid, γ is the ratio of specific heats at constant pressure (C_p) and constant volume (C_v), $\gamma=\frac{C_p}{C_v}$.

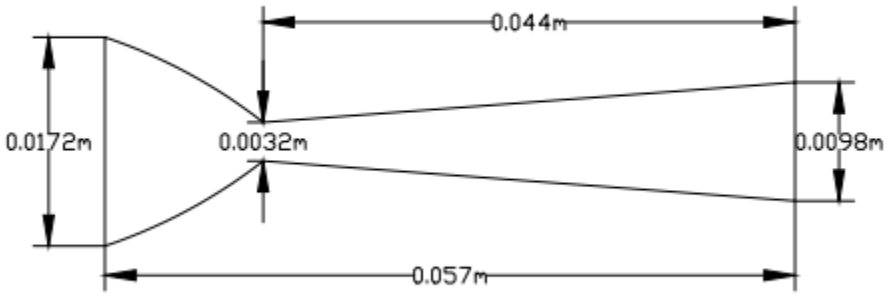

Figure 3.1: *Geometry of the converging-diverging nozzle used for the continuum CFE flow analysis [100]. © 2026 The Author(s). Advanced Engineering Materials published by Wiley-VCH GmbH.*

The converging-diverging nozzle geometry used for the continuum CFE flow analysis is shown in ***Figure 3.1***. To validate the quasi-1D Euler predictions, CFD simulations were performed using COMSOL Multiphysics v5.3a, employing a Reynolds-averaged Navier–Stokes (RANS) framework with a k–ϵ turbulence model, which solves for the turbulent kinetic energy (k) and its dissipation rate (ϵ). The simulation was set up using the high-Mach-number flow physics module and assumed steady, compressible, axisymmetric flow about the centerline (r = 0). Standard boundary conditions were applied, including no-slip walls, adiabatic wall behavior, and atmospheric pressure at the nozzle exit (14.7 psi). These assumptions allowed COMSOL to capture the overall velocity and Mach number trends through the nozzle for comparison with the quasi-1D solution.

The particle-laden nature of the CFE flow was then analyzed by calculating the forces responsible for breaking interlayer and in-plane bonds within two-dimensional materials as they traverse the CD nozzle under high-velocity gas flow conditions. It is crucial to understand that energy thresholds must be surpassed to facilitate this disruption process. The influence of these forces on nanomaterials can be comprehensively evaluated using the drag equation [96, 98]:

$$F_D = \frac{1}{2} C_D \rho A (dV)^2 \qquad 3.2$$

where F_D represents the drag force, ρ is the fluid density, A is the effective cross-sectional area of the particle, C_D is the drag coefficient, and dV is the relative velocity between the fluid and the particle.

The drag force calculation provides insights into the forces acting on the nanomaterials during their passage through the CD nozzle. These forces play a crucial role in the exfoliation process by breaking the interlayer and in-plane bonding. Since the starting bulk particles, prior to exfoliation, are assumed to be spherical, the effective cross-sectional area (A) can be calculated using the formula $A = \frac{\pi {d_p}^2}{4}$, where d_p represents the diameter of the particle. For the h-BN sample particles, the diameter is assumed to be 13×10^{-6} m, as provided by the h-BN supplier. The particle density (ρ) is assumed to be 2100 kg/m^3, representing the density of h-BN particles.

In Equation 3.2., C_D represents the drag coefficient [96, 98] which varies depending on the particle Reynolds number R_N. The particle Reynolds number is calculated using the formula $R_N = \rho(dV)\frac{d_p}{\mu}$, where μ represents the dynamic viscosity of the fluid.

The fluid velocities for the four different cases, namely helium at 1.4 MPa, helium at 5.6 MPa, nitrogen at 1.4 MPa, and nitrogen at 5.6 MPa, were determined using the quasi-one-dimensional Euler equation. This computational approach allows for the estimation of fluid flow behavior and dynamics within the CD nozzle.

To calculate the particle velocities, the time marching method was employed, utilizing the 2N-storage low dissipation and dispersion Runge-Kutta scheme [101]. This numerical scheme enables accurate and efficient computation of particle velocities based on the governing equations and boundary conditions. By combining the fluid velocities obtained from the quasi-one-dimensional Euler equation with the computed particle velocities using the time marching method, a comprehensive understanding of the flow characteristics and the behavior of particles within the CD nozzle can be achieved. These calculations contribute to the overall analysis of the exfoliation process and help elucidate the influence of fluid dynamics on the exfoliation efficiency.

The work done on a particle as it traverses the flow can be approximated by multiplying the forces on the particle throughout the length of the nozzle by the particle velocity and then integrating over time using the following equation:

$$W_p = \int F_D . V_p \, dt \tag{3.3}$$

where F_D is the drag force and V_p is the particle velocity.

3.3 Results and Discussion

3.3.1 Flow Acceleration, Mach Number, and Shock Structure

Figure 3.2 compares the flow velocity and Mach number profiles for upstream pressure of 5.6 MPa obtained from COMSOL Multiphysics and the quasi-1D Euler solution using the original CD-nozzle geometry. Both approaches predict a similar velocity peak of ~1700 m/s near 0.18 m along the axis, although the COMSOL results exhibit fluctuations due to oblique shocks, while the quasi-1D model produces a single normal shock at ~0.3 m. After this point, both simulations show

a similar decay in velocity. The Mach number comparison in ***Figure 3.2(b)*** shows that the quasi-1D model reaches a maximum Mach ~11, whereas COMSOL reaches ~8, a difference attributed to limited mesh resolution in the CFD model. Due to computational limitations of the COMSOL, particularly the inability to refine the mesh sufficiently within the nozzle, prevented accurate resolution of the boundary layer and shock structure. As a result, reliable downstream flow information could not be extracted. Since our objective was to analyze the shock profile and flow behavior before and after the throat to study shock–particle interactions, the achievable grid resolution in COMSOL proved inadequate for capturing these features, and thus the quasi-1D Euler model was used for subsequent analysis.

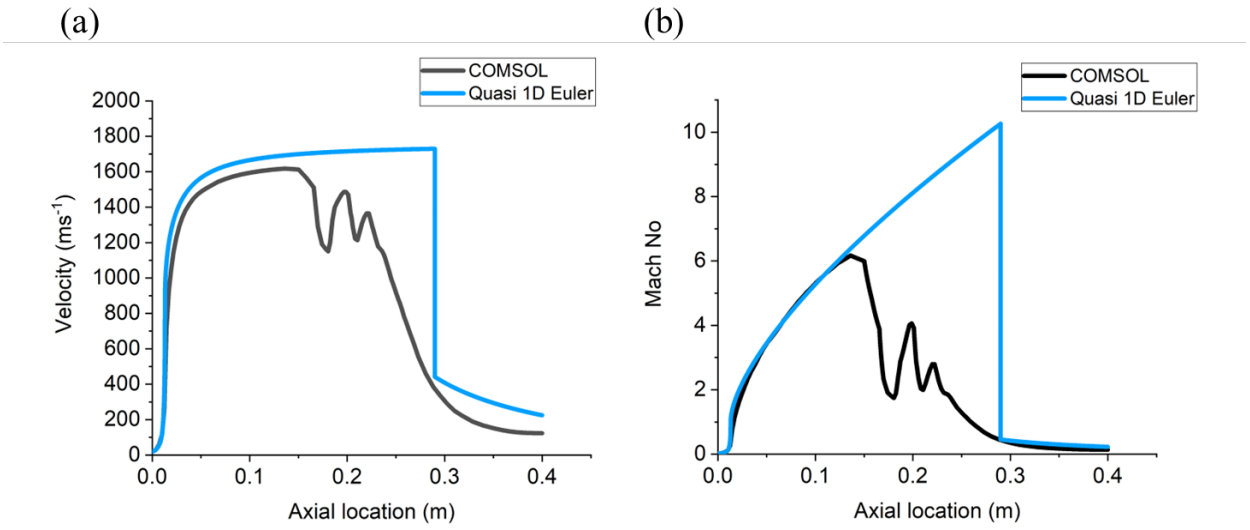

Figure 3.2**:** *(a) Comparison of axial flow velocity profiles at 5.6 MPa obtained from COMSOL Multiphysics and the quasi-1D Euler model using the same CD-nozzle geometry. (b) Corresponding Mach number distributions for both methods [100]. © 2026 The Author(s). Advanced Engineering Materials published by Wiley-VCH GmbH.*

As shown in ***Figure 3.3(a)***, for helium at 5.6 MPa, a maximum velocity of approximately ~1730 m/s was achieved, corresponding to a Mach number of approximately 10 (***Figure 3.3(b)***). This high velocity was sustained up to a distance of ~0.3 m along the CD nozzle before encountering a normal shock wave. In the case of helium at 1.4 MPa, a maximum velocity of ~1690 m/s was attained, resulting in a Mach number of about 6. However, due to the lower upstream stagnation pressure, the shock wave occurred at a distance of ~0.15 m inside the nozzle.

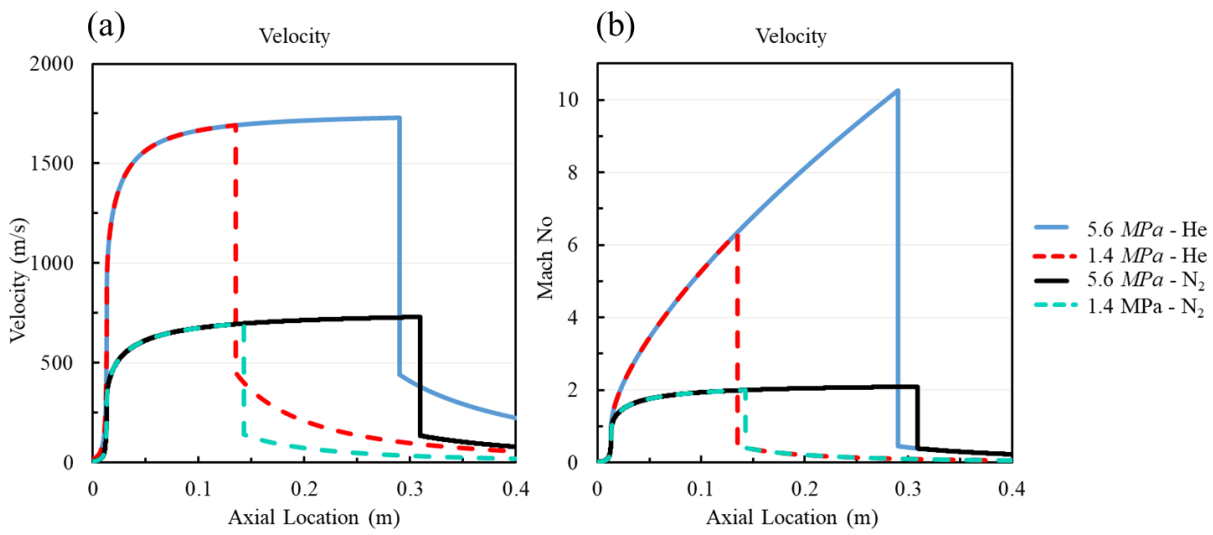

Figure 3.3: *(a) Axial velocity and (b) Mach number profiles predicted by the quasi-1D Euler model for helium and nitrogen at different upstream pressure [100]. © 2026 The Author(s). Advanced Engineering Materials published by Wiley-VCH GmbH.*

In contrast, nitrogen at both 5.6 MPa and 1.4 MPa exhibited lower velocities. Nitrogen at 5.6 MPa achieved a maximum velocity of ~730 m/s, while nitrogen at 1.4 MPa reached a maximum velocity of ~700 m/s. The corresponding Mach numbers for both cases were approximately 2. Notably, nitrogen at 5.6 MPa traveled a further distance of up to ~0.3 m before encountering a shock wave, compared to nitrogen at 1.4 MPa, which experienced the shock wave at a distance of ~0.15 m.

These results demonstrate the significant influence of gas properties and pressure on the velocity and Mach number profiles within the CD nozzle. Helium, being a lighter monoatomic gas, exhibited higher velocities and Mach numbers compared to nitrogen, which is a heavier diatomic gas. Additionally, variations in pressure affected the flow characteristics and the location at which the shock wave formed within the nozzle.

The analysis presented in ***Figure 3.3*** provides crucial insights into the flow dynamics and shock wave behavior for different gas configurations and pressures. These findings contribute to a better understanding of the exfoliation process and enable the optimization of CD nozzle-based experimental conditions to achieve greater yields.

The presence of a shock wave confirms that the nozzle produces a strongly compressible flow field, however, shock formation alone should not be interpreted as the complete exfoliation

mechanism. The flow profiles indicate that large velocity gradients and high particle–gas relative motion occur around the acceleration region, particularly near and downstream of the throat. Therefore, the following section focuses on the quantities that more directly determine particle forcing: relative velocity, local gas density, drag force, and cumulative work done on the particles.

3.3.2 Relative Velocity, Drag Force, and Effective Work

The particle Reynolds numbers obtained during the flow at different upstream pressures (1.4 MPa, 5.6 MPa) using both helium and nitrogen gases are presented in ***Figure 3.4***. The flow properties, such as density and viscosity, have been considered to determine these particle Reynolds numbers. It is worth mentioning that even higher velocities achieved by helium, its Reynold's number is lower compared to nitrogen due to higher kinematic viscosity of helium.

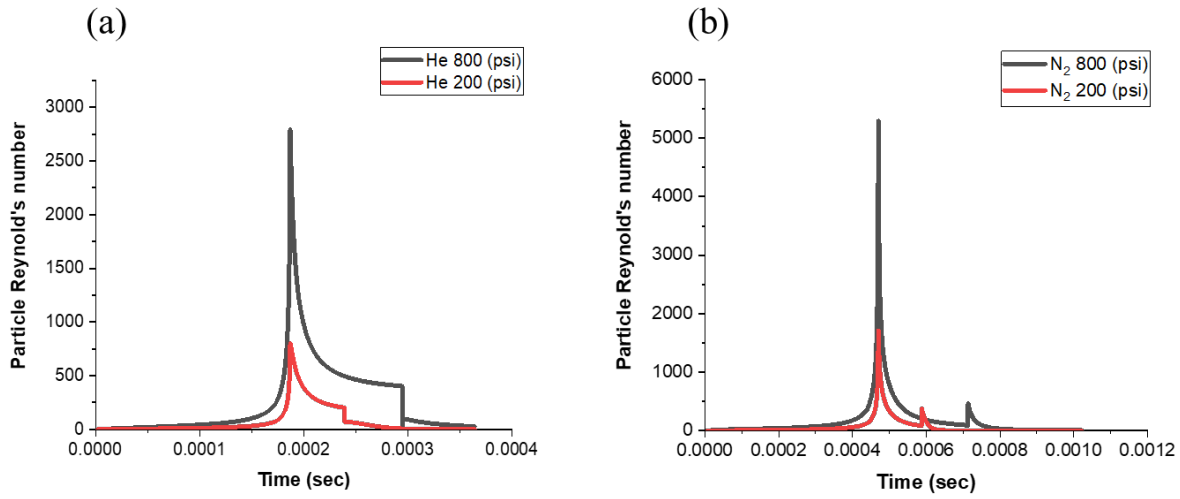

Figure 3.4: *(a) Particle Reynold's number obtained using helium and (b) nitrogen at different upstream pressures [100]. © 2026 The Author(s). Advanced Engineering Materials published by Wiley-VCH GmbH.*

The fluid velocities for the four different cases, namely helium at 1.4 MPa, helium at 5.6 MPa, nitrogen at 1.4 MPa, and nitrogen at 5.6 MPa, have been determined using the Quasi 1D Euler equation. This computational approach allows for the estimation of fluid flow behavior and dynamics within the CD nozzle.

By combining the fluid velocities obtained from the Quasi 1D Euler equation with the computed particle velocities using the time marching method, a comprehensive understanding of the flow

characteristics and the behavior of particles within the CD nozzle can be achieved. These calculations contribute to the overall analysis of the exfoliation process and help elucidate the influence of fluid dynamics on the exfoliation efficiency.

Figure 3.5 shows the results of the Quasi 1D Euler analysis of a particle-laden flow in a CD nozzle. ***Figure 3.5(a)*** shows the relative velocity, which is defined as the difference between the flow velocity and the particle velocity. Similarly, ***Figure 3.5(b)*** shows the gas density changes during the same flow profile. According to ***Figure 3.5(a)***, just after the throat of the CD nozzle, situated at a distance of 0.013 meters from datum, is where the largest difference between the flow velocity and particle velocity (peak relative velocity) is achieved. After this peak, the relative velocity stabilizes until the flow and particles encounter the normal shock wave (around 0.14 m and 0.3 m from the nozzle inlet) resulting in a sudden decrease in the relative velocity in the opposite direction. It is worth mentioning that the Quasi 1D Euler equation, being a one-dimensional model, predicts a normal shock wave rather than an oblique shock wave, which is of more frequent occurrence in supersonic flows. The fluid density as measured during the same cross-sectional flow profile (shown in ***Figure 3.5(b)***) undergoes a decrease by several orders of magnitude as the flow accelerates followed by sudden increase in density at the point of normal shock. For all four cases of flow configurations considered, the density change experienced post-shock is only about one order of magnitude higher. Contrast this with pre-shock flow, where the density of the fluid decreases by up to three orders of magnitude.

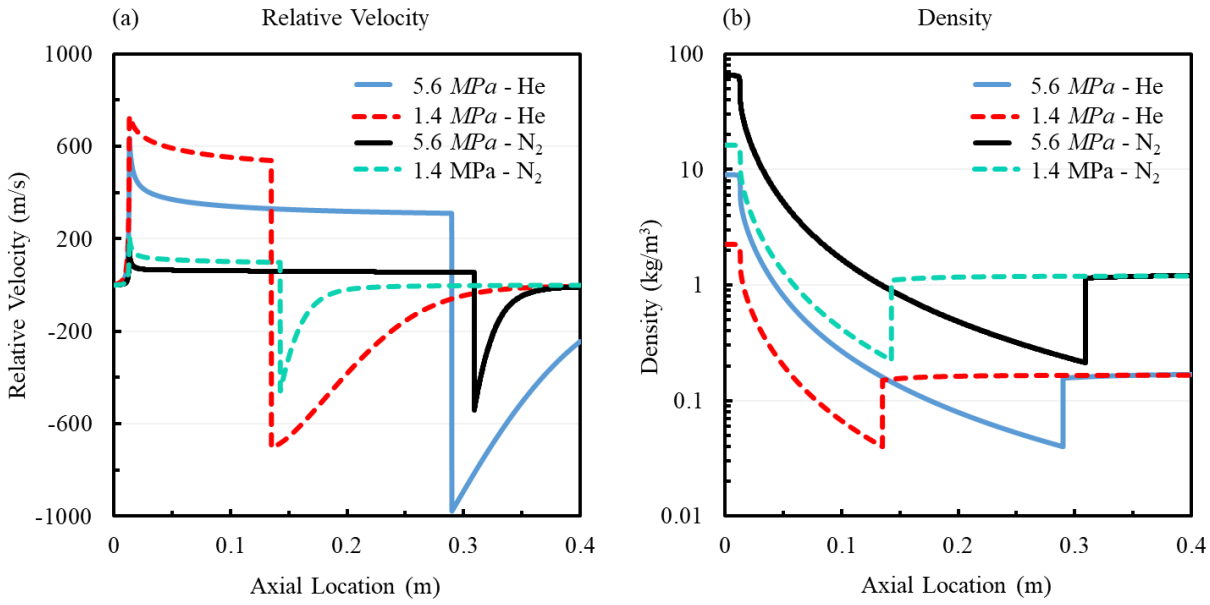

Figure 3.5: *(a) Relative velocity and (b) density variations through the axial distance of the CD nozzle for different upstream pressures of He:5.6 and 1.4 MPa, and N_2: 5.6 and 1.4 MPa [100]. © 2026 The Author(s). Advanced Engineering Materials published by Wiley-VCH GmbH.*

The drag force that a particle experience is shown in ***Figure 3.6*** and it depends on the relative velocity between the fluid and particles, as well as local fluid density around the particle, as indicated in equation 3.2. In the case of helium gas at an upstream pressure of 5.6 MPa, the particles experience a peak drag force of 225 µN just past the throat, and well before the occurrence of the shock wave. However, when these particles confront a shock wave, the drag force drops to 50 µN but in the opposite direction. When the upstream pressure is reduced to 1.4 MPa, the drag force after the throat is 90 µN and within the shock wave region, it changes to a lower value of 30 µN in the opposite direction. For nitrogen gas at an upstream pressure of 5.6 MPa, the particles face a maximum drag force of 100 µN just beyond the throat. This force changes to 50 µN in the opposite direction when encountering a shock wave. At a lower upstream pressure of 1.4 MPa, the drag force after the throat is 40 µN and remains almost the same within the shock wave region. Consequently, it can be observed that helium gas at 5.6 MPa exerts the highest force on the particle among the four cases. This finding indicates that higher pressures and lighter gases can impose greater forces on the particles due to the higher velocity and density changes during the flow.

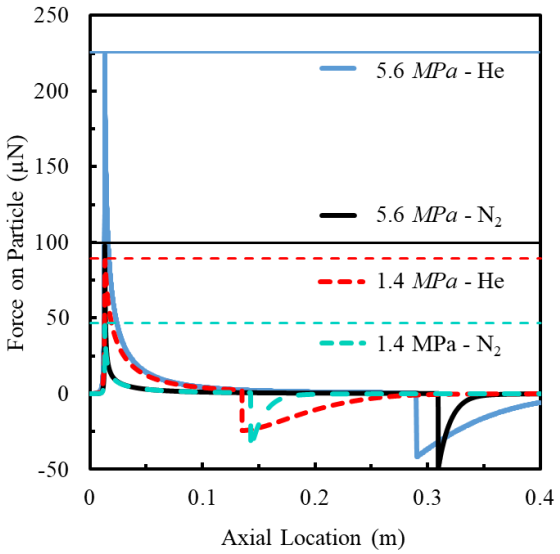

Figure 3.6: *Drag force acting on an h-BN particle travelling through the converging-diverging nozzle under helium and nitrogen flow at different upstream pressures [100]. © 2026 The Author(s). Advanced Engineering Materials published by Wiley-VCH GmbH.*

The cumulative work done on particles for the four different cases (helium at upstream pressures of 1.4 MPa, 5.6 MPa, and nitrogen at 1.4 MPa, 5.6 MPa) is presented in ***Figure 3.7***, allowing for a comparison. Among the cases, the maximum work done on a particle is approximately 2.4 μJ for helium at 5.6 MPa. This value is higher than the maximum work done in the other three cases due to the higher velocity and density changes experienced at the throat and after the shock wave. The maximum work done by helium at 1.4 MPa, nitrogen at 5.6 MPa, and nitrogen at 1.4 MPa are approximately 1.6 μJ, 0.6 μJ, and 0.4 μJ, respectively.

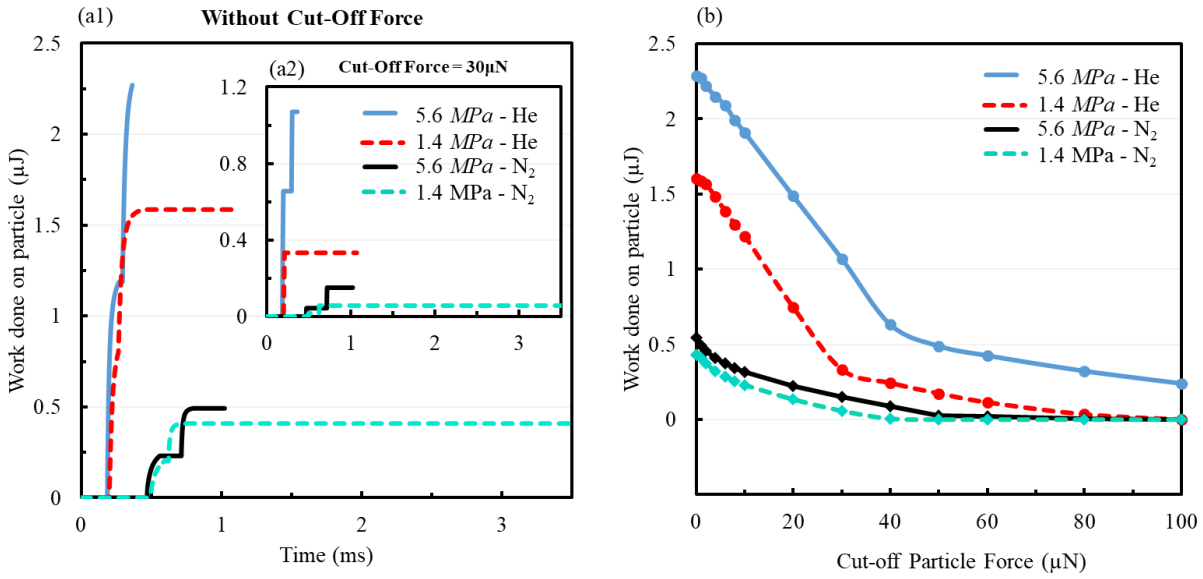

Figure 3.7: *(a) Cumulative work done on a nanoparticle at different upstream pressures using helium and nitrogen gas (a1) without cut-off force and (a2) at cut-off force=30 µN. (b) Work done on the particle at different cut-off forces compared across helium and nitrogen flow conditions [100]. © 2026 The Author(s). Advanced Engineering Materials published by Wiley-VCH GmbH.*

Moreover, it is noteworthy that the graph in ***Figure 3.7(a)*** demonstrates the effects of faster flow characteristics of helium compared to nitrogen. Helium at 5.6 MPa takes only 0.45 ms to reach the nozzle exit, whereas nitrogen at 1.4 MPa exhibits the slowest movement, taking approximately 3.6 ms to reach the exit.

A common approach for understanding layer separation of 2D materials has been to start from first principles and generate a model particle and compute the energetics of bond breakage [102]. However, agreements with experimental results are often weak [103] due to the polydisperse geometries and characteristics of layered particles and their exfoliated nanomaterials, along with inability to capture the complex dynamics of energy transfer during exfoliation. Instead, a simpler approach could be to rely on the concept of cut-off forces, which is rooted in the requirement that a minimum force (stress) must be exerted for breaking bonds (yielding). Any force applied to a particle greater than the cut-off force will contribute to bond breakage and layer separation (exfoliation). While a force below this threshold will only result in the particle's elastic deformation and other dissipation mechanisms that exclude bond breakage and layer separation. Although unknown, this required minimum force for layer separation can be gleaned from the

experimental results and flow analysis presented thus far. ***Figure 3.7(b)*** depicts the cumulative work (as calculated from Equation 3.3) exerted on particles, but only after various cut-off force thresholds (x-axis) - within the range of 0-100 μN - have been overcome. Within the examined range of ***Figure 3.7(b)***, helium at 5.6 MPa shows significantly higher work done on the particle compared to the other three scenarios.

To determine the minimum cut-off force required for the exfoliation of nanomaterials, the ratio of the work done on a particle for each case is compared with the ratio of the UV–Vis absorbance results at 5.6 MPa and 1.4 MPa, considering both helium and nitrogen gases. The absorbance results at a wavelength of 300 nm are used for this calculation, as it is commonly employed as a reference wavelength to estimate concentrations and process yields [104, 105]. Further analysis of these ratios can provide insights into the relationship between the work done on particles and the resulting exfoliation efficiency, enabling the determination of optimal conditions for effective nanomaterial exfoliation.

To provide experimental reference context for the work-ratio analysis, UV–Vis absorbance ratios from h-BN dispersions produced under different gas and pressure conditions are included in ***Table 3.1***. These values are not introduced here as a separate experimental study, rather, they are used as a comparative reference to evaluate whether the calculated work ratios follow the same relative trend as the measured CFE output. The purpose of including this table in the continuum-modelling chapter is therefore to connect the predicted particle-scale mechanical work with an experimentally observed gas- and pressure-dependent exfoliation trend.

The comparison should be interpreted cautiously. UV–Vis absorbance reflects recovered dispersed material after collection and post-processing, whereas the continuum model estimates the work transferred to a representative particle inside the nozzle. Therefore, agreement between the absorbance ratios and calculated work ratios should be treated as mechanistic support for the effective-work interpretation, not as a direct proof of a unique force threshold.

The ratio of UV–Vis absorbance results and the work ratio at different cut-off forces are presented in ***Table 3.1*** and **Table 3.2**. Notably, the simulated work ratio value at 30 μN of ***Table 3.2*** closely matches the actual absorbance ratio values in ***Table 3.1***. This alignment suggests that an effective-force scale near 30 μN provides a useful reference threshold for comparing the simulated work trends with the experimental absorbance ratios. However, this value should be interpreted as an

approximate modelling threshold for the representative particle and flow conditions considered here, rather than as a universal exfoliation force for all CFE materials or geometries. This finding is consistent with experimental measurements [106] and theoretical calculations [107], which indicate that weak Van der Waals interactions between the layers do not require a large force for exfoliation. It is reported that slip between layers in a graphite flake with a lateral size of 10 μm occurs at a small shear force of 3.9 μN [106], However, investigations into interlayer sliding in h-BN reveal that the shear strength of an h-BN bilayer is approximately five times greater than that of a Graphene bilayer [108]. The plot in ***Figure 3.7(a2)*** at this cut-off force of 30 μN provides a visualization of the work done on the particles under conditions that are favorable for initiating the exfoliation process. By examining the stepwise nature of the plots of cumulative work done at this specific cut-off force in ***Figure 3.7(a2)***, it can be seen that certain flow configurations (i.e. helium at 5.6 MPa and nitrogen at 5.6 and 1.4 MPa) impart sufficient energetics for layer separation during the flow acceleration (pre-shock) and flow deceleration (post-shock) stages. While other configurations (i.e. helium at 1.4 MPa) can only impart sufficient energetics for layer separation during the flow acceleration (pre-shock) stage. This indicates that the pre-shock flow where the densities due to higher upstream (stagnant) pressures can contribute further to particle drag (thrust) forces and hence to the work done on particles rather than post-shock flows. This indicates that optimized nozzle design meant to maximize particles forces can result in effective nanomaterial exfoliation during compressible flows.

Table 3.1: *UV–Vis absorbance ratios at 300 nm for h-BN dispersions produced under different gas and pressure conditions.*

He (5.6 MPa)/ He (1.4 MPa)	**He (5.6 MPa) / N2 (5.6 MPa)**	**He (5.6 MPa)/ N2 (1.4 MPa)**
3.81	**8.10**	**18.88**

Table 3.2: *Work ratios calculated at different cut-off forces for helium and nitrogen CFE conditions.*

Cut-off forces (μN)	**He (5.6 MPa)/ He (1.4 MPa)**	**He (5.6 MPa) / N_2 (5.6 MPa)**	**He (5.6 MPa)/ N_2 (1.4 MPa)**
0.01	1.43	4.21	5.29
1.0	1.43	4.61	5.56

Cut-off forces (μN)	He (5.6 MPa)/ He (1.4 MPa)	He (5.6 MPa) / N_2 (5.6 MPa)	He (5.6 MPa)/ N_2 (1.4 MPa)
2.0	1.41	4.86	5.96
4.0	1.45	5.27	6.66
6.0	1.51	5.62	7.31
8.0	1.53	5.80	7.76
10.0	1.56	6.01	8.29
20.0	1.99	6.65	11.08

Based on the force dynamics and energy thresholds established above, we propose that the dominant exfoliation mechanism in CFE is acceleration-driven aerodynamic shear. As the carrier gas accelerates to high Mach numbers (Mach ~10 for Helium) at the nozzle throat, the relatively heavier h-BN particles lag behind due to inertia, creating a significant relative velocity (dv) between the fluid and the solid. This relative motion generates substantial viscous drag forces on the particle surface. Unlike the instantaneous pressure spike of a shock wave, which acts compressively, this drag force acts tangentially along the particle surface. When this aerodynamic shear force exceeds the cut-off threshold of ~30 μN, it overcomes the Van der Waals forces holding the layers together, causing the outer nanosheets to slide off the bulk crystal. This model explains why Helium, with its higher velocity and resulting thrust capability, significantly outperforms Nitrogen, even though Nitrogen might generate different shock structures.

These results indicate that the strongest particle forcing does not necessarily coincide with the shock location. Instead, the highest drag force occurs in the acceleration region where the particle–gas relative velocity and local density combine to produce large aerodynamic forcing. This supports the interpretation that CFE should be understood through effective momentum and work transfer to particles, rather than through shock formation alone.

3.4 Chapter Summary and Bridge to Atomistic Modelling

This chapter analyzed Compressible Flow Exfoliation from a continuum gas-dynamics perspective in order to identify the nozzle-scale flow conditions that can generate particle forcing, momentum transfer, and mechanical work. By treating the high-velocity carrier gas as a compressible

continuum and modelling its acceleration through a converging-diverging nozzle, the analysis mapped the spatial variations in velocity, Mach number, pressure, density, particle–gas relative velocity, drag force, and cumulative mechanical work. The quasi-one-dimensional compressible-flow model and nozzle-flow analysis showed that the CFE nozzle produces rapid gas acceleration, large pressure and density variations, high-Mach-number regions, and shock formation. Depending on gas type and upstream pressure, the flow reached supersonic conditions with predicted Mach numbers of approximately 1.5–2.5, confirming that CFE creates an intense compressible-flow environment.

However, the results also show that shock formation alone is not sufficient to describe the exfoliation mechanism. Although shock waves are an important feature of the compressible nozzle flow, the exfoliation-relevant forcing is more directly connected to the regions where particle–gas relative velocity, local gas density, aerodynamic drag, and cumulative mechanical work are high. The strongest drag forces were predicted near the high-acceleration regions of the nozzle, particularly around and downstream of the throat, where relative velocity and density changes combine to produce large particle forcing. Therefore, the continuum results support an acceleration-driven and work-transfer-based interpretation of CFE. In this interpretation, the gas does not simply create a shock wave; it transfers momentum and mechanical work to suspended layered particles through rapid acceleration, aerodynamic drag, strong flow gradients, and particle–gas relative motion.

The drag-force analysis provides quantitative support for this interpretation. For helium at 5.6 MPa, the highest calculated drag force was approximately 225 μN, occurring just downstream of the throat and before the shock wave. Near the shock region, the force decreased to approximately 50 μN and changed direction. At the lower helium pressure of 1.4 MPa, the drag force decreased to approximately 90 μN after the throat and approximately 30 μN in the opposite direction near the shock. For nitrogen, the calculated maximum drag forces were lower, reaching approximately 100 μN at 5.6 MPa and approximately 40 μN at 1.4 MPa. These values show that higher upstream pressure and lighter carrier gas can increase particle forcing by producing higher gas velocity and stronger particle–gas relative motion.

The cumulative-work analysis further shows that the magnitude of the peak force alone does not determine exfoliation effectiveness. Instead, the useful mechanical contribution depends on where

the force acts, how long it acts, and whether it exceeds a relevant threshold for layer separation. The comparison between calculated work ratios and reference UV–Vis absorbance ratios provided additional support for the effective-work interpretation. The UV–Vis data were used only as experimental reference context, while the main purpose of the comparison was to determine whether the calculated work trends were consistent with observed gas- and pressure-dependent exfoliation behavior. The approximate cut-off-force analysis suggests that only the portion of particle forcing above a relevant threshold contributes effectively to layer separation, while lower forces may be dissipated through particle motion, elastic deformation, or non-exfoliating interactions. In this analysis, a cut-off force near 30 μN provided a useful modelling threshold for comparing effective work trends with the experimental absorbance ratios.

Overall, the continuum analysis indicates that CFE should not be treated as a shock-wave-only or wall-shear-only process. Instead, the process is better described as a coupled gas-dynamic mechanism in which gas acceleration, particle–gas relative motion, drag force, aerodynamic shear, and effective work together create conditions favorable for exfoliation. Shock waves are part of the compressible flow structure, but the most relevant exfoliation drivers are the local flow conditions that transfer momentum and mechanical work to the suspended particles. This distinction is important because it shifts the interpretation of CFE from a single-event shock mechanism toward a distributed work-transfer mechanism occurring across the acceleration and deceleration regions of the nozzle.

These quantitative continuum results provide the macroscopic flow conditions required for the multiscale interpretation developed in the next chapters. However, continuum modelling cannot directly show how individual nanosheets respond to gas flow, how energy is transferred at the atomic scale, or whether the imposed gas-dynamic conditions promote sliding, bending, peeling, or layer separation. Therefore, Chapter 4 extends the analysis to atomistic molecular dynamics simulations to examine how gas velocity, pressure, temperature, and gas type influence Graphene layer fluctuation, energy transfer, and nanosheet separation.

Chapter 4: Atomistic Perspective Simulation of CFE [2]

Chapter 3 established the continuum-scale gas-dynamic environment of CFE, including gas acceleration, Mach number variation, pressure and density gradients, particle–gas relative velocity, drag force, and cumulative mechanical work. However, continuum modelling cannot directly resolve how individual nanosheets respond to high-speed gas-particle collisions or how kinetic energy is transferred into nanosheet fluctuation, sliding, and interlayer weakening. Since exfoliation is ultimately controlled by atomic-scale interactions between adjacent layers, an atomistic modelling approach is required.

In this chapter, classical molecular dynamics (MD) simulations are used to examine how high-velocity gas flow interacts with layered nanosheets at the atomic scale. Graphene is selected as the model material because it is a structurally simple and well-characterized van der Waals layered system. Its strong in-plane sp^2 carbon network and weak interlayer interactions make it suitable for isolating the fundamental physics of gas-assisted layer motion. Therefore, the simulations are not intended to represent every material-specific feature of Graphene, h-BN, and MoS_2 quantitatively. Instead, Graphene is used as a representative model system to identify mechanistic trends relevant to the broader CFE platform. The MD results in this chapter should therefore be interpreted as mechanistic and qualitative guidance for gas-assisted exfoliation rather than as a direct quantitative prediction of the exfoliation efficiency of different materials.

The main objective of this chapter is to determine how gas velocity, pressure, temperature, and gas type influence Specifically, this section utilizes nanosheet motion and energy transfer. These variables are directly connected to the continuum-scale results of Chapter 3 and to the experimental optimization strategy developed in Chapter 6. In particular, the role of temperature is important

---

[2] *Publication and Author Contribution Statement. Portions of this chapter are adapted from: Ahmed, S., Arabha, S., Gonzalez, R. I., and Rizvi, R. "Interactions of Gas Particles with Graphene during High-Throughput Compressible Flow Exfoliation: A Molecular Dynamics Simulations Study."* The Journal of Physical Chemistry C *126, no. 22 (2022): 9378–9385. https://doi.org/10.1021/acs.jpcc.2c00425.*

Saeed Arabha made substantial contributions to the molecular-dynamics study design and refinement, data analysis, visualization, interpretation of the results, development of the scientific discussion, manuscript drafting and revision, and final preparation of the published article. His contributions were particularly important in connecting gas velocity, pressure, temperature, and gas identity with graphene-layer motion, energy transfer, and the resulting exfoliation mechanisms.

because gas preheating later becomes a central experimental modification for improving nitrogen- and air-based CFE. By tracking nanosheet displacement, thermal fluctuation, energy transfer, and interlayer interaction energy, this chapter provides the atomistic bridge between the macroscopic flow field and the energy-barrier analysis presented in Chapter 5.

4.1 Introduction

While the continuum mechanics analysis in Section 3.1 successfully mapped the macroscopic gas dynamics of the CFE process, the actual separation of two-dimensional (2D) layers is inherently an atomistic phenomenon. The continuum perspective quantified the severe velocity gradients, shock events, and peak drag forces within the converging divergent nozzle, yet it cannot resolve the discrete molecular collisions that ultimately cleave the van der Waals bonds between adjacent nanosheets. Therefore, an atomistic perspective must be integrated to fully understand the fundamental exfoliation mechanisms at the nanoscale.

The utility of molecular dynamics (MD) simulations in unraveling exfoliation mechanisms is well established in the broader literature. Previous computational studies have extensively utilized MD frameworks to investigate the liquid-phase exfoliation of various 2D materials. For instance, Mukhopadhyay and Datta [109] employed MD simulations to decipher the specific role of different solvents in the layer separation of h-BN, revealing how solvent molecules intercalate and stabilize the nanosheets. Similarly, Kamath and Baker [110] utilized atomistic models to evaluate the thermodynamic suitability of ionic liquids as media for boron nitride exfoliation and dispersion. While these studies have provided profound insights into fluid solid interactions and the thermodynamics of layer separation in liquid environments, the atomistic dynamics of high speed gas phase exfoliation remain largely unexplored.

To bridge this gap and investigate these unique micro scale interactions, classical MD simulations are employed in this study. MD simulations provide a powerful computational framework to observe the precise interactions between high velocity carrier gas particles and pristine, unfunctionalized 2D lattices, such as Graphene. In the highly energetic environment of the CFE process, the bulk nanomaterials are subjected to intense, continuous gas particle bombardment. By tracking the trajectories, velocities, and energy transfers of individual atoms over time, MD

simulations can reveal exactly how the kinetic energy from the supersonic gas flow translates into localized mechanical work and increased thermal vibrations within the 2D material [18].

The continuum results from Chapter 3 are used to guide the physically relevant range of gas velocities, pressures, and gas types considered in the atomistic simulations. However, the MD simulations are not treated as a direct one-to-one reconstruction of the full CFE nozzle environment. Instead, they provide a simplified atomistic representation of gas-assisted layer motion under controlled conditions. This approach allows the influence of individual variables, such as gas velocity, pressure, temperature, and gas type, to be examined separately, while avoiding overinterpretation of the MD results as exact quantitative predictions of the full experimental process.

This atomistic investigation focuses on understanding how the thermal vibration of the Graphene layers increases with the elevation of temperature during the process, and how the kinetic energy transferred during high speed molecular collisions successfully overcomes the interlayer van der Waals interactions. Consequently, this atomistic perspective completes the multi scale modeling of the CFE process, directly linking the controllable macroscopic flow parameters established in Section 3.1 to the successful nanoscale exfoliation events observed experimentally.

4.2 Computational Details

In this section, the Large-scale Atomic/Molecular Massively Parallel Simulator (LAMMPS) package is used for performing molecular dynamics calculations [111]. The accuracy of estimated properties by MD simulation mainly depends on the precision of potential functions used. Here, we employed the Adaptive Intermolecular Reactive Empirical Bond Order – Morse (AIREBO-M) [112] potential, which is more suitable for high pressure simulation of Graphene systems [112].

We first studied the effect of temperature on exfoliation behavior of Graphene nanosheets. In this regard two approaches were adapted at static (no flow) conditions: simulation of Graphene bilayer, 1) without any gaseous medium (vacuum), and 2) with helium gas particles. For both cases, we have constructed two armchair Graphene nanosheets each having the dimension of 6×4 nm^2 and separated by 0.33 nm, as shown in ***Figure 4.1***. The bilayer Graphene was placed at the center of a simulation box of dimension $10\times40\times10$ nm^3. Afterwards, a range of temperature (300-2000 K) was applied to system using NVT ensemble.

Next, we incorporated different flow velocities to the gaseous particles to observe the exfoliation phenomena of in a Graphene bilayer. The system was equilibrated in NVT ensemble at 300K which was followed by a production run in NVE ensemble. The desired flux of gas was achieved and kept at a constant velocity through a stepwise method. To keep velocity at a constant value, velocity of gas atoms inside the $10\times10\times10$ nm^3 box at the entrance of the simulation box (***Figure 4.1*(a)**) was monitored during the simulation, and every 2 ps the difference between the desired velocity and current velocity was added to gas atoms. In all simulations, one of the Graphene sheets was harmonically constrained with a force constant of 185 kcal/mol/$Å^2$ during production period to monitor the exfoliation of the opposite Graphene sheet which was allowed to move freely. Hence, the fixed Graphene sheet was considered as a terminal sheet for a bulk graphite system [113].

The equations of motion were integrated with a time step of 0.5 fs using the Velocity Verlet Algorithm [114] and the non-bonded interactions were calculated setting a cut-off distance of 0.75 nm. Noose-Hoover [115] thermostat and barostat were implemented to control the temperature and pressure of the system. Periodic boundary condition was applied in x and y directions and the z direction remained fixed.

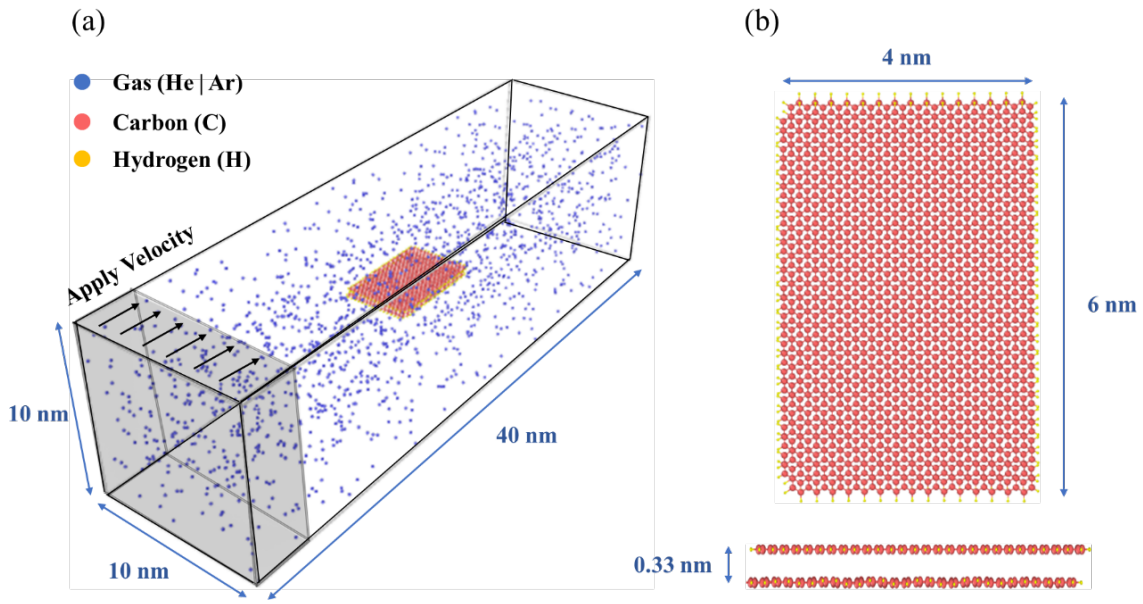

Figure 4.1: *(a) System setup, a 10×40×10 nm^{3}box is considered with 5 nm entrance to apply velocity to gas particles (b) top view and side view of Graphene nanosheet of 6 × 4 nm^2 with 0.33 nm interlayer separation distance [116] Copyright © 2022 American Chemical Society.*

AIREBO force-field is widely used for hydrocarbon system to determine their dynamic bonding process at ambient condition [117] .Unfortunately, this energy function fails when the system subjected to higher pressure. So AIREBO-M [112] force field was used in this study where diverging singular Lennard-Jones potential is replaced by a non-divergent Morse potential. It has an additional parameter that allows the repulsive region to be softened with little change to the minimum and attractive regions. The equation of the potential energy function used in the simulation has the form

$$E = \frac{1}{2}\sum_i \sum_{j\neq i} [E_{ij}^{REBO} + E_{ij}^{LJ} + \sum_{k\neq i,j} \sum_{l\neq i,j,k} E_{ijkl}^{TORSION}] \quad 4.1$$

There are three terms in this energy function. The E_REBO term in AIREBO-M potential gives the model its reactive capabilities and only describes short-ranged C-C, C-H and H-H interactions (r<2 Angstroms). The E-LJ term adds longer-ranged interactions (2<r<cutoff) using a form like the standard 12-6 Lennard Jones potential, but this fails at many pressure systems. To improve the accuracy of the function in such situation, the LJ potentials was replaced with Morse potential [112]:

$$E_{ij}(r) = -\varepsilon_{ij}\,[1 - (1 - e^{-\alpha_{ij}(r - r_{ij}^{eq})})\,2] \quad 4.2$$

Where ε and r^{eq} define the depth and location of the minimum energy, and the new parameter α modifies the curvature of the potential energy at its minimum separation. This extra degree of freedom in the Morse potential is fit to experimental measurements of the layer spacing of graphite up to 14 GPa while retaining most equilibrium properties of AIREBO [117]. And the remaining E_TORSION term in the potential function is an explicit 4-body potential that describes various dihedral angle preferences in hydrocarbon configurations.

Two different monoatomic gases are used in this study to investigate the interactions of gas particles with Graphene during exfoliation. One is the lightest noble gas – Helium and another one is its heavier counterparts – Argon. Lennard-Jones (LJ) potential function is used here for mapping their interatomic interactions (***Table 4.1***) [118, 119]. All non-bonded interactions are calculated from OPLS-AA (Optimized Potentials for Liquid Simulations – All Atom) potential function [120]. Lorentz-Berthelot mixing rules [121] are used for approximating the interactions between unlike pairs like C-He, H-He, C-Ar, H-Ar.

Table 4.1. *Lennard-Jones interaction parameters used for gas–Graphene and interlayer molecular dynamics simulations [118, 119].*

Interaction	σ (Å)	ε (kcal/mol)
He - He	0.020	2.57
C – He	0.037	3.06
Ar - Ar	0.236	3.41
C – Ar	0.128	3.48

4.3 Results and Discussion

To analyze the role of temperature on the exfoliation phenomena of bulk graphite, we considered two armchair Graphene nanosheets separated by 0.33 nm which is placed in the center of an empty simulation box. As noted earlier, the bottom layer of the Graphene is harmonically fixed to easily monitor the separation of another layer. It is always better to consider multilayers of Graphene sheets to replicate the effects of bulk graphite, but the extended size of the system becomes

computationally very expensive and makes the exfoliation intractable at longer timescales. That's why, a two-layer model of Graphene nanosheets is considered here which has been extensively used in various literatures [109, 110]. ***Figure 4.2*** shows the root-mean-square deviation (RMSD) of the exfoliating layer of Graphene at different temperatures. First, we simulate only the Graphene layers without the presence of any gaseous medium which is presented in ***Figure 4.2*****(a)**. Elevating the temperature of any molecular system increases the thermal vibration of the particles in that system. Eric Ganz et. al. [122] performs *ab initio* MD simulations to find out the melting point of Graphene and reports that the phase change temperature starts at 4000K, and Graphene appears to be in a quasi-2D liquid state at 4500K. The other limitation is that bilayer Graphene is not stable at T > 3000K using AIREBO-M potential. In this regard, three different temperatures are tested starting from 300K to 2000K to investigate the inherent mechanism. It was observed that the fluctuations of the top layer Graphene with respect to the bottom layer were increasing in both cases, with and without Helium, as the temperature rose. However, Carbon atoms in Graphene were found to absorb more thermal energy while in the presence of Helium gas than without. As shown in ***Figure 4.2*****(b),** the relative RMSD of top layer Graphene is approximately 2 times higher in the presence of Helium than without any gas at 2000K. This deviation of top layer Graphene in the presence of gas particles could help to weaken the van-der-Waals bonding between Graphene layers, since the gas particles might find a way to ingress between layers.

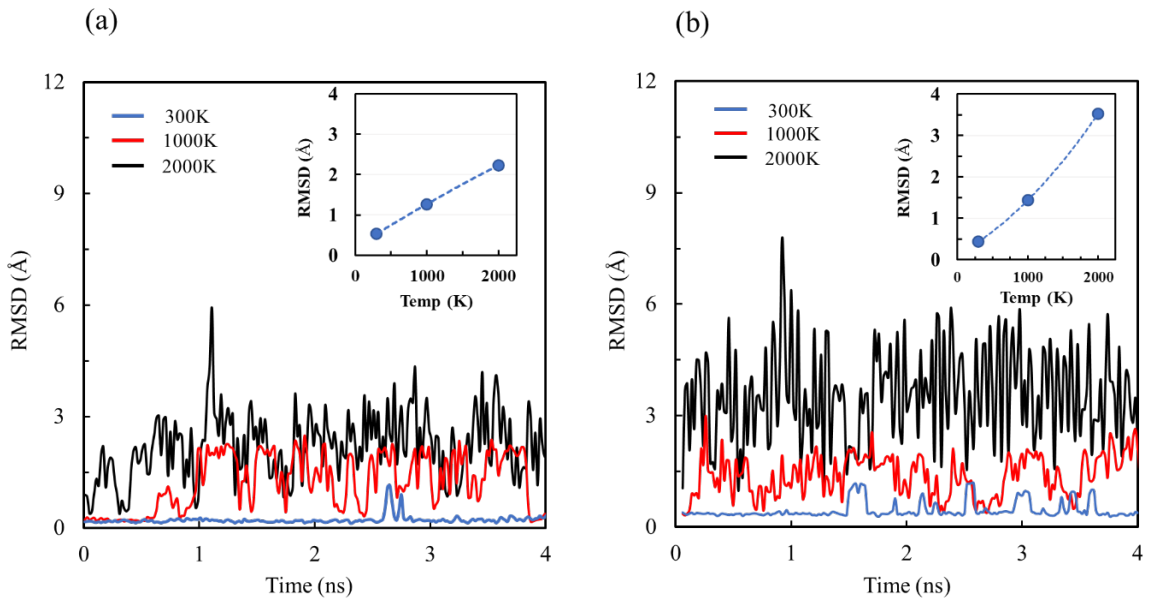

Figure 4.2: *RMSD plot of exfoliating Graphene layer at five different temperatures ranging from 273K to 2000K (a) Graphene bilayer without any gaseous medium (b) Graphene bilayer with helium gas particle [116] Copyright © 2022 American Chemical Society.*

In CFE process, the velocity of gas reaches supersonic flow after passing through a converging-diverging channel because of certain pressure differentials. This is based on the theory of conservation of mass and momentum [123]:

$$\frac{dV}{V}[M^2 - 1] = \frac{dA}{A} \qquad 4.3$$

Where $\frac{dV}{V}$ is the fluids relative change in instantaneous velocity, $\frac{dA}{A}$ is the relative change in the flow channel's instantaneous area and M is the fluid's Mach number, defined as its' velocity V relative to the velocity of the speed of sound, V_s. The flow velocity of gas can achieve even higher velocities than Mach 1 depending on the design of the diverging portion. Since we are more concern about the area after the throat, where these high Mach numbers are experienced (supersonic flow), our focus then is to replicate such experimental conditions in our MD simulations. We imparted different flow velocities to helium particles ranging from 1000 ms^{-1} to 2000 ms^{-1}. ***Figure 4.3(a)*** shows the temperature rise of Graphene bilayer with the increase of flow velocities of helium gas. When gas particles collide with carbon atoms, the kinetic energy of the gas flux transfers to the Graphene bilayers as thermal energy which increase its temperature. So

higher flow velocity means more energy transfer and more thermal fluctuations. Regarding the limitation of AIREBO potential, the results are only valid for T < 3000K, so in this section we focused on the results in this regime of temperature. As shown in ***Figure 4.3(a)***, not only does the Graphene reach a temperature of 3000K faster at higher speeds of Helium gas, but the RMSD of the top layer Graphene, ***Figure 4.3(b)***, is higher for V = 2000 ms^{-1} (RMSD = 16.1 ± 0.2 Å) than at lower velocities (RMSD = 13.2 ± 0.2 Å and 12.0 ± 0.3 Å for V = 1500 ms^{-1} and 1000 ms^{-1}, respectively). Examining the relation of temperature and RMSD (***Figure 4.3(c)***) at constant velocities, it can be observed that increasing velocity results in greater RMSD fluctuations of Graphene layers, and that too in shorter time – conditions favorable for exfoliation in the CFE process. We also observed some bond breaking for all three velocities as the RMSD exceed ~10 Å.

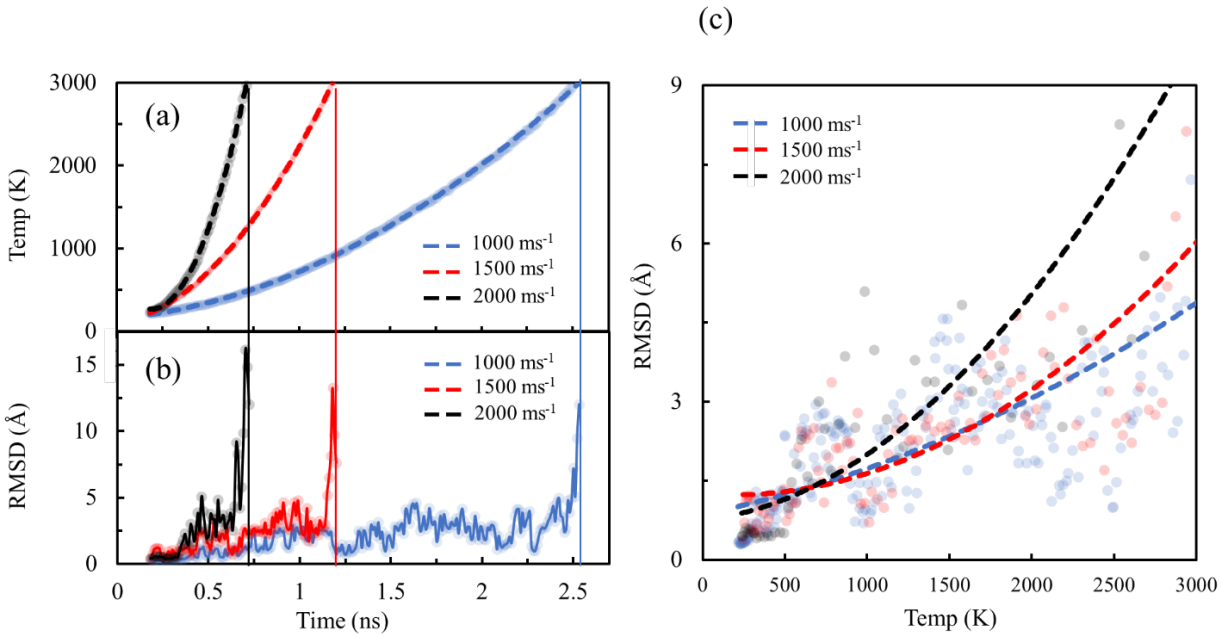

Figure 4.3: *Effect of flow velocity of helium gas ranging from 1000 ms^{-1} to 2000 ms^{-1} on Graphene exfoliation (a) temperature and (b) RMSD of bilayer Graphene. (c) The correlation of temperature and RMSD [116] Copyright © 2022 American Chemical Society.*

The energy that transferred from gas particles to Graphene sheets is demonstrated in ***Figure 4.4***. The figure shows that by increasing the velocity of helium, a higher amount of energy would be transferred to Graphene sheets in a shorter time. Collision of gas particles and Graphene sheets at

higher gas velocities raises the kinetic energy that is transferred to the Graphene bilayers as thermal energy, which consequently increase the temperature of Graphene sheet.

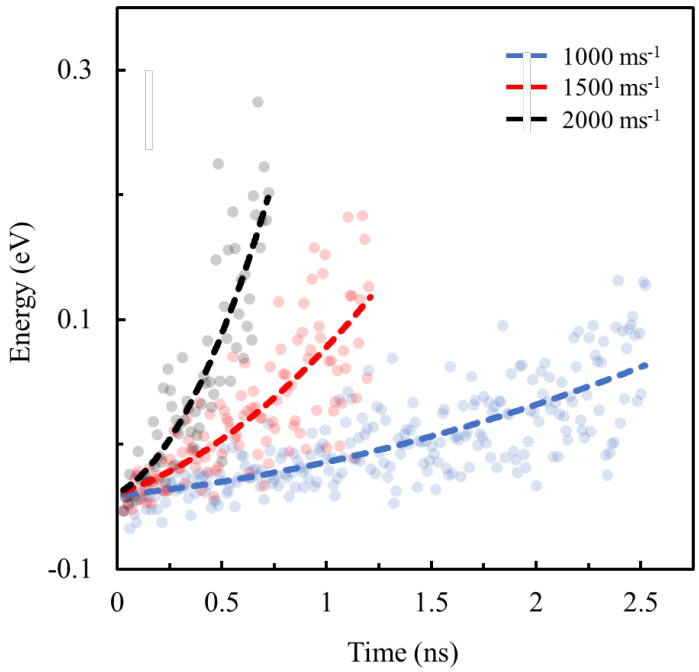

Figure 4.4: *The energy transferred from Helium gas to bilayer Graphene at different Helium velocities ranging from 1000 ms^{-1} to 2000 ms^{-1} [116] Copyright © 2022 American Chemical Society.*

Analyzing the structural mechanics of an exfoliating layer of Graphene can be done by calculating the parallel or sliding distance D_{xy} and vertical distance D_z between the centroids of Graphene nanosheets during the production simulation. ***Figure 4.5*** shows the normalized distribution of sliding and vertical separation distance between Graphene layers at three different flow velocities of helium gas and ***Table 4.2*** exhibits their corresponding mean values with standard deviation. The mean D_{xy} at 1000 ms^{-1} is 0.17 ± 0.93 Å which increases and with a higher standard deviation to 1.47 ± 2.22 Å when the velocity of helium is doubled to 2000 ms^{-1}. The distribution of D_z also exhibits the same trend with the increase of flow velocity, as shown in ***Figure 4.5(c)***. At 1000 ms^{-1}, the average D_z is 3.56 ± 0.02 Å which is very close to the equilibrium separation distance between Graphene layers. Because of the interlayer van der Waals interactions, a low flow velocity cannot provide sufficient kinetic energy to overcome diffusion energy barriers. Increasing the flow velocity enables the Graphene layers to absorb more energy from the gas and the average D_z

reaches 3.66 ± 0.26 Å at 2000 ms^{-1}. Here, the thermal agitation of carbon atoms in Graphene escalates with the ramp of flow velocity, which is the reason for higher sliding and vertical separation between Graphene nanosheets. It also reported similar results during Graphene exfoliation by shear-assisted sCO_2 using rotating mixer [124]. Moreover, the relative in-plane (D_{xy}) fluctuations of Graphene layers are much larger compared to those out-of-plane (D_z), as shown by their respective normalized probability distributions in ***Figure 4.5***. In our study, we've incorporated one-dimensional supersonic flow of gas along the parallel direction, analogous to our CFE experiment, and found that the displacement of Graphene layers along the vertical axis is impeded. Thus, we can conclude that sliding is a more likely direction of exfoliation of Graphene than vertical direction during CFE process.

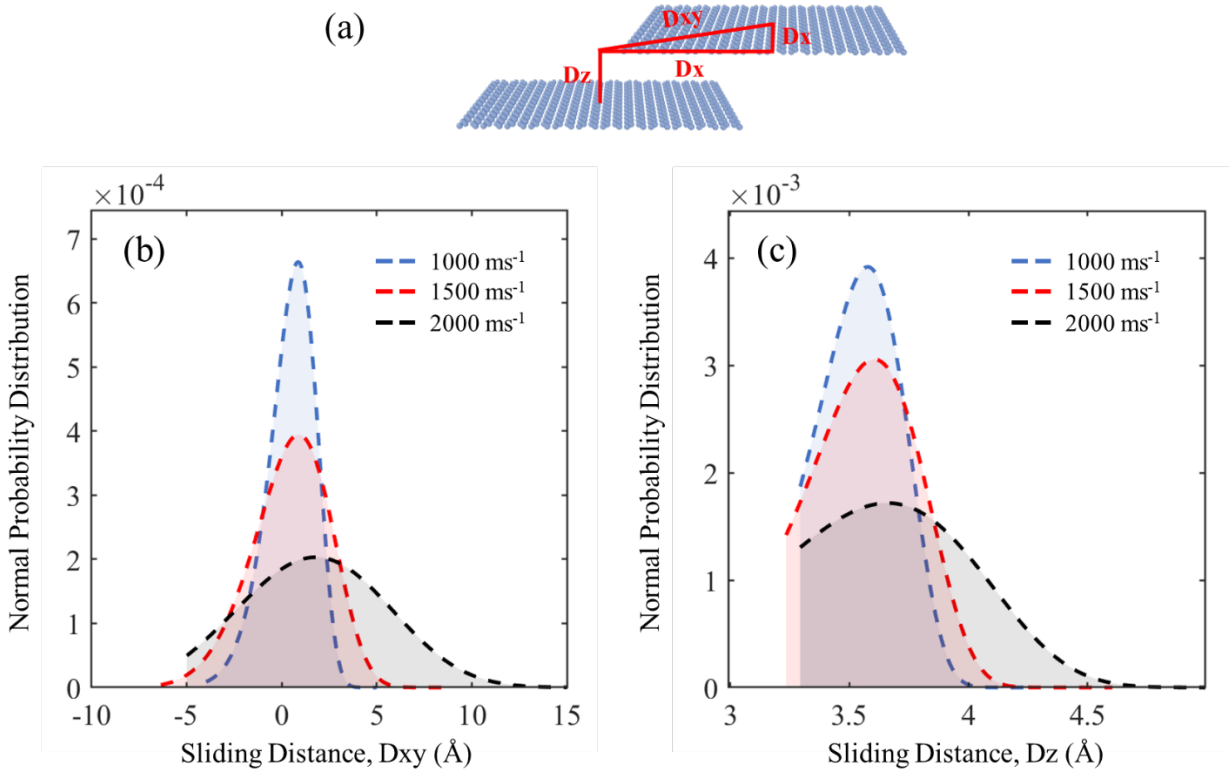

Figure 4.5: *Structural properties of Graphene bilayer at 1000 - 2000 ms^{-1} velocities of helium gas (a) definition of sliding and vertical direction of exfoliation. Normalized probability distribution of (b) sliding distance D_{xy}, and (c) vertical distance D_z of Graphene bilayer [116] Copyright © 2022 American Chemical Society.*

Table 4.2: *Mean lateral sliding distance (D_{xy}) and vertical separation distance (D_z) between Graphene nanosheets under different helium flow velocities.*

Flow Velocity (ms^{-1})	Mean D_{xy} (Å)		Mean D_z (Å)	
1000	1.47 ± 2.22	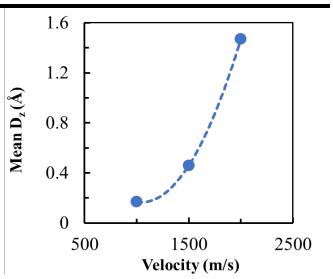	3.66 ± 0.26	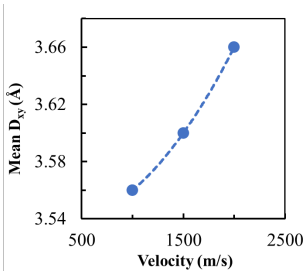
1500	0.17 ± 0.93		3.56 ± 0.02	
2000	0.46 ± 1.01		3.60 ± 0.06	

The density and the flow velocity of fluid rely on the pressure differential of the convergent - divergent section of CD nozzle. If the upstream supply pressure is not notably above ambient at all times, the CD nozzle will only choke at the throat. In that case, it will act as a Venturi tube and no supersonic flow will be achieved. Again, the density of fluid particles is interlinked with the pressure at that point according to the ideal gas law. So, the upstream pressure of gas plays a significant role in the exfoliation of Graphene nanosheets during CFE process. In our study, we have used two different upstream stagnant pressures of gas – 1.4 and 5.5 MPa to investigate the effect of pressure. From the temperature plot of exfoliating layer of Graphene, it is evident that it would take more than 4 times longer to reach T = 3000K at low pressure compared to the high pressure, as shown in ***Figure 4.6(a)***. Because of the low density at 1.4 MPa, there are fewer collision between carbon atoms and helium gas particles. As a result, Graphene layers cannot absorb sufficient kinetic energy to overcome the energy barriers of interlayer vdW interactions. ***Figure 4.6(b)*** shows the energy absorbed by Graphene from helium gas at 1.4 and 5.5 MPa pressures. The Graphene at lower pressure (1.4 MPa) has an absorbed energy of only E ~ 0.04eV at T = 3000K, while this number is E ~ 0.25 at higher pressures. Increasing the pressure from 1.4 to 5.5 MPa, increases the density of helium gas from ~0.78 to ~3.08 Kgm^{-3}, which intensifies the absorbed energy by Graphene. Therefore, a high supply pressure of gas is more suitable for exfoliation of 2D nanomaterials using CFE process. Moreover, the rising temperature (kinetic energy) mostly depends on the relative atomic mass of monoatomic gas and is only slightly changed by atmospheric pressure. Tao et. al. [125], investigated aerodynamic heating of a hypersonic silicon cube, in a dense monatomic gas environment. Their molecular-collision

analysis showed that surface heating can arise from phonons excited by repeated gas–surface collisions.

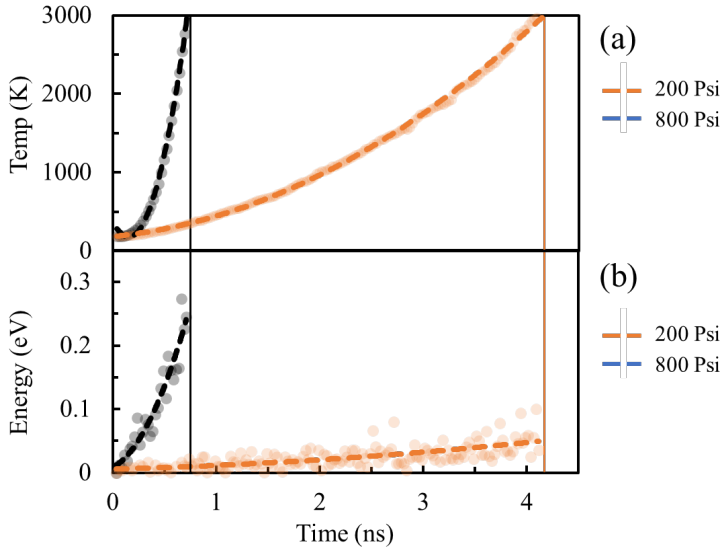

Figure 4.6: *Effect of supply pressure of gas on Graphene exfoliation (a) temperature of Graphene (b) the energy transferred from Helium gas to bilayer Graphene at different Helium at 1.4 and 5.5 MPa [116]*

Copyright © 2022 American Chemical Society.

The final series of MD simulations investigated the effect of two different monoatomic gases on exfoliation of Graphene nanosheets, and the results are summarized in ***Figure 4.7***. Argon has atomic mass of 39.948u which is significantly higher than helium (4.003u) - is considered here for comparison. Monoatomic gases are chosen in this study for simplicity of modeling the MD simulation. Although argon has a higher density than helium at the same experimental conditions, it has much slower speeds due to its larger atomic mass. The Mach profile (velocity profile) in convergence-divergence nozzles is the same for ideal gases. In the same nozzle, the speed of argon gas is lower than helium, because the speed of sound is lower in a heavier ideal gas (V_{sound}: Ar (300K) = 323 m/s, He (300K) = 965 m/s). Hence, here we used a lower speed for Ar than He in the MD simulations (V_{Ar}/V_{He} = ~1/3). The maximum deviation of the exfoliating layer of Graphene is only ~3 Å in Argon whereas it reaches up to more than 16 Å for the case of helium, as shown in ***Figure 4.7(a)***. Therefore, the Graphene layers cannot absorb sufficient kinetic energy from the argon gas flux to cause temperature rise and bond breaking leading to exfoliation. To get the same level of fluctuations from gases with high atomic mass, the upstream pressure or the cross-sectional area

of divergent section must be considerably increased. But continuous operations at high pressure may bring serious safety concerns and incur more cost to the process. The interlayer interaction energy of Graphene (Egg) in the existence of argon and helium and its distribution is shown in ***Figure 4.7(b)***. The Egg in argon and helium exhibits distinctively different distributions. The average of absolute value of Egg in argon is 19.57 ± 0.56 meV/atom which is higher than that of helium (17.15 ± 2.45 meV/atom). This indicates that the collision between helium and Graphene can better weaken the interaction energy between Graphene layers than collisions between argon and Graphene. Based on seven different exchange-correlation ab-initio functional theory, the absolute binding energy between Graphene layers [53] was calculated as 23.67 meV/atom for AB stacked Graphene in vacuum at equilibrium interlayer distance (3.334 Å). Furthermore, this energy decreases with increasing layer separation distance. In our simulations, the distance between Graphene layers in helium gas is considerably higher than that for argon due to higher thermal fluctuations. Consequently, this difference of interlayer separation manifests as a lower binding energy for the case of helium.

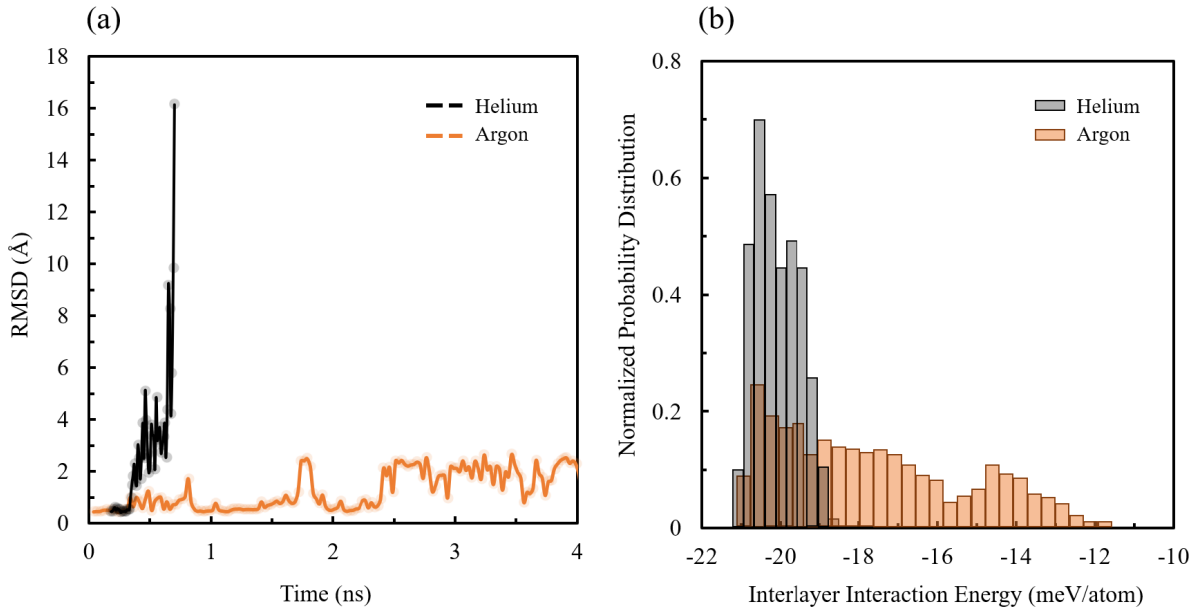

Figure 4.7: *Simulated exfoliation phenomena of Graphene bilayer in two different gas medium (a) RMSD of exfoliating layer of Graphene (b) Normalized interlayer interaction energy between Graphene layers in helium and argon gas [116] Copyright © 2022 American Chemical Society.*

4.4 Conclusion

To comprehend the effect of gas particles on the exfoliation properties of graphite during the CFE process, a classical molecular dynamics based study was performed on a system composed of two Graphene nanosheets placed along the direction of supersonic gas flow. A versatile hybrid formulation of AIREBO-M and LJ potential functions was used to describe the interactions of the Graphene and noble gas system. The findings of this study provide crucial information that allows for the maximization of process yield through experimental design, thereby increasing the versatility of the overall process.

Our results demonstrate that increasing the temperature of the system intensifies the thermal fluctuations of the Graphene layers. Flow simulation analysis indicates that the relative fluctuations and diffusivity of the exfoliating Graphene layer are significantly higher at elevated gas particle flow velocities. Conversely, lower gas velocities fail to provide sufficient kinetic energy to the carbon atoms to overcome the diffusion energy barriers dictated by the interlayer interaction energy. Furthermore, our calculations reveal that exfoliation is heavily favored in a sliding motion rather than in the vertical direction, a direct consequence of the one dimensional in plane supersonic gas flow.

The density and flow velocity of the gas are inherently interlinked with upstream pressure. Consequently, the delamination of Graphene is facilitated at high pressures due to a corresponding increase in the number of collisions between gas particles and carbon atoms. The selection of the gas medium also plays a pivotal role in the CFE process. This computational study establishes that a lighter gas, such as helium, exhibits superiority over a heavier gas, like argon, in exfoliating Graphene due to its higher flow velocity under identical primary conditions. The larger fluctuations of Graphene sheets induced by helium gas also result in a more favorable interlayer interaction energy, which is -2.42 ± 1.89 meV/atom higher than that observed with argon. Therefore, we propose that a lighter gas medium coupled with high upstream pressure provides the optimal conditions for Graphene exfoliation through the CFE process.

The insights regarding the effects of temperature, pressure, and gas type derived from this study are qualitatively applicable to many layer Graphene systems as well. As discussed, while increasing temperature facilitates separation in bilayer Graphene by transferring thermal energy,

many layer Graphene will similarly absorb more energy at higher temperatures, even if this energy might initially be insufficient to overcome the van der Waals forces of every individual layer. Ultimately, this atomistic study provides the necessary molecular level insights that serve as a comprehensive guideline for the exfoliation of not only Graphene but also a broad spectrum of 2D layered materials using compressible gases.

However, it must be acknowledged that classic MD is highly computationally demanding. Because these simulations are strictly limited to the nanoscale in terms of both physical system size and simulated timeframe, capturing the complete, continuous CFE mechanism and the full macroscopic trajectory of layer separation is not computationally viable using this approach alone. Therefore, to overcome these scale limitations and evaluate the exfoliation process comprehensively, the next section will shift the focus toward Energy-Based Analysis.

Chapter 5: Energy-Based Analysis of CFE[3]

5.1 Introduction

As concluded in Chapter 4, direct molecular-dynamics simulations provide valuable insight into the localized, high-speed collisions between gas particles and adjacent 2D nanosheets. However, the computational cost of conventional MD restricts accessible simulation trajectories to nanosecond timescales. Within this limited time window, the complete spontaneous separation of stacked layers may not be observed because exfoliation requires overcoming interlayer free-energy barriers and may occur over timescales longer than those accessible by direct simulation. To address this limitation and evaluate the energetics of exfoliation more comprehensively, an energy-based approach using steered molecular dynamics and potential-of-mean-force analysis was adopted.

The most robust computational method to map the thermodynamic governing laws at the gas and solid interface is the calculation of the Potential of Mean Force (PMF). PMF evaluates the free energy profile of a system along a specific, predefined reaction coordinate. By forcing the system through a sequence of states, PMF allows researchers to rigorously quantify the exact free energy barriers required to separate interacting surfaces. This energy-based approach has been successfully and widely employed in the literature to understand the nanoscale mechanics of carbon-based materials. Notably, PMF calculations, often coupled with umbrella sampling, have been extensively utilized to map the free energy landscapes associated with the interfacial interactions, peeling, and sliding behaviors of Graphene and carbon nanotubes [19, 126]. This work demonstrated that PMF is uniquely capable of capturing the nuanced thermodynamic

---

[3] *Publication and Author Contribution Statement. This chapter is adapted from: Arabha, S., Jian, C., Hixon, R., and Rizvi, R. "Free-Energy Mapping of Gas-Assisted Exfoliation Pathways for Graphene under Compressible Flow: Implications for High-Volume Nanocomposite Applications."* ACS Applied Nano Materials *9, no. 19 (2026): 9092–9104. https://doi.org/10.1021/acsanm.6c01419.*

Saeed Arabha was the lead author and primary contributor to this study. He developed the research concept and computational framework, designed and conducted the steered molecular-dynamics and potential-of-mean-force analyses, performed the data analysis and visualization, interpreted the results, prepared the original manuscript, and led the revision and final publication process. The chapter presents this work within the broader mechanistic and experimental context of compressible flow exfoliation developed in this dissertation.

pathways of nanomaterial deformation and separation. Similarly, other relevant computational studies have leveraged PMF to decode the mechanisms of liquid-phase exfoliation, successfully calculating how specific solvents, polymers, or ionic liquids lower the free energy barrier required to peel or slide 2D layers apart [88].

Building upon these established computational methodologies, this section establishes a fundamental free energy framework specifically tailored for the CFE process. While previous applications of PMF have largely focused on static vacuum, aqueous, or liquid phase environments, this study uniquely maps the gas assisted exfoliation pathways under dynamic compressible flow conditions. Specifically, we investigate how the macroscopic gas dynamics established in Section 3.1, namely velocity, temperature, and pressure, actively alter the free energy required for Graphene exfoliation. To capture the full physical reality of the process, this energy based analysis is conducted along three distinct reaction coordinates: normal separation, edge peeling, and lateral sliding.

Furthermore, this section explores the influence of intrinsic material properties on the free energy landscape, including the effects of Graphene sheet size, the number of interacting layers, and the presence of structural defects. The thermodynamic efficiencies of alternative carrier gases, such as nitrogen, argon, and their mixtures with helium, are also systematically evaluated. By mapping these comprehensive free energy profiles, this energy based analysis provides a definitive thermodynamic evaluation of the CFE process, identifying the most energetically favorable and cost effective pathways for the industrial scale up of high volume 2D nanocomposites.

5.2 Computational Details

Two approaches were adopted to investigate the exfoliation behavior of Graphene nanosheets: (1) simulating a Graphene bilayer in a vacuum environment and (2) simulating the bilayer with helium gas particles present. In both scenarios, we modeled two armchair Graphene nanosheets, each with dimensions of 7×7 nm^2, separated by 0.33 nm, as illustrated in ***Figure 5.1***. The Graphene bilayer was positioned at the center of a simulation box with dimensions of 20×80×20 nm^3. To explore the thermal effects, the system was subjected to a temperature of 300–600 K using the NVT ensemble.

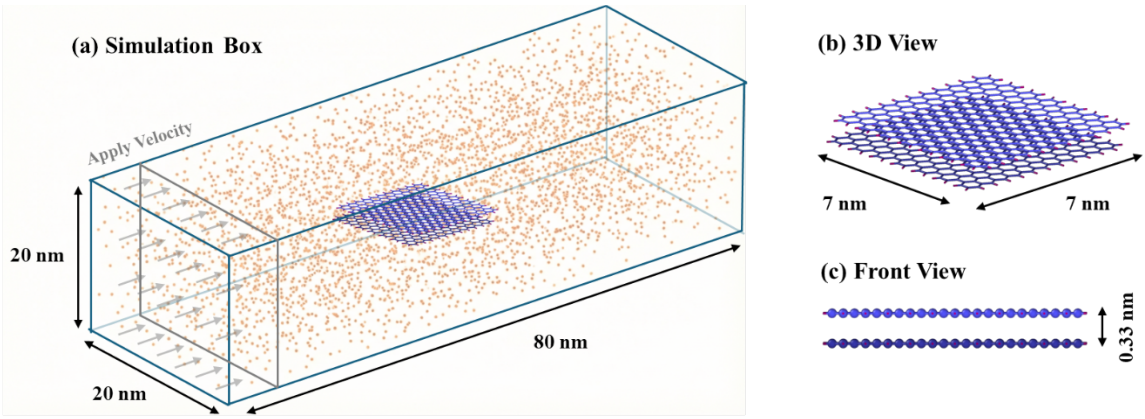

Figure 5.1: *(a) Simulation domain (20 × 80 × 20 nm³) with 10 nm inlet slab for velocity assignment; (b) Graphene bilayer (7 × 7 nm²) with (c) 0.33 nm spacing (3D/side views)* [127] Copyright © 2026 American Chemical Society.

Subsequently, various flow velocities were applied to the gas particles to observe the exfoliation behavior in the Graphene bilayer. The system was first equilibrated at 300 K using the NVT ensemble, followed by a production run using the NVE ensemble. The desired gas flux was maintained at a constant velocity using a stepwise adjustment method. To ensure the velocity remained constant, the gas atoms' velocity at the entrance of the simulation box (measuring 20×20×20 nm³, see ***Figure 5.1(a)***) was monitored throughout the simulation. Every 2 ps, the velocity deviation from the target value was corrected by adjusting the gas atoms' velocity accordingly (see ***Figure 5.2*** for a representative time-history plot of these velocity fluctuations, demonstrating the stability of the control algorithm. The selected ranges for gas velocity, density, and temperature were chosen to directly map to realistic experimental operating windows for CFE [18]. Specifically, the velocities (e.g., up to ~1000 m/s for helium) and localized gas densities (2–8 $g \cdot L^{-1}$) represent the theoretical limits derived from quasi-one-dimensional Euler expansion through a converging-diverging nozzle operating at a typical experimental upstream stagnation pressure of 2000 psi. The temperature range of 300–600 K reflects the operational limits of pre-heating the carrier gas to enhance kinetic energy transfer prior to expansion.

To simulate the exfoliation process, one Graphene sheet was held fixed using a harmonic constraint, representing a terminal sheet in bulk graphite systems [19]. We used a large force constant (77500 $kJ \cdot mol^{-1} \cdot nm^{-2}$) to keep the fixed sheet effectively immobile. This allowed the

other sheet to move freely and interact under applied conditions, mimicking realistic exfoliation behavior.

The equations of motion were integrated using the Velocity Verlet Algorithm [128] with a time step of 0.5 fs, and non-bonded interactions were calculated using a 0.75 nm cutoff. The Nosé–Hoover thermostat and barostat controlled temperature and pressure [115]. Periodic boundary conditions were applied in all directions.

To examine the interactions between Graphene and different gaseous media during exfoliation, several gases were tested. The accuracy of MD results is highly dependent on the precision of the potential functions utilized. For the intralayer carbon–carbon interactions within the Graphene sheets, we employed the Adaptive Intermolecular Reactive Empirical Bond Order–Morse (AIREBO-M) potential [112]. While pristine exfoliation primarily involves overcoming non-bonded interactions, a reactive potential is strictly necessary for this study for two reasons. First, it allows for the natural physical relaxation and topological edge reconstruction of the lattice around the modeled vacancy defects. Second, the inclusion of the Morse term correctly captures the flexural dynamics under the high-pressure, high-shear conditions characteristic of compressible flow, preventing the artificial stiffening and unphysical artifacts observed in standard harmonic or basic REBO potentials under extreme localized deformation [112, 117]. To model the non-bonded interactions, specifically the van der Waals forces between the separate Graphene layers, the gas–gas interactions, and the gas–carbon collisions, the standard 12-6 Lennard-Jones (LJ) potential was utilized (***Table 4.1***) [118, 119]. The Lorentz–Berthelot mixing rules [121] were applied to approximate interactions between dissimilar atom pairs.

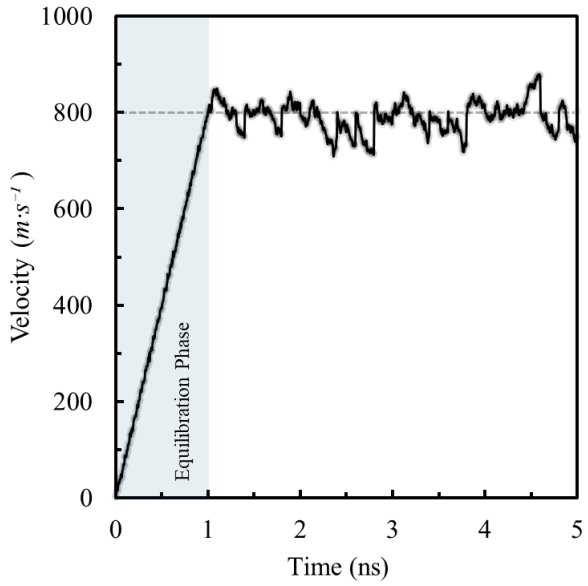

Figure 5.2: *Instantaneous gas velocity tracking during a molecular dynamics simulation (target velocity $V = 800\ m \cdot s^{-1}$ for Helium) [127] Copyright © 2026 American Chemical Society.*

5.3 Steered Molecular Dynamics (SMD)

To investigate the separation mechanisms of Graphene nanosheets, steered molecular dynamics (SMD) simulations were used to drive interlayer separation along defined reaction coordinates and evaluate the associated energetic requirements. SMD is an extension of conventional molecular dynamics in which an external pulling potential, typically represented by a virtual harmonic spring, is applied to selected atoms or collective variables. Whereas conventional MD samples thermally accessible atomic motion without an imposed separation pathway, SMD deliberately drives the system across interlayer separation barriers that may be difficult to capture during unbiased nanosecond-scale simulations. SMD is therefore well suited to comparing the energetic requirements of different Graphene exfoliation pathways [129]. In this study, accuracy is defined by maintaining a statistical uncertainty that is significantly smaller than the macroscopic exfoliation barriers, ensuring that the calculated PMF profiles can accurately distinguish the thermodynamic favourability of the different reaction coordinates. Initially, dynamic pulling simulations were conducted to generate a continuous trajectory of the separation process. The bottom Graphene sheet was held fixed, while the center of mass (COM) of the top sheet (for RC I, ***Figure 5.3(a)***, and RC III, ***Figure 5.3(c)***), or the edge atom of the top sheet (for RC II, ***Figure***

5.3(b)), was connected to a virtual spring with a stiffness of 1000 $kJ \cdot mol^{-1} \cdot nm^{-2}$. This spring was pulled at a constant velocity of 0.005 $nm \cdot ps^{-1}$ to induce separation (***Figure 5.4***). The forces from these continuous pulling trajectories were initially compared to identify the pathways with the lowest resistance. The preferred RC was subsequently used to calculate the PMFs for other gaseous media. To extract the exact PMF curves, a series of independent simulations were performed at discrete intervals along the separation pathway. In these localized stationary windows, the continuous pulling was ceased. Instead, for each selected RC, a harmonic biasing potential with a force constant of 5000 $kJ \cdot mol^{-1} \cdot nm^{-2}$ was applied to restrain the RC within each corresponding range during the simulations. This strong static restraint confined the nanosheet to oscillate around fixed target distances, ensuring adequate localized phase-space sampling to construct the final free-energy maps.

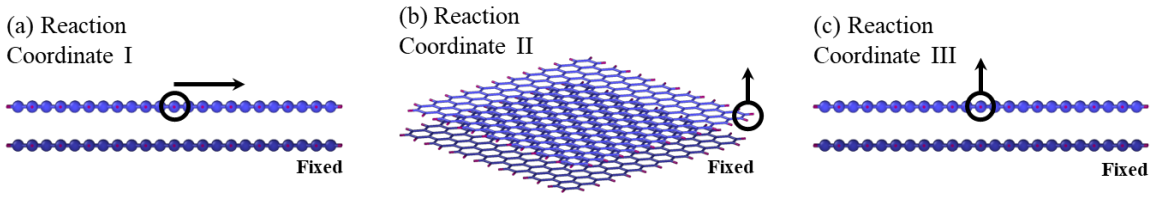

Figure 5.3: *Illustrates the three reaction coordinates (RCs) explored for the separation of two Graphene nanosheets. (a), RC I: depicts the distance between the COMs of the two nanosheets in the lateral (parallel) direction. (b) RC II: shows the distance between the edge atoms of the two sheets in the normal direction. Finally, (c) RC III: the distance between the center of mass (COM) of the two sheets is measured along the normal (vertical) direction [127] Copyright © 2026 American Chemical Society.*

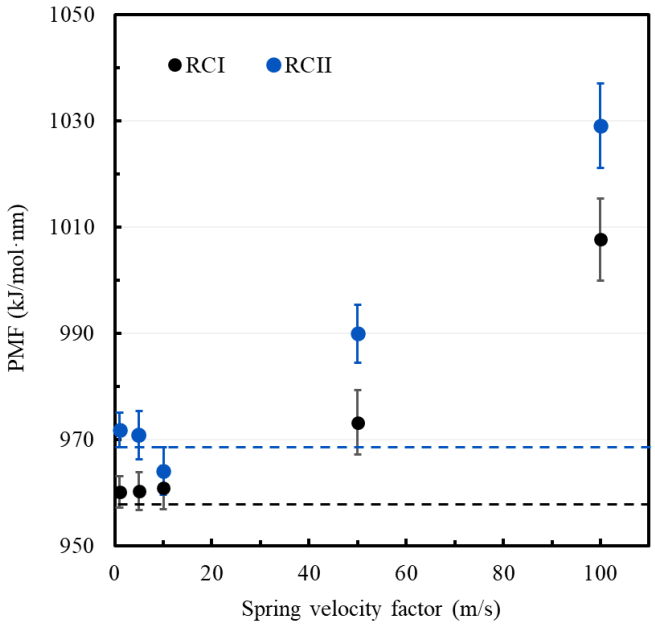

Figure 5.4: *Effect of SMD pulling velocity on the calculated potential of mean force for Graphene separation along RC I and RC II [127] Copyright © 2026 American Chemical Society.*

5.4 Results and Discussion

5.4.1 Reaction Coordinate and Validation

Building upon prior experimental work demonstrating the macroscopic proof-of-concept for CFE [18], the present MD models are specifically designed to both uncover the fundamental atomic-scale separation mechanisms and computationally optimize the process efficiencies utilizing targeted gas mixtures. To determine the most probable exfoliation pathway, pulling simulations were performed for bilayer Graphene sheets along the three reaction coordinates, RC I (lateral sliding), RC II (edge peeling), and RC III (normal separation), under vacuum conditions. The force-displacement curves for each reaction coordinate (RC) are presented in ***Figure 5.5***. It is critical to note that the displacement on the x-axis of ***Figure 5.5*** represents the distance traveled by the virtual SMD pulling spring, which illustrates the mechanical tension building in the system, rather than the physical gap between the Graphene layers.

In RC I (***Figure 5.5(a)***), a peak force of 3.75×10^{3} $kJ\cdot mol^{-1}\cdot nm^{-1}$ is required at a spring displacement of approximately 0.45 nm. Following this peak, the force decreases sharply as the interaction weakens, reflecting diminishing interlayer forces as separation begins. RC II (***Figure***

5.5(b)) shows a more stable force profile, with the required force fluctuating around 3.2×10^{3} $kJ\cdot mol^{-1}\cdot nm^{-1}$ over a broader displacement range. Although the peak force is lower, the interactions between the sheets persist over a longer pulling distance. In RC III (***Figure 5.5(c)***), a much higher peak force of $\sim4.6\times10^{4}$ $kJ\cdot mol^{-1}\cdot nm^{-1}$ is required to overcome the strong π-π interactions between the Graphene sheets [130] (***Figure 5.6***). However, once the spring tension overcomes this massive barrier, the sheets snap apart and the force drops dramatically.

These findings demonstrate that normal separation (RC III) is the least favorable pathway due to its prohibitively high peak force and total work. Consequently, subsequent thermodynamic analyses focus exclusively on the more viable pathways: RC I (sliding) and RC II (peeling).

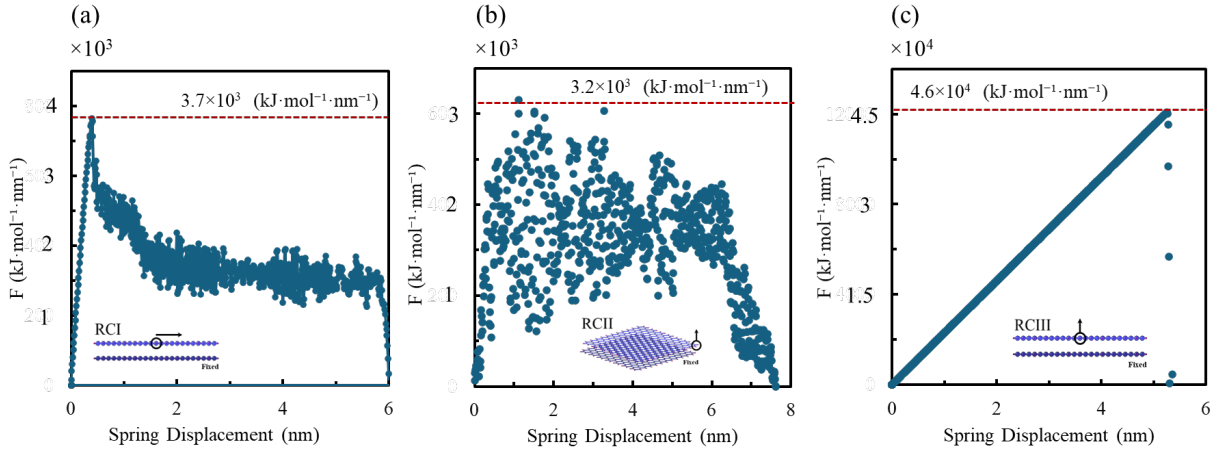

Figure 5.5: *Force–displacement curves for two initially stacked Graphene nanosheets in vacuum condition, pulled apart along the three reaction coordinates: RC I (lateral sliding), (b) RC II (edge peeling), and (c) RC III (normal) [127] Copyright © 2026 American Chemical Society.*

For the subsequent Potential of Mean Force (PMF) profiles, the free energy is plotted against the root-mean-square deviation (RMSD) rather than spring displacement. RMSD quantifies the average spatial deviation of all atoms in the top layer relative to their initial stacked positions over the bottom layer. Because Graphene is highly flexible, it undergoes significant bending, rippling, and asymmetric deformation during gas-assisted exfoliation, especially during the peeling phase. Therefore, RMSD was deliberately chosen as the collective reaction coordinate for the thermodynamic profiles. By integrating the positional shifts of all atoms, it captures the complete global conformational state and flexural dynamics of the separating sheet, providing a highly comprehensive measure of the exfoliation progress.

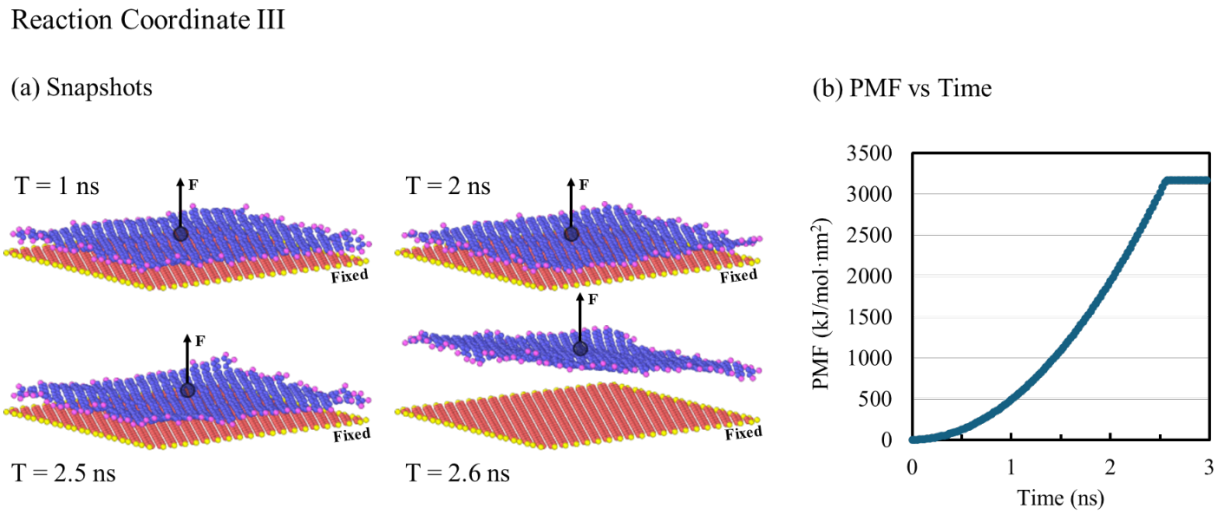

Figure 5.6: *(a) snapshots and (b) PMF of exfoliation of bilayer 7nm Graphene sheets as a function of time [127] Copyright © 2026 American Chemical Society.*

5.4.2 PMF and Free Energy of CFE

The PMF associated with RC I and RC II is studied under two distinct scenarios: (a) where two 7 nm^2 layers of Graphene are situated in a vacuum environment, and (b) where the same Graphene layers are suspended within a box containing helium gas at a density of 8 $g \cdot L^{-1}$ and a velocity of 800 $m \cdot s^{-1}$ in the Y-direction, parallel to the direction of RC I. In the case of RC I, the absence of gas results in a lower energy requirement for complete layer separation, indicating that the presence of gas renders the separation process more challenging. For RC II, the cumulative PMF required to fully separate the 7 nm Graphene layer from the bottom layer is around ~180 $kJ \cdot mol^{-1} \cdot nm^{-2}$, while for RC I, the PMF of ~200 $kJ \cdot mol^{-1} \cdot nm^{-2}$ is needed when the Graphene layers are floating in helium (***Table 5.1***). The presence of gas particles imparts energy to the surface through collisions, thereby influencing the interlayer interactions and affecting the exfoliation process. While the PMFs for both RC I and RC II exhibit similar orders of magnitude for 7 nm bi-layer Graphene, in the RC II scenario, the flowing gas facilitates separation by ~7%. These results corroborate foundational MD studies [19], which demonstrated that the peeling mechanism is energetically more favorable than lateral sliding due to the high frictional barriers associated with moving Graphene sheets out of commensurate registry.

Table 5.1: *$|\Delta G_{CFE}|$ in vacuum and helium gas at static and V=800 m·s^{-1} conditions for RC I and RC II.*

	$|\Delta G_{CFE}|$ (kJ·mol^{-1}·nm^{-2})		
	Vacuum	**He — Static**	**He — V=800 m·s^{-1}**
RC I (lateral sliding)	195.2	211.1	202
RC II (edge peeling)	182.6	208.3	172.3

We define the parameter $|\Delta G_{CFE}|$ as the barrier extracted from the PMF profile (maximum minus minimum along the RC). Exfoliation is considered complete when the PMF plateaus, indicating that further movement of the top layer does not change the free energy (***Figure 5.7***). As observed in the PMF profiles, the geometric mechanism of separation dictates when this plateau is reached. For the lateral sliding mode (RC I), complete exfoliation requires a displacement of approximately 7 nm. Because the simulated sheets are 7×7 nm², the top sheet must be sheared across the entire lateral span of the bottom sheet to fully escape the interaction area. In contrast, the edge peeling mode (RC II) reaches its PMF plateau at roughly half this displacement (~3.5 nm). Because the applied force in RC II lifts the edge out-of-plane and given the short-range nature of van der Waals (π-π) forces, this progressive vertical lifting rapidly moves the atoms beyond the interaction cutoff distance. Therefore, the interlayer cohesive forces are completely severed at a significantly shorter overall displacement.

This plateau in the PMF curve indicates that complete detachment has occurred, with no remaining interactions between the layers, such as van der Waals forces or other adhesive forces. A lower $|\Delta G_{CFE}|$ value indicates easier exfoliation, meaning less external energy is needed from the gas. The $|\Delta G_{CFE}|$ values exhibit the following order: RC I-He > RC I-vacuum, and RC II-He > RC II-vacuum. This trend suggests that while the presence of a static gas medium (V = 0 m·s^{-1}) initially increases the baseline energy required for exfoliation across all reaction coordinates due to fundamental fluid resistance.

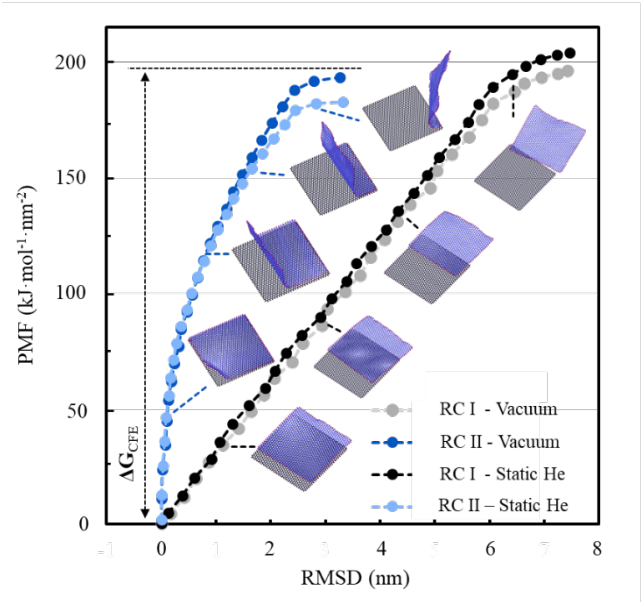

Figure 5.7: *Potential of mean force curves for bilayer Graphene nanosheet separation under vacuum and helium gas environments [127] Copyright © 2026 American Chemical Society.*

5.4.3 Effect of Flow Characteristic on CFE

To analyze the role of flow characteristics on the exfoliation phenomenon of bulk layered materials, we utilized armchair Graphene nanosheets as a representative model for determining the energy transfer dynamics at gas–2D material interfaces. In this section, the effects of gas density/pressure, velocity, and temperature on the exfoliation process are examined (***Figure 5.8***). To quantify the influence of these flow characteristics on the potential of mean force (PMF) required for layer separation, a PMF-Factor is introduced:

$$\text{PMF} - \text{Factor} = \left(\frac{\Delta G_{Gas} - \Delta G_{\text{Vacuum}}}{\Delta G}\right) \qquad 5.1$$

Where ΔG_{Gas} is PMF barrier in existence of gas at different flow characteristics, and ΔG_{Vacuum} is PMF barrier of exfoliation in the vacuum condition.

Figure 5.8(a) illustrates the effect of velocity on Graphene exfoliation along RC I (sliding) and RC II (peeling). It shows that increasing the gas velocity from 0 to 1000 $m \cdot s^{-1}$ reduces the energy required for exfoliation. However, the influence of velocity on PMF is more pronounced along RC II compared to RC I. In the case where the velocity is zero (static gas), exfoliation in the presence of gas molecules requires approximately 5% more energy in both reaction coordinates

compared to vacuum conditions. As the velocity increases to 1000 $m \cdot s^{-1}$, the PMF decreases by approximately 1% in RC I and 13% in RC II. This indicates that velocity has a greater impact on RC II because the flow interacts more significantly with the Graphene layer during the peeling process. Specifically, the lifted edge in the peeling mode acts as a sail, maximizing the effective cross-sectional area perpendicular to the flow. This configuration significantly enhances the inelastic momentum transfer from impinging gas atoms, whereas in the lateral sliding mode (RC I), the gas primarily flows tangentially over the surface with minimal momentum transfer. While a maximum 13% reduction in the absolute PMF barrier may appear modest, macroscopic exfoliation yield depends exponentially on activation energy. Therefore, this linear thermodynamic reduction translates to a highly non-linear increase in the probability of successful separation.

Another important factor in the CFE process is the upstream pressure or gas density. ***Figure 5.8(b)*** illustrates the impact of density on Graphene exfoliation in both RCs. For this study, the gas velocity was maintained at v=800 $m \cdot s^{-1}$ and the temperature at T=300 K. At a constant flow velocity, increasing the gas density directly increases the number of gas atoms per unit volume. Mechanistically, this leads to a proportionally higher collision frequency between the impinging gas atoms and the Graphene surface. Because the aerodynamic force exerted on the sheet is fundamentally the time-averaged rate of momentum transfer from these discrete atomic collisions ($F = dp/dt$), bombarding the surface with more atoms per unit time imparts a greater total momentum. Consequently, this higher collision rate manifests as an enhanced aggregate shear force exerted on the Graphene layers, dynamically facilitating their separation. Furthermore, denser gas can improve momentum transfer efficiency, causing more effective energy distribution across the Graphene sheets. In RC I, the PMF drops by approximately 3% when the helium density is increased from 2 $g \cdot L^{-1}$ to 8 $g \cdot L^{-1}$; this decrease is about 8% for RC II under the same conditions. This difference suggests that RC II is more sensitive to changes in gas density because the average area of Graphene sheets perpendicular to the flow is higher in RC II, leading to increased interaction with the gas flow.

Figure 5.8(c) illustrates the effect of gas temperature on the PMF for Graphene exfoliation in both RC I and RC II. The PMF at different temperatures was investigated with a gas velocity of V=800 $m \cdot s^{-1}$ and a density of D=6 $g \cdot L^{-1}$. The figure shows that increasing the temperature linearly

affects the energy required for Graphene separation. Specifically, increasing the temperature from 200 K to 600 K lowers the exfoliation PMF by ~5% for RC I and ~15% for RC II. This indicates that higher temperatures facilitate Graphene exfoliation. Higher temperatures result in gas molecules possessing greater kinetic energy, leading to more energetic gas–Graphene collisions. As demonstrated by our RMSD tracking Graphene layers at elevated temperatures (***Figure 4.2***) [116], these mechanisms are highly synergistic. The high-kinetic-energy gas collisions actively couple with the Graphene lattice, drastically amplifying its thermal vibrations compared to heating in a vacuum. These gas-amplified flexural vibrations dynamically weaken the short-range van der Waals interactions between the layers, creating transient interlayer gaps. Consequently, the high-energy gas kinetics act as the dominant driver, fueling the exaggerated lattice vibrations that ultimately allow gas molecules to ingress and facilitate full separation. The more significant reduction in PMF observed in RC II suggests that it is more sensitive to temperature changes, due to the larger average area of Graphene sheets perpendicular to the flow.

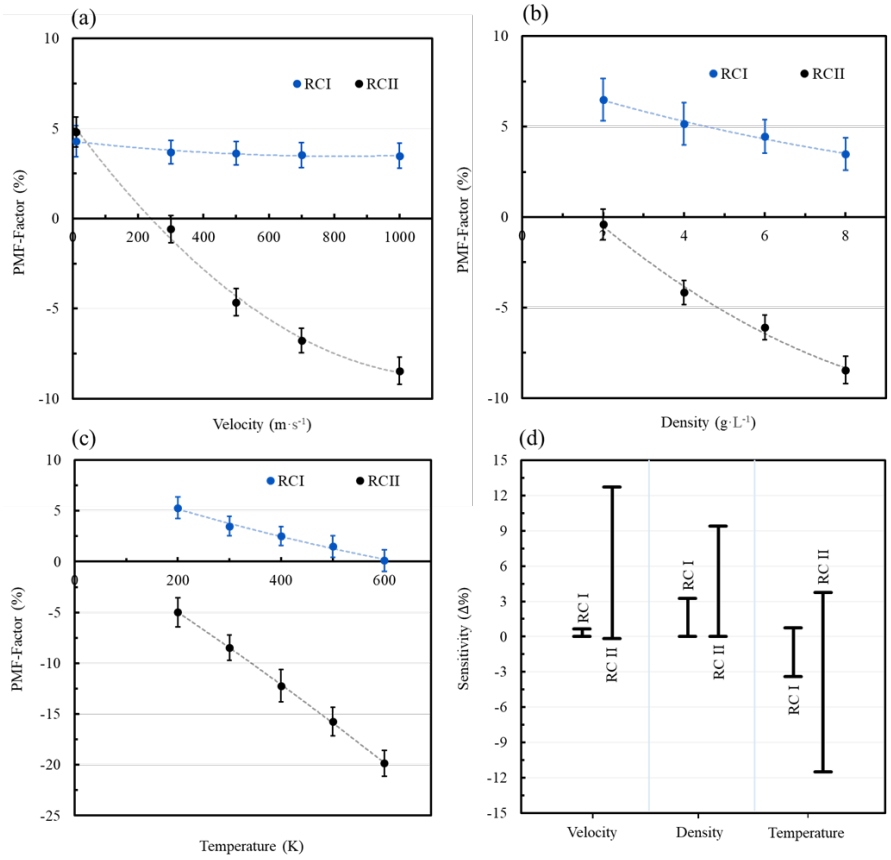

Figure 5.8: *Effects of gas characteristics on the PMF-Factor: (a) velocity, (b) density, and (c) temperature. The PMF-Factor is defined as the ratio of the PMF to the PMF under vacuum conditions. In each study, one gas characteristic varies while keeping the others constant. (d) Sensitivity Analysis: This metric compares how different flow characteristics affect the PMF required for exfoliation. A larger vertical range indicates that the exfoliation energy barrier is highly sensitive to that specific gas characteristic [127] Copyright © 2026 American Chemical Society.*

To quantitatively compare the absolute impact of each gas characteristic on the energy required for Graphene exfoliation, a modified Sensitivity parameter is introduced. To avoid artificial mathematical inflation, Sensitivity is rigorously defined as the absolute percentage point difference (Δ%) from the baseline state:

$$\text{Sensitivity } (\Delta\%) \;=\; \text{PMF} - \text{Factor} - \text{PMF} - \text{Factor}_{\text{Baseline}} \qquad 5.2$$

where $\text{PMF-Factor}_{\text{Baseline}}$ is the PMF-Factor under baseline conditions (T = 300 K, V = 800 $m \cdot s^{-1}$ and D = 6 $g \cdot L^{-1}$). Formulating the sensitivity as a direct percentage point shift provides a reflection of how each variable alters the total thermodynamic barrier. ***Figure 5.8(d)*** shows the $\text{PMF} - \text{Factor}_{\text{Baseline}}$ for both RCs and compare the influence of each gas characteristic, Temperature, velocity and density, on Graphene separation. In ***Figure 5.8(d)***, a wider range indicates that the specific variable exerts a more pronounced influence on the exfoliation energy barrier. RC I is less sensitive to velocity and density but shows some variability with temperature. RC II, on the other hand, is highly sensitive to all three parameters, with temperature showing the most significant impact (***Figure 5.8(d)***).

5.4.4 Effect of Gas Type

In the CFE process, the choice of base gas is critical because the entire exfoliation mechanism relies on the dynamics of the gas flow interacting with the material. Helium has been used as the base gas due to its low molecular weight and high Mach number, which facilitates high-speed gas flows essential for effective exfoliation. However, the price of helium is increasing because of its finite supply and growing demand in various industries, making it economically challenging to use exclusively. Therefore, there is a need to investigate alternative gases. Several other gases, such as argon, nitrogen, hydrogen, air, and others, can potentially be used in the CFE process. Each of these alternatives presents its own set of challenges. For instance, hydrogen has a low molecular weight like helium but is highly flammable, posing significant safety risks in industrial settings. Air is a mixture of different gases, primarily nitrogen and oxygen, which complicates its use in molecular-scale studies due to the varying interactions of its constituent gases with the exfoliating material. Therefore, finding a suitable replacement requires a careful balance of safety, economic viability, and performance in the exfoliation process.

In this section, we investigate the effects of different base gases, helium, argon, and nitrogen, on the PMF of exfoliation to understand the process at a molecular level. To achieve this understanding, we need to have flow characteristics within the nozzle, which can be provided by the quasi-one-dimensional Euler equations. The analysis is based on considering the 1D Euler equations (eq. 3.1).

Figure 5.9(a) presents the densities of He, Ar, and N_2 gases within the same nozzle configuration at 2000 psi, alongside the relative velocity of particles with a 5 μm diameter as they traverse the nozzle (d_{out} = 0.017 m and d_{in}= 0.01 m). The particle velocity relative to the gas peaks at approximately 0.013 meters into the nozzle. The gases exhibit densities around 3.4 $g \cdot L^{-1}$ for He, 35 $g \cdot L^{-1}$ for Ar, and 24 $g \cdot L^{-1}$ for N_2, corresponding to velocities of 660 $m \cdot s^{-1}$, 200 $m \cdot s^{-1}$, and 240 $m \cdot s^{-1}$, respectively. Due to their differing molecular weights and specific heat ratios, lighter monoatomic gases like helium achieve significantly higher flow velocities (up to ~Mach 10) compared to heavier gases like nitrogen (~Mach 2) during supersonic expansion [100]. A detailed macroscopic fluid dynamics investigation of CFE showed that normal shock waves inevitably form in the divergent section of the nozzle [100]. However, because these shock events cause a sudden decrease in relative velocity between the fluid and the particles, the primary aerodynamic shear forces responsible for layer separation are maximized during the high-Mach supersonic expansion phase prior to the shock. The conditions corresponding to this peak velocity were selected as the input parameters for the MD simulations.

Figure 5.9(b) illustrates the energy transfer from the gas flow to a Graphene sheet as it moves along RC I (sliding) and RC II (peeling) when it remains stationary at the center of the box. The energy transferred to the Graphene sheet during the peeling and sliding motions is consistently higher than when it is static, regardless of the gas present. Notably, Graphene moving along RC II receives more energy than along RC I, with the extent of this difference varying by gas type. Specifically, the transferred energy in RC II is approximately 19% greater than in RC I when He is the base gas, while this increase reaches around 50% with N_2 and nearly doubles (~100%) with Ar. This substantial variation in energy transfer is primarily attributed to the atomic or molecular weight of the gases. As the Graphene sheet moves along RC II, its effective cross-sectional interaction with the gas flow is greater than in RC I. Consequently, gases with higher molecular weights transfer more energy upon collision with the Graphene. This results in a distinct hierarchy of energy transfer, while Helium provides the highest velocity, the heavier atomic mass of Argon facilitates more efficient inelastic momentum transfer during the peeling phase (RC II). This highlights that exfoliation efficiency is not solely a function of flow velocity, but of the kinetic energy transfer efficiency factor, where the heavier Argon atoms maximize the impact force per collision on the exposed Graphene edges.

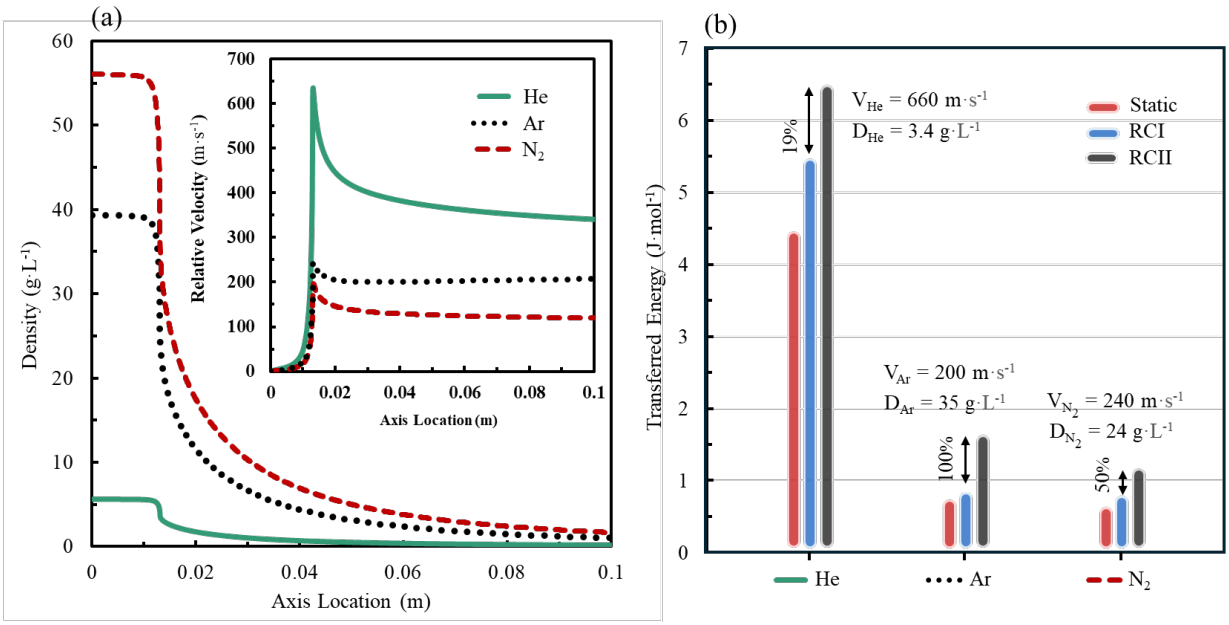

Figure 5.9: *Variations in density and relative velocity ($v_{fluid} - v_{particle}$) along the axial distance of the CD nozzle for different gases: helium, argon, and nitrogen. (b) Energy transferred from gas to Graphene sheets under static conditions (no velocity) and for flowing gas in reaction coordinates (RC) I and II [127] Copyright © 2026 American Chemical Society.*

Helium demonstrates the highest absolute energy transfer to the Graphene sheet across all scenarios, with transferred energy levels reaching ~6.4 J·mol^{-1} along RC II and ~5.4 J·mol^{-1} along RC I. This increased energy transfer from He is due to its significantly higher velocity, over three times that of Ar and N_2, allowing He to impart more kinetic energy to the Graphene during collisions. In contrast, Ar and N_2 exhibit comparable velocities and thus have similar energy transfer values along RC I, both ~0.75 J·mol^{-1}. However, due to its greater atomic weight, Ar transfers more energy than N_2 along RC II, with values of ~1.6 J·mol^{-1} and ~1.1 J·mol^{-1}, respectively. This discrepancy arises because the increased interaction cross-section along RC II amplifies the influence of molecular weight in energy transfer efficiency. Therefore, while He's high velocity enables maximum energy transfer overall, the heavier atomic mass of Ar makes it more efficient than N_2 in RC II, highlighting the combined effects of speed and molecular weight on inelastic momentum transfer (p=m·v).

CFE is, in many aspects, similar to the manufacturing process of cold spray coating [18]; in both processes, particles are carried through a nozzle by high-pressure gases. In cold spray applications,

helium is typically used as the primary gas due to the high velocities that can be achieved, which are essential for effective particle deposition. However, the increasing cost of helium has prompted studies to explore gas mixtures as a cost-effective alternative that can maintain acceptable performance standards [131, 132] In this study, the effects of different gas mixtures of He-Ar and He-N_2 on the energy transfer for Graphene layer separation, which is critical for effective exfoliation, were investigated. ***Figure 5.10*** shows that pure helium delivers the highest energy transfer to Graphene, while pure argon and pure nitrogen exhibit similar but lower energy transfer capabilities.

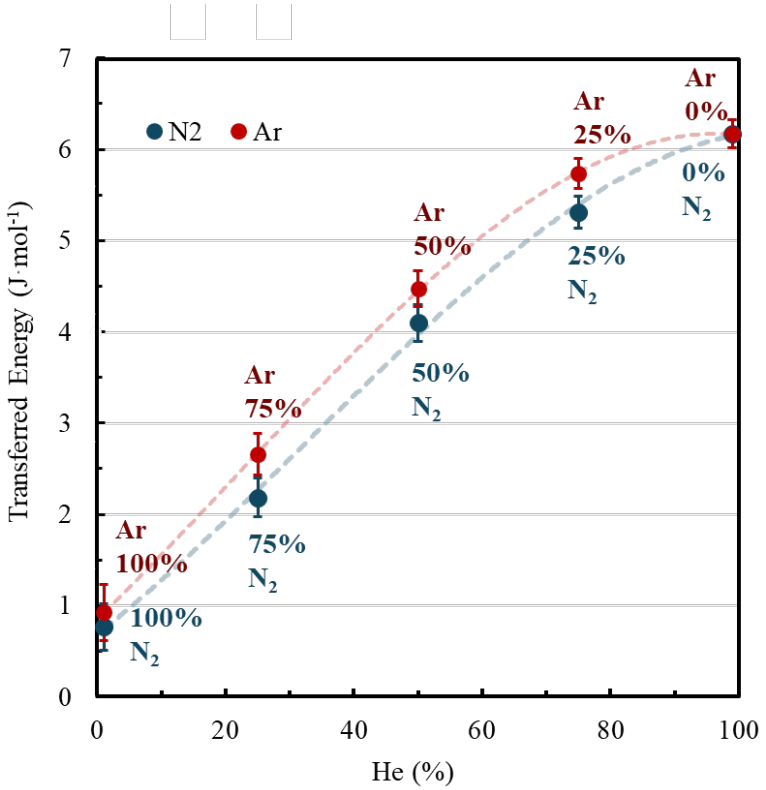

Figure 5.10: *Average energy transferred to Graphene particles using gas mixtures of helium with argon and nitrogen at varying helium concentrations (0%, 25%, 50%, 75%, and 100%) [127]*
Copyright © 2026 American Chemical Society.

To further understand the impact of gas mixtures, combinations of 0%, 25%, 50%, 75%, and 100% helium with argon and nitrogen were analyzed, as depicted in ***Figure 5.10***. Each mixture exhibits distinct velocity and density profiles due to the differing physical properties of the constituent gases. The flow characteristics in all cases were derived from a 1D Euler analysis (Eq. 3.1). The

results indicate similar trends for both He-Ar and He-N_2 mixtures, with argon mixtures consistently demonstrating a higher capability for energy transfer compared to nitrogen mixtures across all helium concentrations. Notably, reducing the helium content by 25% resulted in only a marginal ~7.5% decrease in transferred energy for He–Ar mixtures. This non-linear retention of performance indicates a distinct aerodynamic and collisional synergy rather than a simple compositional average. Mechanistically, this synergy occurs in two phases. First, during the nozzle expansion, the high thermal velocity of the lighter helium fraction modifies the bulk flow field. Through gas-dynamic drag, the helium effectively entrains and accelerates the heavier argon atoms to velocities they could not achieve as a pure gas under the same pressure constraints. Second, upon impingement with the Graphene sheet, the collision mechanics bifurcate. The abundant helium atoms provide a high-frequency baseline of continuous kinetic energy transfer, maintaining the flow momentum. Meanwhile, the entrained argon atoms act as high-momentum impactors. Although argon collisions are less frequent in the mixture, their massive individual impulse transfer ($p = m \cdot v$), especially during the peeling phase (RC II) where the effective cross-section is maximized, dominates the localized energy transfer landscape. This dual 'carrier and hammer' dynamic enables the mixture to retain the kinetic benefits of helium while exploiting the superior momentum transfer efficiency of the heavier species, offering a decisive strategy for cost-effective scale-up.

This non-linear retention of performance indicates a synergistic effect in the flow, the high velocity of the Helium fraction effectively entrains the heavier Argon atoms, creating a high-momentum flux that pure Argon and Helium cannot achieve individually. This flow dynamic enables the mixture to retain the kinetic benefits of Helium while exploiting the momentum transfer efficiency of the heavier species, offering a decisive strategy for cost-effective scaling.

5.4.5 Effect of Graphene Specifications

Since the CFE process begins with high-pressure gas carrying graphite through a nozzle to exfoliate Graphene layers, studying size and layer-count scaling helps clarify exfoliation mechanism and the energy required during peeling and sliding. In this section, we explore Graphene sheets of various sheet sizes and layer counts on the energy necessary for exfoliation . The impact of gas dynamics on the exfoliation process of Graphene sheets is analyzed at varying

sheet lengths (L = 3–9 nm) and layer counts (N = 2–5 layers). To evaluate the effect of sheet length, bi-layer Graphene sheets of different sizes (3, 5, 7, and 9 nm) are positioned at the center of a simulation box filled with helium. In these simulations, the bottom layer remains fixed, while the top layer moves along the reaction coordinate.

In a separate series of simulations, Graphene sheets consisting of 2, 3, 4, and 5 layers are analyzed. For these simulations, the bottom layer (layer 1) is fixed, while the remaining layers are free to move. The exfoliation process proceeds sequentially, beginning with the separation of the topmost layer. Once the top layer is completely detached and passes the boundary condition, it is removed from the simulation box. This process is repeated for the next layer along the same reaction coordinate until all layers are fully exfoliated.

For the lateral sliding pathway (RC I, ***Figure 5.11(a),(b)***), the exfoliation mechanism is fundamentally altered by the gas environment. Applying shear force to the top layer under vacuum conditions results in a sequential, layer-by-layer separation. The first layer separates with a PMF of approximately 250 kJ·mol^{-1}·nm^{-2} (***Figure 5.11(a)***). Because the $\pi - \pi$ friction is insufficient to rigidly lock the sheets together against the pulling force, the unconstrained underlying layers experience slip, requiring a distinct, sequential application of work to separate the second layer (***Figure 5.11(b)***).

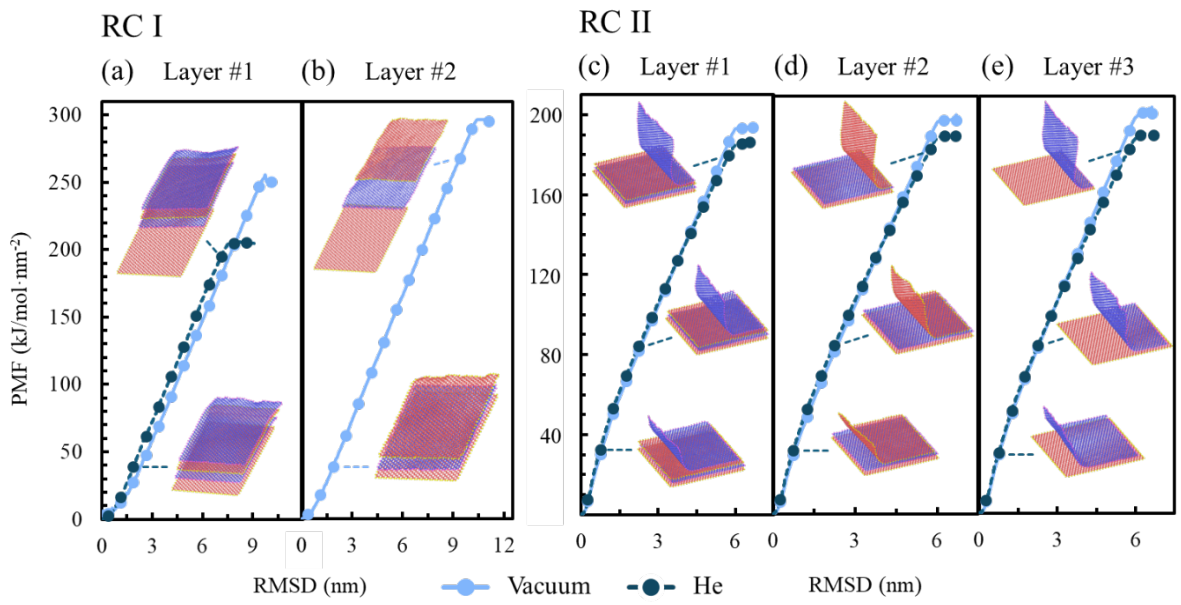

Figure 5.11: *PMF required for the exfoliation of four-layer Graphene under vacuum and helium gas conditions. Panels (a) and (b) show the PMF profiles for the separation of the first and second layers, respectively, along the sliding pathway (RC I). Panels (c), (d), and (e) depict the PMF profiles for the separation of the first, second, and third layers, respectively, along the peeling pathway (RC II) [127] Copyright © 2026 American Chemical Society.*

However, in the presence of high-speed helium flow, the continuous momentum transfer from the gas atoms bombarding the exposed leading edges provides a supplemental kinetic driving force. This gas-dynamic assistance prevents sequential decoupling, causing all three unconstrained upper layers to slide off the fixed bottom layer simultaneously as a single block. Because this occurs concurrently, the entire separation event is captured in ***Figure 5.11(a)***, yielding no subsequent Layer 2 event for the helium case in ***Figure 5.11(b)***. To explicitly visualize this dragging effect, the interlayer center-of-mass (COM) trajectories were tracked during the SMD simulations (***Figure 5.12***). These trajectories mathematically confirm a diverging detachment in vacuum, contrasted against perfectly synchronized block-sliding under helium flow. This indicates that shear force transfers from the first layer to the other layers in both scenarios; however, helium particles exert additional force on the Graphene layers, facilitating separation in four-layer Graphene.

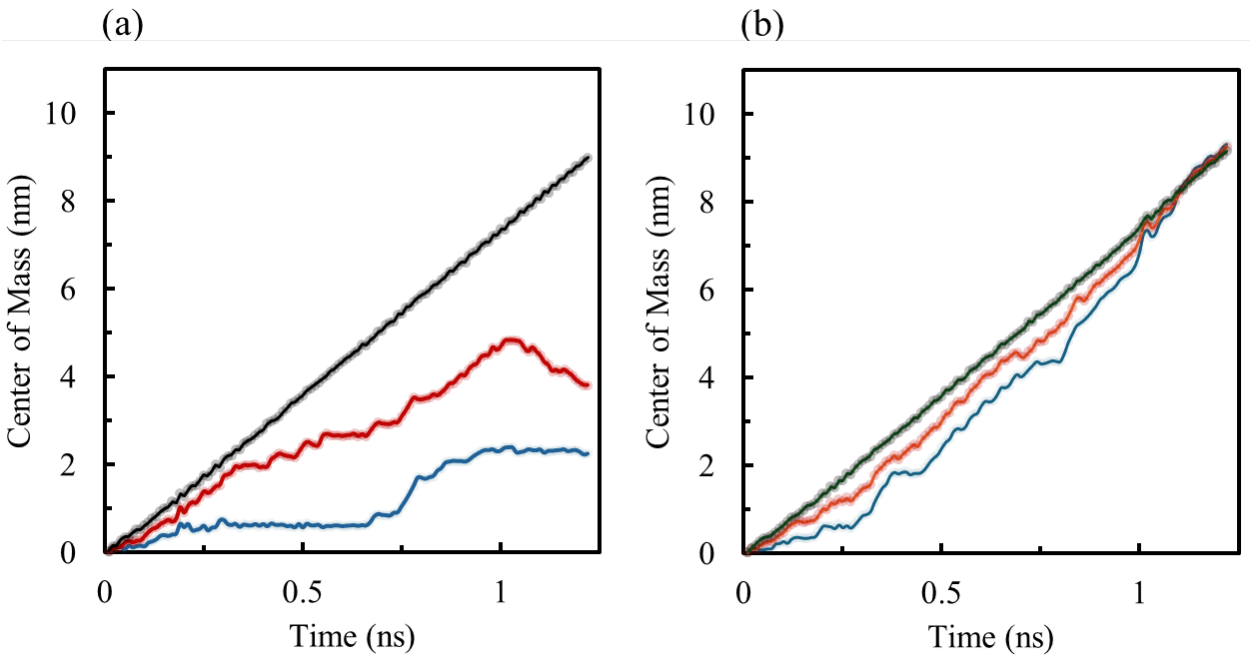

Figure 5.12: *Interlayer center-of-mass (COM) trajectories along the lateral sliding pathway (RC I) during steered molecular dynamics simulations. (a) Under vacuum conditions, the applied pulling force on the top layer results in sequential separation, as evidenced by the diverging layer-wise velocities and distinct decoupling events. (b) Under high-speed helium flow (V = 800 m·s⁻¹), continuous kinetic momentum transfer from gas atoms bombarding the exposed leading edges provides a supplemental driving force. This gas-dynamic assistance overcomes interlayer slip, synchronizing the layer velocities and resulting in the simultaneous block-sliding of all three unconstrained upper layers [127] Copyright © 2026 American Chemical Society.*

For RC II, separation occurs layer by layer in both vacuum and high-speed gas conditions, requiring roughly the same energy for each layer: PMF ≈ 190 $kJ \cdot mol^{-1} \cdot nm^{-2}$ under vacuum and PMF ≈ 180 $kJ \cdot mol^{-1} \cdot nm^{-2}$ with high-speed helium. In this exfoliation mechanism, force also transfers to the next layers at the onset of separation. However, because the peeling mechanism involves breaking π-π interactions, it is easier to separate layers individually, as disrupting these interactions demands a high initial force.

By comparing the mechanisms (RC I and RC II), we observe that RC II requires less energy for each layer separation when converting four-layer Graphene into multiple single-layer Graphene.

Nevertheless, CFE may yield few-layer rather than single-layer Graphene. In such cases, RC I can facilitate simultaneous separation of multiple layers.

To investigate how gas dynamics affect exfoliation across sheet length and layer count, we studied Graphene separation at different length of L=3-9 nm (***Figure 5.13(a)***) and various number of layers at N=2-5 layers (***Figure 5.13(b)***). As shown in ***Figure 5.13(a)***, increasing the length of the Graphene sheet enhances the role of gas dynamics in determining the PMF required for exfoliation in both RC I and RC II. For instance, at a sheet length of 3 nm, exfoliation at RC I requires approximately 10% higher PMF in the presence of helium. However, this difference reduces to about 3% when the sheet length increases to 9 nm. Similar trends are observed for RC I; however, the magnitude of the effect is less pronounced than in RC II. As previously discussed, the peeling mechanism (RC II) presents a larger perpendicular cross-section to the flow, thereby maximizing the gas-dynamic assistance. This positive impact continues from ~3% to more than ~13% when the size of Graphene sheet increases from 3 nm to 9 nm, respectively. In both RC I and RC II scenarios, increasing the sheet size inherently increases the total number of carbon-carbon van der Waals interactions, which strictly raises the absolute energy barrier required for complete separation (as evidenced by the increasing absolute PMF values in the ***Figure 5.13(a)*** inset). However, the expanded surface area simultaneously provides a correspondingly larger aerodynamic cross-section for high-velocity gas collisions. Because this gas-dynamic momentum transfer scales highly efficiently with surface area, the relative contribution of the gas flow in overcoming the cohesive forces more pronounced for larger sheets.

In ***Figure 5.13(b)***, the effect of number of layers in Graphene separation in gas flow condition is investigated, for sliding condition (RC I) a substantial decrease in PMF requires for separation in gas flow with respect to vacuum condition is observed by increasing number of layers from 2 to 5 layers, which is ~ 28%. By observing the PMF required in each condition it appears that increasing the number of layers from 2 to 5 could increase the absolute PMF by 5 times, from ~ 100 $kJ \cdot mol^{-1} \cdot nm^{-2}$ to ~600 $kJ \cdot mol^{-1} \cdot nm^{-2}$ in gas flow condition, while this number is tripled, from 100 $kJ \cdot mol^{-1} \cdot nm^{-2}$ to ~400 $kJ \cdot mol^{-1} \cdot nm^{-2}$ in vacuum condition. On the other hand, PMF-Factor remained almost constant at ~-7% for peeling (RC II) at different number of layers, since the increase in PMF required for separation increased with the same rate in both vacuum and gas flow condition by increasing the number of layers. This result shows that, while exfoliating larger Graphene sheets

with more layers requires greater energy, the exfoliation process is more significantly influenced by gas dynamics in such cases. The increased interactions between the gas molecules and the expanded surface area of larger or thicker Graphene sheets facilitate energy transfer, making it easier to overcome interlayer van der Waals forces during exfoliation. Furthermore, this dimensional scaling directly translates to real-world CFE scenarios. While a baseline 13% PMF reduction applies to a 7 nm bilayer, actual bulk precursors are on the order of microns. Because of these larger dimensions in practical applications, the vastly increased interaction volume significantly amplifies the kinetic momentum transfer. It is precisely this amplified driving force that multiplies the macroscopic yield in real-life processes.

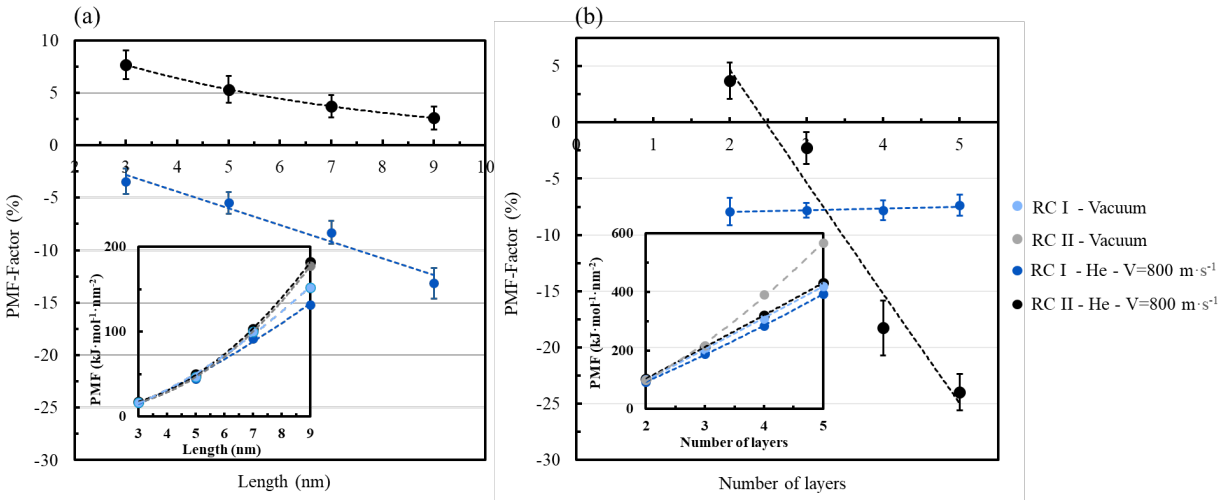

Figure 5.13: *PMF required for the exfoliation of Graphene for, (a) PMF for bi-layer Graphene at varying lengths. (b) PMF as a function of the number of Graphene layers at a fixed length of L=7 nm, under vacuum and helium gas environments [127] Copyright © 2026 American Chemical Society.*

5.4.6 Effect of Structural Defects on Exfoliation Energetics

While pristine Graphene provides a fundamental baseline, experimental CFE processes inherently involve bulk materials with pre-existing structural imperfections. To quantify the impact of these imperfections on the exfoliation barrier, we introduced varying concentrations of point defects, specifically random mono- and di-vacancies, into our bi-layer Graphene models.

Defects were modeled by randomly deleting carbon atoms to achieve uniform spatial distributions with overall atomic vacancy concentrations of 1%, 3%, and 5%. Following deletion, the systems were thermally equilibrated at 300 K using the reactive AIREBO-M potential. The use of this

bond-order potential is crucial here, as it naturally allows for the local relaxation and reconstruction of the carbon lattice around the vacancy sites prior to the application of the gas flow.

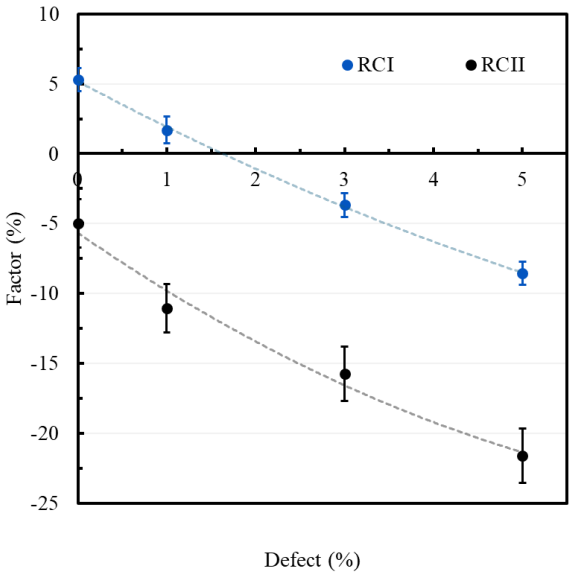

Figure 5.14: *The effect of structural defect concentration (1%, 3%, and 5% random vacancies) on the PMF-Factor for lateral sliding (RC I) and edge peeling (RC II) under a helium gas flow (V = 800 m·s⁻¹, D = 6 g·L⁻¹). The increasingly negative Factor (%) indicates that gas dynamics become significantly more effective at lowering the exfoliation barrier as structural imperfections increase [127] Copyright © 2026 American Chemical Society.*

The resulting influence of these defects on the PMF-Factor under a high-speed helium flow (V = 800 m·s⁻¹, density = 6 g·L⁻¹) is presented in ***Figure 5.14***. The data reveals a pronounced trend: increasing the defect concentration significantly amplifies the gas-dynamic assistance during exfoliation. For lateral sliding (RC I), the PMF-Factor shifts from approximately +5% for pristine Graphene to ~-9% at a 5% defect concentration. The effect is even more dramatic for the edge peeling mechanism (RC II), where the PMF-Factor decreases from -5% to nearly -22% under the same conditions.

Physically, this enhanced separation efficiency arises from two synergistic mechanisms. First, the missing carbon atoms disrupt the continuous, delocalized π-electron network, weakening the baseline van der Waals cohesive energy between the layers. Second, and more importantly for the CFE process, the atomic-scale voids and reconstructed edges associated with the defects act as localized scattering sites. These structural irregularities increase the effective surface roughness of

the Graphene sheet, greatly enhancing the inelastic momentum transfer from the impinging high-velocity gas atoms. Consequently, while defective Graphene fundamentally requires less energy to separate, the gas flow becomes disproportionately more effective at delivering that necessary work, particularly during the peeling phase.

It is important to acknowledge the limitations of this computational approach. Due to the inherent spatiotemporal constraints of molecular dynamics, these simulations represent an idealized, highly localized operating regime. The model isolates a single exfoliation event of nanoscale Graphene flakes (up to 9 nm) over picosecond timescales, whereas macroscopic CFE involves complex, turbulent, and multi-particle interactions over longer durations. Nevertheless, this idealized atomic window provides the necessary fundamental thermodynamic baseline required to optimize macroscopic fluid-dynamic parameters. The observed trends, specifically that gas-dynamic energy transfer scales favorably with sheet size and layer count, provide critical theoretical insights and a predictive thermodynamic baseline for future experimental validation aimed at scaling up Graphene production for bulk structural applications.

5.5 Conclusion

This section provides an atomistic-level understanding of the CFE process for Graphene production. Using molecular dynamics simulations and PMF calculations, we investigated how gas dynamics, specifically velocity, temperature, and pressure, affect the energy required for Graphene exfoliation along different reaction pathways. We also examined the influence of Graphene sheet size, number of layers, and the presence of defects, as well as the effects of alternative gases like nitrogen and argon and their mixtures with helium.

Our simulations revealed several key insights:

- **Exfoliation Pathways:** Among the reaction coordinates studied, the peeling mechanism (RC II) consistently required less energy for layer separation compared to sliding (RC I). This is attributed to the fact that peeling involves breaking π-π interactions more efficiently, and the larger cross-sectional area exposed to the gas flow enhances energy transfer from gas molecules to the Graphene sheets.
- **Impact of Gas Dynamics:** Increased gas velocity, temperature, and pressure systematically reduced the absolute PMF required for exfoliation, especially along the peeling pathway.

While these thermodynamic barrier reductions are mathematically modest (e.g., up to ~15%), macroscopic exfoliation yield depends exponentially on this activation energy. Therefore, these linear reductions in the PMF barrier translate to a highly non-linear, exponential increase in the probability of successful layer separation. Higher velocities enhance momentum transfer, while elevated temperatures increase kinetic energy and thermal vibrations within the Graphene lattice, weakening interlayer forces.

- **Effect of Gas Type:** Helium gas, owing to its low molecular weight and high velocity, was most effective in reducing the PMF required for exfoliation. However, mixtures of helium with argon or nitrogen also demonstrated substantial energy transfer capabilities. While pure helium provided the highest energy transfer, reducing helium content by 25% in mixtures resulted in only a marginal decrease (approximately 7.5% for argon mixtures) in transferred energy. This finding establishes a critical design rule for economic scale-up: a 75%He-25%Ar mixture retains ~92.5% of the exfoliation efficiency of pure helium. This synergy occurs because the high-velocity helium fraction effectively entrains the heavier argon atoms, maintaining a high momentum flux while significantly lowering operational costs.
- **Graphene Sheet Size and Layer Number:** Our results demonstrate that larger Graphene sheets and higher numbers of layers amplify the influence of gas flow on the exfoliation process. As the sheet size increased from 3 nm to 9 nm, the impact of gas dynamics on the potential of mean force (PMF) grew from approximately 3% to over 13%. Similarly, increasing the number of layers resulted in a more pronounced effect of gas flow conditions compared to vacuum, indicating that thicker samples benefit more from the gas dynamics due to increased surface area and collision frequency.

These insights provide an atomic scale understanding of CFE and establish generalizable design rules for optimizing the gas phase processing of broad classes of layered nanomaterials tailored for high throughput macroscopic applications, such as bulk structural composites, concrete reinforcement, and thermal management materials.

Crucially, the theoretical framework and quantitative energy barriers established in this section will serve as the direct foundation for the physical implementation of the CFE process. In the next chapter, we will utilize these specific computational results, such as the optimal gas mixtures, required velocities, and preferred peeling mechanisms, to guide and optimize the macroscopic

experimental setup. By translating these nanoscale thermodynamic findings into targeted macroscopic operating parameters, we aim to experimentally validate the predicted efficiencies and achieve the scalable, high yield production of 2D materials.

Chapter 6: Experimental Optimization of CFE[4]

6.1 Introduction

The modelling chapters established that Compressible Flow Exfoliation is governed by coupled gas-dynamic and thermally assisted mechanisms. The continuum analysis in Chapter 3 showed that particle forces is controlled by gas acceleration, particle–gas relative velocity, local density, drag force, and cumulative effective work. The molecular dynamics simulations in Chapter 4 showed that gas velocity, pressure, temperature, and gas type influence nanosheet fluctuation, sliding, and energy transfer. The energy-based analysis in Chapter 5 further showed that gas flow and temperature can reduce the energetic resistance to interlayer sliding and edge peeling. Together, these results suggest that CFE output should be improved by controlling experimentally adjustable variables such as gas temperature, carrier gas type, pressure, precursor particle size, and post-exfoliation recovery.

This chapter tests that hypothesis experimentally. The central objective is to determine whether the mechanistic insights from the modelling chapters can be translated into a practical CFE process with improved recovered nanosheet concentration. In particular, gas preheating is treated as the key enabling modification because it changes the thermo-kinetic state of the carrier gas before expansion. By increasing the thermal and kinetic energy available during rapid gas acceleration, preheating is expected to improve particle entrainment, particle–gas momentum transfer, lattice vibration, and thermally assisted interlayer weakening.

The experimental strategy is organized in four stages. First, a reference-based CFE apparatus was developed in this study using the operating concept and key components reported for the earlier valve-based CFE configuration. Its baseline performance was then evaluated using h-BN as the reference material by examining whether the expected gas-dependent exfoliation trend could be reproduced. Second, h-BN was used as the optimization platform to evaluate the effects of precursor particle size, gas preheating, raw-material loading, and upstream pressure. Third, the

[4] Intellectual Property and Publication Status. The apparatus modifications, process conditions, recovery strategies, and experimental results presented in this chapter form part of an ongoing intellectual-property assessment. Journal publication of these findings has therefore been delayed while the associated protection and commercialization strategy is being finalized.

optimized heated condition was extended to Graphene and MoS_2 to evaluate the transferability of the process across conductive, insulating, and semiconducting layered materials. Fourth, post-exfoliation recovery, centrifugation, starting particle size, and sediment re-exfoliation were examined to distinguish exfoliation performance from recovery efficiency.

A key point in this chapter is that the measured output of CFE is not controlled only by the gas-phase exfoliation event inside the nozzle. It also depends on how efficiently nanosheets are captured, stabilized, separated, and recovered after exfoliation. Therefore, concentration, cumulative concentration, recovered mass, recovery percentage, and production intensity are treated as related but distinct metrics. This distinction is necessary to avoid overinterpreting recovered concentration as a direct measure of intrinsic exfoliation yield.

6.2 Methodology and Experimental Configuration

This section describes the experimental methodology used to validate, optimize, and recover products from the CFE process. The methodology is organized into precursor materials and carrier gases, collection solvent, CFE apparatus and operating protocol, gas-preheating design, centrifugation/recovery protocols, and concentration determination by gravimetry and UV–Vis spectroscopy. In this chapter, gas pressure, temperature, loading, and precursor size are treated as CFE processing variables, while repeated re-dispersion and centrifugation are treated as post-processing recovery and fractionation steps.

6.2.1 Precursor Materials and Carrier Gases

The experimental validation of the CFE process required representative van der Waals layered materials with different crystal structures, densities, and interlayer bonding characteristics. Graphite, MoS_2, and BN were selected as model conductive, semiconducting, and insulating layered materials, respectively.

High-purity Natural graphite flakes (ACS Material, SKU GTF03121) were used as the precursor for Graphene production. Two grades were evaluated to determine the effect of starting particle size: 1000-mesh graphite (nominal flake size: 13 μm; purity: 99.9%) and 3500-mesh graphite (nominal flake size: 4.3 μm; purity: 99.9%).

MoS_2 powders with different average particle sizes were used to study the effect of precursor size on CFE output. MoS_2 powders with average particle sizes of approximately 1.5 µm (Superfine Grade), 4.5 µm (Technical Fine Grade), and 12.5 µm (Technical Grade) were supplied by M K Impex Corp (Mississauga, ON, Canada). An additional MoS_2 powder with an approximate particle size of 6 µm was obtained from Sigma-Aldrich.

h-BN powders were obtained from ACS Material. Three grades were used to investigate the role of initial particle size and surface area: Type A h-BN with D50 of 2–3 µm and BET surface area of approximately 15 $m^2 \cdot g^{-1}$, Type B h-BN with D50 of approximately 3 µm and BET surface area of 8–12 $m^2 \cdot g^{-1}$, and Type C h-BN with D50 of approximately 10 µm and BET surface area of 3–10 $m^2 \cdot g^{-1}$.

To generate the high-pressure supersonic flow environment and evaluate the thermodynamic energy transfer predictions established in Chapter 3, a selection of carrier gases was utilized. High-pressure cylinders of Ultra-High Purity (UHP) Helium (He) and Nitrogen (N_2), each possessing a certified mean purity of ≥ 99.999% (Grade 5.0), alongside standard compressed air, were supplied by Linde. This gas selection was chosen to evaluate how carrier-gas properties influence CFE performance. Helium provides a high speed of sound and serves as a benchmark for high-velocity compressible-flow exfoliation, whereas nitrogen and compressed air are lower-cost, more practical gases for scale-up. Comparing these gases allowed the effect of gas thermophysical properties, especially acoustic velocity, density, and heat capacity, to be tested under the reconstructed and heated CFE conditions.

6.2.2 Collection Solvent and Dispersion Medium

A liquid collection medium was used to capture and stabilize the exfoliated nanosheets immediately after gas-phase expansion. For all experimental runs, the exfoliated material was collected in 200 mL of a co-solvent mixture composed of 60 vol.% deionized water and 40 vol.% isopropyl alcohol (IPA). Analytical-grade IPA (≥ 99.5%) was obtained from Sigma-Aldrich.

The DI water/IPA mixture was selected as a practical low-boiling co-solvent for immediate capture and stabilization of the nanosheets after gas-phase expansion. Pure DI water has relatively high surface tension and may not adequately wet or stabilize hydrophobic graphitic surfaces, whereas addition of IPA lowers the liquid surface tension and modifies the polar/dispersive

balance of the medium [133]. This improves nanosheet wetting and reduces the interfacial energy penalty associated with maintaining exfoliated sheets in suspension, thereby decreasing their tendency to re-stack or aggregate. More broadly, solvent and co-solvent selection for liquid exfoliation is commonly guided by matching the liquid's surface-energy characteristics to those of the layered material, because this reduces the energetic cost of forming new nanosheet–liquid interfaces. Alcohol/water co-solvent systems are therefore widely used as lower-boiling, more easily handled alternatives to high-boiling solvents such as NMP. The 60 vol.% DI water/40 vol.% IPA composition used here was selected as a common collection medium and a practical compromise across Graphene, h-BN, and MoS_2.

The use of a standardized 200 mL collection volume also allowed a constant liquid-to-solid ratio and dilution factor across all runs, allowing measured UV–Vis absorbance and recovered concentration to be compared directly between processing conditions, carrier gases, and starting materials.

6.2.3 CFE Apparatus and Operating Protocol

The reconstructed CFE apparatus was designed to expose bulk layered powders to a short burst of heated, high-pressure carrier gas before rapid expansion through a narrow flow restriction. Relative to the reference CFE configuration, the key modification was the addition of an upstream gas-heating stage. This stage was introduced to increase the thermal state of the carrier gas before expansion and to test whether heating improves particle acceleration, gas-particle momentum transfer, and layer separation, particularly for nitrogen and compressed air. The system consisted of a high-pressure gas supply, pressure regulation and isolation valves, an in-line gas-heating section, a stainless-steel powder entrainment chamber, an adjustable Swagelok needle-valve/nozzle restriction, and a downstream collection vessel containing the DI water/IPA solvent.

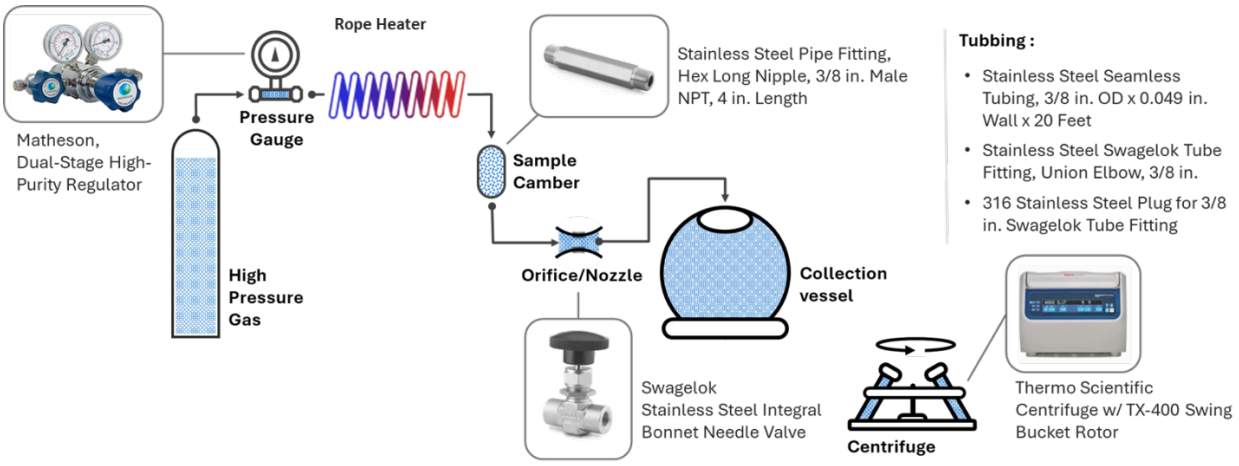

Figure 6.1: *Schematic illustration of the Compressible Flow Exfoliation (CFE) Process for gas-phase exfoliation and liquid-phase collection of two-dimensional (2D) nanomaterials. The system consists of a high-pressure carrier-gas source, pressure regulation and isolation valves, an in-line gas-heating section, a powder entrainment chamber, an adjustable Swagelok nozzle/orifice, and a downstream collection vessel containing 200 mL of DI/IPA co-solvent. The apparatus enables rapid fluidization, gas-phase acceleration, and shear-driven exfoliation of bulk layered materials, followed by immediate liquid-phase capture and stabilization of the exfoliated nanosheets.*

As shown in ***Figure 6.1***, the CFE synthesis process began by accurately weighing and loading the selected bulk precursor powder, including Mesh 1000 graphite, superfine MoS_2, or Type A h-BN, into the high-pressure stainless-steel entrainment chamber. The upstream gas line was then pressurized to the target stagnation pressure while the powder chamber remained isolated. Before each experiment, the in-line gas-heating section was activated using an external heating band maintained at a constant surface temperature of $T_s = 250°C$, allowing the 3/8-inch stainless-steel tube to reach thermal equilibrium.

After thermal stabilization, the pressurized carrier gas was rapidly introduced into the powder chamber, producing a short-duration, high-energy gas–particle flow. This sudden pressure-driven influx fluidized the bulk precursor powder and carried the particle-laden suspension through the adjustable Swagelok nozzle. As the multiphase flow accelerated through the 0.1 mm annular gap, the suspended particles experienced intense aerodynamic shear, rapid acceleration, interparticle interactions, and thermally enhanced lattice vibrations that promoted layer sliding and delamination. The energetic jet was discharged downward into 200 mL of DI–IPA co-solvent,

where the exfoliated nanosheets were rapidly decelerated and stabilized as a colloidal dispersion. For all comparative experiments, the flow burst duration was standardized at approximately 2 s.

The in-line gas-preheating stage was incorporated to experimentally evaluate the temperature-dependent exfoliation behavior predicted by the multiscale simulations. This heating stage represents the key modification of the reconstructed CFE apparatus because it increases the thermal state of the carrier gas before nozzle expansion. Under choked-flow conditions, gas preheating can increase the attainable exit velocity and improve particle acceleration, gas–particle momentum transfer, and shear exposure inside the nozzle. At the material scale, elevated temperature can also increase atomic-scale fluctuations within layered crystals, reducing the effective resistance to interlayer sliding and peeling. Therefore, the reconstructed system should be interpreted as a thermally assisted compressible-flow exfoliation process, rather than a purely pressure-driven gas-flow exfoliation process. This distinction is particularly important for nitrogen and compressed air, which do not provide the same acoustic-velocity advantage as helium under unheated conditions but become significantly more effective when additional thermal energy is supplied upstream of the nozzle.

6.2.4 Gas Preheating Design and Heat-Transfer Estimate

The in-line gas-preheating stage was incorporated to translate the temperature-dependent exfoliation trends predicted by the multiscale simulations into the experimental system. This heating stage is the central modification of the reconstructed CFE apparatus because it allows lower-cost gases such as nitrogen and compressed air to provide sufficient thermo-kinetic energy for effective exfoliation. Heating the carrier gas increases thermal energy transfer and can increase gas velocity under choked-flow conditions, thereby improving particle acceleration, momentum transfer, and shear exposure during CFE.

Heating the carrier gas increases thermal energy transfer and can increase gas velocity under choked-flow conditions, thereby improving particle acceleration and shear exposure during CFE. Chapter 3 analysis quantified how this intensified atomic-scale fluctuation systematically reduces the energy barriers for successful exfoliation, effectively lowering the PMF required to initiate both the sliding and peeling delamination pathways. By thermally activating the layered material and increasing atomic-scale fluctuations, the effective resistance to layer separation is reduced,

lowering the aerodynamic shear threshold required for delamination. Therefore, gas preheating transforms the CFE process from a primarily kinetic, shear-driven system into a thermo-kinetic delamination mechanism. This transformation is particularly important for nitrogen and compressed air, because these gases do not provide the same acoustic velocity advantage as helium under unheated conditions. By adding thermal energy upstream of the nozzle, the modified system compensates for this limitation and enables useful exfoliation yields using more accessible carrier gases. This optimization ensures that a larger fraction of the suspended bulk particles achieve successful layer separation at a given stagnation pressure, directly translating to a substantial increase in the final exfoliated concentration and overall manufacturing throughput.

To physically implement the thermo-kinetic mechanism, a rigorous heat transfer analysis was performed to determine the minimum required length of the in-line heating tube (L) to successfully elevate the high-pressure carrier gas from ambient temperature ($T = 20^{o}C$) to the target operational temperature ($T = 200^{o}C$). The following details the analytical calculations utilized, with Helium selected as the representative carrier gas at an optimized stagnation pressure of 5.5 MPa.

The design optimization utilizing Helium at a stagnation pressure of 5.5 MPa required defining the system-specific thermophysical and operational variables. The physical domain was constrained by a heating tube possessing an inner diameter (D) of 3/8 inch (9.53 mm). The operational thermal boundaries were established with a target gas inlet temperature (T_{in}) of $20^{o}C$ (293 K) and a desired exit temperature (T_{out}) of $200^{o}C$ (473 K), driven by an external heating band providing a constant wall surface temperature (T_s) of $250^{o}C$ (523 K). Based on these boundary conditions, the bulk mean temperature of the fluid was calculated as $110^{o}C$ (383 K). To facilitate the convective heat transfer analysis, the thermophysical properties of helium were evaluated at this bulk mean temperature, yielding a specific heat capacity of 5193 $J \cdot kg^{-1} \cdot K^{-1}$, a thermal conductivity of 0.18 $W \cdot m^{-1} \cdot K^{-1}$, a dynamic viscosity of 2.3×10^{-5} $Pa \cdot s$, and a Prandtl number of 0.67.

To perform a conservative design analysis, the calculation was initialized utilizing the targeted operating condition of maximum pressure and target temperature, assuming an ideal non-adiabatic system.

To accurately model the convective heat transfer, the initial flow velocity (V) within the upstream 3/8-inch heating tube was extracted directly from the one-dimensional Euler flow simulation results established in Chapter 3. For a targeted stagnation pressure of 5.5 MPa, this prior continuum mapping established a sustained upstream fluid velocity of $\mathrm{V} \approx 5.1$ m/s. Utilizing this velocity alongside the tube cross-sectional area ($\mathrm{A_{tube}} = 7.12 \times 10^{-5} m^2$ and the high-pressure Helium gas density ($\rho = 6.91$ kg/m^3), the continuous system mass flow rate ($\dot{m}$) was derived via the continuity equation:

$$\dot{m} = \rho V A_{tube} = \left(6.91 \text{ kg/m}^3\right)(5.1 \text{ m/s})\left(7.12 \times 10^{-5 \text{ m}^2}\right) = 0.00252 \text{ kg/s} \quad 6.1$$

The total thermal power required to elevate the continuous mass flow of Helium by $180°C$ was determined using the basic thermodynamic energy balance:

$$q = \dot{m} c_p (T_{out} - T_{in}) = (0.00252 \text{ kg/s})(5193 \text{ J/kg} \cdot \text{K})(180 \text{ K}) = 2355 \text{ W} \quad 6.2$$

Given the high stagnation pressures and the derived fluid velocity, the Reynolds Number (Re) was calculated to identify the flow regime within the heating tube:

$$Re = \frac{\rho V D}{\mu} = \frac{(6.91)(5.1)(0.009525)}{2.3 \times 10^{-5}} \approx 14640 \quad 6.3$$

Since $\mathrm{Re} > 10000$, the flow is fully turbulent. Therefore, the convective heat transfer coefficient (h) was determined utilizing the Dittus-Boelter correlation for internal forced convection heating:

$$Nu = \frac{hD}{k} = 0.023 Re^{0.8} Pr^{0.4} = 0.023(14640)^{0.8}(0.67)^{0.4} \approx 42.0 \quad 6.4$$

$$h = \frac{Nu \cdot k}{D} = \frac{42.0 \cdot 0.18}{0.009525} = 793 \text{ W/m}^2 \cdot \text{K} \quad 6.5$$

The total required heat transfer (q) was set equal to the convective heat transfer governed by Newton's law of cooling utilizing the Log Mean Temperature Difference (ΔT_{lm})

$$q = h(\pi D L)\Delta T_{lm} \quad 6.6$$

$$\Delta T_{lm} = \frac{(T_s - T_{in}) - (T_s - T_{out})}{\ln\left(\frac{T_s - T_{in}}{T_s - T_{out}}\right)} = \frac{(250-20)-(250-200)}{\ln\left(\frac{230}{50}\right)} \approx 117.9°C \quad 6.7$$

Solving for the theoretical minimum length (L_{min}):

$$L_{min} = \frac{2355\ \text{W}}{(793\ \text{W/m}^2\cdot\text{K})(\pi\cdot 0.009525\ \text{m})(117.9\ \text{K})} = 0.84\ \text{m (84 cm)} \quad 6.8$$

The analytical minimum length (L_{min}) of 84 cm was derived assuming perfect, idealized conditions for Helium gas. In reality, the physical laboratory setup experiences unavoidable heat losses to the ambient environment, despite the external heating rope being actively regulated by a dedicated temperature controller and covered with thermal insulation.

Furthermore, the experimental protocol required testing carrier gases with different thermal properties, including helium, nitrogen, and compressed air. To ensure that each gas stream consistently reached the target operational temperature despite gas-specific heat-transfer differences and external heat losses, a substantial safety factor was integrated into the final design. Therefore, an implemented length greater than twice the calculated minimum was applied to the custom heating tube. This conservative design ensured that the observed yield improvement in nitrogen and compressed air was associated with a reproducible heated operating condition rather than uncontrolled thermal variation between gases. Therefore, an implemented length of more than twice the calculated minimum ($L_{design} > 2 \times L_{min}$) was applied to the custom-fabricated heating tube, guaranteeing sufficient residence time for heat transfer across all experimental trials. This conservative approach ensured reliable thermal energy transfer during exfoliation, independent of the chosen carrier gas.

6.2.5 Post-Exfoliation Recovery and Centrifugation Protocols

After CFE processing, the collection vessel contained a multiphase dispersion composed of exfoliated nanosheets, partially exfoliated aggregates, and unexfoliated parent particles. Because this broad particle distribution is expected in top-down exfoliation, centrifugation was used to separate dispersed nanosheets from heavier particles and to recover material trapped in the sediment.

The raw CFE dispersion was transferred into 50 mL centrifuge tubes for post-processing. Three centrifugation-based protocols were used depending on the objective of the experiment. First, repeated sediment re-dispersion was used to recover nanosheets trapped in the sediment after each centrifugation cycle. Second, centrifugation-speed fractionation was used to examine the size and

thickness distribution of CFE-produced MoS_2 at 1500, 3000, and 4500 rpm for a duration of 2 hours. Third, sediment recycling was used for Graphene, where the remaining sediment was freeze-dried and reprocessed through the CFE system.

The application of this cascading centrifugal force precisely fractionates the constituent particles based on their mass and physical dimensions. During the initial low-speed cycle (1500 rpm), the heaviest, unexfoliated bulk particles rapidly overcome the stabilizing forces of the solvent and sediment into a solid pellet at the bottom of the tube. The top fraction of the liquid, known as the supernatant, was then carefully pipetted, decanted, and utilized as the feed for the subsequent higher-speed cycle (3000 rpm). This process was repeated for the final 4500 rpm stage. These successive higher-speed stages progressively enrich the supernatant in smaller and thinner nanosheet fractions by sedimenting larger and thicker particles. The optimized surface tension of the DI/IPA co-solvent minimizes the enthalpy of mixing, allowing the final, low-mass 2D structures to remain stably suspended.

The successful isolation of a stable colloidal suspension in the final supernatant was initially confirmed by the presence of a strong Tyndall effect when the dispersion was illuminated by a laser source, indicating extensive light scattering by the suspended nanoscale particulates.

6.2.6 Concentration Determination and UV–Vis Calibration

The concentration of CFE-produced suspensions was determined using a combination of gravimetric analysis and UV–Vis spectroscopy. For gravimetric analysis, a known volume of suspension was dried, and the remaining solid mass was measured. The concentration was calculated as:

$$C = \frac{m}{V} \tag{6.9}$$

where C is the concentration, m is the dry recovered mass, and V is the suspension volume. In gravimetric concentration plots, the slope of dry mass versus suspension volume was therefore equal to the suspension concentration.

In addition to suspension concentration, the recovered mass and CFE production intensity were used as supporting performance metrics. The recovered mass was calculated as:

$$m_{\mathrm{rec}} = CV \tag{6.10}$$

where $C$is the measured suspension concentration and $V$is the collection volume. Since all CFE products were collected in 200 mL of DI/IPA solvent, the recovered mass in milligrams was calculated as $m_{\mathrm{rec}} = 200C$, where C is expressed in g·L⁻¹. CFE production intensity was defined as:

$$I_{\mathrm{CFE}} = m_{\mathrm{rec}}/t_{\mathrm{burst}} \quad 6.11$$

where t_{burst} is the active gas-discharge time. For the standardized 2 s CFE burst used in this chapter, $I_{\mathrm{CFE}} = 100C$ in mg·s⁻¹. This metric is reported only as a short-burst process intensity, not as a continuous industrial production rate, which would be lower as it would account for process preparation and post-processing steps.

UV–Vis spectroscopy was then calibrated using gravimetrically measured stock suspensions. For each material, one stock suspension was first quantified by gravimetric analysis. This stock was then diluted to known concentrations using defined dilution ratios. UV–Vis spectra were collected for each dilution, and the absorbance at a selected wavelength was plotted against concentration. The Beer–Lambert relationship was used:

$$\frac{A}{l} = \alpha C \quad 6.12$$

where A is the absorbance, $l$is the optical path length, C is the concentration, and $\alpha$is the extinction coefficient. Since A, l, and C were known for each dilution, the slope of the calibration plot provided the material-specific extinction coefficient. These values were then used to estimate unknown suspension concentrations from UV–Vis absorbance.

6.3 Experimental Validation of the Reconstructed CFE System

Before modifying the CFE system, the operating conditions reported in the reference study were reviewed to identify the most effective baseline configuration for experimental validation. The experimental validation sequence used to reconstruct and benchmark the CFE system is summarized in ***Figure 6.2***. In the original CFE study, h-BN powder was entrained in a high-pressure carrier-gas stream and passed through a narrow valve restriction before collection in a solvent.

The preferred valve configuration was a Swagelok needle valve opened by one-quarter turn, corresponding to an annular gap of approximately 0.1 mm. This setting was selected because it

provided a favorable balance between flow confinement and reliable powder transport. Rather than affecting only a single shear-rate value, changing the valve opening changes the effective throat area, local flow-acceleration region, velocity and density gradients, and the extent to which particles are exposed to near-wall high-gradient flow. These features influence particle–gas relative velocity, aerodynamic drag, and the mechanical work transferred from the expanding gas to the layered precursor particles.

At larger valve openings, the flow field becomes less confined and the relative fraction of the high-gradient near-wall region decreases. Consequently, the gas–particle coupling and localized aerodynamic forces available for exfoliation may be reduced, even though the total gas-flow capacity is higher. At smaller openings, the restriction becomes more susceptible to powder accumulation, clogging, and blockage. Therefore, the one-quarter-turn valve setting with an approximately 0.1 mm annular gap was used as the reference condition because it represented the best experimentally observed compromise between strong localized flow–particle interaction and stable operation.

The reference study [18] also tested the effects of several process variables, including initial BN loading, upstream pressure, flow geometry, tube diameter, and carrier gas type. The process was very fast, with exfoliation occurring in approximately 2 s, and the reported CFE yield for h-BN was generally in the range of 5–10%. Increasing the starting BN concentration increased the final dispersed h-BN concentration, but only up to a limit. At high BN loading, the valve configuration became more prone to clogging because densely packed BN powder restricted the flow.

Pressure was another major factor. In the valve configuration, increasing the upstream pressure increased the final h-BN concentration because higher pressure produced higher gas velocity and stronger shear. The reference paper reported that h-BN concentrations of approximately 0.04 $g \cdot L^{-1}$ could be achieved even at 1.4 MPa, while the highest reported concentration in the pressure study was approximately 0.2 $g \cdot L^{-1}$ at 11 MPa. However, the authors noted that operating continuously at very high pressure may introduce safety and economic concerns. Therefore, for validation and comparison, a moderate pressure condition such as 5.5 MPa with helium is a practical baseline, while higher pressures can be considered during optimization if the system is designed safely.

The carrier gas strongly influenced the exfoliation performance. Helium produced the highest h-BN concentration compared with nitrogen and carbon dioxide. At the same pressure of 5.5 MPa,

helium gave a much higher final concentration than nitrogen or carbon dioxide in both the valve and straight-tube configurations. This was attributed to the higher speed of sound in helium, which allows higher gas velocities and therefore higher shear rates under compressible/choked-flow conditions. Argon and compressed air were also mentioned as behaving similarly to nitrogen, with lower performance than helium.

Straight-tube geometries were also examined to understand the role of flow geometry. Stainless-steel tubes with inner diameters of 1.3, 2.1, 3.1, 3.8, and 4.6 mm were tested. The best straight-tube result was obtained with the 2.1 mm inner diameter tube, which reached approximately 0.11 $g \cdot L^{-1}$ at 5.5 MPa. Larger diameters produced lower shear, while the smaller 1.3 mm tube suffered from excessive frictional losses and did not reach the same effective choked-flow behavior. However, the valve configuration still performed better than the straight tube because the 0.1 mm converging–diverging restriction generated stronger acceleration and shear.

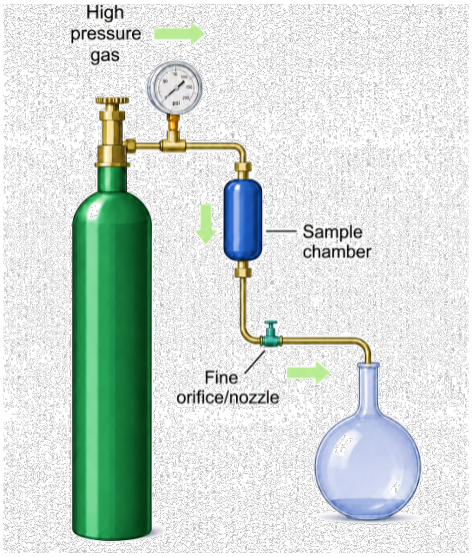

***Figure 6.2**: Experimental validation workflow for the reconstructed CFE system. The reference valve-based CFE condition was first reproduced using h-BN and helium/nitrogen carrier gases.*

Based on the operating conditions reported in the reference CFE study, the initial validation experiments were designed around the most effective valve-based configuration. The reference work identified a Swagelok needle valve opened by 1/4 turn as the preferred flow restriction, producing an annular gap of approximately 0.1 mm with a converging–diverging geometry. This condition was selected because it generated sufficiently high shear for exfoliation while avoiding

the two main problems observed at other valve settings: reduced yield at larger openings due to insufficient shear and complete flow restriction at smaller openings due to clogging.

The reference paper showed that h-BN exfoliation was sensitive to gas pressure, carrier gas, and flow geometry. Increasing the upstream pressure increased the final h-BN concentration in the valve configuration, with the highest reported value reaching approximately 0.2 $g \cdot L^{-1}$ at 11 MPa. However, because continuous operation at very high pressure introduces safety and economic concerns, helium at 5.5 MPa represents a practical validation condition before moving to higher-pressure optimization. Helium was selected as the preferred carrier gas because it produced substantially higher h-BN concentrations than nitrogen, carbon dioxide, argon, or compressed air. This behavior was attributed to the higher speed of sound in helium, which enables higher gas velocities and higher shear rates under compressible-flow conditions.

Therefore, the validation stage of the present work used the reference CFE condition as a benchmark: h-BN powder processed through a narrowly opened valve/orifice using high-pressure gas and collected in solvent for UV–Vis analysis. Reproducing the reported UV–Vis behavior of h-BN under this baseline condition confirmed that the reconstructed system followed the same exfoliation mechanism. After this validation, the system was modified and the process was optimized by adjusting pressure, flow geometry, and gas conditions to improve exfoliation performance and reproducibility.

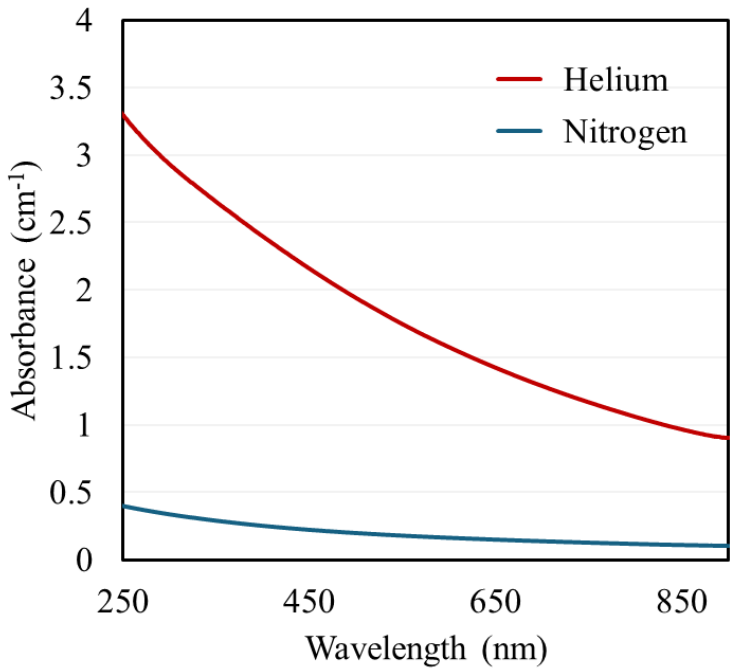

***Figure 6.3**: UV–Vis validation of h-BN exfoliation using the reconstructed CFE system. He-CFE and N_2-CFE h-BN suspensions were compared with the reference gas-dependent CFE trend. The reconstructed system produced approximately 0.23 $g \cdot L^{-1}$ using helium and 0.04 $g \cdot L^{-1}$ using nitrogen, reproducing the reference gas-dependent trend in which helium produces a higher h-BN concentration than nitrogen under comparable valve-based CFE conditions.*

The corresponding UV–Vis validation results are shown in ***Figure 6.3***, where the reconstructed system reproduces the expected higher h-BN concentration for helium compared with nitrogen. The reconstructed CFE device was experimentally validated using both helium and nitrogen as carrier gases, following the gas-comparison approach reported in the reference CFE study. The UV–Vis spectra of the h-BN suspensions obtained using He-CFE and N_2-CFE are shown in ***Figure 6.1***. The concentration was estimated using the Beer–Lambert relation (equation 6.12). Absorbance is proportional to the concentration of dispersed h-BN at a fixed wavelength, path length, solvent, and material system. Based on this analysis, the present system produced an estimated h-BN concentration of 0.23 $g \cdot L^{-1}$ using helium and 0.04 $g \cdot L^{-1}$ using nitrogen. In comparison, the reference paper reported maximum concentrations of approximately 0.15 $g \cdot L^{-1}$ for helium and 0.03 $g \cdot L^{-1}$ for nitrogen under the valve-based gas-comparison condition. Therefore, the present device reproduced the same gas-dependent trend, with helium producing a substantially

higher h-BN concentration than nitrogen. The slightly higher concentrations obtained in the present work may be partly attributed to differences in the starting h-BN material, since the reference study used bulk BN with an initial particle size of approximately ~13 μm [18]. The slightly smaller h-BN starting powder used in the present work may have increased the available surface area and improved entrainment relative to the reference material. Overall, the UV–Vis results show good agreement with the reference trend and confirm that the reconstructed device operates effectively. After the reconstructed system reproduced the expected gas-dependent h-BN trend, the next objective was not simply to maximize concentration empirically, but to identify which controllable variables could convert nitrogen from a low-performing carrier gas into a practical exfoliation medium.

6.4 Parameter Optimization of CFE Process

h-BN was selected as the optimization material because it provides continuity with previous CFE studies and allows the effect of process modification to be evaluated before extending the optimized condition to other layered materials. After validating the reconstructed CFE device using h-BN, the process was optimized by systematically tuning four key parameters: bulk h-BN particle size, stagnation temperature, initial raw-material loading, and upstream stagnation pressure. Among these variables, stagnation temperature was treated as the key enabling modification because the addition of gas preheating directly changes the thermo-kinetic state of the carrier gas before expansion. The other variables control material availability, particle entrainment, and pressure-driven acceleration, while preheating increases the energy available for particle acceleration, lattice vibration, and layer separation. The results are summarized in ***Figure 6.4***. These parameters were selected because they directly influence the main physical mechanisms involved in compressible flow exfoliation, including particle entrainment, gas velocity, aerodynamic shear, particle–gas momentum transfer, and the intensity of rapid gas expansion through the nozzle. In the reference CFE study, exfoliation was attributed to high shear rates generated by high-velocity compressible gas flow through narrow restrictions and converging–diverging geometries.

The baseline CFE condition was first defined as 7 MPa upstream pressure**,** 0.3 g initial h-BN loading**,** no external heating**,** and 10 μm starting bulk h-BN powder. Under this baseline condition,

the final h-BN concentration was only approximately 0.003 $g \cdot L^{-1}$. Therefore, the optimization study was designed to systematically improve this initial low-performing condition by changing one major parameter at a time: reducing the starting particle size, increasing the stagnation temperature, increasing the initial raw-material loading, and increasing the upstream pressure.

In the optimized setup, the collection flask volume was increased from 100 mL to 200 mL to accommodate the expanded gas volume more effectively and reduce particle loss during collection. Experimentally, when the same process was performed using 200 mL instead of 100 mL solvent, the measured concentration decreased by approximately half. This confirms that the reduction in concentration was mainly caused by dilution rather than a loss in exfoliation or collection efficiency. Therefore, the optimized process should be evaluated not only by concentration, but also by the total recovered mass of dispersed h-BN.

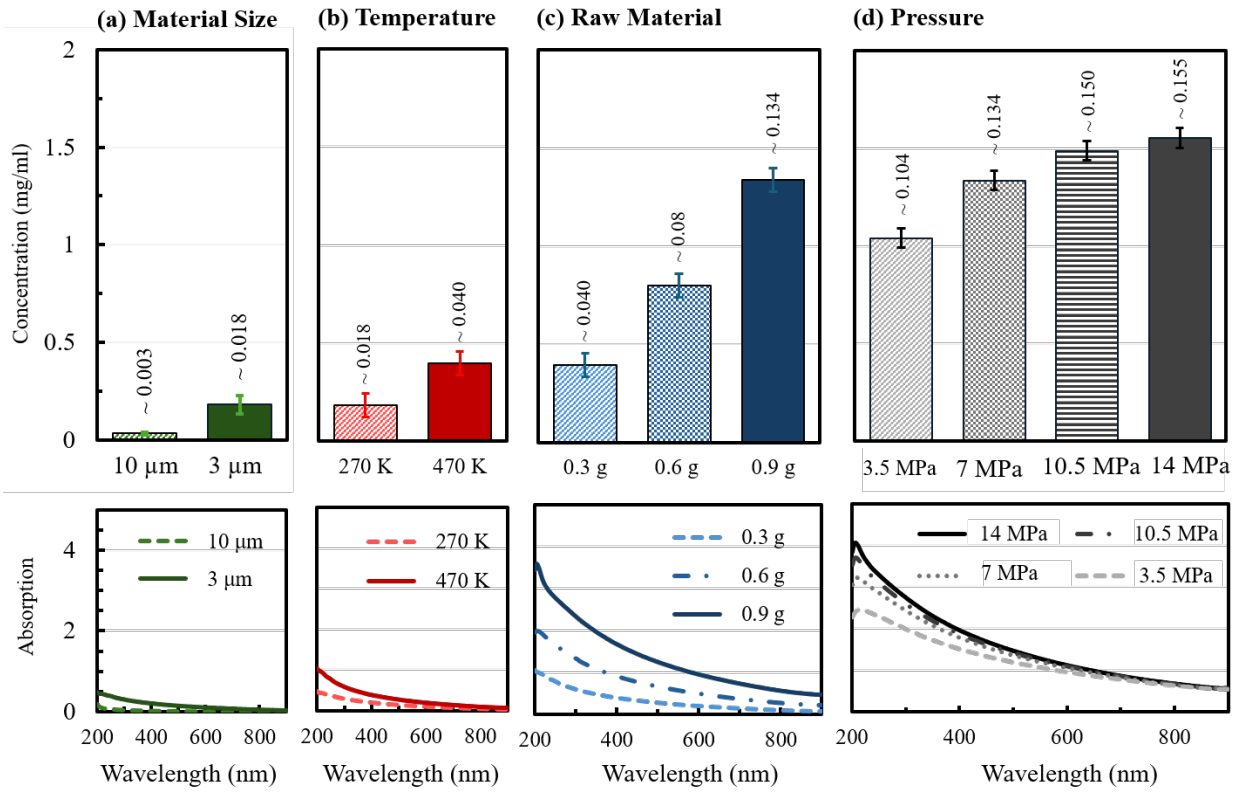

***Figure 6.4**: Optimization of the modified CFE process for h-BN exfoliation using nitrogen. Effect of (a) starting h-BN particle size, (b) stagnation temperature, (c) initial raw-material loading, and (d) upstream pressure on the final h-BN concentration. The optimized condition increased the concentration from 0.003 g·L⁻¹ to 0.155 g·L⁻¹ using a 200 mL collection volume, showing improved exfoliation and material recovery in the modified CFE system.*

As shown in ***Figure 6.4*(a)**, the starting h-BN particle size had a strong influence on the final concentration. The larger 10 µm powder produced only approximately 0.003 g·L⁻¹, whereas the smaller 3 µm powder increased the concentration to approximately 0.018 g·L⁻¹. This improvement can be explained by the higher number of particles and larger available surface area produced from the same starting mass when smaller powder is used. Smaller h-BN particles are also more easily entrained and accelerated by the gas stream, allowing a larger fraction of the material to pass through the high-shear region of the nozzle. In contrast, larger particles have greater inertia and are less responsive to rapid changes in gas velocity, reducing their exposure to the strongest velocity gradients. Therefore, the smaller starting powder produced more dispersed nanosheets because more particles were effectively accelerated, and sheared during the CFE process.

As shown in ***Figure 6.4*****(b)**, increasing the processing temperature from 270 K to 470 K increased the h-BN concentration from approximately 0.017 $g \cdot L^{-1}$ to 0.039 $g \cdot L^{-1}$. This more-than-twofold increase shows that gas preheating is a major yield-enhancing mechanism in the modified CFE process, rather than a secondary operating variable. In practical recovery terms, this corresponds to an increase in recovered h-BN mass from approximately 3.4 mg to 7.8 mg in 200 mL, and an increase in short-burst CFE production intensity from 1.7 to 3.9 $mg \cdot s^{-1}$. Under choked-flow conditions, the gas velocity at the throat is related to the local speed of sound, which increases with absolute temperature according to $= \sqrt{\gamma RT}$, where c is the speed of sound, γ is the heat-capacity ratio, R is the gas constant, and T is the absolute temperature. Therefore, increasing the stagnation temperature increases the achievable gas velocity and improves particle acceleration, particle-gas momentum transfer, and aerodynamic shear exposure. In addition, elevated temperature increases atomic-scale vibrations in the layered material, reducing the effective barrier for interlayer separation. This combined thermal and aerodynamic effect is the main reason why nitrogen and compressed air become effective carrier gases under the optimized CFE condition.

As shown in ***Figure 6.4*****(c)**, increasing the initial mass of raw h-BN resulted in an almost proportional increase in the final collected concentration. The concentration increased from approximately 0.038 $g \cdot L^{-1}$ at 0.3 g, to approximately 0.078 $g \cdot L^{-1}$ at 0.6 g, and finally to approximately 0.132 $g \cdot L^{-1}$ at 0.9 g. These concentrations correspond to recovered masses of approximately 7.6, 15.6, and 26.4 mg in 200 mL, equivalent to short-burst production intensities of 3.8, 7.8, and 13.2 $mg \cdot s^{-1}$, respectively. Loadings above 1.2 g were not included in ***Figure 6.4*****(c)** because they caused clogging and unstable discharge in the CFE configuration. This trend indicates that increasing the amount of h-BN placed at the beginning of the CFE process directly increases the amount of material available for exfoliation. Within the tested range, the gas stream was still able to carry and accelerate the added material without severe clogging or flow instability. Therefore, more starting material led to more particles passing through the high-shear region, resulting in a proportional increase in the final collected h-BN concentration. Therefore, this parameter improves production output but does not necessarily prove higher exfoliation efficiency per gram of feed.

As shown in ***Figure 6.4*****(d)**, increasing the upstream pressure significantly improved the final h-BN concentration. Raising the pressure from 3.5 MPa to 7 MPa, 10.5 MPa, and 14 MPa increased

the concentration from approximately 0.102 $g \cdot L^{-1}$ to 0.132 $g \cdot L^{-1}$, 0.147 $g \cdot L^{-1}$, and 0.155 $g \cdot L^{-1}$, respectively. In the 200 mL collection volume, this corresponds to recovered h-BN masses of approximately 20.4, 26.4, 29.4, and 31.0 mg, with corresponding short-burst CFE production intensities of 10.2, 13.2, 14.7, and 15.5 $mg \cdot s^{-1}$. Higher upstream pressure increases the driving force for gas expansion through the nozzle, producing higher gas velocity, stronger particle acceleration, and larger shear forces. These conditions increase the interaction between the gas flow and h-BN particles, helping to overcome the weak van der Waals forces between adjacent layers. The smaller improvement between 10.5 MPa and 14 MPa suggests that the process begins to approach a plateau at high pressure. This plateau occurs because the system approaches a maximum useful energy-transfer limit, where additional upstream pressure no longer translates efficiently into particle acceleration, shear exposure, or recoverable exfoliated mass.

Overall, the optimization increased the h-BN concentration from approximately 0.003 $g \cdot L^{-1}$ in the initial low-performing condition to 0.155 $g \cdot L^{-1}$ under the optimized nitrogen-based CFE condition. Because the optimized process used a 200 mL collection volume, the total recovered dispersed h-BN mass was 31 mg, ($0.155\ g \cdot L^{-1} \times 200\ mL = 31\ mg$).

This result is significant because the standard CFE benchmark reported using helium achieved approximately 0.15 $g \cdot L^{-1}$ in a 100 mL volume. In the present optimized system, nitrogen achieved a similar concentration while producing a larger total collected mass due to the 200 mL collection volume. Therefore, the optimized nitrogen-based CFE process demonstrates that high-output h-BN exfoliation can be achieved without relying on helium. This improvement is mainly attributed to the added gas-preheating stage, which increased the thermo-kinetic energy available to the nitrogen stream and improved particle acceleration and layer separation during rapid expansion. This is important from a practical perspective because nitrogen is cheaper, more accessible, and easier to implement for larger-scale CFE processing than helium. Once the optimized condition was established using h-BN, the same operating window was applied to other layered materials to test whether the modified CFE process was material-specific or broadly transferable.

6.5 Extension of Optimized CFE to Multiple 2D Materials

Once the optimized h-BN condition was established, the same heated operating window was applied to Graphene and MoS_2 to determine whether the modified CFE process was material-

specific or broadly transferable. The starting materials used were approximately 3 μm h-BN, 4.3 μm graphite, and 6 μm MoS_2. The starting materials used were ~3 μm h-BN, ~4.3 μm graphite, and ~6 μm MoS_2. The produced suspensions are shown in ***Figure 6.5***, where all three materials show visible colloidal dispersion after CFE processing. The red laser path through the suspensions confirms light scattering by dispersed nanosheets, indicating successful formation of stable exfoliated particles in the solvent.

To further compare the role of carrier gas under the heated optimized condition, compressed air was tested and compared with nitrogen. The improved performance of both gases is primarily attributed to the added gas-preheating stage, which increases the thermo-kinetic energy available for particle acceleration and layer separation. Air and nitrogen have similar acoustic velocities under comparable temperature and pressure conditions; however, compressed air has a slightly higher density than pure nitrogen. This may increase the momentum flux of the expanding gas stream and slightly improve momentum transfer to the suspended particles during CFE. Therefore, the overall yield improvement for both gases is mainly enabled by gas preheating, while the difference between air and nitrogen is mainly associated with gas density and momentum flux. In addition, compressed air is inexpensive, widely available, and easier to supply continuously than high-purity nitrogen, making it a practical carrier gas for industrial-scale CFE operation.

The concentration of each material was determined by gravimetric analysis, where the dry recovered mass was plotted as a function of suspension volume. The slope of each mass–volume curve represents the concentration, ($C = \frac{m}{V}$), the slopes shown in the plots can be directly interpreted as concentrations in $g \cdot L^{-1}$ or $mg \cdot mL^{-1}$.

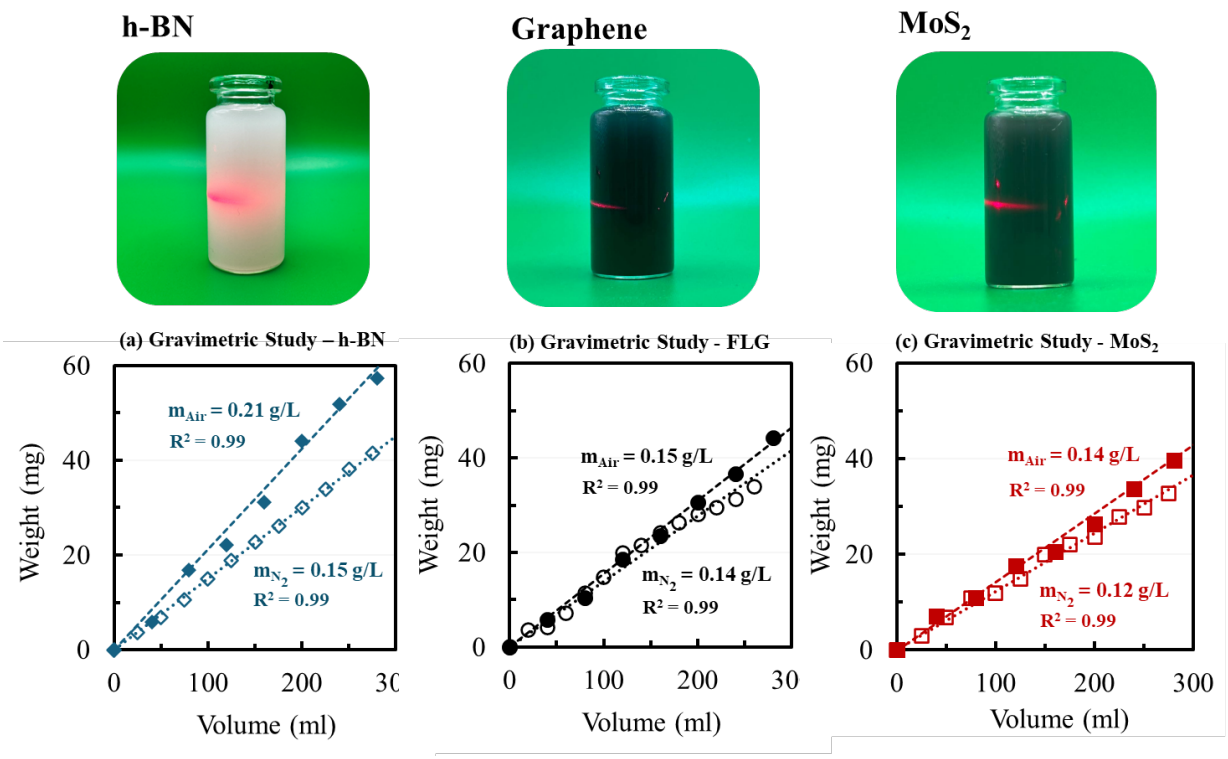

***Figure 6.5**: Extension of the optimized heated CFE process to h-BN, few-layer Graphene, and MoS_2 using compressed air and nitrogen carrier gases.*

For h-BN, starting from 3 µm bulk h-BN powder, the optimized CFE condition produced approximately ~0.21 $g \cdot L^{-1}$ using air and ~0.15 $g \cdot L^{-1}$ using nitrogen. The nitrogen value agrees well with the optimized nitrogen-based h-BN result discussed earlier, confirming reproducibility of the optimized condition.

For Graphene, starting from ~4.5 µm graphite precursor powder, the optimized CFE condition produced approximately 0.15 $g \cdot L^{-1}$ using air and 0.14 $g \cdot L^{-1}$ using nitrogen. The close agreement between air and nitrogen suggests that Graphene exfoliation under this condition is mainly controlled by gas-driven mechanical effects rather than gas chemistry.

For MoS_2, starting from approximately ~6 µm MoS_2 powder, the optimized CFE condition produced approximately 0.14 $g \cdot L^{-1}$ using air and 0.12 $g \cdot L^{-1}$ using nitrogen. Although slightly lower than h-BN and Graphene, these values confirm that the optimized CFE condition can also exfoliate semiconducting transition-metal dichalcogenides.

All gravimetric plots showed strong linearity with $R^2 = 0.99$, confirming reliable concentration estimation and uniform suspension sampling. Based on the 200 mL collection volume, these concentrations correspond to recovered masses of approximately 42 mg for Air-CFE h-BN (21 $mg \cdot s^{-1}$), 30 mg for N_2-CFE h-BN (15 $mg \cdot s^{-1}$), 30 mg for Air-CFE Graphene (15 $mg \cdot s^{-1}$), 28 mg for N_2-CFE Graphene (14 $mg \cdot s^{-1}$), 28 mg for Air-CFE MoS_2 (14 $mg \cdot s^{-1}$), and 24 mg for N_2-CFE MoS_2 (12 $mg \cdot s^{-1}$). These results demonstrate that the optimized CFE condition is not limited to h-BN. The same modified system can process insulating h-BN, conductive Graphene, and semiconducting MoS_2, confirming the versatility of optimized CFE for different classes of 2D layered materials.

The differences in final concentration among h-BN, Graphene, and MoS_2 can be interpreted by considering both the starting particle size and the material-dependent resistance to layer separation. In this work, the starting particle sizes were approximately 3 μm for h-BN, 4.5 μm for graphite, and 6 μm for bulk MoS_2. Smaller particles are expected to be more easily entrained and accelerated in the compressible gas stream, giving more effective exposure to the high-shear region of the CFE nozzle. However, particle size alone does not fully explain exfoliation behavior because each material has a different interlayer interaction and density. Graphite has a reported ideal cleavage energy of 0.39 ± 0.02 $J \cdot m^{-2}$, corresponding to an exfoliation energy of approximately 0.46 $J \cdot m^{-2}$ [106]. For h-BN, reported exfoliation energy is approximately 0.45 $J \cdot m^{-2}$ (equivalent to 28.35 $meV \cdot Å^{-2}$), which is comparable to graphite [134]. MoS_2 has been reported to have an interlayer binding energy of 0.55 ± 0.13 $J \cdot m^{-2}$ by an in-situ peeling-to-fracture method, while DFT calculations in the same study gave approximately 0.422 J m^{-2} [135]. In addition, MoS_2 has a much higher density, about 5.06 $g \cdot cm^{-3}$, compared with graphite at about 2.26 $g \cdot cm^{-3}$ and h-BN at about 2.27 $g \cdot cm^{-3}$ [136, 137]. Therefore, the lower MoS_2 concentration is likely caused by the combined effects of its larger starting particle size, higher density, and relatively high interlayer binding energy, which reduce particle acceleration, exfoliation efficiency, and stable suspension formation compared with h-BN and graphite. Taken together, the h-BN, Graphene, and MoS_2 results show that the improved performance is not limited to one material system. Instead, the heated CFE condition provides a general thermo-kinetic processing window in which nitrogen and compressed air can transfer sufficient energy to different layered materials and enable the practical useof low-cost carrier gases across insulating, conductive, and semiconducting 2D materials.

6.6 Recovery of Entrapped Nanosheets by Re-Dispersion and Re-Centrifugation

Although the heated optimized CFE condition improved the initial production of dispersed nanosheets, the first centrifugation step did not necessarily recover all exfoliated material. Therefore, repeated sediment re-dispersion was used as a post-processing recovery strategy to collect nanosheets trapped within the sediment cake. In this section, gas preheating is treated as the primary yield-enabling modification during exfoliation, while repeated re-dispersion is treated as a downstream recovery method that increases the usable concentration of the product.

During the first centrifugation of a highly concentrated CFE suspension, the separation is not perfectly selective. In this work, the CFE suspensions were transferred into 50 mL centrifuge tubes for post-processing. During centrifugation, the large, heavy, unexfoliated or partially exfoliated particles sediment rapidly and form a compact particle cake at the bottom of the tube. However, part of the exfoliated nanosheets can become physically trapped inside this sediment rather than remaining in the supernatant. Therefore, the first centrifugation step may underestimate the actual amount of nanosheets generated during CFE.

This phenomenon is consistent with the “Graphene reflux” mechanism reported by Rountree et al [138]. They showed that exfoliated Graphene nanosheets can be trapped in the sediment together with the parent graphite material, and that these trapped nanosheets can be recovered by adding fresh solvent, re-dispersing the sediment, and repeating the separation process. They also suggested that this washing/reflux approach is applicable to other nanosheet systems, including h-BN.

Based on this mechanism, repeated centrifugation was applied to the CFE-processed h-BN, Graphene, and MoS_2 suspensions. After each centrifugation cycle, the supernatant was collected, and the sediment remaining in the 50 mL tube was re-dispersed in fresh solvent. This re-dispersion step breaks apart the compact sediment cake and releases smaller nanosheets that were previously trapped between larger particles. During the following centrifugation step, the larger particles sediment again, while the released nanosheets remain in the supernatant. Therefore, this process increases the recovered nanosheet concentration without repeating the CFE exfoliation step. Because no additional CFE burst is applied during these re-dispersion steps, the increase should

be interpreted as improved post-processing recovery rather than increased CFE production intensity.

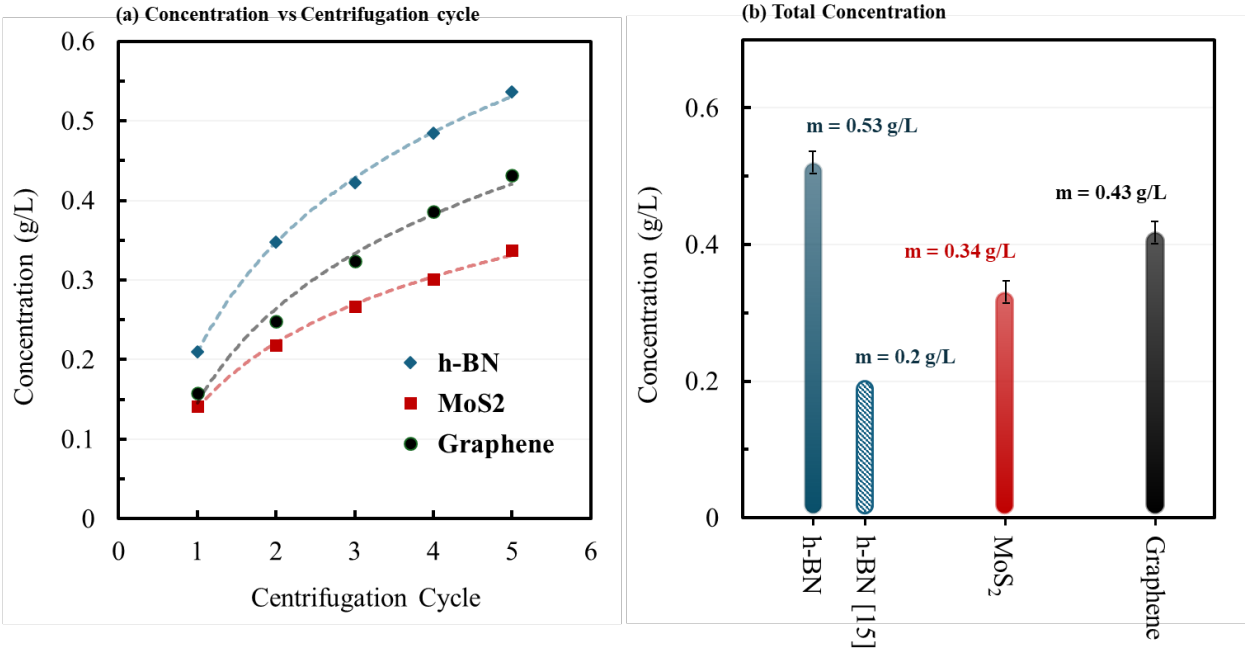

***Figure 6.6**: Concentration analysis of various 2D nanomaterials produced using compressed air. (a) Cumulative concentration of h-BN, MoS_2, and Graphene dispersions plotted against the number of centrifugation cycles. (b) Comparison of the total final concentrations achieved for h-BN, MoS_2, and Graphene. A reference value for h-BN processed with helium from previous literature is included for comparison [18].*

As shown in ***Figure 6.6***, the concentration increased with each re-dispersion/centrifugation cycle for all three materials. For h-BN, the concentration increased from approximately 0.21 $g \cdot L^{-1}$ after the first cycle to approximately 0.53 $g \cdot L^{-1}$ after five cycles, corresponding to an increase of about 2.5 times. For Graphene, the concentration increased from approximately 0.15 $g \cdot L^{-1}$ to 0.43 $g \cdot L^{-1}$, corresponding to an increase of about 2.7 times. For MoS_2, the concentration increased from approximately 0.14 $g \cdot L^{-1}$ to 0.34 $g \cdot L^{-1}$, corresponding to an increase of about 2.4 times. Overall, repeated sediment re-dispersion and centrifugation increased the recovered concentration by approximately 2.5× after five cycles. The final recovered concentration followed the order h-BN > Graphene > MoS_2, with final values of approximately 0.53, 0.43, and 0.34 $g \cdot L^{-1}$, respectively.

This recovery step also shows a clear improvement compared with the original helium-assisted CFE benchmark for h-BN. In the original CFE study [18], helium-assisted CFE-produced approximately 0.15 $g \cdot L^{-1}$ h-BN at 5.5 MPa, and the pressure study reached approximately 0.20 $g \cdot L^{-1}$ at 11 MPa [18]. In the present work, after repeated re-dispersion and centrifugation, the recovered h-BN concentration using air as the carrier gas reached approximately 0.53 $g \cdot L^{-1}$, which is about 3.5 times higher than the 0.15 $g \cdot L^{-1}$ helium-assisted benchmark and about 2.7 times higher than the 0.20 $g \cdot L^{-1}$ maximum reported in the original pressure study. However, this comparison should be interpreted carefully because the present value includes an additional post-processing recovery step, rather than representing only the first-pass CFE concentration. These results demonstrate that repeated sediment recovery is an effective strategy for increasing the usable concentration of CFE-produced 2D materials.

To convert the UV–Vis absorbance data into reliable suspension concentrations, a gravimetric calibration study was first performed for each material. To determine the extinction coefficient for each CFE-produced material, a calibration curve was prepared by combining gravimetric analysis with UV–Vis spectroscopy. First, one stock suspension was selected for each material, and its concentration was determined gravimetrically by drying a known volume of the suspension and measuring the remaining solid mass. This gravimetrically measured concentration was then used as the stock concentration.

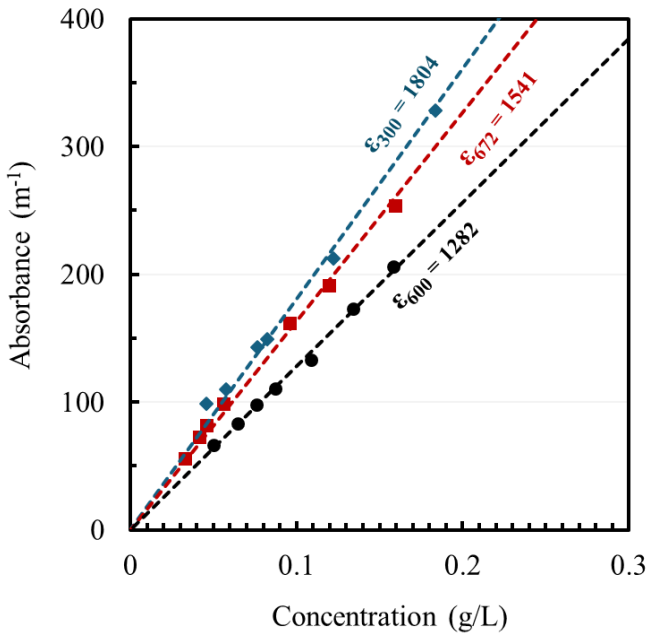

***Figure 6.7**: Beer–Lambert calibration curves for the determination of extinction coefficients. Optical absorbance plotted as a function of concentration for h-BN, MoS_2, and Graphene dispersions. The calculated extinction coefficients are 1804 L $g^{-1}m^{-1}$ at 300 nm for h-BN, 1541 L $g^{-1}m^{-1}$ at 672 nm for MoS_2 , and 1282 L $g^{-1}m^{-1}$ at 600 nm for Graphene.*

Each gravimetrically measured stock suspension was diluted to known concentrations using defined dilution ratios. UV–Vis spectra were then collected for each dilution, and the absorbance at the selected wavelength was plotted against the known concentration. as shown in ***Figure 6.7***. The extinction coefficients were determined from the calibration plots using Equation 6.12. For h-BN, the absorbance was taken at 300 nm, which is commonly used for h-BN nanosheet concentration analysis by Beer–Lambert calibration. The calculated value in this work was $\alpha_{\text{h-BN},300} = 1804$ L $g^{-1}m^{-1}$ [139]. For MoS_2, the absorbance was taken at 672 nm, corresponding to the A-exciton region commonly used for MoS_2 nanosheet concentration estimation; the calculated value was $\alpha_{MoS_2,672} = 1541$ L $g^{-1}m^{-1}$, which is close to the reported value of 1517 L $g^{-1}m^{-1}$at 672 nm [140]. For Graphene, the absorbance was taken at 600 nm, a standard wavelength used for Graphene dispersion concentration measurements; the calculated value was $\alpha_{\text{Graphene},600} = 1282$ L $g^{-1}m^{-1}$, which is close to the reported Graphene value of 1293 mL $mg^{-1}m^{-1}$ [138]. These experimentally determined extinction coefficients were then

used to estimate unknown CFE-produced nanomaterials suspension concentrations from UV–Vis. Although the optimized CFE condition produced stable dispersions, the first centrifugation step did not necessarily recover all exfoliated nanosheets. Therefore, the next step focused on improving usable yield through sediment re-dispersion.

6.7 UV–Vis Extinction Analysis of MoS_2 Nanosheet Dispersions

UV–Vis spectroscopy was used not only to estimate the concentration of the CFE-produced MoS_2 suspension, but also to provide qualitative information about nanosheet exfoliation. For liquid-exfoliated transition-metal dichalcogenides such as MoS_2 and WS_2, the optical extinction spectrum contains structural information because the spectrum changes with nanosheet lateral size, thickness, and monolayer/few-layer content. Backes et al. [16] showed that size-selected liquid-exfoliated nanosheet dispersions can be analyzed by standard spectroscopic measurements, and that spectral features can be correlated with mean nanosheet length, mean thickness, and monolayer content. The concentration of the MoS_2 dispersion was first calculated using the Beer–Lambert relationship (equation 6.12). The wavelength of 672 nm corresponds to the A-exciton region of MoS_2, which is commonly used because it is sensitive to the optical response of dispersed MoS_2 nanosheets. However, the absolute absorbance at this wavelength mainly provides concentration information. To extract structural information, the shape, position, and relative intensity of the extinction spectrum must also be considered.

In MoS_2, the UV–Vis spectrum typically contains excitonic features associated with the electronic transitions of the layered semiconductor. The most important features are the A- and B-exciton peaks, which arise from spin–orbit split transitions near the K point of the Brillouin zone. These excitonic peaks are sensitive to the number of layers because monolayer, few-layer, and bulk-like MoS_2 have different electronic structures and interlayer coupling. As the nanosheets become thinner, quantum confinement and reduced interlayer interaction can shift the excitonic features and change their relative intensity. Therefore, the A-exciton position and shape can be used as indicators of whether the dispersion contains thicker MoS_2 particles, few-layer nanosheets, or a more monolayer-enriched population.

The extinction spectrum can also provide information about lateral size. Smaller nanosheets have a higher edge-to-basal-plane ratio. Because edge regions and basal-plane regions contribute

differently to the optical response, the spectral profile changes as nanosheet size changes. Backes et al. [16] showed that for liquid-exfoliated TMDs nanosheets, the ratio of extinction intensities at selected wavelengths can be correlated with mean nanosheet length. This means that changes in peak ratios or high-energy-to-exciton intensity ratios can be used as a spectroscopic indicator of lateral size, provided that the relationship is calibrated for the material and solvent system.

The spectrum can also provide information about mean nanosheet thickness. The A-exciton position was shown to depend on the mean nanosheet thickness because confinement effects shift the excitonic transition as the number of layers changes. The general concept can be written as an empirical relationship:

$$\langle N \rangle = f(\lambda_A) \tag{6.13}$$

The mean nanosheet thickness can be estimated from the A-exciton position using the calibrated spectroscopic relationship reported by Backes et al. [16]. The A-exciton center-of-mass position was correlated with AFM-measured nanosheet thickness, allowing the average number of layers, ⟨N⟩, to be extracted from the extinction spectrum. Therefore, here, the A-exciton position is used as a literature-calibrated indicator of MoS_2 layer number rather than only as a qualitative sign of exfoliation. This UV–Vis-based estimate is then interpreted together with Raman spectroscopy and microscopy to confirm the exfoliation state.

For monolayer or few-layer content, the shape of the A-exciton region is particularly useful. In monolayer-enriched transition-metal dichalcogenide dispersions, the A-exciton feature becomes more distinct because monolayer and few-layer nanosheets absorb at slightly different energies. Backes et al. [16] showed that spectral deconvolution, including second-derivative analysis of the excitonic region, can separate monolayer and few-layer contributions in highly enriched dispersions. This approach allows the monolayer and few-layer volume fraction to be estimated from the excitonic peak shape when an appropriate calibration is available.

Therefore, the UV–Vis analysis of MoS_2 in this work is interpreted at two levels. First, the Beer–Lambert calibration at 672 nm provides a quantitative concentration value for the dispersed MoS_2 suspension. Second, the excitonic spectral features provide qualitative or semi-quantitative evidence of exfoliation. A strong and well-defined A-exciton feature indicates that MoS_2 retains its semiconducting layered structure after CFE processing. Changes in the A-exciton position, peak

width, and spectral shape can then be discussed as evidence of layer reduction, thickness distribution, and possible enrichment of few-layer nanosheets.

After optimizing the CFE process and confirming that repeated sediment re-dispersion can recover trapped nanosheets, the centrifugation speed was varied to control the balance between material recovery and nanosheet size/thickness selection. This step is important because centrifugation is not only a separation process; it also determines which particles remain in the supernatant. Lower centrifugation speeds allow more MoS_2 nanosheets and partially exfoliated particles to remain suspended, giving higher concentration. In contrast, higher centrifugation speeds remove larger and thicker particles more effectively, producing a lower-concentration but more size-selected dispersion.

This approach follows the same general principle reported for repeated nanosheet recovery from sediment. Rountree et al. [138] showed that exfoliated nanosheets can become trapped in sediment with heavier parent material and can be recovered by repeatedly adding solvent, re-dispersing the sediment, and separating again. In the present work, this repeated recovery strategy was applied to CFE-produced MoS_2 using 50 mL centrifuge tubes. After each centrifugation step, the supernatant was collected, and the sediment was re-dispersed in solvent for the next cycle.

As shown in ***Figure 6.8*****(a)**, the visual appearance of the recovered MoS_2 supernatants changed progressively with centrifugation cycle number. The earlier recovered suspensions were darker, indicating higher MoS_2 concentration, while later cycles became lighter as the amount of recoverable material remaining in the sediment decreased. The visible laser path through the vials confirms light scattering from dispersed MoS_2 nanosheets in the supernatant. This visual trend supports the idea that repeated washing gradually extracts nanosheets trapped in the sediment cake.

The concentration evolution with recovery cycle is shown in ***Figure 6.8*****(b)**. At 1500 rpm, the MoS_2 concentration increased rapidly over the first few cycles and reached approximately 1.65 $g \cdot L^{-1}$ after repeated recovery. At 3000 rpm, the final concentration was lower, reaching approximately 1.0 $g \cdot L^{-1}$. At 4500 rpm, the concentration further decreased to approximately 0.49 $g \cdot L^{-1}$. This trend indicates that the as-produced CFE MoS_2 dispersion is polydisperse. The largest recovered fraction consists of larger and thicker nanosheets that remain suspended at lower centrifugation speed, while smaller and thinner nanosheets are retained under stronger centrifugal selection as lower-mass refined fractions.

As shown in ***Figure 6.8*(c)**, the recovered MoS_2 concentration decreased as the centrifugation speed increased. The largest fraction of material was recovered at 1500 rpm, with a concentration of approximately 1.65 $g \cdot L^{-1}$, corresponding to about 52.5% of the total recovered material across the three centrifugation conditions. At 3000 rpm, the recovered concentration decreased to approximately 1.00 $g \cdot L^{-1}$, corresponding to about 31.8% of the total recovered material. The smallest fraction was recovered at 4500 rpm, with a concentration of approximately 0.49 $g \cdot L^{-1}$, corresponding to about 15.6% of the total. This trend shows that most of the dispersed MoS_2 remains in the supernatant at lower centrifugation speed, while increasing the centrifugation speed removes a larger fraction of the material from suspension.

The centrifugation results should be interpreted as fractionation rather than as a simple improvement or deterioration in product quality. Lower centrifugation speed allows a larger portion of the CFE-processed material to remain in the supernatant, leading to higher recovered concentration. However, this fraction can include larger and thicker nanosheets as well as smaller exfoliated sheets. In contrast, higher centrifugation speed removes more large or thick particles into the sediment, producing a more refined supernatant fraction with smaller and thinner nanosheets, but at the cost of lower recovered concentration. Therefore, centrifugation speed provides a post-processing tool for tuning the balance between mass recovery and nanosheet refinement. This distinction is important because the CFE product is not a single uniform population. It contains a distribution of particle sizes, thicknesses, and exfoliation states. Repeated sediment re-dispersion releases nanosheets trapped with larger particles, while centrifugation determines which fraction remains in the usable supernatant. Therefore, the measured MoS_2 concentration after centrifugation reflects both the extent of exfoliation and the selected recovery window.

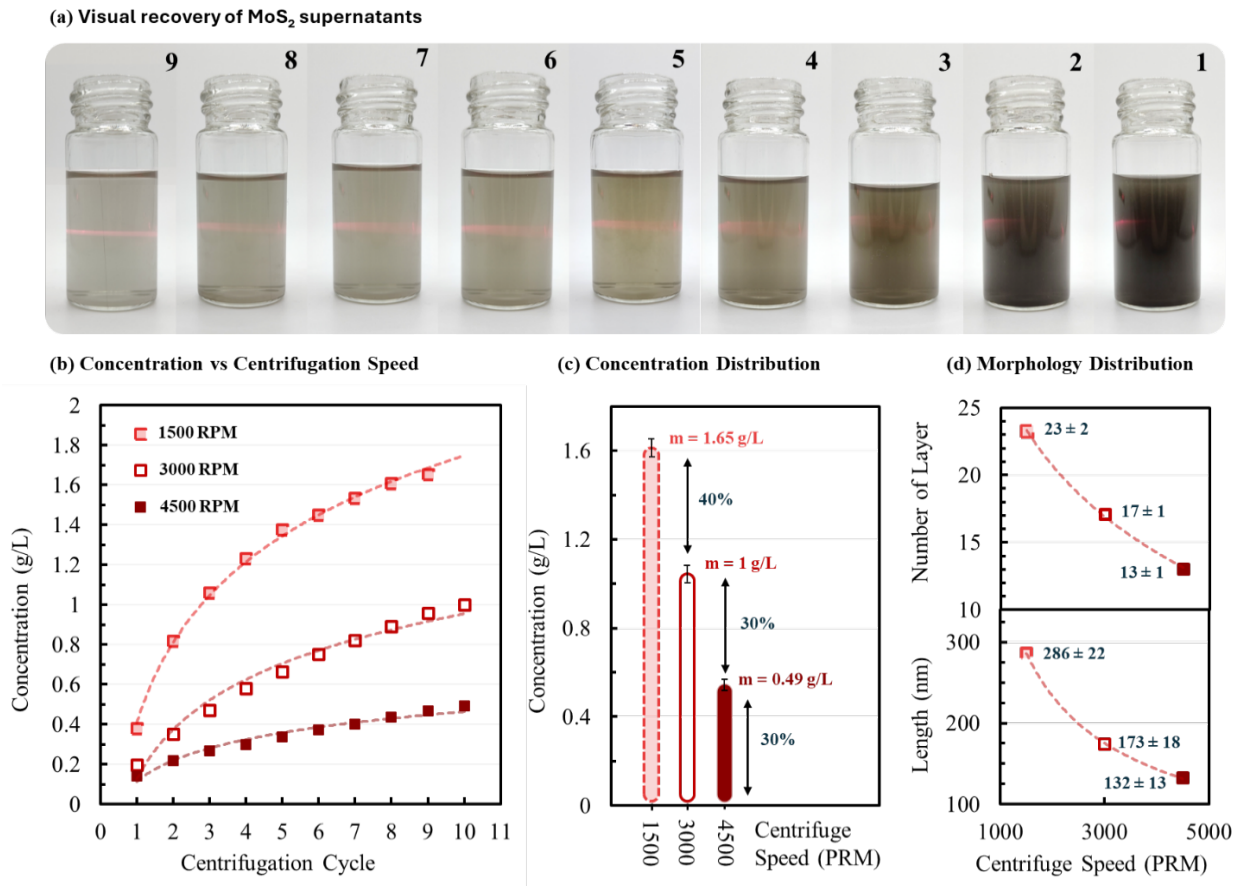

***Figure 6.8**: Effect of centrifugation speed and repeated sediment re-dispersion on MoS_2 recovery and nanosheet dimensions. (a) Photographs of MoS_2 supernatants collected from successive re-dispersion/centrifugation cycles, showing a gradual decrease in suspension darkness as the recoverable nanosheet content decreases with repeated cycles. The visible laser path confirms light scattering from dispersed MoS_2 nanosheets. (b) Cumulative concentration plotted over 10 cycles for centrifugation speeds of 1500, 3000, and 4500 rpm. A clear inverse relationship is observed where higher speeds result in lower cumulative yields. (c) Analysis of the total concentration yields reveals the mass distribution of the exfoliated material and (d) UV–Vis-derived nanosheet dimensions at different centrifugation speeds.*

However, the lower concentration at higher centrifugation speed is accompanied by improved nanosheet selection. As shown in ***Figure 6.8*(d)**, the UV–Vis-derived dimensions confirm this fractionation behavior. At 1500 rpm, the recovered MoS_2 fraction had an average lateral length of 286 ± 22 nm and an estimated thickness of 23 ± 2 layers. At 3000 rpm, the average length decreased to 173 ± 18 nm, and the thickness decreased to 17 ± 1 layers. At 4500 rpm, the fraction became

even smaller and thinner, with an average lateral length of 132 ± 13 nm and an estimated thickness of 13 ± 1 layers. Therefore, the centrifugation study shows both the yield distribution and the structural distribution of the CFE-produced MoS_2 product. The highest-recovery 1500 rpm condition corresponds to approximately 330 mg of recovered MoS_2 in 200 mL and a short-burst CFE production intensity of 165 $mg \cdot s^{-1}$, whereas the more selective 3000 and 4500 rpm fractions correspond to approximately 200 mg and 98 mg, respectively.

Therefore, ***Figure 6.8(c,d)*** demonstrates that the CFE process produces a polydisperse MoS_2 dispersion containing larger/thicker nanosheets as the dominant fraction and smaller/thinner nanosheets as a lower-yield refined fraction. Thus, centrifugation acts not only as a recovery step, but also as a diagnostic tool to reveal the composition of the CFE product and to tune the final suspension based on the desired balance between concentration and nanosheet thickness.

6.8 Solution Stability of CFE-Produced Nanosheet Dispersions

Dispersion stability is an important requirement for solution-processable 2D nanomaterials. Even when exfoliation produces nanosheets successfully, the material must remain suspended long enough for handling, storage, mixing, and downstream processing. Rapid sedimentation can reduce concentration, change the effective nanosheet population in the supernatant, and lead to poor reproducibility in applications such as coatings, inks, polymer nanocomposites, membranes, and functional additives. Therefore, the stability of CFE-produced dispersions was evaluated and compared with LPE method, which is a widely used solution-based exfoliation route [15, 16].

For the dispersion-stability comparison in Figure 6.9, the LPE reference dispersion was prepared by suspending bulk MoS_2 powder with an average particle size of ~6 μm (Sigma-Aldrich) in 200 mL of a co-solvent containing 60 vol.% DI water/40 vol.% IPA. The suspension was subjected to tip sonication for 7 h, following the sonication-assisted liquid-exfoliation approach described by Backes et al. [141] . Acoustic cavitation generated local mechanical stresses that promoted separation of the layered precursor into nanosheets, while the liquid medium supported their dispersion. After sonication, the suspension was transferred into 50 mL centrifuge tubes and centrifuged at 1500 rpm for 2 h to separate dispersed nanosheets from larger particles and unexfoliated material. The recovered LPE dispersion was then monitored by time-dependent UV–Vis spectroscopy over the 350 h storage period shown in ***Figure 6.9***. This procedure provided a

sonication-produced reference for evaluating the stability and dimensional evolution of CFE-produced MoS_2 dispersions.

UV–Vis spectroscopy was used to monitor the dispersions over time because absorbance is directly related to the concentration of suspended nanosheets through the Beer–Lambert relationship [17, 138]. In addition, UV–Vis spectral features can be used to estimate nanosheet dimensions, including flake length and layer number, when appropriate empirical correlations are applied [16]. The time-dependent UV–Vis spectra of the CFE and LPE dispersions are shown in ***Figure 6.9(a,b)***. Both dispersions retained their characteristic spectral features during the monitored period, indicating that the suspended nanosheet populations remained stable over time.

For the CFE dispersion, the UV–Vis spectra remained clearly measurable throughout the stability test, as shown in ***Figure 6.9(a)***. The LPE dispersion showed a similar time-dependent spectral response, as shown in ***Figure 6.9(b)***. This indicates that the overall dispersion stability of the CFE-produced nanosheets was comparable to that of the LPE-produced nanosheets. Therefore, the main distinction between the two methods was not a loss of stability, but the size and thickness of the nanosheets that remained dispersed.

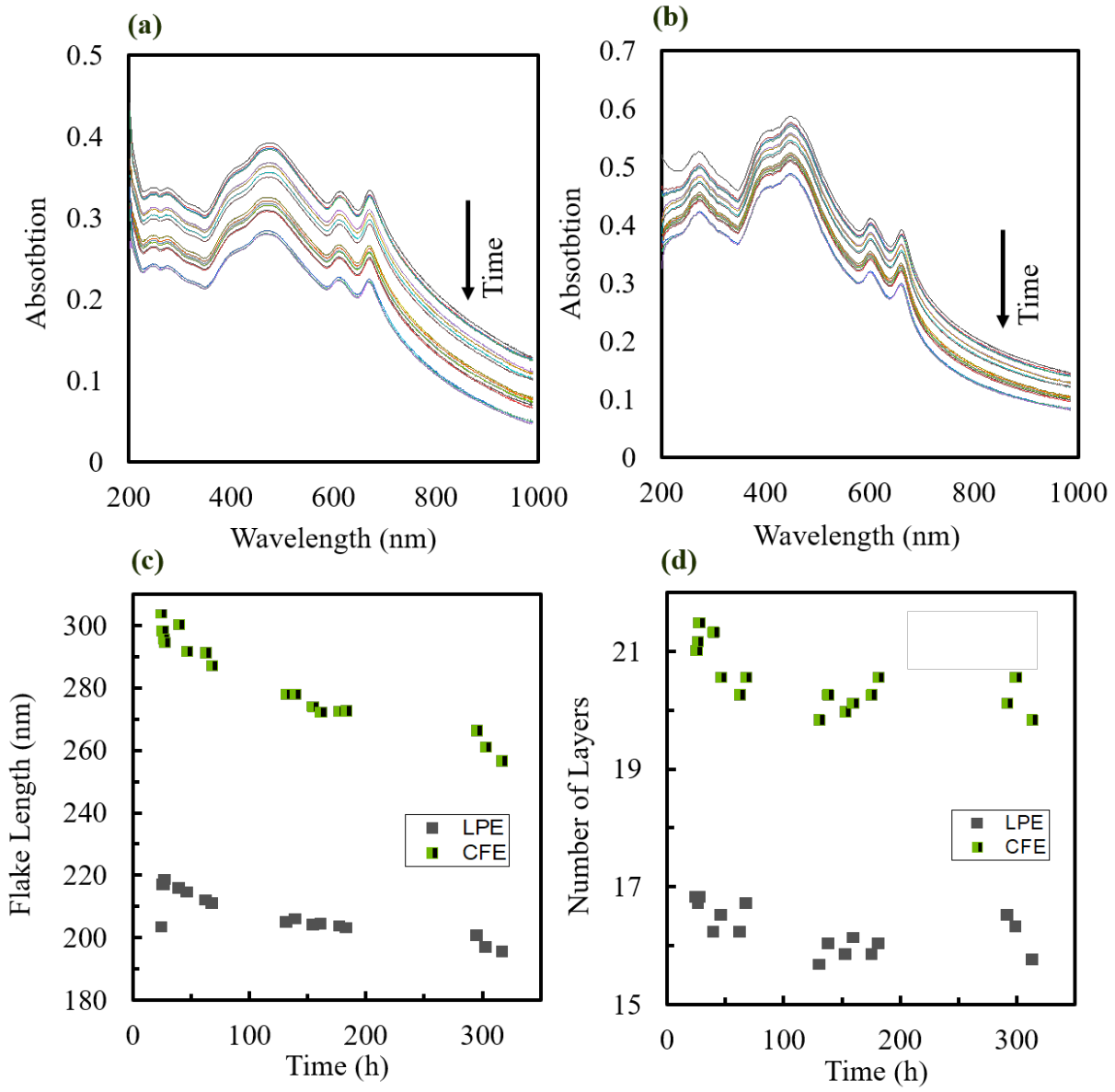

Figure 6.9*: Solution stability and nanosheet-dimension analysis of CFE and LPE dispersions over a 350h storage period.* ***(a)*** *UV–Vis spectra of CFE dispersions collected at different times.* ***(b)*** *UV–Vis spectra of LPE dispersions collected at different times.* ***(c)*** *Flake-length evolution over time for CFE and LPE samples.* ***(d)*** *Layer-number evolution over time for CFE and LPE samples.*

The flake-length evolution shown in ***Figure 6.9(c)*** indicates that the CFE-produced nanosheets remained larger than the LPE-produced nanosheets throughout the monitored period. The CFE flakes were generally in the range of approximately 260-300 nm, while the LPE flakes were generally in the range of approximately 190-220 nm. This suggests that CFE preserves larger

lateral nanosheet dimensions during exfoliation, instead of strongly fragmenting the material into smaller flakes. This is important because larger nanosheets can be beneficial for applications that rely on aspect ratio, percolation, barrier formation, mechanical reinforcement, or continuous transport pathways [95].

The layer-number evolution shown in ***Figure 6.9*****(d)** also shows that the CFE-produced nanosheets remained thicker than the LPE-produced nanosheets over time. The CFE nanosheets had an estimated layer-number range of approximately 20-21, while the LPE nanosheets had an estimated layer-number range of approximately 16-17. This indicates that CFE produces a few-layer or multilayer nanosheet population rather than a highly monolayer-rich product. For scalable application-oriented production, this is not necessarily a disadvantage, because many industrial uses of 2D materials require stable, processable nanosheet dispersions rather than purely monolayer materials.

For both CFE and LPE dispersions, the estimated flake length and layer number decreased over time. This decrease should not be interpreted as direct evidence that individual nanosheets are continuously breaking or exfoliating during storage. Instead, it more likely reflects time-dependent fractionation of the suspended population. Larger and thicker nanosheets have greater effective mass and are more prone to gravitational settling, while smaller and thinner nanosheets remain suspended for longer periods. A similar behaviour has been reported for liquid-phase-exfoliated graphene dispersions, where larger flakes sedimented over time and smaller flakes remained dispersed [44]. As a result, the supernatant gradually becomes enriched in smaller and thinner nanosheets, leading to lower UV–Vis-derived average flake length and layer number over time. Therefore, the observed decrease in nanosheet dimensions is better interpreted as selective sedimentation during storage rather than structural degradation or additional exfoliation.

The stability result is significant because larger and thicker nanosheets would generally be expected to sediment more readily than smaller and thinner nanosheets due to their greater effective mass. However, the CFE-produced dispersions showed stability comparable to LPE while retaining larger lateral dimensions and higher layer numbers. This suggests that CFE can produce nanosheets that remain sufficiently dispersed without requiring excessive fragmentation. In other words, CFE provides a balance between exfoliation, dimensional preservation, and dispersion stability.

Overall, the purpose of this analysis was to determine whether CFE-produced nanosheets remain usable as solution dispersions after exfoliation. The results show that CFE dispersions maintain stability comparable to LPE dispersions while preserving larger and thicker nanosheets. This supports the interpretation that CFE is a relatively mild gas-driven exfoliation process capable of producing stable few-layer or multilayer nanosheet dispersions for downstream solution-based applications.

6.9 Effect of Starting Particle Size on CFE Output

After establishing the post-processing approach, the effect of starting bulk MoS_2 particle size was investigated under the same optimized CFE condition. Three MoS_2 powders with average starting sizes of approximately 12.5 µm, 4.5 µm, and 1.5 µm were processed and then recovered using repeated re-dispersion/centrifugation cycles at a fixed centrifugation speed of 1500 rpm. Therefore, the differences observed in this figure are attributed mainly to the starting material size rather than changes in centrifugation intensity.

As shown in ***Figure 6.10*****(a)**, the UV–Vis spectra of the recovered MoS_2 suspensions show the characteristic MoS_2 excitonic features, confirming that the layered semiconducting structure was preserved after CFE processing. The spectra were used together with the previously determined MoS_2 extinction coefficient at 672 nm to calculate the suspension concentration.

The concentration results in ***Figure 6.10*****(b)** show that reducing the starting MoS_2 particle size strongly increased the recovered concentration. Using the 200 mL collection volume, this trend corresponds to a recovered-mass increase from approximately 58 mg for 12.5 µm MoS_2 to 154 mg for 4.5 µm MoS_2 and 276 mg for 1.5 µm MoS_2 after five recovery cycles. The largest starting powder, 12.5 µm, produced the lowest concentration, increasing from approximately 0.11 $g \cdot L^{-1}$ after the first cycle to approximately 0.29 $g \cdot L^{-1}$ after five cycles. The intermediate 4.5 µm powder reached approximately 0.77 $g \cdot L^{-1}$ after five cycles. The smallest 1.5 µm powder produced the highest concentration, reaching approximately 1.38 $g \cdot L^{-1}$ after five cycles. Therefore, at the same centrifugation speed of 1500 rpm, the 1.5 µm starting powder produced about 4.8 times higher recovered concentration than the 12.5 µm powder and about 1.8 times higher than the 4.5 µm powder.

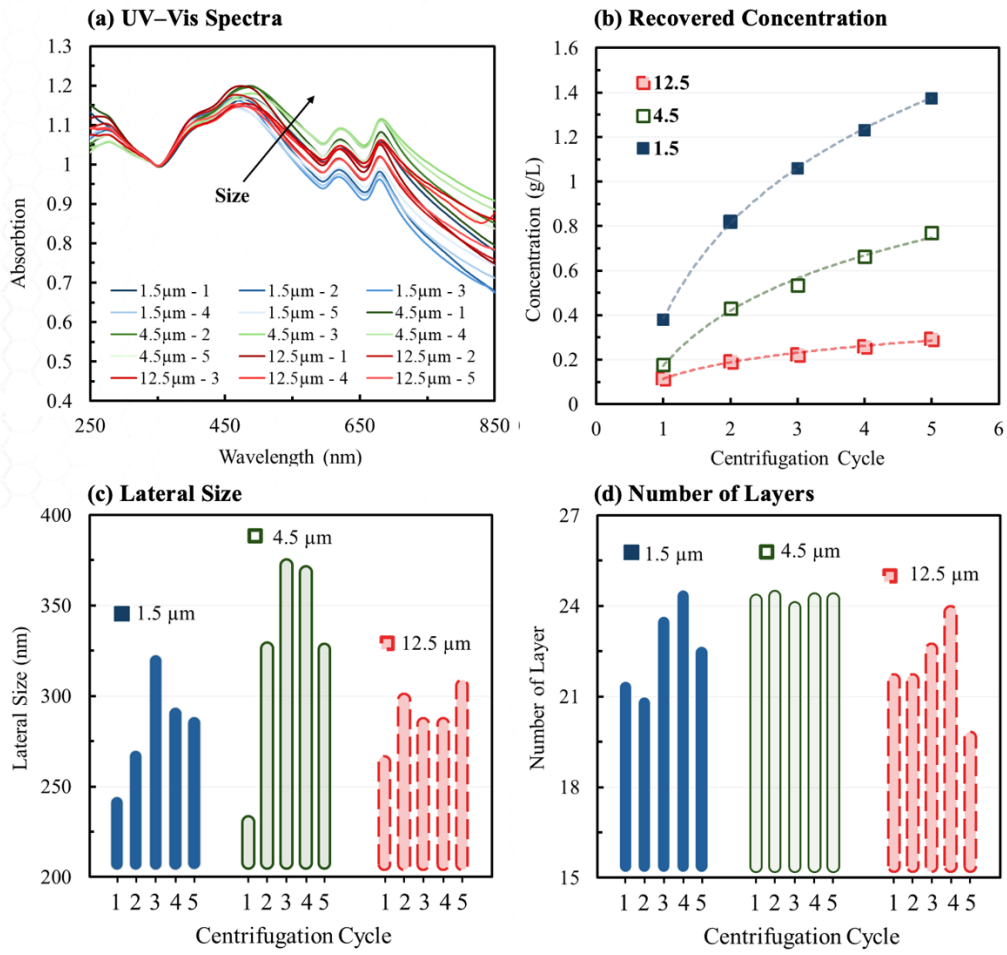

Figure 6.10: *(a) UV–Vis spectra of MoS_2 suspensions recovered from different starting bulk particle sizes of 12.5 μm, 4.5 μm, and 1.5 μm after repeated re-dispersion/centrifugation cycles. (b) Recovered MoS_2 concentration as a function of centrifugation cycle at a fixed centrifugation speed of 1500 rpm, showing that smaller starting particles produce higher final concentrations. After five cycles, the concentration increased to approximately 0.29 $g \cdot L^{-1}$, 0.77 $g \cdot L^{-1}$, and 1.38 $g \cdot L^{-1}$ for 12.5 μm, 4.5 μm, and 1.5 μm starting powders, respectively. UV–Vis-derived (c) lateral size and (d) number of layers for the recovered MoS_2 nanosheets, showing similar final nanosheet dimensions despite different starting particle sizes. The average lateral sizes were 280 ± 23 nm, 325 ± 47 nm, and 289 ± 13 nm, while the estimated layer numbers were 22 ± 2.1, 24 ± 2.3, and 23 ± 2.2 for 12.5 μm, 4.5 μm, and 1.5 μm starting powders, respectively.*

This trend indicates that smaller starting particles are more favorable for CFE processing of MoS_2. Smaller particles have lower inertia and can be entrained and accelerated more effectively by the

high-speed gas stream. They also provide more exposed surface area and edge sites per unit mass, increasing the probability of gas–particle interaction and shear-assisted delamination. In contrast, larger MoS_2 particles are more difficult to accelerate and may experience less effective interaction with the high-shear regions of the CFE flow path, resulting in lower recovered concentration. However, ***Figure 6.10*****(c,d)** and ***Table 6.1*** show no clear monotonic relationship between starting-particle size and the final UV–Vis-derived nanosheet dimensions under the fixed 1500 rpm post-processing condition. The average lateral sizes were 280 ± 23nm, 325 ± 47nm, and 289 ± 13nm for the 12.5 µm, 4.5 µm, and 1.5 µm starting powders, respectively. Although the 4.5 µm precursor produced the highest numerical mean lateral size, the uncertainty ranges overlap with those of the other conditions. Similarly, the estimated layer numbers were broadly comparable, at 22 ± 2.1, 24 ± 2.3, and 23 ± 2.2layers, respectively. These results suggest that, under the present CFE and fixed centrifugation conditions, starting-particle size primarily affected recovered concentration rather than producing a systematic change in the dimensions of the selected nanosheet fraction.

Table 6.1: *UV–Vis-derived lateral size and estimated layer number of MoS_2 nanosheets produced from different starting particle sizes after CFE and repeated recovery at 1500 rpm.*

Starting Material Size (µm)	Lateral Size (nm)	Number of Layers
12.5	280 ± 23	22 ± 2.1
4.5	325 ± 47	24 ± 2.3
1.5	289 ± 13	23 ± 2.2

Therefore, under the same CFE and 1500 rpm recovery condition, starting particle size mainly affected the amount of MoS_2 recovered, not the average lateral size or layer number of the final nanosheets. The smallest starting material produced the highest concentration, while the final nanosheet dimensions remained in a similar range for all three starting powders. This suggests that reducing the starting MoS_2 particle size is an effective strategy for increasing CFE output, while the final nanosheet size and thickness are controlled more strongly by the flow condition and the fixed centrifugation/recovery protocol.

6.10 Yield Enhancement by Re-Exfoliating Graphene Sediment

To further improve the overall recovery of CFE-produced Graphene, the sediment remaining after centrifugation was not discarded. Instead, the sediment was collected, freeze-dried, and then re-used as the feed material for another CFE pass. For each exfoliation cycle, 1 g of material was used as the starting feed. In the first cycle, fresh graphite precursor was processed, while in the second and third cycles, the freeze-dried sediment from the previous cycle was re-exfoliated. This approach was used to determine whether the sediment still contained partially exfoliated or unexfoliated graphitic material that could be further exfoliated into additional dispersed Graphene nanosheets.

This strategy is based on the sediment-recovery concept reported for liquid-exfoliated Graphene, where exfoliated nanosheets can become trapped in the sediment with heavier parent graphite material and recovered by repeated washing/redispersion [138]. Here, this concept was extended by not only washing the sediment but also freeze-drying and reprocessing it through the CFE system. Since CFE exfoliation is driven by high-velocity gas flow and strong shear generated through narrow restrictions, re-exposing the sediment to the CFE flow can further exfoliate partially separated graphitic particles (***Figure 6.11*****(a)**).

As shown in ***Figure 6.11*****(b)**, the cumulative recovered Graphene concentration increased with repeated centrifugation/re-dispersion cycles for each exfoliation pass. In Exfoliation Cycle 1, the concentration increased from approximately 0.16 $g \cdot L^{-1}$ after the first centrifugation cycle to 0.43 $g \cdot L^{-1}$ after five cycles. After freeze-drying and re-exfoliating the sediment, Exfoliation Cycle 2 reached a higher final concentration of approximately 0.54 $g \cdot L^{-1}$. A third re-exfoliation of the freeze-dried sediment further increased the final concentration to approximately 0.61 $g \cdot L^{-1}$.

Because each exfoliation cycle used the same feed mass of 1 g, the increase in recovered concentration cannot be attributed to using more starting material. Instead, it suggests that the sediment becomes more processable after each CFE exposure. The first CFE pass likely weakens the graphitic structure, reduces particle size, and partially separates stacked layers. After freeze-drying, the recovered sediment can be reintroduced into the CFE system, where the already-weakened or partially exfoliated particles experience additional gas-driven shear and particle–gas interactions. This leads to progressively higher Graphene recovery in later exfoliation cycles.

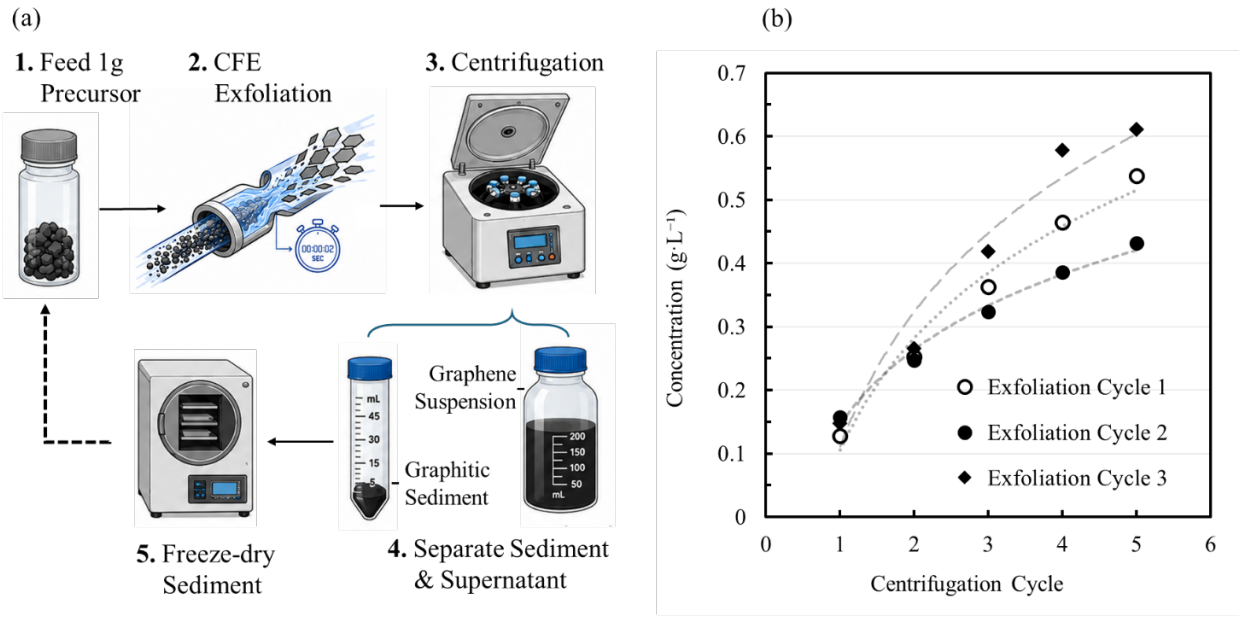

***Figure 6.11**: Sediment recycling for Graphene yield enhancement. (a) Workflow showing CFE exfoliation, centrifugation/re-dispersion, sediment freeze-drying, and reuse of the sediment for the next exfoliation pass. (b) Final cumulative Graphene concentration after five recovery cycles for three successive exfoliation passes, increasing from 0.431 to 0.538 and 0.611 g·L⁻¹.*

Quantitatively, each exfoliation cycle was performed using 1 g of feed material and 200 mL of DI/IPA solvent. In Exfoliation Cycle 1, the final concentration after five centrifugation cycles was 0.43 g·L^{-1}, corresponding to ~86 mg of recovered Graphene, giving a yield of 8.6%. After freeze-drying and re-exfoliating the sediment, Exfoliation Cycle 2 reached 0.54 g·L^{-1}, corresponding to 108 mg, giving a yield of 10.8%. In Exfoliation Cycle 3, the concentration further increased to 0.61 g·L^{-1}, corresponding to 122 mg, giving a yield of 12.2%. Thus, the yield increased from 8.6% in the first cycle to 10.8% and 12.2% in the second and third cycles, respectively. This represents an improvement of approximately 25% in Exfoliation Cycle 2 and 42% in Exfoliation Cycle 3 compared with Exfoliation Cycle 1. Combining the recovered material from all three exfoliation cycles gives a total recovered concentration of 1.58 g·L^{-1}, equivalent to approximately 316 mg of Graphene in 200 mL solvent. Normalized to the 2 s discharge event, these recovered masses correspond to short-burst CFE production intensities of approximately 43, 54, and 61 mg·s^{-1} for exfoliation cycles 1–3, respectively. Because the sediment was recycled from the previous cycle without adding fresh graphite, the cumulative recovered mass is reported relative to the original 1

g feed basis. This cumulative recovery corresponds to an overall recovered mass of 31.6% relative to the original 1 g graphite feed and reflects cumulative recovery after repeated sediment reprocessing.

Normalized to the 2 s discharge event, the recovered masses correspond to short-burst, recovery-normalized CFE intensities of approximately 43, 54, and 61 $mg \cdot s^{-1}$ for Exfoliation Cycles 1–3, respectively. Importantly, these results were achieved using compressed air rather than helium, supporting the practical scale-up potential of the modified CFE process through the use of a widely available and lower-cost carrier gas.

These results show that the sediment should be considered a recyclable intermediate stream rather than waste. Repeated CFE treatment of freeze-dried sediment improves Graphene recovery, increases material utilization, and provides a practical route for reducing feedstock loss in the modified CFE process.

6.11 Chapter Summary

This chapter experimentally validated and optimized the modified CFE process. The reference-based CFE apparatus reproduced the gas-dependent h-BN exfoliation trend reported in the reference study, confirming successful baseline validation of the modified CFE process. h-BN was then used as a model material to identify the most important controllable parameters. Reducing starting particle size, increasing material loading, and increasing upstream pressure all improved recovered concentration; however, the addition of gas preheating was the key modification that enabled nitrogen and compressed air to achieve practical exfoliation yields under the optimized CFE condition. The optimized heated process was then extended to Graphene and MoS_2, confirming the versatility of the modified CFE system across insulating, conductive, and semiconducting layered materials. Repeated sediment re-dispersion increased the recovered concentration of all tested materials, while MoS_2 centrifugation studies showed that post-processing can reveal and tune the size/thickness composition of the CFE product. Finally, freeze-drying and re-exfoliating Graphene sediment increased cumulative Graphene recovery to 316 mg, corresponding to 31.6% on a 1 g feed basis. Across the chapter, recovered nanosheet concentration was the primary performance metric, while recovered mass, yield, and short-burst CFE production intensity were used as supporting indicators. These metrics show that the optimized CFE process

increased both suspension concentration and the amount of usable nanosheet material recovered per 200 mL collection volume and per 2 s discharge event. Production intensity is reported as a laboratory short-burst metric because the present system uses manual powder loading and batch collection. Importantly, these results were achieved using compressed air rather than helium. Replacing helium with a widely available, lower-cost carrier gas substantially improves the practical and economic potential of CFE for scale-up. Overall, these results establish heated CFE as a tunable, recyclable, and scalable gas-driven route for producing multiple 2D nanomaterials.

Chapter 7: Material Characterization of Optimized CFE[5]

7.1 Introduction

Chapter 6 demonstrated that the optimized heated CFE process substantially improved the recovered concentration of h-BN, Graphene, and MoS_2 using practical carrier gases such as compressed air and nitrogen. However, higher recovered concentration alone is not sufficient to establish the value of the process. A central question remains: did the optimized CFE process increase output while preserving the structural and chemical quality of the exfoliated materials, or did it mainly produce concentration gains through destructive fragmentation, oxidation, or severe lattice damage?

This chapter addresses that question by characterizing the morphology, surface chemistry, and structural fingerprints of the optimized CFE products. The purpose is not only to confirm that nanosheets were produced, but also to determine whether the main material identity of Graphene, h-BN, and MoS_2 was retained after gas-driven exfoliation. This quality-control role is especially important because CFE uses rapid gas expansion, particle acceleration, aerodynamic forcing, and thermally assisted delamination. These conditions can promote exfoliation, but they could also introduce defects, edge modification, or surface oxidation if the process is too aggressive.

The characterization strategy combines complementary techniques. TEM, STEM, and HRTEM are used to evaluate nanosheet morphology, lateral continuity, thickness contrast, and local lattice preservation. XPS is used to examine surface chemistry, bonding environments, oxidation, and gas-dependent chemical modification. Raman spectroscopy is used to assess structural fingerprints, defect- or edge-related scattering, layer-sensitive peak changes, and phase-related signatures, particularly for MoS_2. Together, these techniques provide a more complete assessment than any single method alone.

The chapter is organized around three material systems: Graphene, h-BN, and MoS_2. For each material, the results are interpreted in terms of whether CFE produced nanosheet-like structures

[5] Intellectual Property and Publication Status. The apparatus modifications, process conditions, recovery strategies, and experimental results presented in this chapter form part of an ongoing intellectual-property assessment. Journal publication of these findings has therefore been delayed while the associated protection and commercialization strategy is being finalized.

while preserving the dominant chemical and structural identity of the parent layered material. The final integrated summary links the characterization results back to Chapter 6 by evaluating whether the improved recovered concentration was achieved without severe pulverization, amorphization, or destructive chemical degradation.

7.2 Material Characterization Techniques

The characterization methods were selected to answer three linked questions: (i) whether CFE produced sheet-like nanosheets rather than only fractured powder; (ii) whether the dominant bonding environments of Graphene, h-BN, and MoS_2 were preserved after processing; and (iii) whether the Raman-active lattice fingerprints and layer-sensitive spectral trends support exfoliation without severe amorphization. UV–Vis spectroscopy was used mainly for concentration estimation and process-output comparison, as discussed in Chapter 6. In Chapter 7, TEM/STEM/HRTEM, XPS, and Raman spectroscopy provide the main evidence for morphology, surface chemistry, and structural quality.

7.2.1 X-ray Photoelectron Spectroscopy (XPS)

X-ray photoelectron spectroscopy (XPS) was used to evaluate the near-surface elemental composition and chemical bonding states of the CFE-processed materials. Because the analysis depth of XPS is limited to the near-surface region, the spectra were interpreted as evidence of surface and edge chemistry rather than as a direct measurement of bulk crystallinity or total exfoliation yield. This distinction is important for CFE products because exfoliation increases the number of exposed edges and fresh surfaces, which can increase the relative contribution of oxygenated, defect-associated, or adventitious surface species.

For Graphene, the C 1s region was used to compare graphitic sp^2 carbon, sp^3/defect-associated carbon, and oxygen-containing carbon species [142]. For h-BN, the B 1s and N 1s regions were used to determine whether B-N and N-B bonding remained dominant, while B-O, N-C, C-containing, and O 1s features were used to evaluate surface or edge modification [37, 139]. For MoS_2, the S 2s-Mo 3d and S 2p regions were used to assess Mo-S bonding, minor MoO_x/SO_x contributions, and possible 2H/1T phase signatures [143, 144]. Therefore, XPS was used to

determine whether CFE preserved the dominant lattice bonding environments while identifying any carrier-gas-dependent surface modification.

7.2.2 Transmission Electron Microscopy (TEM)

Transmission electron microscopy (TEM) and high-resolution TEM (HRTEM) were used to examine nanosheet morphology and local crystalline order. Bright-field TEM images provided qualitative evidence of laterally extended, electron-transparent nanosheets, while local contrast variations were interpreted as possible differences in thickness, overlap, or folding. Because TEM image contrast is influenced by specimen thickness, diffraction conditions, defocus, overlap, support-film effects, and sample preparation, it was not used alone to determine an exact number of layers [145, 146].

Fast Fourier transform (FFT) analysis of selected HRTEM regions was used to examine local lattice periodicity and orientation. The observed hexagonal reflection patterns were consistent with the expected basal-plane crystalline symmetry of Graphene, MoS_2, and h-BN [8, 28, 49]. When multiple rotated hexagonal FFT patterns were observed, they were interpreted as being consistent with overlapping or rotationally misaligned crystalline domains. Such features may result from stacked or twisted layers, restacking, or overlap introduced during TEM-grid deposition; therefore, they were not attributed exclusively to the CFE process [147]

7.2.3 Raman Spectroscopy

Raman spectroscopy was employed to assess layer reduction and identify any process-induced structural defects. The centrifuged colloidal suspensions were drop-cast onto silicon substrates, dried, and subsequently analyzed using a 532 nm laser excitation source.

For Graphene, the Raman analysis focused on the G peak near $1580\ cm^{-1}$, the 2D peak near $2690\ cm^{-1}$, and the defect-activated D peak near $1330\ cm^{-1}$. The evolution of the 2D band from a broader, asymmetric profile toward a sharper and more symmetric peak indicates a reduction in layer number and possible formation of few-layer Graphene. The I_D/I_Gratio was also calculated from the D and G bands to assess edge-related defects and possible disruption of the sp^2carbon network [148, 149, 150].

For MoS_2, the analysis was based on the separation between the in-plane E^1_{2g} mode and the out-of-plane A_{1g} mode. Bulk MoS_2 typically shows a peak separation of approximately 25–26 cm^{-1}, while this distance decreases as the material is thinned toward few-layer and monolayer MoS_2. Therefore, changes in the E^1_{2g}–A_{1g} peak separation were used as an indicator of exfoliation and layer-number reduction [151].

For h-BN, the position of the high-frequency in-plane E_{2g} phonon mode was monitored. Bulk h-BN typically exhibits this peak near 1366 cm^{-1}. With exfoliation and reduced interlayer interaction, this mode can shift toward lower wavenumbers, approaching approximately 1362 cm^{-1} for highly thinned h-BN. Therefore, the position and shape of the E_{2g} peak were used to evaluate exfoliation while also checking whether the main vibrational signature of the h-BN lattice was preserved [152, 153].

7.3 Qualitative Morphological Analysis (TEM, STEM)

The primary morphological objective of CFE is to convert layered precursor particles into nanosheet-rich products while preserving the in-plane basal-plane framework. Unlike liquid-phase routes that often depend on sonication-induced cavitation, solvent-surface matching, surfactants, or intercalating chemicals, CFE applies high-speed gas-driven forces in a dry environment. The electron microscopy analysis in this section tests whether the optimized process produced sheet-like nanosheets rather than only pulverized powder fragments.

Figure 7.1 presents the STEM, TEM, and HRTEM images of CFE-exfoliated Graphene. The Graphene nanosheet appears broad, flexible, and laterally continuous over several hundred nanometres. Wrinkles, folds, and local contrast variations are visible, which are commonly observed in thin Graphene-based sheets due to their mechanical flexibility during coating on TEM grids. The partial electron transparency and local contrast variation are consistent with a thinned, exfoliated Graphene-based sheet, although TEM contrast alone cannot provide an exact layer count. In the HRTEM image, graphitic lattice features and curved layered regions are visible, indicating that local graphitic ordering is retained after CFE. These observations support the conclusion that CFE produces sheet-like Graphene-rich nanosheets rather than only pulverized carbon debris.

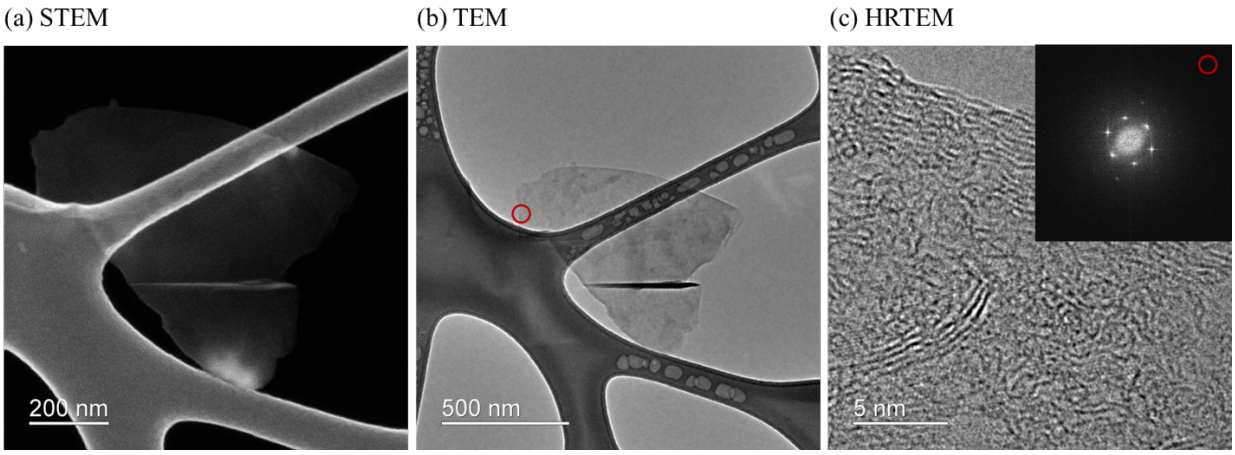

***Figure 7.1**: Morphological characterization of CFE-exfoliated Graphene: (a) STEM image, (b) TEM image, and (c) HRTEM image with corresponding diffraction/FFT pattern.*

Figure 7.2 shows the morphology of CFE-exfoliated MoS_2 using STEM, TEM, and HRTEM. The STEM and TEM images reveal a laterally extended nanosheet with a compact plate-like morphology, irregular edges, and visible thickness contrast across the flake. These features indicate that CFE successfully delaminates MoS_2 into thin nanosheets while maintaining a continuous basal-plane structure. The HRTEM image shows clear lattice fringes, confirming that the crystalline structure is preserved after exfoliation. The corresponding diffraction/FFT pattern further supports the presence of ordered MoS_2 domains, suggesting that the process does not cause severe structural damage to the nanosheet.

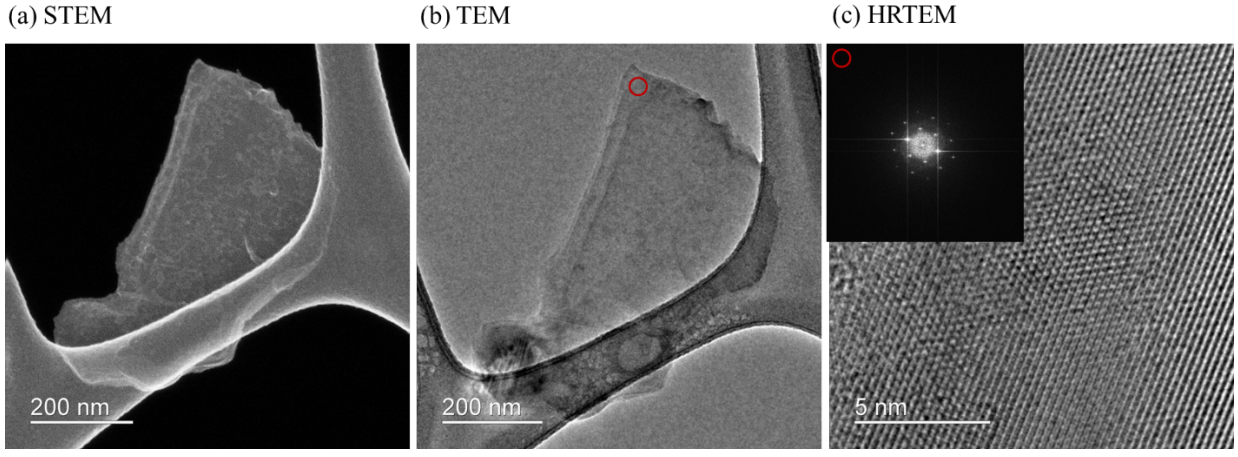

***Figure 7.2**: Morphological characterization of CFE-exfoliated MoS_2: (a) STEM image, (b) TEM image, and (c) HRTEM image with corresponding diffraction/FFT pattern.*

Figure 7.3 shows the morphology of CFE-exfoliated h-BN. The STEM and TEM images display a thin, elongated nanosheet with irregular edges and local thickness variations. Compared with Graphene, the h-BN flake shows a more stretched and directional morphology, which may be related to its fracture and delamination behaviour under gas-driven mechanical forces. The HRTEM image shows visible lattice ordering, confirming that the crystalline h-BN structure is largely retained after exfoliation. Together, the low-magnification and high-resolution images indicate that CFE produces thin h-BN nanosheets while preserving the in-plane structure of the material.

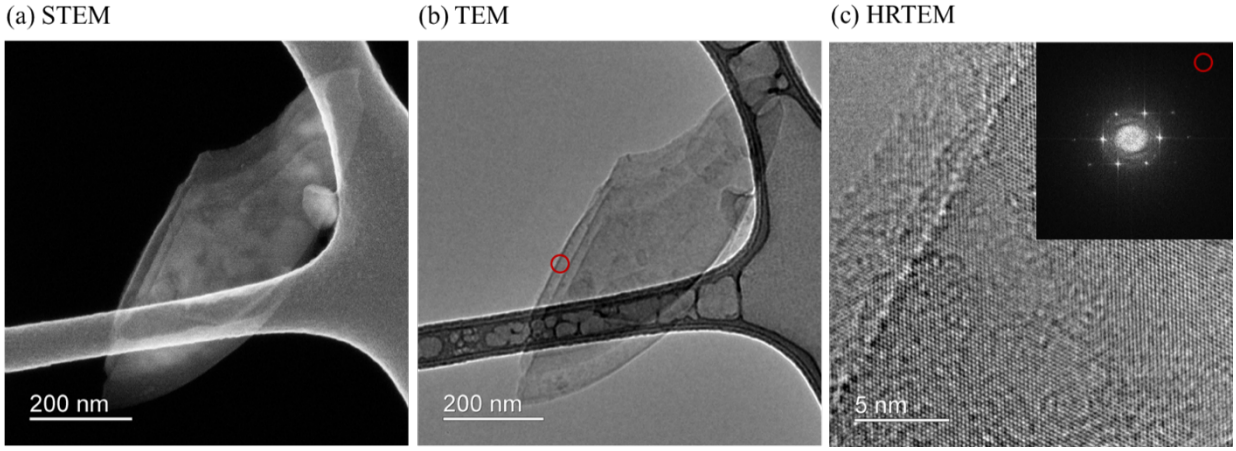

Figure 7.3*: Morphological characterization of CFE-exfoliated h-BN: (a) STEM image, (b) TEM image, and (c) HRTEM image with corresponding diffraction/FFT pattern. The h-BN nanosheet shows an elongated morphology, local thickness variation, and preserved crystalline lattice features.*

Overall, the STEM, TEM, and HRTEM images show that CFE produces laterally extended nanosheet-like products for Graphene, h-BN, and MoS_2. The observed flakes retain continuous sheet-like or platelet-like morphologies with irregular edges, wrinkles, folds, and local contrast variations. These features are consistent with exfoliated few-layer materials and indicate that the process promotes delamination rather than only uncontrolled pulverization. Importantly, HRTEM images show local lattice features in all three materials, supporting preservation of crystalline basal-plane regions after CFE. Because these images are representative, they should be interpreted as morphological evidence of nanosheet formation rather than as a full statistical distribution of all flakes in the product.

Quantitative geometric analysis was performed on representative TEM images to estimate the projected dimensions of the exfoliated nanosheets. The measured values should be interpreted as representative image-based dimensions, not as a full statistical flake-size distribution. A larger dataset would be required for population-level size analysis. Nevertheless, the current measurements provide useful evidence that CFE preserves relatively large lateral dimensions after exfoliation.

Table 7.1: *Representative projected dimensions and aspect ratios of CFE-produced Graphene, h-BN, and MoS_2 nanosheets measured from TEM images.*

Materials	Length	Width	Lateral Aspect ratio	Projected area
Graphene	913 nm	669 nm	1.36	0.404 μm²
h-BN	839 nm	295 nm	2.84	0.167 μm²
MoS_2	736 nm	443 nm	1.66	0.234 μm²

The values in ***Figure 7.4***, ***Figure 7.1*** and ***Table 7.1*** are measured from representative TEM images, therefore, they should be used to support the presence of laterally extended nanosheets, not to define the full product size distribution. A statistically robust flake-size distribution would require automated or manual analysis of a larger number of flakes across multiple TEM grids and sample regions. The dimensional measurements show that all three materials retain sub-micrometre to near-micrometre projected lateral dimensions after CFE. The few-layer Graphene flake has the largest projected area, approximately 0.404 μm², and the largest equivalent circular diameter, approximately 717 nm. This is consistent with the observed broad, flexible morphology of the Graphene nanosheet. The h-BN flake has the highest aspect ratio, 2.84, indicating a more elongated morphology. This elongated morphology may reflect anisotropic fracture/delamination pathways, precursor particle morphology, or preferential breakage during gas-driven processing; however, a larger flake population would be required to assign the aspect-ratio trend to a specific

fracture mechanism. The MoS_2 flake shows an intermediate aspect ratio of 1.66 and a projected area of 0.234 μm², indicating a compact but clearly exfoliated platelet morphology.

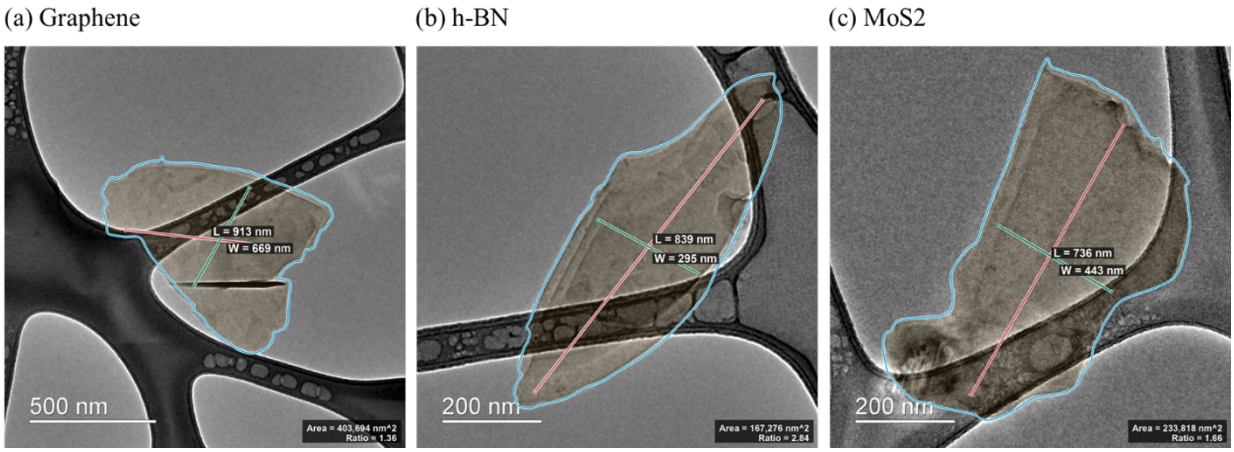

***Figure 7.4**: TEM-based representative dimensional analysis of CFE-exfoliated (a) Graphene, (b) h-BN, and (c) MoS_2 nanosheets. Representative dimensional analysis of CFE-exfoliated nanosheets.*

These dimensions support the key claim that CFE does not merely grind the powders into small debris. Instead, it produces few-layer nanosheets with preserved lateral dimensions in the hundreds-of-nanometres range. This is important because lateral size strongly affects many practical applications, including conductive networks, membranes, coatings, composites, and catalytic or electronic interfaces.

The microscopy results establish that CFE produces nanosheet-like morphologies with preserved local lattice contrast. However, microscopy alone cannot determine whether newly generated surfaces and edges undergo oxidation or chemical modification during gas-driven processing. Therefore, XPS was used next to evaluate whether the dominant bonding states of Graphene, h-BN, and MoS_2 were preserved after CFE and whether the carrier gas influenced near-surface chemistry.

7.4 Surface Chemistry and Chemical State Analysis (XPS)

XPS was used to evaluate whether CFE retained the dominant bonding environments of each material and to identify surface- or edge-associated chemical changes introduced during processing. As a surface-sensitive technique, XPS primarily probes the outermost region of the material; therefore, the results are interpreted in terms of relative changes in surface chemistry

rather than as direct measurements of bulk crystallinity or exfoliation yield [154]. Exfoliation can expose new basal surfaces and edge sites, while processing and subsequent air exposure may introduce oxygenated or defect-associated surface components. Accordingly, the XPS results are discussed in terms of dominant lattice-bond retention together with moderate surface or edge modification, rather than complete chemical invariance.

7.4.1 Graphene

X-ray photoelectron spectroscopy was used to compare the surface chemistry and bonding states of the reference graphite powder and the Graphene products obtained by CFE using air and helium as carrier gases. The high-resolution C 1s spectra were used to compare the relative contributions of graphitic sp^2 carbon, non-sp^2 carbon associated with defects or edges, and oxygen-containing carbon species after processing. Interpretation of the C 1s envelope follows current XPS fitting guidance, which treats graphitic, non-sp^2/defect-associated, and oxygenated carbon contributions as overlapping near-surface environments rather than direct bulk-phase fractions [142]

Survey spectra were first examined to identify the overall elemental composition of the samples, as shown in ***Figure 7.5(a–c)***. Carbon is the dominant element in all three samples, while oxygen appears at different levels as a surface contribution. The air- and helium-processed samples also show a weak F 1s signal near 685 eV. The weak F 1s signal is most reasonably interpreted as a trace surface residue, potentially from PTFE-containing sealing, tubing, or sample-handling components, rather than as an intrinsic structural component of Graphene. Within the detection limits of the survey spectra, no significant heavy-metal or solvent-related contamination is evident. High-resolution C 1s spectra, shown in ***Figure 7.5(d–f)***, were then fitted to compare the surface carbon bonding environments. The fitted C 1s component areas for reference graphite, Air-CFE Graphene, and He-CFE Graphene are summarized in ***Table 7.2***.

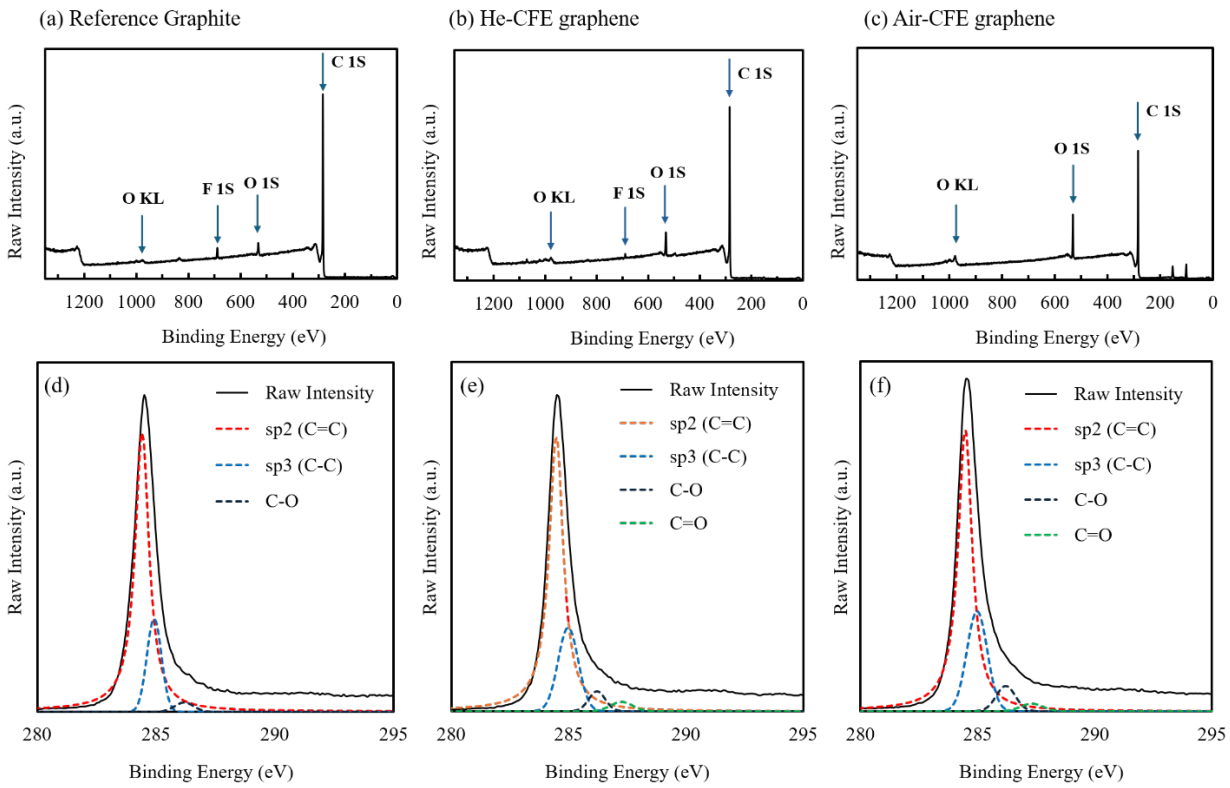

***Figure 7.5**: XPS survey spectra of (a) reference graphite, (b) Air-CFE Graphene, and (c) He-CFE Graphene, together with high-resolution C 1s spectra of (d) reference graphite, (e) Air-CFE Graphene, and (f) He-CFE Graphene. The survey spectra confirm carbon as the main element and show minor surface oxygen and trace fluorine in the processed samples. The C 1s spectra were used to evaluate changes in sp² carbon, sp³ carbon, and oxygen-containing surface species after CFE.*

***Table 7.2:** High-resolution C 1s deconvolution of reference and CFE-processed Graphene samples.*

Material	sp² C=C (%)	sp³ C–C (%)	Total oxygenated carbon (%)
Reference graphite	79.55	18.18	2.27
He-CFE Graphene	70.83	19.94	9.23
Air-CFE Graphene	67.51	22.91	9.57

The reference graphite is dominated by sp² carbon, as expected for a graphitic lattice. The fitted sp² contribution is 79.55%, while the sp³ contribution is 18.18%. This sp³-related signal should not

be interpreted as bulk conversion of graphite to sp^3 carbon. Instead, it likely reflects a combination of surface defects, exposed edges, adventitious carbon, and fitting contributions associated with the finite surface sensitivity of XPS. Therefore, the reference sample provides a useful baseline for comparing the additional surface modification introduced by CFE. The relative distribution of oxygenated C 1s components is visualized in ***Figure 7.6***, highlighting the increased oxygen-containing surface contribution after CFE.

Table 7.3: *High-resolution C 1s peak parameters for reference and CFE-processed Graphene samples.*

Chemical State	Parameter	Reference graphite	He-CFE Graphene	Air-CFE Graphene
C=C (sp^2)	Position (eV)	284.43	284.47	284.48
	FWHM (eV)	0.82	0.85	0.84
C-C (sp^3)	Position (eV)	284.93	284.97	284.98
	FWHM (eV)	0.72	1.01	1.02
C-O	Position (eV)	286.20	286.2	286.20
	FWHM (eV)	0.93	0.83	0.96

The peak positions in ***Table 7.3*** are consistent with graphitic sp^2 carbon near 284.4–284.5 eV, sp^3/defect-related carbon at slightly higher binding energy, and C–O-type oxygenated carbon near 286.2 eV [142, 154]. The use of consistent fitting constraints across the three samples improves the reliability of the comparison. However, the fixed separation between the sp^2 and sp^3 components should be treated as part of the fitting model and not as independent proof of a physically ideal lattice. The small change in the sp^2 peak FWHM, from 0.82 eV in the reference

sample to 0.84–0.85 eV after CFE, suggests that the main graphitic carbon environment remains relatively well preserved after processing.

The CFE process increases both the sp^3-related and oxygenated carbon contributions. For Air-CFE Graphene, the sp^3 fraction increases to 22.91% and the total oxygenated contribution increases to 9.57%. For He-CFE Graphene, the sp^3 fraction is lower, 19.94%, while the total oxygenated contribution is 9.23%. These results indicate that both gases produce surface and edge modification, which is expected when layered graphite is exposed to intense shear, particle-particle collisions, wall impacts, and rapid pressure changes. The increased sp^3 contribution is consistent with the formation of additional edges and defect sites during delamination.

The carrier gas can influence the balance between preservation of the graphitic surface and defect- or edge-associated surface modification during CFE. Air-CFE produced the lowest fitted sp^2 fraction (67.51%) and the highest fitted sp^3 fraction (22.91%), whereas He-CFE retained a modestly higher sp^2 fraction (70.83%) and lower sp^3 fraction (19.94%). This difference is consistent with slightly greater near-surface disruption in the air-processed sample.

The comparison is relevant because helium and nitrogen are single-component carrier gases, whereas compressed air is a multicomponent mixture containing nitrogen, molecular oxygen, and minor gaseous constituents. Thus, in addition to mechanical exfoliation, air processing may expose freshly generated edges and defect sites to a chemically more complex gas environment. However, because the total oxygenated C 1s contribution was very similar for Air-CFE Graphene and He-CFE Graphene, the observed difference should not be interpreted as strong additional oxidation caused by air. Instead, the results indicate a modest reduction in fitted sp^2 retention and slightly greater defect-/edge-associated surface modification for Air-CFE relative to He-CFE under the tested conditions.

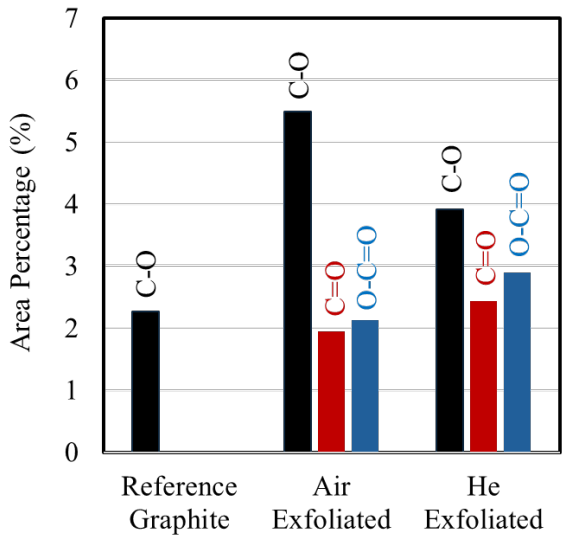

***Figure 7.6**: Relative distribution of oxygenated C 1s components in reference graphite, Air-CFE Graphene, and He-CFE Graphene. Both CFE conditions increase oxygen-containing surface species relative to the reference sample, while helium preserves a slightly higher sp^2 carbon contribution.*

Overall, the C 1s XPS results indicate that CFE modifies graphite mainly through surface and edge chemistry while retaining a dominant graphitic carbon environment. Both Air-CFE and He-CFE increase the oxygenated-carbon contribution relative to the reference graphite, consistent with the generation and exposure of new surfaces and edge sites during delamination. The total oxygenated C 1s contribution remains moderate, reaching 9.57% for Air-CFE Graphene and 9.23% for He-CFE Graphene. Within this comparison, the main difference is not a large change in total oxidation, but the lower fitted sp^2 fraction and higher sp^3/defect-associated fraction in Air-CFE compared with He-CFE. This indicates modestly greater near-surface modification under compressed-air processing relative to helium under the tested conditions.

The Air–He comparison provides a useful contrast between an inert single-component carrier gas and the more chemically complex compressed-air environment. In the broader CFE carrier-gas framework, nitrogen is the primary practical reference because it is a single-component gas, is more accessible and scalable than helium, and avoids the oxygen-containing environment of compressed air. Helium therefore serves as an inert benchmark, while compressed air provides a practical multicomponent comparison for evaluating the additional influence of gas composition on surface and edge modification. Overall, the results are consistent with CFE acting as a dry

mechanical exfoliation process that causes moderate, material-dependent surface modification without severe oxidation or complete amorphization of the graphitic framework.

7.4.2 Hexagonal Boron Nitride (h-BN)

XPS was used to investigate the surface composition and bonding states of reference h-BN, Air-CFE h-BN, and He-CFE h-BN. The analysis was performed in two stages. First, survey spectra were used to identify the main elements present in the samples. Second, high-resolution B 1s, N 1s, C 1s, and O 1s spectra were fitted to assess changes in the local chemical environment after exfoliation. Because h-BN is a layered ceramic with strong in-plane B–N bonding and weaker interlayer interactions, XPS is particularly useful for identifying surface oxidation, hydroxylation, and edge-related chemical changes introduced during processing.

The survey spectra confirm the presence of B and N as the main elements in all samples, together with smaller C and O contributions, as shown in **Figure 7.7**. The dominant B and N signals indicate that the h-BN framework remains the primary structure after CFE. Carbon is attributed mainly to adventitious surface carbon and possible carbon-containing surface species. Oxygen is associated with surface oxygen species, adsorbed oxygen or water, and partial oxidation or hydroxylation of boron-rich edge sites. Therefore, the survey spectra support chemical retention of the h-BN framework while also showing that surface species are present, as expected for air-exposed powders.

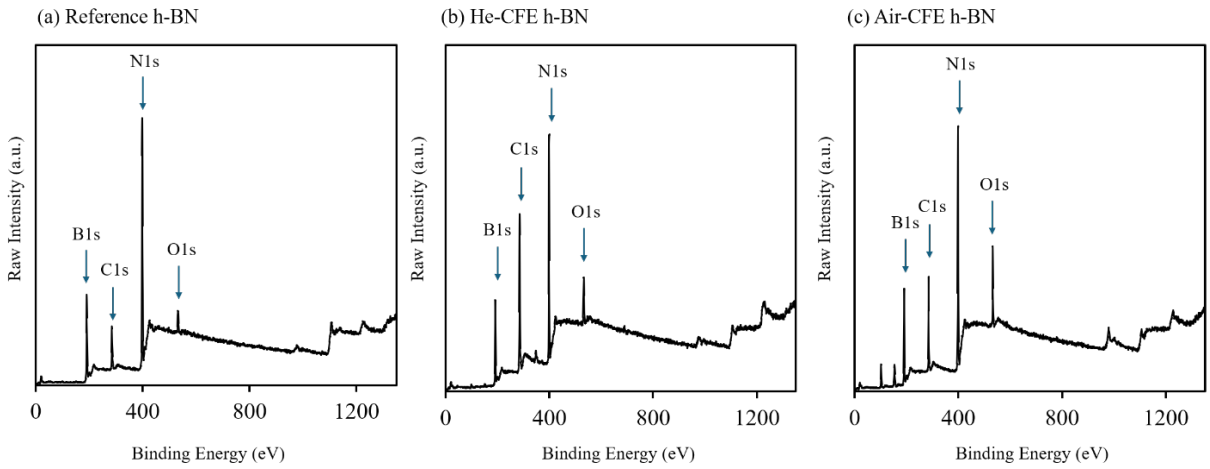

Figure 7.7**:** *XPS survey spectra of (a) reference h-BN, (b) He-CFE h-BN, and (c) Air-CFE h-BN. The spectra confirm B and N as the main components of the h-BN structure, together with smaller C and O surface contributions attributed to adventitious carbon, adsorbed oxygen-containing species, and CFE-induced surface/edge functionalization.*

The high-resolution B 1s spectra provide the most direct evidence for changes in the boron chemical environment after CFE. The spectra were fitted using components assigned to C–B–N, B–N, C–N–B, and B–O bonding environments. The dominant component in all samples is B–N, confirming that boron remains mainly bonded within the h-BN lattice. The B–N component appears at approximately 190.60 eV for the CFE-processed samples and 190.74 eV for the reference sample, consistent with reported B–N binding energies for h-BN [37, 139].

Table 7.4: *High-resolution B 1s deconvolution of reference and CFE-processed h-BN samples.*

Material	**C–B–N (%)**	**B–N (%)**	**C–N–B (%)**	**B-O (%)**
Reference h-BN	5.89	84.05	6.94	3.11
He-CFE h-BN	11.20	79.64	5.29	3.87
Air-CFE h-BN	17.84	69.10	5.21	7.85

The reference h-BN sample shows the highest B-N contribution, 84.05%, confirming that the unprocessed powder is dominated by the expected boron nitride bonding environment. After CFE,

the B-N contribution decreases to 79.64% for He-CFE h-BN and 69.10% for Air-CFE h-BN. This decrease should not be interpreted as wholesale destruction of the h-BN lattice. Instead, because XPS is surface-sensitive, the decrease reflects the larger relative contribution of newly exposed edges, boron-rich sites, carbon-associated surface species, and oxygen-containing boron environments after exfoliation.

The high-resolution B 1s spectra and corresponding fitted components are shown in ***Figure 7.8*** and summarized quantitatively in ***Table 7.4***. The clearest gas-dependent trend in the B 1s spectra is the B–O contribution. The B–O component increases from 3.11% in the reference h-BN to 3.87% for He-CFE h-BN and 7.85% for Air-CFE h-BN. This indicates that compressed-air processing produces stronger oxygen-containing boron surface environments than helium processing. However, this should be interpreted as surface or edge oxygenation, not bulk oxidation or decomposition of the h-BN lattice. The dominant B–N contribution remains present after processing, confirming preservation of the primary h-BN framework. A reasonable explanation is that CFE exposes boron-rich edges, defect sites, and high-energy surface regions that can interact with oxygen- and moisture-containing species during compressed-air processing, DI/IPA solvent collection, centrifugation/re-dispersion, drying, and ambient handling. Because boron-rich sites can form B–O, B–OH, or related oxygen-containing surface environments, Air-CFE h-BN shows the clearest oxygenation signature among the CFE-processed materials.

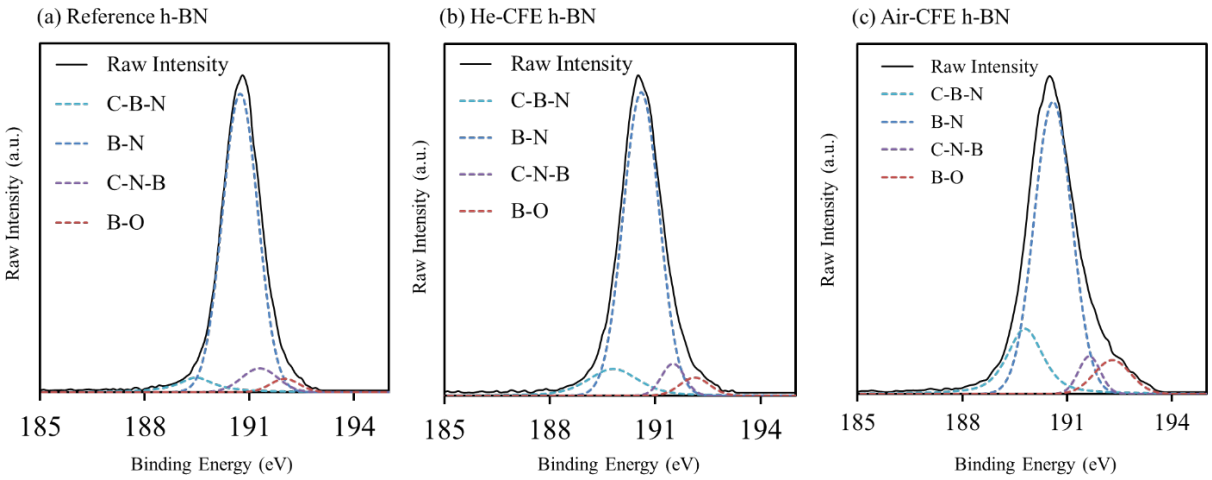

Figure 7.8**:** *High-resolution B 1s XPS spectra and fitted components of (a) reference h-BN, (b) He-CFE h-BN, and (c) Air-CFE h-BN. The dominant B–N contribution confirms preservation of the h-BN framework, while the stronger B–O component in Air-CFE h-BN indicates enhanced oxygen-containing boron surface environments.*

The high-resolution N 1s spectra and fitted component areas are shown in ***Figure 7.9*** and ***Table 7.5***. The N 1s spectra further support preservation of the h-BN framework. The reference and He-CFE samples are fitted entirely by the N–B component, while Air-CFE h-BN contains a small additional N–C contribution. The dominant N–B peak appears at approximately 398.10–398.31 eV, consistent with nitrogen bonded to boron in h-BN [37, 139].

Table 7.5: *High-resolution N 1s deconvolution of reference and CFE-processed h-BN samples.*

Material	**N–B (%)**	**N–C (%)**
Reference h-BN	100	-
He-CFE h-BN	100	-
Air-CFE h-BN	96.40	3.60

The N 1s results show that nitrogen remains predominantly bonded to boron in all samples. This is important because it confirms that CFE does not cause major chemical decomposition of the nitrogen environment in h-BN. The small N–C contribution in Air-CFE h-BN may arise from

defect-associated carbon species, edge bonding, or minor surface contamination activated during processing. Because the N–B contribution remains 96.40%, this feature should be interpreted as a secondary surface effect rather than a major structural transformation.

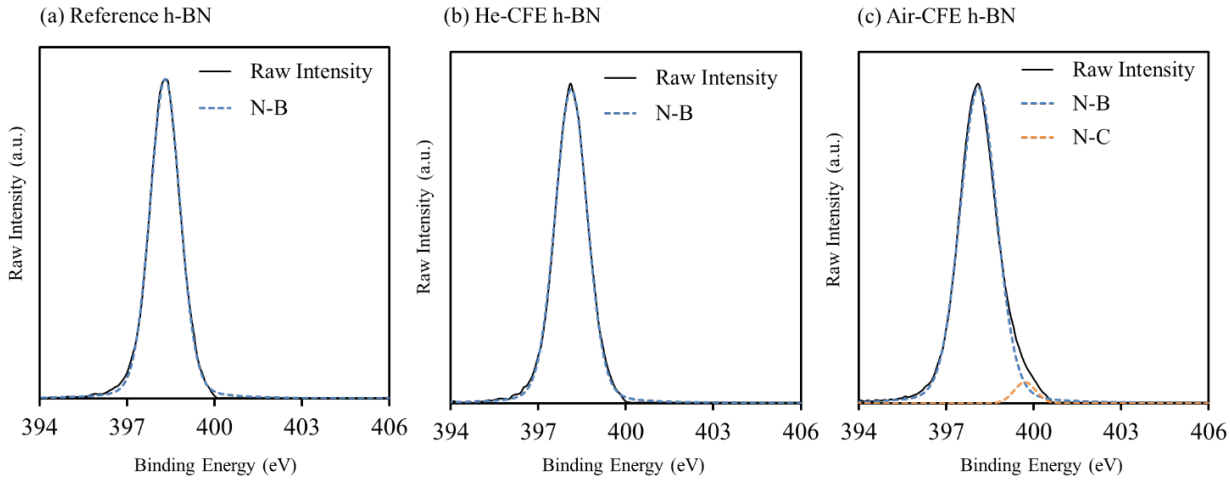

Figure 7.9**:** *High-resolution N 1s XPS spectra and fitted components of (a) reference h-BN, (b) He-CFE h-BN, and (c) Air-CFE h-BN. The spectra are dominated by N–B bonding, confirming that the nitrogen environment of h-BN is largely preserved after CFE. The small N–C contribution in Air-CFE h-BN suggests slightly higher defect- or surface-associated bonding in the air-processed sample.*

The C 1s spectra for reference and CFE-processed h-BN are shown in ***Figure 7.10***, with the fitted component areas summarized in ***Table 7.6***. The C 1s spectra are dominated by a C–C/C–H component near 284.8–284.9 eV. This peak is mainly attributed to adventitious carbon, which is commonly observed on air-exposed powders. A higher-binding-energy component centered near 288.6 eV is also present and is assigned here to mixed C–N/C–N–B/oxygenated carbon contributions. Because this component is broad, it should not be interpreted as a single pure bonding state. Instead, it likely contains overlapping contributions from C–N, C–N–B and background or tail features.

Table 7.6: *High-resolution C 1s deconvolution of reference and CFE-processed h-BN samples.*

Material	C–B–N (%)	C–C/C–H (%)	C–N/C–N–B/oxygenated carbon (%)
Reference h-BN	-	98.32	1.68
He-CFE h-BN	0.26	98.05	1.69
Air-CFE h-BN	—	94.77	5.23

The Air-CFE sample shows the highest high-binding-energy C 1s contribution, 5.23%, compared with 1.69% for He-CFE h-BN and 1.68% for the reference sample. This trend agrees with the B 1s and N 1s results, where Air-CFE h-BN also shows a higher B–O contribution and a small N–C component. The increase in the high-binding-energy C 1s contribution after Air-CFE indicates a higher concentration of oxygenated carbon, C–N/C–N–B surface states, or defect-associated carbon species. In contrast, the He-CFE sample remains close to the reference in the C 1s region, indicating less chemical modification under helium.

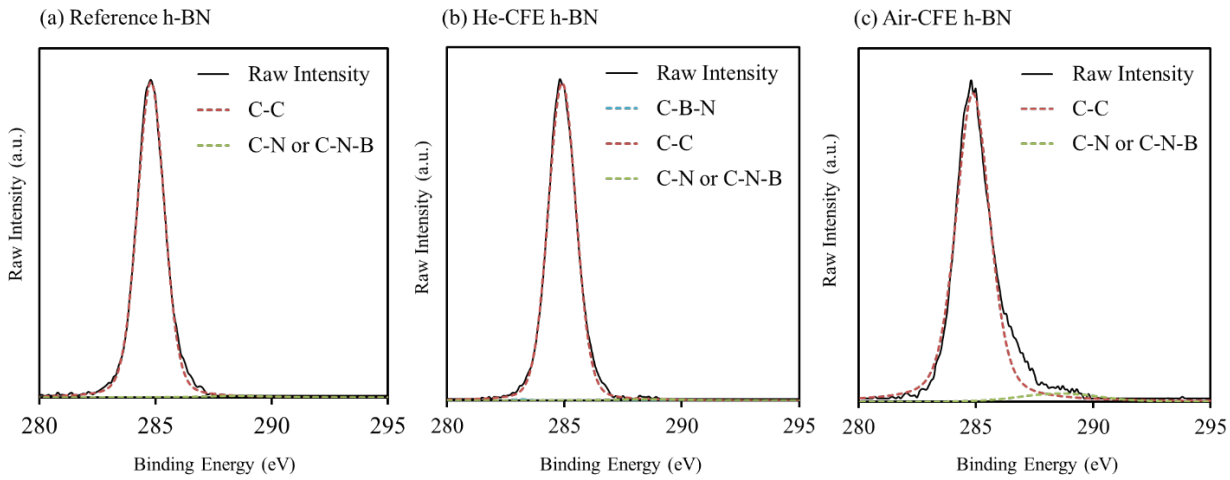

Figure 7.10**:** *High-resolution C 1s XPS spectra and fitted components of (a) reference h-BN, (b) He-CFE h-BN, and (c) Air-CFE h-BN. The spectra are dominated by C–C/C–H carbon. The broad high-binding-energy component near 288.6 eV is assigned to mixed C–N/C–N–B/oxygenated carbon surface species and is most pronounced in Air-CFE h-BN.*

The broad O 1s spectra used to evaluate oxygen-containing surface species are shown in ***Figure 7.11***. The O 1s spectra were fitted using a broad component centered near 532.0-532.4 eV. This binding-energy range is consistent with oxygen-containing surface environments such as B-O-type bonding, hydroxylated sites, adsorbed water/oxygen species, or other surface oxygen contributions. Because these contributions overlap strongly in the O 1s region, the broad O 1s envelope should not be used to assign a single precise oxygen species [37, 154]. The O 1s peak width increases after exfoliation, from 1.48 eV in the reference sample to 2.24 eV for He-CFE h-BN and 3.35 eV for Air-CFE h-BN. The broader O 1s envelope in the air-processed sample indicates a wider distribution of oxygen-containing surface environments. This trend is consistent with the B 1s result, where Air-CFE h-BN has the highest B-O contribution. Therefore, the O 1s spectra supports the conclusion that compressed air introduces stronger oxygen-containing surface or edge chemistry than helium, while the dominant B-N and N-B framework remains preserved.

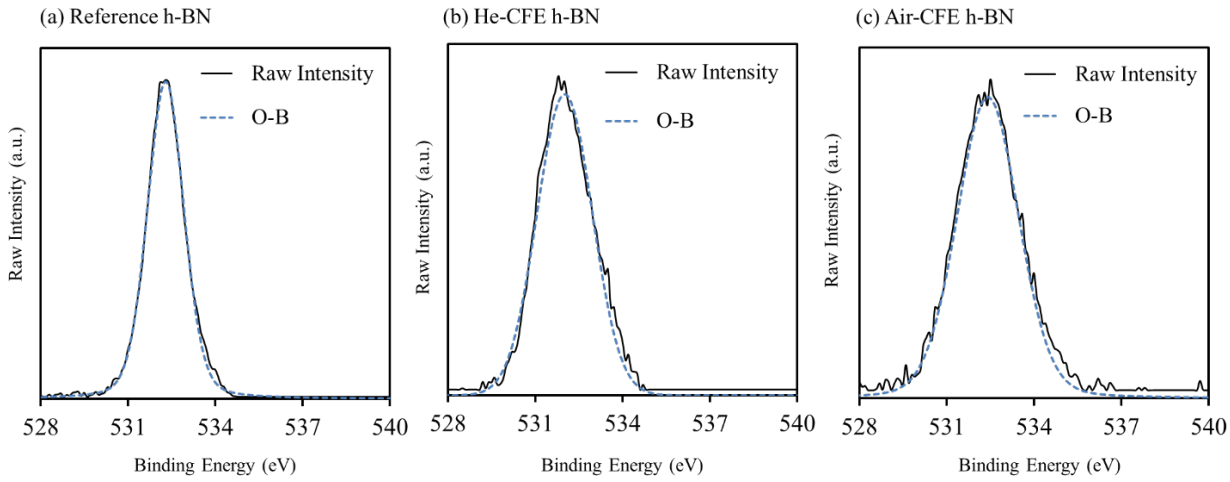

Figure 7.11*: *High-resolution O 1s XPS spectra of (a) reference h-BN, (b) He-CFE h-BN, and (c) Air-CFE h-BN. The broad O 1s envelope is assigned to overlapping O–B/O–H/oxygen-containing surface species rather than to a single pure oxygen bonding environment.

The XPS results can be understood from the mechanics of CFE. During processing, h-BN particles are accelerated by high-pressure gas flow and experience drag forces, shear, interparticle collisions, wall impacts, and rapid expansion. These forces can overcome weak interlayer interactions and expose new surfaces and edges. At the same time, the strong in-plane B–N network remains largely preserved, as shown by the dominant B–N and N–B components in the B 1s and N 1s spectra. The main chemical difference between the carrier gases arises from the processing atmosphere. In air, freshly exposed boron-rich sites can react with oxygen, producing more B–O/B–OH-like environments. In helium, the inert environment limits in-process oxidation, so the surface chemistry remains closer to that of the reference sample.

Overall, the XPS results show that CFE modifies h-BN mainly through mild surface and edge chemistry rather than bulk lattice destruction. The reference h-BN is dominated by B-N and N-B bonding, and these bonding states remain dominant after both Air-CFE and He-CFE, confirming preservation of the main boron nitride framework. This is an important advantage when compared with common h-BN exfoliation techniques, including LPE, where solvents, stabilizers, or chemical interactions are often required to assist delamination and dispersion [139, 155]. In other exfoliation methods, XPS interpretation can be complicated by B-O/B-OH species, carbon-containing residues, surfactants, or functional groups introduced during processing. In contrast,

CFE exfoliates h-BN in a dry gas stream without added solvent, surfactant, or acid/base chemistry, so the observed B-O, N-C, C 1s, and O 1s changes are more directly related to newly exposed surfaces and edges. Air-CFE h-BN shows stronger surface modification, reflected by the higher B-O contribution in B 1s, the small N-C contribution in N 1s, the larger high-binding-energy C 1s contribution, and the broader O 1s envelope. He-CFE h-BN remains closer to the reference material, indicating that helium provides a more chemically inert exfoliation environment. Therefore, compressed air offers a practical low-cost route, while helium gives a modest but clear advantage in preserving native h-BN surface chemistry.

7.4.3 Molybdenum Disulfide (MoS_2)

XPS was used to investigate the surface chemical states and phase stability of reference MoS_2, Air-CFE MoS_2, and He-CFE MoS_2. For MoS_2, the most informative high-resolution regions are the overlapping S 2s–Mo 3d region and the S 2p region. These spectra identify Mo–S bonding, molybdenum oxidation, sulfur oxidation, and possible 2H/1T phase contributions. Because XPS is surface-sensitive, the analysis primarily reflects near-surface chemical changes at basal surfaces, edges, and defect sites generated during exfoliation.

The survey spectra, shown in **Figure 7.12**, confirm Mo and S as the main elements in all samples. Minor surface contributions may be present, but the structural interpretation of MoS_2 is based mainly on the high-resolution S 2s–Mo 3d and S 2p spectra, which are the standard regions used to evaluate MoS_2 bonding and phase chemistry [144, 155, 156].

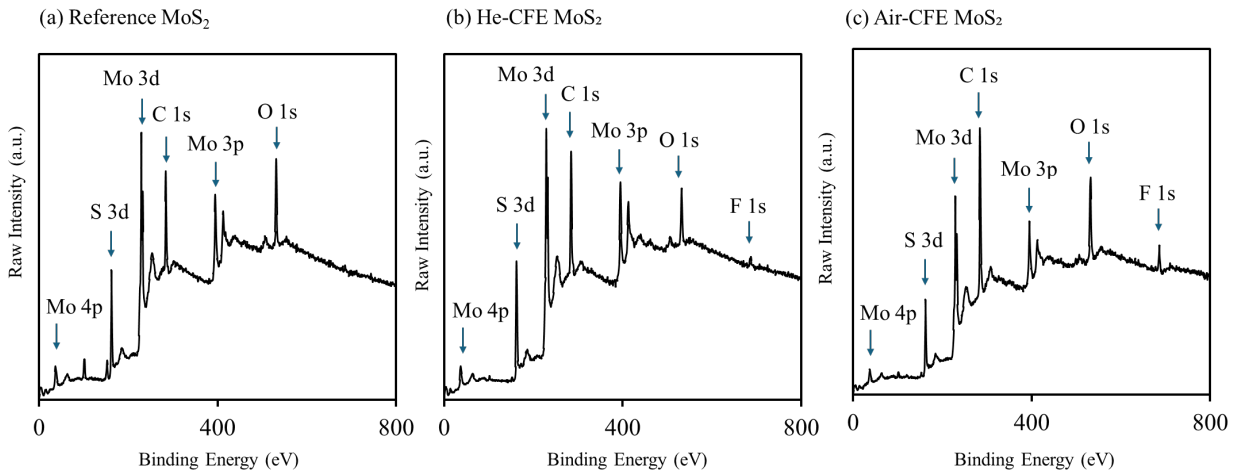

Figure 7.12**:** *XPS survey spectra of (a) reference MoS_2, (b) He-CFE MoS_2, and (c) Air-CFE MoS_2. The spectra confirm Mo and S as the primary elements of the MoS_2 samples. Minor surface signals are treated as extrinsic surface species and are not used as the main evidence for intrinsic MoS_2 structure.*

The high-resolution S 2s–Mo 3d spectra are shown in ***Figure 7.13***, and the corresponding fitted components are summarized in ***Table 7.7***. The dominant MoS_2 doublet appears at 229.05 eV and 232.20 eV for the reference, Air-CFE, and He-CFE samples. The constant Mo 3d spin-orbit separation of 3.15 eV confirms that the main Mo–S chemical environment is preserved after CFE. These binding energies are characteristic of 2H-MoS_2, while metallic 1T-MoS_2 is typically associated with an additional Mo 3d doublet shifted to lower binding energy.

Table 7.7: *High-resolution S 2s–Mo 3d deconvolution of reference and CFE-processed MoS_2 samples.*

Material	**S 2s (%)**	**MoS_2 Mo $3d_{5/2}$ (%)**	**MoS_2 Mo $3d_{3/2}$ (%)**	**MoO_x Mo $3d_{5/2}$ (%)**	**MoO_x Mo $3d_{3/2}$ (%)**
Reference MoS_2	20.06	45.71	31.21	1.81	1.20
He-CFE MoS_2	21.65	42.86	29.24	3.77	2.50
Air-CFE MoS_2	17.35	47.59	32.60	1.45	1.02

The MoS_2 Mo 3d doublet remains the dominant Mo-containing contribution in all samples. The Mo $3d_{5/2}$:Mo $3d_{3/2}$ area ratio is approximately 1.46–1.47, close to the expected 3:2 ratio for a

physically meaningful doublet. This internal consistency supports the reliability of the fitting and indicates that the main Mo–S framework is not significantly disrupted by CFE.

The Mo $3d_{5/2}$ peak at 229.05 eV supports assignment of the samples to predominantly semiconducting 2H-MoS_2 [144, 155]. Metallic 1T-MoS_2 would normally require a distinct lower-binding-energy Mo 3d doublet, often shifted by approximately 0.8–1.0 eV relative to 2H-MoS_2. No clear 1T-related lower-binding-energy doublet is observed in the present fits. Therefore, the XPS data indicate that the reference, Air-CFE, and He-CFE samples remain predominantly 2H-MoS_2 after CFE.

Minor MoO_x-related components are present in all samples. When the oxide contribution is normalized only to the Mo-containing Mo 3d components, excluding the overlapping S 2s peak, the MoO_x-related fraction is approximately 3.77% for the reference sample, 2.99% for Air-CFE MoS_2, and 8.00% for He-CFE MoS_2. These values indicate that molybdenum oxidation is limited overall. Because the MoO_x components are weak and overlap with the main MoS_2 Mo 3d envelope, they should be interpreted as semi-quantitative surface/suboxide contributions rather than as precise bulk oxidation-state fractions. The higher fitted MoO_x contribution in He-CFE MoS_2 should not be interpreted as oxidation caused by helium. A more reasonable interpretation is that He-CFE may expose fresh edge or defect sites that subsequently oxidize during collection, transfer, drying, storage, or ambient air exposure.

The MoO_x-related features should be interpreted cautiously because their intensity is small and they overlap with the main MoS_2 Mo 3d envelope. The oxide components are best described as broad MoO_x/suboxide-type surface contributions rather than as precise oxidation-state quantification. The main conclusion from the Mo 3d region is therefore preservation of the dominant MoS_2 doublet with only minor surface oxidation.

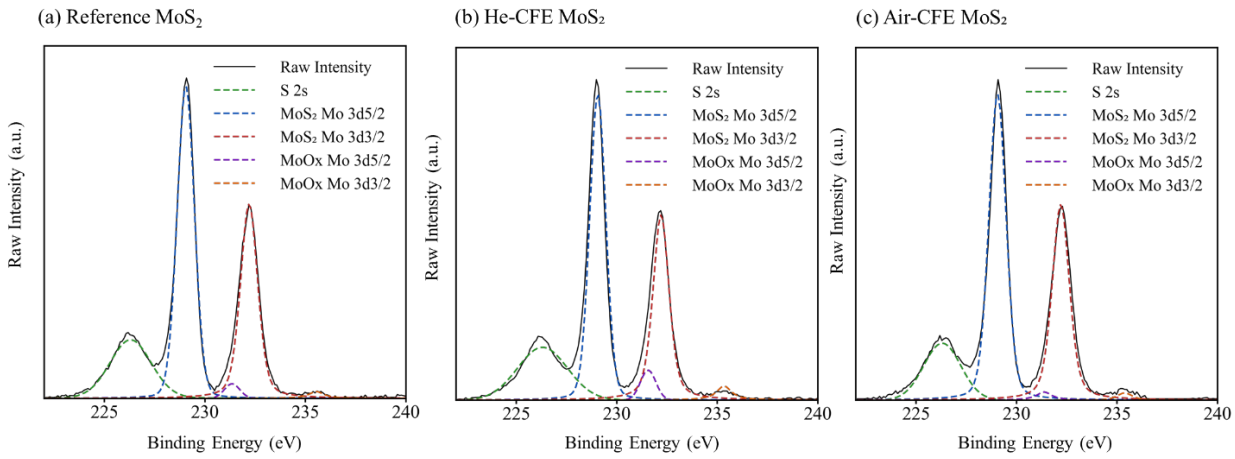

Figure 7.13**:** *High-resolution S 2s–Mo 3d XPS spectra and fitted components of (a) reference MoS_2, (b) He-CFE MoS_2, and (c) Air-CFE MoS_2.*

The high-resolution S 2p spectra are shown in ***Figure 7.14***, with the fitted sulfide and SO_x contributions summarized in ***Table 7.8*** to further confirm preservation of the MoS_2 sulfide structure. The reference sample shows the characteristic MoS_2 S $2p_{3/2}$–S $2p_{1/2}$ doublet at 161.91 eV and 163.11 eV. After CFE, the doublet remains nearly unchanged, appearing at 161.94/163.14 eV for Air-CFE MoS_2 and 161.84/163.04 eV for He-CFE MoS_2. These values are consistent with sulfur in the Mo–S bonding environment of 2H-MoS_2 [144, 155].

Table 7.8: *High-resolution S 2p deconvolution of reference and CFE-processed MoS_2 samples.*

Material	MoS_2 S $2p_{3/2}$ (%)	MoS_2 S $2p_{1/2}$ (%)	SO_x S $2p_{3/2}$ (%)	SO_x S $2p_{1/2}$ (%)
Reference MoS_2	66.30	33.70	—	—
He-CFE MoS_2	64.78	33.07	1.37	0.78
Air-CFE MoS_2	64.95	33.18	1.25	0.63

The S 2p spin-orbit separation remains approximately 1.20 eV for all samples, and the S $2p_{3/2}$:S $2p_{1/2}$ area ratio remains close to the expected 2:1 ratio. This confirms that the fitted S 2p doublet is physically consistent. The sulfide contribution remains strongly dominant in all samples, showing that sulfur remains primarily in the Mo–S bonding state after CFE.

A small oxidized sulfur contribution appears only after exfoliation. The reference sample shows no detectable SO_x component, while Air-CFE MoS_2 shows 1.88% total SO_x and He-CFE MoS_2 shows 2.15% total SO_x. These values indicate limited sulfur oxidation after CFE. Because the sulfide contribution remains above 97% of the fitted S 2p envelope in both exfoliated samples, CFE does not significantly oxidize or decompose the sulfur sublattice.

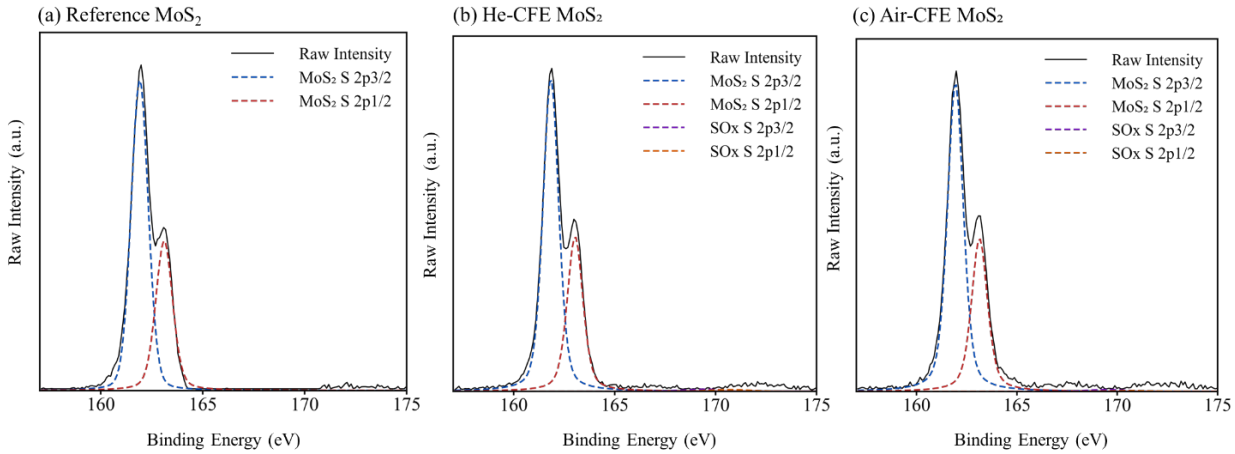

***Figure 7.14*:** *High-resolution S 2p XPS spectra and fitted components of (a) reference MoS_2, (b) He-CFE MoS_2, and (c) Air-CFE MoS_2.*

Comparison of Air-CFE and He-CFE shows that the carrier-gas effect on MoS_2 surface chemistry is measurable but mild. Both gases preserve the dominant MoS_2 Mo 3d and S 2p doublets, and neither gas produces clear evidence of a 2H-to-1T phase transformation. This indicates that CFE exfoliates MoS_2 mainly through mechanical forces without strongly altering the intrinsic MoS_2 phase. Air-CFE MoS_2 shows a MoS_2 Mo 3d contribution close to the reference sample and a small SO_x contribution in S 2p. He-CFE MoS_2 shows slightly higher MoO_x-related and SO_x contributions than Air-CFE MoS_2. This trend differs from h-BN, where air produced the stronger oxidation signature. For MoS_2, the final oxidation state appears to depend not only on carrier gas chemistry but also on the density of fresh edges and defect sites generated during exfoliation and on post-processing exposure to ambient air.

During CFE processing, MoS_2 particles experience rapid gas acceleration, drag, shear, interparticle collisions, wall impacts, and pressure-driven expansion. These forces can overcome weak interlayer interactions and expose fresh MoS_2 surfaces, edges, sulfur-vacancy-associated sites, and defect-rich regions. Once exposed, these sites may undergo limited oxidation or surface

modification during DI/IPA liquid collection, centrifugation/re-dispersion, drying, transfer, storage, or later ambient exposure, even if the exfoliation gas is helium. Therefore, helium provides an inert processing environment, but it does not necessarily prevent post-processing oxidation of newly exposed MoS_2 edges or defect sites. This explains why the slightly higher fitted MoO_x/SO_x contribution in He-CFE MoS_2 should not be interpreted as oxidation caused by helium itself.

Overall, the XPS results show that CFE preserves the primary MoS_2 lattice and does not cause a significant phase transformation. The S 2s-Mo 3d spectra remain dominated by the MoS_2 Mo $3d_{5/2}$-Mo $3d_{3/2}$ doublet at 229.05 and 232.20 eV, while the S 2p spectra remain dominated by the sulfide doublet near 162 and 163 eV. These peak positions are comparable to recent phase-preserving LPE MoS_2 studies, including sonication in suitable solvents, aqueous ammonia, and microwave-assisted liquid-phase exfoliation, where exfoliated nanosheets retain the 2H-MoS_2 chemical signature when phase transformation is avoided [156]. The present CFE samples therefore show the key advantage of physical exfoliation: they retain a predominantly 2H-MoS_2 XPS signature while avoiding liquid solvents, intercalants, and extensive chemical post-treatment.

This phase-preserving behavior is especially important when CFE is compared with chemical or ion-intercalation exfoliation routes. Such methods can intentionally or unintentionally generate metallic 1T/1T′ MoS_2 or MoS_{2-x}-like components, which appear at lower binding energies relative to semiconducting 2H-MoS_2 and require careful constrained peak fitting [144, 155]. In the present CFE spectra, no distinct lower-binding-energy 1T-MoS_2 doublet is observed, and the Mo-S and sulfide doublets remain dominant. The main chemical change after exfoliation is limited surface or edge oxidation, reflected by small MoO_x-related features in the Mo 3d region and minor SO_x components in the S 2p region. The difference between compressed air and helium is present but not severe: Air-CFE MoS_2 retains a strong MoS_2 doublet and shows only limited sulfur oxidation, while He-CFE MoS_2 shows slightly higher MoO_x-related and SO_x contributions. This should not be interpreted as oxidation by helium; a more reasonable explanation is that He-CFE exposes fresh edge or defect sites that oxidize during collection, transfer, storage, or subsequent air exposure. Therefore, compressed air remains a practical and lower-cost carrier gas for scalable MoS_2 exfoliation when mild surface oxidation is acceptable, while helium offers a controlled inert processing environment without fully eliminating post-processing oxidation.

7.4.4 Overall XPS Conclusion

Overall, the XPS results show that CFE introduces moderate surface or edge modification while largely preserving the dominant lattice bonding environments of Graphene, h-BN, and MoS_2. Across all three material systems, the main framework-related bonding states remain dominant after processing: graphitic carbon remains the principal contribution in Graphene, B–N/N–B bonding remains dominant in h-BN, and Mo–S/sulfide bonding remains dominant in MoS_2. Therefore, the XPS results support the interpretation that CFE is primarily a physical exfoliation process rather than a chemically destructive oxidation or conversion process.

At the same time, the XPS results show that CFE is not chemically invisible. Exfoliation increases accessible surface area and exposes fresh basal surfaces, edges, defects, and high-energy sites. However, the gas-phase exfoliation event occurs over a very short time scale during high-speed passage through the nozzle and immediate discharge into the collection medium. Therefore, the duration of direct carrier-gas exposure is limited compared with the subsequent liquid-phase recovery and ambient handling steps. Once generated, the fresh surfaces and edges remain available to interact with the DI/IPA collection medium, dissolved oxygen, moisture, and the ambient environment during centrifugation, re-dispersion, drying, transfer, and storage. For this reason, oxygen-containing components observed in the fitted XPS spectra should be interpreted as the combined result of rapid gas-phase exposure, material-specific surface chemistry, solvent-mediated interactions, and post-processing ambient exposure. They should not be attributed only to the carrier gas.

The Air-CFE versus He-CFE comparison is therefore material-dependent rather than universal. For Graphene, both CFE conditions increase oxygenated carbon relative to reference graphite, indicating the formation of additional surface or edge oxygen-containing sites after exfoliation. However, the total oxygenated C 1s contribution is very similar for Air-CFE and He-CFE Graphene. Thus, the Graphene data should not be interpreted as strong evidence that compressed air causes substantially greater oxidation than helium. The more meaningful gas-dependent difference is the preservation of graphitic bonding: He-CFE Graphene retains a slightly higher sp^2 contribution, whereas Air-CFE Graphene shows a slightly larger sp^3-related contribution. This suggests that helium better preserves the graphitic surface environment, while compressed air

produces somewhat stronger defect-, edge-, or adventitious-carbon-associated surface modification. Importantly, the moderate oxygenated carbon contribution does not justify describing the CFE product as Graphene oxide.

For h-BN, the gas-dependent oxygenation trend is the clearest. The B 1s and N 1s spectra remain dominated by B–N and N–B bonding, confirming that the primary boron nitride framework is retained after both Air-CFE and He-CFE. However, Air-CFE h-BN shows a stronger B–O contribution than He-CFE h-BN, together with a small N–C signal, a larger high-binding-energy C 1s component, and a broader O 1s envelope. These features indicate stronger oxygen-containing surface or edge modification in the air-processed sample. This should be interpreted as surface/edge oxygenation rather than bulk oxidation or decomposition of the h-BN lattice. A reasonable explanation is that CFE exposes boron-rich edges, defect sites, and high-energy surface regions that can form B–O, B–OH, or related oxygen-containing environments during compressed-air exposure, DI/IPA solvent collection, centrifugation/re-dispersion, drying, and subsequent ambient handling. Therefore, Among the three materials investigated, h-BN showed the clearest distinction between compressed-air and helium processing. Air-CFE h-BN exhibited a higher B–O contribution and a broader O 1s envelope than He-CFE h-BN, indicating stronger oxygen-containing boron surface environments. In contrast, the air–helium differences were small for Graphene and were not directionally consistent for MoS_2.

For MoS_2, the XPS results show a different trend. The S 2s–Mo 3d and S 2p regions remain dominated by the characteristic Mo–S and sulfide doublets, and the Mo $3d_{5/2}$ position near 229.05 eV is consistent with predominantly semiconducting 2H-MoS_2. The absence of a clear lower-binding-energy 1T-related doublet indicates that CFE does not produce a significant 2H-to-1T phase transformation detectable by XPS. The oxide-related components are small and should be interpreted as mild surface or edge oxidation rather than decomposition of the MoS_2 lattice. Unlike h-BN, MoS_2 does not follow a simple trend in which Air-CFE produces the highest oxide-related contribution. The slightly higher fitted MoO_x/SO_x contribution in He-CFE MoS_2 should not be interpreted as oxidation caused by helium, because helium is chemically inert. Instead, it likely reflects oxidation or surface modification of freshly exposed MoS_2 edges, sulfur-vacancy-associated sites, or defect-rich regions during liquid collection, re-dispersion, drying, storage, or ambient exposure.

Taken together, across Graphene, h-BN, and MoS_2, the XPS results show retention of the dominant bonding environments after CFE processing. The observed changes are limited mainly to material-specific surface and edge contributions, rather than extensive chemical transformation of the parent structures. Helium generally provides a more inert processing environment, while compressed air can promote oxygen-containing surface species when newly exposed edges or reactive sites are present. The final chemical response depends on carrier-gas identity together with precursor condition, material reactivity, and the amount of new surface area generated during exfoliation.

Because the exfoliation event is very rapid, while solvent collection and post-processing exposure last much longer, the final surface chemistry measured by XPS should be understood as the outcome of both CFE-generated fresh surfaces and subsequent solvent-mediated or ambient modification. This interpretation removes the apparent contradiction between the strong Air-CFE oxygenation observed for h-BN, the weaker Air/He difference observed for Graphene, and the weak, non-systematic oxide signal observed for MoS_2.

Although XPS confirms preservation of the dominant near-surface bonding environments, it does not directly evaluate layer-sensitive vibrational signatures or defect/edge-related Raman scattering. Raman spectroscopy was therefore used as a complementary structural probe to assess whether CFE-induced exfoliation changes the characteristic vibrational fingerprints of Graphene, h-BN, and MoS_2.

7.5 Structural Integrity and Exfoliation Quality (Raman)

Raman spectroscopy was used as a complementary structural characterization method to evaluate the crystalline quality, exfoliation state, and defect evolution of the CFE-produced 2D nanomaterials. This technique is especially useful for layered materials because Graphene, h-BN, and MoS_2 each have characteristic Raman-active vibrational modes that respond to changes in layer number, stacking order, strain, disorder, and chemical modification. Therefore, Raman spectroscopy provides information that is different from, but complementary to, electron microscopy and XPS. Electron microscopy directly reveals nanosheet morphology, lateral dimensions, wrinkles, folds, local thickness contrast, and lattice fringes, while XPS identifies near-surface chemical bonding and oxidation states. Raman spectroscopy connects these two forms of

evidence by confirming whether the parent lattice vibrational fingerprints are retained after exfoliation.

For Graphene, Raman interpretation is mainly based on the D, G, and 2D bands. The G band near 1580 cm^{-1} corresponds to the in-plane vibration of sp^2-bonded carbon atoms, while the D band near 1350 cm^{-1} is defect-activated and appears when the graphitic symmetry is disturbed by edges, finite flake size, vacancies, disorder, or other structural interruptions [148, 149, 150]. The 2D band near 2700 cm^{-1} is a second-order Raman feature that is highly sensitive to layer number, stacking order, and electronic band structure. Therefore, I_D/I_G, I_{2D}/I_G, and the 2D-band width are commonly used to evaluate defect/edge contribution, graphitic quality, and few-layer Graphene formation [150, 157]. However, I_D/I_G should not be interpreted only as basal-plane damage in exfoliated Graphene dispersions, because smaller lateral flake size and newly exposed edges can also increase the D-band intensity.

For MoS_2, Raman analysis is commonly based on the in-plane E_2g^1 mode and the out-of-plane A_1g mode. The separation between these two peaks changes with thickness because the two phonon modes respond differently as the number of layers decreases [151, 152, 153]. Therefore, the A_1g - E_2g^1 peak separation is widely used as a Raman indicator of MoS_2 layer reduction and exfoliation quality. For h-BN, the main Raman feature is the E_2g^1 phonon mode near 1366 cm^{-1}, which corresponds to in-plane B–N bond vibration . Changes in this peak position, intensity, and width can indicate thickness variation, strain, or disorder, although h-BN usually has a weaker Raman response than Graphene. For this reason, Raman interpretation for h-BN should be supported by TEM and XPS evidence rather than treated as a standalone conclusion [151, 152, 153].

7.5.1 Graphene

Figure 7.15 presents the Raman spectra of the graphite precursor and CFE-exfoliated Graphene samples. Two comparisons are included: **Figure 7.15(a)** shows the effect of cascade centrifugation for air-exfoliated Graphene, while **Figure 7.15(b)** compares the effect of different carrier gases. All spectra show the characteristic D, G, and 2D bands of graphitic carbon. The processed samples also show an increased D band compared with the graphite precursor, indicating that exfoliation introduces or exposes additional defect-activated scattering sites. However, for exfoliated Graphene nanosheets, the D band should not be interpreted only as basal-plane damage. Increased

I_D/I_G can also arise from smaller lateral dimensions and newly exposed edges after delamination, especially in dispersed or centrifuged Graphene nanosheets. Cançado et al. showed that I_D/I_G is linked to defect density and excitation energy [150], while Backes et al. showed that Raman metrics in liquid-exfoliated Graphene depend on both nanosheet lateral size and thickness [157].

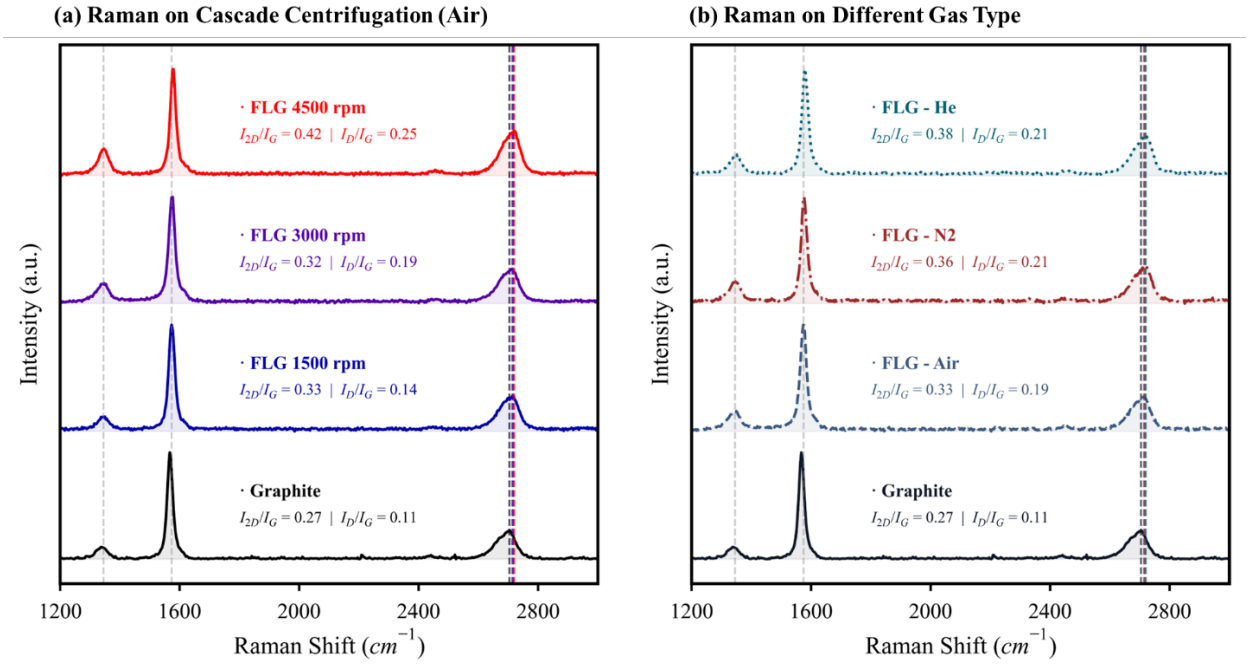

Figure 7.15: *Raman spectra of graphite and CFE-exfoliated Graphene. (a) Raman spectra of graphite and air-exfoliated Graphene fractions obtained after cascade centrifugation at 1500, 3000, and 4500 rpm. (b) Raman spectra of graphite and Graphene exfoliated using air, nitrogen, and helium carrier gases. Spectra are normalized to the G band and vertically offset for clarity. Dashed guide lines indicate the D, G, and 2D bands.*

The cascade centrifugation results in ***Figure 7.15(a)*** and ***Table 7.9*****Table 7.9:** Raman metrics for the cascade centrifugation series of air-exfoliated Graphene. show that I_{2D}/I_G increases from 0.27 for graphite to 0.33, 0.32, and 0.42 for the 1500, 3000, and 4500 rpm fractions, respectively. This increase indicates that CFE and subsequent centrifugation enrich the product in exfoliated Graphene-like nanosheets relative to the starting graphite. Among the centrifuged samples, the 4500 rpm fraction shows the highest I_{2D}/I_G, suggesting the strongest few-layer Graphene contribution. This trend is consistent with the use of centrifugation to separate dispersed

nanosheets according to size and thickness, where higher-speed fractions can become enriched in smaller or thinner nanosheets [157].

Table 7.9: *Raman metrics for the cascade centrifugation series of air-exfoliated Graphene.*

Material	I_D/I_G	I_{2D}/I_G	**2D FWHM cm⁻¹**
Graphite	0.11	0.27	76.15
Air 1500 rpm	0.14	0.33	78.50
Air 3000 rpm	0.19	0.32	73.65
Air 4500 rpm	0.25	0.42	74.63

At the same time, ***Table 7.9*** shows that I_D/I_G increases from 0.11 for graphite to 0.14, 0.19, and 0.25 for the 1500, 3000, and 4500 rpm fractions, respectively. This indicates a progressive increase in defect-activated Raman scattering after CFE and centrifugation. For exfoliated Graphene nanosheets, this increase should not be interpreted only as basal-plane damage. It can also arise from newly exposed edges, reduced lateral dimensions, finite crystallite size, and moderate mechanically induced disorder during delamination [157]. The continued presence of clear G and 2D bands indicates that the graphitic framework is retained rather than converted into amorphous carbon. This interpretation is consistent with TEM observations of finite, irregular nanosheet edges and with XPS evidence of increased sp^3/edge-associated and oxygenated surface contributions after CFE.

The carrier gas comparison in ***Figure 7.15(b)*** and ***Table 7.10*** shows that all CFE-processed samples have higher I_{2D}/I_G values than graphite. Air, nitrogen, and helium give I_{2D}/I_G values of 0.33, 0.36, and 0.38, respectively, compared with 0.27 for the graphite precursor. This confirms that CFE increases the few-layer Graphene Raman signature regardless of carrier gas. The differences among the gases are modest, but helium gives the highest I_{2D}/I_G value, followed by nitrogen and air, suggesting a slightly stronger layer-sensitive Raman response under inert processing.

The I_D/I_Gvalues in ***Table 7.10*** are 0.19, 0.21, and 0.21 for air, nitrogen, and helium, respectively.

This narrow range indicates that the carrier gas does not produce a large difference in defect/edge-related D-band intensity. Therefore, the gas-dependent Raman trend should be described as moderate, all gases generate Graphene-rich few-layer signatures, while helium and nitrogen show slightly higher I_{2D}/I_G than air without a substantial increase in I_D/I_G. This interpretation is consistent with XPS, where all processed Graphene samples remain dominated by graphitic carbon, but Air-CFE shows slightly stronger sp^3/edge-associated and oxygenated surface contributions than He-CFE.

Table 7.10: *Raman metrics for Graphene exfoliated using different carrier gases.*

Material	I_D/I_G	I_{2D}/I_G	**2D FWHM cm⁻¹**
Graphite	0.11	0.27	76.15
Air exfoliated	0.19	0.33	74.73
N_2 exfoliated	0.21	0.36	73.61
He exfoliated	0.21	0.38	73.73

The 2D-band FWHM values listed in ***Table 7.9*** and ***Table 7.10*** remain broad, approximately 73–79 cm^{-1}, across both comparisons. Together with $I_{2D}/I_G < 1$, this indicates that the CFE products should not be described as predominantly monolayer Graphene. A sharper and more symmetric 2D band is generally associated with monolayer Graphene, while broader 2D features are expected for few-layer Graphene, multilayer Graphene, and exfoliated graphitic nanosheets because of stacking effects, layer distribution, and interlayer electronic coupling [148, 149]. Therefore, the Raman data in **Figure 7.15** and the quantitative metrics in Tables 7.9 and 7.10 support the formation of few-layer Graphene-rich nanosheets rather than isolated monolayer Graphene.

The Raman results correlate well with the other characterization methods in this chapter. The retained G and 2D bands in **Figure 7.15** agree with the TEM/STEM/HRTEM observations, where CFE-produced Graphene is described as sheet-like, flexible, semi-transparent, wrinkled, folded, and laterally continuous with preserved graphitic lattice features. The increased I_D/I_G values in ***Table 7.9*** and ***Table 7.10*** are also consistent with the irregular edges and finite lateral dimensions

observed by electron microscopy. Similarly, the Raman trends agree with the XPS results, and preservation of graphitic sp^2 carbon is consistent with the retained G and 2D bands, while increased sp^3 and oxygenated surface components are consistent with the stronger D-band response after processing.

Overall, Raman spectroscopy shows that CFE converts graphite into few-layer Graphene-rich nanosheets while largely preserving the graphitic sp^2 framework. The main spectral changes are increased layer-sensitive 2D-band response, increased exposed-edge/defect-related D-band scattering, and broad 2D-band features characteristic of few-layer or multilayer graphitic nanosheets. When combined with electron microscopy and XPS, these results indicate that CFE causes delamination and moderate edge/surface modification rather than complete amorphization or severe destruction of the graphitic lattice.

7.5.2 Hexagonal Boron Nitride (h-BN)

Figure 7.16 presents the Raman spectra of the h-BN precursor and CFE-exfoliated h-BN samples. ***Figure 7.16(a)*** shows the cascade centrifugation series for air-exfoliated h-BN, while ***Figure 7.16(b)*** compares the effect of carrier gas type. All spectra show one dominant Raman peak near 1366–1368 cm^{-1}, corresponding to the in-plane E_{2g} vibrational mode of h-BN. This peak is the primary Raman fingerprint of h-BN and confirms that the characteristic B–N lattice vibration remains present after CFE processing [152, 153]. Unlike Graphene, h-BN does not show a D/G/2D band system; therefore, the interpretation is based mainly on the E_{2g} peak position, peak width, and preservation of a single well-defined Raman mode [158].

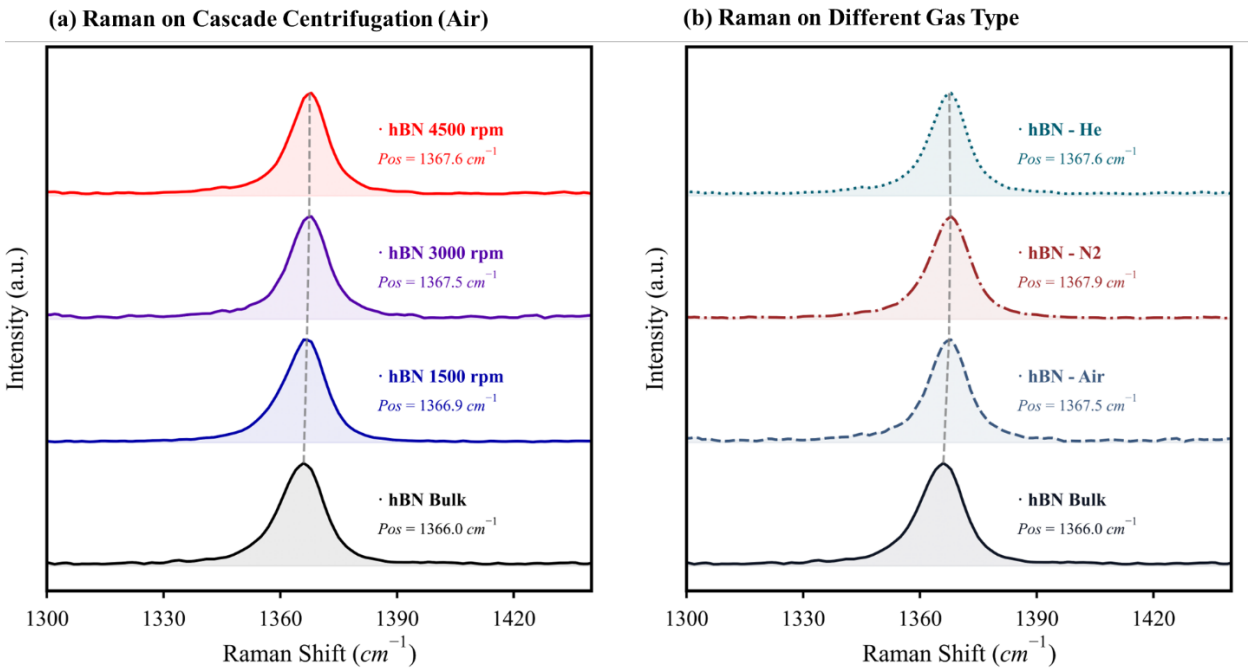

Figure 7.16: *Raman spectra of bulk h-BN and CFE-exfoliated h-BN. (a) Raman spectra of bulk h-BN and air-exfoliated h-BN fractions obtained at different centrifugation speed of 1500, 3000, and 4500 rpm. (b) Raman spectra of bulk h-BN and h-BN exfoliated using air, nitrogen, and helium carrier gases. Spectra are vertically offset for clarity. The dashed guide line identifies the E_{2g} Raman mode of h-BN near 1366–1368 cm^{-1}.*

Table 7.11: *Raman metrics for the cascade centrifugation series of air-exfoliated h-BN.*

Material	E_{2g} position (cm^{-1})	Shift from bulk (cm^{-1})	E_{2g} FWHM (cm^{-1})
h-BN bulk	1366.04	0.00	13.62
h-BN 1500 rpm	1366.86	+0.82	12.98
h-BN 3000 rpm	1367.46	+1.42	11.90
h-BN 4500 rpm	1367.56	+1.52	11.56

The results for different centrifugation speed in ***Figure 7.16(a)*** and ***Table 7.11*** show that the E_{2g} peak remains clearly visible for all centrifuged h-BN fractions. The peak position shifts from 1366.04 cm^{-1} for bulk h-BN to 1366.86, 1367.46, and 1367.56 cm^{-1} for the 1500, 3000, and 4500 rpm fractions, respectively. These shifts are small, with the maximum upshift being +1.52 cm^{-1} for the 4500 rpm fraction. Previous Raman studies report the characteristic h-BN E_{2g} mode near 1366 cm^{-1} and show that small shifts can arise from reduced thickness, local strain, substrate interaction, or surface environment [152, 153]. Therefore, the observed upshift should not be treated as a direct standalone measurement of layer number. Instead, it indicates that the local vibrational environment of h-BN changes after CFE and centrifugation while the main B–N lattice fingerprint remains preserved.

The E_{2g} FWHM values in ***Table 7.11*** decrease from 13.62 cm^{-1} for bulk h-BN to 12.98, 11.90, and 11.56 cm^{-1} for the 1500, 3000, and 4500 rpm fractions, respectively. This progressive narrowing suggests that higher-speed centrifugation isolates a more refined or more uniform h-BN nanosheet population. Since exfoliated h-BN Raman spectra are generally dominated by a single Raman line, peak width is a useful supporting indicator of changes in nanosheet population, thickness distribution, and structural uniformity [158]. In the present CFE samples, the narrowest peak occurs for the 4500 rpm fraction, suggesting the most clearly defined E_{2g} response among the centrifuged air-processed samples.

Table 7.12: *Raman metrics for h-BN exfoliated using different carrier gases.*

Material	**E_{2g} position (cm^{-1})**	**Shift from bulk (cm^{-1})**	**E_{2g} FWHM (cm^{-1})**
h-BN bulk	1366.04	0.00	13.62
h-BN Air	1367.46	+1.42	11.90
h-BN N_2	1367.86	+1.82	12.38
h-BN He	1367.56	+1.52	11.56

The carrier gas comparison in ***Figure 7.16(b)*** and ***Table 7.12*** shows that the E_{2g} peak remains present for all CFE-processed h-BN samples. Air-, nitrogen-, and helium-CFE h-BN show peak positions of 1367.46, 1367.86, and 1367.56 cm^{-1}, respectively, compared with 1366.04 cm^{-1} for bulk h-BN. These small upshifts confirm that CFE changes the local vibrational environment of h-BN, while the persistence of a single dominant E_{2g} peak confirms that the B–N lattice vibration is retained. Among the gas-processed samples, nitrogen shows the largest peak shift, followed by helium and air. Because the h-BN Raman peak position can be influenced by strain, local environment, and thickness distribution, these differences should be interpreted as gas-dependent changes in the local vibrational environment rather than as a direct layer-number ranking.

The FWHM values in ***Table 7.12*** show that the gas-processed samples all have narrower E_{2g} peaks than the bulk h-BN reference. The bulk h-BN peak has a FWHM of 13.62 cm^{-1}, while air-, nitrogen-, and helium-CFE h-BN show FWHM values of 11.90, 12.38, and 11.56 cm^{-1}, respectively. The narrowest peak is observed for the helium-processed sample, suggesting the most uniform or most sharply defined h-BN vibrational response among the gas-type samples. The nitrogen-processed sample shows the largest peak shift but a slightly broader peak than helium, indicating that peak position and peak width should be interpreted together rather than independently.

The h-BN Raman results correlate well with the XPS results. XPS shows that CFE-processed h-BN remains dominated by B–N and N–B bonding, confirming preservation of the main boron nitride framework after exfoliation. At the same time, the XPS results show stronger oxygen-containing surface chemistry for air-assisted CFE compared with helium-assisted CFE. This is consistent with the Raman observation that helium gives the narrowest E_2g peak, suggesting a more sharply defined h-BN vibrational response in the measured sample. However, because h-BN Raman peak width can also be influenced by thickness distribution, strain, and sample deposition, the Raman result should be interpreted together with XPS rather than as independent proof of chemical purity. Together, Raman and XPS indicate that CFE preserves the main B-N lattice while introducing mild gas-dependent surface or edge modification.

The Raman results also agree with the electron microscopy observations. TEM/STEM/HRTEM show that CFE-exfoliated h-BN forms thin elongated nanosheets with preserved lattice ordering. These observations support the Raman conclusion that CFE causes exfoliation and local structural

or environmental changes without destroying the h-BN lattice. If the process had severely amorphized the material, the E_{2g} peak would be expected to become strongly broadened, weakened, or poorly defined. Instead, **Figure 7.16** shows a clear h-BN Raman fingerprint for all processed samples.

Overall, the results show that CFE-processed h-BN retains the characteristic E_{2g} Raman mode near 1366–1368 cm^{-1}. The main Raman changes after CFE are a modest upshift of the E_{2g} peak and a narrowing of the peak width compared with the bulk reference. These results indicate that CFE modifies the local vibrational environment of h-BN through exfoliation, thickness redistribution, strain, and edge or surface exposure, while largely preserving the B–N crystalline framework. When combined with XPS and electron microscopy, the Raman results support the conclusion that CFE produces h-BN nanosheet-rich fractions rather than amorphized or chemically destroyed boron nitride.

7.5.3 Molybdenum Disulfide (MoS_2)

Figure 7.17 presents the Raman spectra of the MoS_2 precursor and CFE-exfoliated MoS_2 samples. Two comparisons are included: **Figure 7.17(a)** shows the effect of cascade centrifugation for air-exfoliated MoS_2, while **Figure 7.17(b)** compares the effect of different carrier gases. All spectra show the two characteristic high-frequency Raman modes of MoS_2, the in-plane E_2g^1 mode and the out-of-plane A_1g mode. These two peaks are the most used Raman markers for evaluating MoS_2 layer reduction, because their separation decreases as MoS_2 changes from bulk toward few-layer or monolayer thickness [151]. Therefore, the peak separation, defined here as $\Delta = A_1g - E_2g^1$, was used as the main Raman metric for evaluating the exfoliation state of the CFE-processed MoS_2.

The presence of both E_2g^1 and A_1g peaks after CFE indicates that the characteristic MoS_2 lattice vibration is preserved after processing. This is important because CFE is intended to delaminate MoS_2 into thinner nanosheets without destroying the crystalline basal-plane structure. The Raman spectra also provide evidence for the structural phase of the CFE-processed MoS_2. As shown in **Figure 7.17**, all spectra are dominated by the characteristic E_2g^1 and A_1g vibrational modes of MoS_2, with no additional abnormal Raman features appearing in the measured 350–430 cm^{-1} region. These two modes are the expected high-frequency Raman fingerprint of semiconducting

2H-MoS_2, and their persistence after CFE indicates that the MoS_2 lattice structure is retained after exfoliation [151]. The reduction in E_2g^1–A_1g separation after CFE further supports thickness reduction toward few-layer MoS_2, rather than a phase transformation. Therefore, the combined Raman and XPS evidence supports the conclusion that the CFE-processed MoS_2 remains predominantly 2H-MoS_2, while acknowledging that high-frequency Raman spectra alone cannot exclude a trace 1T/1T′ contribution

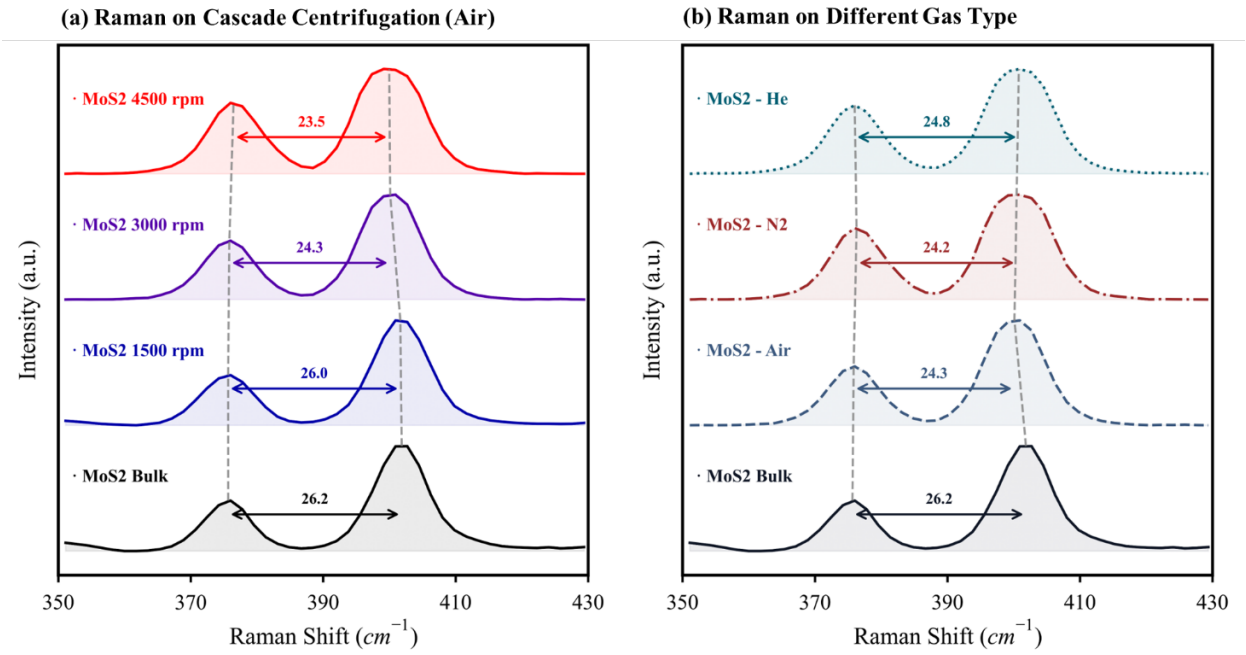

Figure 7.17: *Raman spectra of bulk MoS_2 and CFE-exfoliated MoS_2. (a) Air-exfoliated MoS_2 fractions obtained after cascade centrifugation at 1500, 3000, and 4500 rpm. (b) MoS_2 exfoliated using air, nitrogen, and helium carrier gases. The arrows show $\Delta = A_1g - E_2g^1$, which decreases after CFE and provides evidence of layer reduction or enrichment of few-layer MoS_2 nanosheets.*

Table 7.13: *Raman metrics for the cascade centrifugation series of air-exfoliated MoS_2.*

Material	**E_2g^1 position (cm^{-1})**	**A_1g position (cm^{-1})**	**$\Delta = A_1g - E_2g^1$ (cm^{-1})**
MoS_2 bulk	375.65	401.85	26.21
MoS_2 1500 rpm	375.64	401.64	26.01

Material	E_2g^1 position (cm^{-1})	A_1g position (cm^{-1})	$\Delta = A_1g - E_2g^1$ (cm^{-1})
MoS_2 3000 rpm	375.83	400.11	24.28
MoS_2 4500 rpm	376.46	399.98	23.51

The different speed centrifugation results in ***Figure 7.17(a)*** and ***Table 7.13*** show a clear decrease in the E_2g^1–A_1g peak separation after CFE and centrifugation. The bulk MoS_2 precursor has a separation of 26.21 cm^{-1}. The 1500 rpm fraction remains very close to the bulk value, with a separation of 26.01 cm^{-1}, suggesting that this fraction still contains a large bulk-like or thicker MoS_2 contribution. In contrast, the 3000 rpm and 4500 rpm fractions show lower separations of 24.276 and 23.513 cm^{-1}, respectively. This reduction indicates stronger exfoliation and a shift toward thinner/few-layer MoS_2 nanosheets. The 4500 rpm fraction shows the lowest separation, suggesting that it contains the strongest few-layer MoS_2 contribution among the centrifuged air-processed samples.

This trend agrees with the expected role of speed in centrifugation. In liquid-processed 2D materials, iterative centrifugation can separate nanosheets according to size and thickness, allowing different fractions to become enriched in thinner or smaller nanosheets [16]. In the present MoS_2 results, the gradual reduction in Δ from bulk to the higher-speed centrifuged fractions suggests that centrifugation helps enrich the dispersion in thinner MoS_2 sheets after CFE.

The peak positions also provide useful supporting evidence. From bulk MoS_2 to the 4500 rpm fraction, the E_2g^1 mode shifts slightly upward from 375.645 to 376.462 cm^{-1}, while the A_1g mode shifts downward from 401.850 to 399.976 cm^{-1}. This opposite movement of the two modes is consistent with the known thickness-sensitive behavior of MoS_2 Raman modes, where the E_2g^1 and A_1g modes respond differently as the number of layers decreases [151]. The FWHM values also increase modestly after processing, especially for the A_1g mode, which increases from 9.701 cm^{-1} for bulk MoS_2 to 12.176 cm^{-1} for the 4500 rpm fraction. This broadening may reflect a distribution of nanosheet thicknesses, local strain, edge effects, or mild disorder introduced during exfoliation. Importantly, the peaks remain well defined, indicating that CFE does not severely amorphize the MoS_2 structure.

Table 7.14: *Raman metrics for MoS_2 exfoliated using different carrier gases.*

Material	E_2g^1 position (cm^{-1})	A_1g position (cm^{-1})	$\Delta = A_1g - E_2g^1$ (cm^{-1})
MoS_2 bulk	375.65	401.85	26.21
MoS_2 Air exfoliated	375.83	400.11	24.28
MoS_2 N_2 exfoliated	376.28	400.44	24.17
MoS_2 He exfoliated	375.98	400.77	24.79

The carrier gas comparison in ***Figure 7.17(b)*** and ***Table 7.14*** shows that all gas-processed MoS_2 samples have lower E_2g^1–A_1g separation than the bulk precursor. The separation decreases from 26.205 cm^{-1} for bulk MoS_2 to 24.276, 24.166, and 24.792 cm^{-1} for air-, nitrogen-, and helium-processed MoS_2, respectively. This confirms that CFE produces a Raman response consistent with few-layer MoS_2 under all three carrier gases. However, unlike the cascade centrifugation series, the differences between the gas-processed samples are small. Air and nitrogen are almost identical, with separations of 24.276 and 24.166 cm^{-1}, while helium is only slightly higher at 24.792 cm^{-1}. Therefore, the Raman results do not show a strong carrier-gas-dependent difference in MoS_2 layer reduction. The main conclusion is that all three gases produce broadly similar few-layer MoS_2 Raman signatures.

The A_1g peak broadening in ***Table 7.14*** is also similar for the gas-processed samples. The A_1g FWHM increases from 9.701 cm^{-1} for bulk MoS_2 to 10.854, 12.271, and 12.125 cm^{-1} for air, nitrogen, and helium, respectively. This broadening is consistent with exfoliation-induced thickness distribution, local strain, and increased edge/surface contribution. The nitrogen and helium samples have similar A_1g FWHM values, and their E_2g^1 FWHM values are also close. Therefore, Raman does not provide strong evidence that one gas produces a dramatically different MoS_2 structural quality than the others. The gas comparison should be described as broadly similar, with all gases preserving the MoS_2 Raman fingerprint while reducing the E_2g^1–A_1g separation relative to bulk.

The Raman results correlate well with the electron microscopy observations. TEM/STEM/HRTEM show that CFE-exfoliated MoS_2 forms laterally extended nanosheets with compact plate-like morphology, irregular edges, visible thickness contrast, and preserved lattice fringes. These microscopy observations support the Raman interpretation that CFE causes delamination and thickness reduction while maintaining crystalline MoS_2 domains. If the process had mainly amorphized or chemically destroyed the MoS_2 structure, the E_2g^1 and A_1g modes would be expected to become poorly defined or strongly distorted. Instead, **Figure 7.17** shows clear MoS_2 Raman modes for all processed samples.

The Raman results are also consistent with XPS. XPS provides chemical-state information, while Raman provides vibrational and thickness-sensitive structural information. The retention of MoS_2-like E_2g^1 and A_1g modes agrees with XPS evidence that the processed samples remain dominated by Mo–S bonding. At the same time, the modest Raman broadening and peak shifts are consistent with exfoliation-induced thickness redistribution, exposed edges, and local strain rather than severe phase transformation or complete oxidation. Therefore, the combined Raman, XPS, and electron microscopy results indicate that CFE converts bulk MoS_2 into few-layer-rich nanosheet fractions while largely preserving the crystalline MoS_2 framework.

Overall, Raman spectroscopy shows that CFE reduces the E_2g^1-A_1g separation of MoS_2 from the bulk value of approximately 26.21 cm^{-1} to values between 23.51 and 24.79 cm^{-1} after exfoliation, depending on centrifugation fraction and carrier gas. The centrifugation series gives the clearest thinning trend, with the 4500 rpm fraction showing the lowest separation and therefore the strongest few-layer MoS_2 signature. The gas comparison shows that air, nitrogen, and helium all produce broadly similar few-layer MoS_2 Raman responses, with only minor differences among the gases. The retention of clear E_2g^1 and A_1g modes supports preservation of the MoS_2 vibrational fingerprint, while XPS confirms that the Mo 3d and S 2p regions remain dominated by Mo-S and sulfide bonding without a clear 1T-related lower-binding-energy Mo 3d doublet. Therefore, the combined Raman, XPS, and electron microscopy evidence supports the conclusion that CFE produces MoS_2 nanosheet-rich fractions while preserving predominantly 2H-MoS_2.

7.6 Integrated Characterization Summary

This chapter evaluated the morphology, near-surface chemistry, and structural integrity of Graphene, h-BN, and MoS_2 produced under the optimized CFE conditions. The combined TEM/STEM/HRTEM, XPS, and Raman results show that CFE produces nanosheet-rich materials while preserving the dominant structural and chemical fingerprints of each parent layered crystal. Therefore, the optimized CFE conditions identified in Chapter 6 improve recoverable output without causing severe amorphization, extensive oxidation, or major phase transformation.

Electron microscopy confirmed that CFE produces sheet-like or platelet-like nanosheets rather than only pulverized debris. Graphene appeared as broad, flexible, wrinkled sheets with visible graphitic lattice features. h-BN formed thin, elongated nanosheets with preserved local lattice contrast, while MoS_2 showed compact platelet-like nanosheets with clear lattice fringes. Representative TEM-based dimensional analysis showed lateral dimensions in the hundreds-of-nanometers to near-micrometer range for all three materials. These measurements should be interpreted as representative image-based dimensions rather than a full statistical flake-size distribution; nevertheless, they support the conclusion that CFE promotes delamination while retaining useful lateral size.

XPS analysis showed that the dominant bonding environments of all three materials were retained after CFE, with moderate gas-dependent surface and edge modification. For Graphene, the C 1s spectra remained dominated by graphitic sp^2 carbon, while the increased sp^3/edge-associated and oxygenated carbon contributions indicated moderate surface modification after exfoliation. Helium better preserved the sp^2-rich graphitic surface environment, whereas compressed air produced slightly stronger defect/oxygenated contributions. For h-BN, the B 1s and N 1s spectra remained dominated by B-N and N-B bonding, confirming preservation of the boron nitride framework. Air-CFE produced a stronger B-O and broader O 1s response, indicating greater oxygen-containing surface or edge chemistry than He-CFE. For MoS_2, the S 2s-Mo 3d and S 2p regions remained dominated by Mo-S and sulfide doublets, with only minor MoO_x and SO_x contributions. The Mo 3d peak position and absence of a clear lower-binding-energy 1T-related doublet support the conclusion that the CFE-processed MoS_2 remains predominantly 2H-MoS_2. Raman spectroscopy provided complementary evidence of structural preservation and exfoliation.

For Graphene, the retained G and 2D bands confirm preservation of the graphitic framework, while increased I_D/I_G is consistent with exposed edges, reduced lateral dimensions, and moderate disorder introduced during delamination. The broad 2D-band widths and modest I2D/I_G values indicate few-layer Graphene-rich nanosheets rather than isolated monolayer Graphene. For h-BN, the persistence of a single E_2g peak near 1366-1368 cm^{-1} confirms retention of the characteristic B-N lattice vibration, while small peak shifts and FWHM changes indicate changes in local vibrational environment, thickness distribution, strain, or surface condition after exfoliation. For MoS_2, the reduced E_2g^1-A_1g separation, especially in the higher-speed centrifuged fractions, supports enrichment in thinner/few-layer MoS_2 nanosheets while retaining the characteristic 2H-MoS_2 vibrational fingerprint.

Overall, the results demonstrate that CFE is a mechanically effective and chemically moderate exfoliation route for multiple layered materials. The process generates nanosheet-rich fractions through gas-driven delamination while avoiding severe structural damage, extensive chemical oxidation, or major phase transformation that would limit material performance. Compressed air provides a practical and lower-cost carrier gas for scalable production when moderate surface modification is acceptable, whereas helium provides a more inert processing environment when preservation of native graphitic or h-BN surface chemistry is prioritized. These findings establish the material-quality basis for the scale-up and application-oriented development of CFE discussed in Chapter 8.

Chapter 8: Conclusion and Future Work

8.1 Summary of Research Objectives

The overarching objective of this thesis was to investigate CFE as a gas-driven, scalable, and chemically mild route for producing two-dimensional (2D) nanomaterials. This work was motivated by a central challenge in the 2D materials field: although materials such as Graphene, h-h-BN, and molybdenum disulfide (MoS_2) possess exceptional mechanical, thermal, electrical, optical, and chemical properties, their widespread use remains limited by the lack of production methods that can simultaneously provide scalability, acceptable material quality, process simplicity, and reduced chemical dependency. Previous CFE studies demonstrated promising exfoliation performance using helium as the carrier gas, mainly because helium can reach very high gas velocities during compressible expansion. However, helium is relatively expensive and less practical for large-scale industrial operation. Therefore, an important motivation of this thesis was to determine whether CFE could be redesigned and optimized to use more accessible carrier gases, particularly nitrogen and compressed air, without sacrificing exfoliation performance. In this context, the thesis focused on developing a deeper mechanistic and experimental understanding of how pressure, gas velocity, gas type, particle entrainment, preheating, and post-processing recovery influence the output of CFE as a potential alternative production platform.

The first research objective was to establish the fundamental exfoliation mechanism in CFE and identify how the key flow parameters influence layer separation. This objective was addressed through a multiscale modelling framework. At the continuum scale, compressible-flow analysis was used to examine velocity, Mach number, density, shock formation, relative particle–gas motion, drag force, and cumulative work on suspended particles inside the nozzle. At the atomistic scale, molecular dynamics simulations were used to study how gas velocity, pressure, temperature, gas type, sheet size, layer number, and defect concentration affect the motion and separation of Graphene layers. Together, these analyses were designed to connect the macroscopic gas expansion process to nanoscale exfoliation energetics.

The second objective was to experimentally validate and optimize the CFE process. This involved reconstructing and validating the CFE apparatus using h-BN as a model material, then

systematically studying the influence of controllable operating parameters such as starting particle size, upstream pressure, carrier gas, gas preheating, initial material loading, and post-processing recovery. A particular focus was placed on determining whether low-cost carrier gases such as nitrogen and compressed air could become effective when the thermal and aerodynamic conditions of the process were improved. This objective also included the development of concentration, recovered mass, yield, and short-burst production-intensity metrics to evaluate the process beyond qualitative dispersion appearance.

The third objective was to characterize the physical and chemical features of CFE-produced 2D nanomaterials and assess whether the optimized process preserves the structural identity of the parent layered crystals. This was addressed by applying the optimized CFE condition to three representative materials: conductive Graphene, insulating h-BN, and semiconducting MoS_2. The resulting products were characterized using electron microscopy, X-ray photoelectron spectroscopy, Raman spectroscopy, UV–Vis spectroscopy, and representative dimensional analysis. This objective was essential for determining whether improved output was achieved at the expense of severe oxidation, amorphization, phase transformation, or excessive fragmentation. The results also provide the material-quality basis required for future application-oriented demonstrations in composites, coatings, membranes, inks, and other nano-enabled systems.

Overall, the thesis aimed to connect mechanism, process optimization, and product characterization into one coherent framework. Rather than treating CFE only as an empirical exfoliation method, this work sought to explain why the process works, which operating parameters control its performance, how the recovered output can be improved, and whether the resulting nanosheets retain the structural and chemical features required for practical use.

8.2 Major Contributions of the Thesis

The major finding of this thesis is that CFE is not simply a high-pressure powder dispersion process, but a coupled thermomechanical exfoliation mechanism controlled by gas expansion, particle acceleration, aerodynamic shear, interlayer energy barriers, and post-processing recovery. The thesis progressively developed this understanding by moving from a macroscopic continuum description of the gas flow to atomistic simulations of gas–Graphene interactions, to energy-based molecular dynamics analysis of exfoliation pathways, and finally to experimental validation and

material characterization. This sequential approach was necessary because no single modelling or experimental method could fully capture the multiscale nature of CFE. The continuum analysis identified the dominant flow parameters, the atomistic simulations explained how these parameters influence molecular-scale motion and energy transfer, the energy-based analysis quantified the energetic feasibility of layer separation, and the experimental chapters validated whether these mechanisms could be translated into measurable nanosheet production.

At the macroscopic level, the continuum flow analysis showed that the CFE nozzle generates the flow environment required for exfoliation by converting high-pressure gas energy into high gas velocity, rapid acceleration, large velocity gradients, and strong particle–gas momentum transfer. The quasi-one-dimensional compressible-flow analysis demonstrated that helium reaches substantially higher velocities and Mach numbers than nitrogen under comparable conditions, mainly because of its lower molecular weight and higher speed of sound. Nitrogen produced lower velocities, but the analysis also showed that pressure and nozzle conditions strongly affect the location of shock formation, the residence distance before the shock, and the aerodynamic forces acting on particles. Therefore, the continuum model established velocity, pressure, gas type, density, drag force, and cumulative work as the key process variables that control CFE performance.

An important outcome of the continuum analysis was that the shock wave alone should not be treated as the only exfoliation source. Instead, the strongest exfoliation-relevant interactions arise from the high-velocity acceleration region where particles experience intense relative motion with respect to the gas stream. The force analysis showed that drag force, aerodynamic shear, and particle acceleration can generate sufficient mechanical work to promote layer separation when the local flow conditions exceed a threshold. This finding changed the interpretation of CFE from a shock-dominated process to an acceleration- and shear-dominated process. It also provided the physical basis for selecting the most important parameters for the next modelling stage, gas velocity, gas pressure, gas temperature, gas type, and gas density.

Because continuum modelling cannot directly show how gas molecules interact with layered crystals, the thesis then moved to atomistic molecular dynamics simulations. This second modelling level was used to examine how the flow parameters affect Graphene layer motion, atomic fluctuation, energy transfer, and interlayer weakening. The atomistic simulations showed

that increasing gas velocity increases the kinetic energy delivered to the Graphene surface, leading to stronger sheet fluctuation, larger sliding displacement, and greater disruption of interlayer van der Waals interactions. This finding directly linked the macroscopic velocity field from the nozzle-scale analysis to the nanoscale physical response of the layered material.

The atomistic simulations also clarified the roles of pressure and temperature. Increasing pressure raised the number of gas–surface collisions, which increased the total energy transferred from the gas phase to the Graphene layers. Increasing temperature enhanced atomic vibration and thermal activation of the Graphene sheets, reducing the effective resistance to layer separation. This is a key mechanistic finding because it explains why gas preheating can compensate for the lower velocity of nitrogen and compressed air compared with helium. In other words, helium is effective because it provides very high gas velocity, but nitrogen and air can become effective when the process is modified to add thermal energy and increase the thermo-kinetic contribution to exfoliation.

The gas-type comparison further showed that CFE performance depends on a balance between gas velocity and momentum transfer. Light gases such as helium can reach high velocities and generate strong kinetic interaction with the layered material. Heavier gases can transfer higher momentum per collision, but their lower attainable velocity can limit their exfoliation effectiveness if they are not sufficiently accelerated or thermally activated. This finding is important for scale-up because helium is costly and less attractive for large-scale industrial production. The atomistic results therefore supported the thesis direction of moving beyond helium and optimizing the process for more accessible carrier gases such as nitrogen and compressed air.

However, direct atomistic simulation of the entire CFE process is not computationally feasible. The real process involves a large number of particles, turbulent compressible gas flow, collisions, nozzle-wall interactions, particle entrainment, and complete exfoliation events over length and time scales far beyond conventional molecular dynamics. Therefore, after identifying how gas conditions affect molecular motion, the thesis moved to an energy-based analysis to quantify the energetic feasibility of layer separation. This step provided a bridge between molecular-scale interaction and actual exfoliation by calculating the potential of mean force and the energy barriers associated with different separation pathways.

The energy-based analysis showed that CFE can promote exfoliation through both lateral sliding and edge-peeling pathways. Lateral sliding is directly aligned with the direction of gas flow and is promoted by aerodynamic shear acting across the exposed sheet. Edge peeling becomes favorable when gas molecules interact with an exposed edge and progressively separate the upper layer from the lower layers. The potential of mean force results showed that increasing gas velocity, pressure, density, and temperature lowers the effective energetic resistance to exfoliation, especially for peeling-assisted separation. This confirmed that the flow parameters identified at the continuum scale and examined at the atomistic scale are not only descriptive variables, they directly influence the free-energy barrier for delamination.

The energy-based simulations also showed that sheet geometry and material imperfections affect CFE behavior. Larger sheets, multilayer stacks, and defective structures interact differently with the gas flow because they present different exposed areas, edge sites, and interlayer resistance. Defects can reduce the cohesive barrier and create localized regions where gas momentum transfer more easily initiates delamination. This finding is scientifically important because real exfoliation does not occur in ideal, defect-free, perfectly aligned crystals. The energy-based analysis therefore provided a more realistic mechanistic explanation for why CFE can exfoliate actual powder precursors, where particle size, edge density, defects, and layer number all influence the final output.

The experimental work then tested whether these modelling findings could be translated into a practical CFE process. The reconstructed system was first validated using h-BN, where helium produced much higher exfoliation performance than nitrogen under the initial condition. This result was consistent with the continuum and atomistic predictions that helium benefits from high gas velocity. However, the experimental goal of this thesis was not only to repeat helium-based CFE, but to determine whether the process could be modified to use more practical gases. Based on the modelling results, gas preheating was introduced as a key process modification to increase the thermo-kinetic contribution to exfoliation and improve the performance of nitrogen and compressed air.

The experimental optimization confirmed that gas preheating was one of the most important improvements in the modified CFE system. By adding thermal energy upstream of the nozzle, the process increased gas temperature, promoted stronger particle–gas interaction, and reduced the

energetic resistance to layer separation. This allowed nitrogen and compressed air, which are cheaper and more accessible than helium, to become effective carrier gases for producing 2D nanosheets. For h-BN processed using nitrogen, optimization of particle size, pressure, raw-material loading, and gas heating increased the recovered concentration from approximately 0.003 $g \cdot L^{-1}$ in the initial low-performing condition to approximately 0.155 $g \cdot L^{-1}$ under the optimized nitrogen-based CFE condition using a 200 mL collection volume. This experimentally validated the central mechanism proposed by the modelling chapters: exfoliation depends on a combined kinetic and thermal contribution rather than gas velocity alone.

The optimized heated CFE condition was then extended from h-BN to Graphene and MoS_2, demonstrating that the process is not limited to one material system. This is an important thesis-level finding because Graphene, h-BN, and MoS_2 represent three different classes of 2D materials: conductive, insulating, and semiconducting layered crystals. Starting with nitrogen, the optimized heated CFE condition produced initial concentrations of approximately 0.15 $g \cdot L^{-1}$ for h-BN, 0.14 $g \cdot L^{-1}$ for Graphene, and 0.12 $g \cdot L^{-1}$ for MoS_2. This result is especially important because nitrogen has a lower attainable gas velocity than helium, but the energy-based simulations showed that increasing thermal energy can lower the energetic resistance to layer separation and support exfoliation through thermally assisted sliding and peeling pathways. Therefore, the successful use of nitrogen experimentally supports the modelling conclusion that CFE performance depends on the combined contribution of gas velocity, pressure, collision frequency, and temperature, rather than velocity alone. After this nitrogen-based validation, compressed air was also tested as an even more accessible carrier gas. Air-CFE produced initial concentrations of approximately 0.21 $g \cdot L^{-1}$ for h-BN, 0.15 $g \cdot L^{-1}$ for Graphene, and 0.14 $g \cdot L^{-1}$ for MoS_2. The comparable or higher concentrations obtained with compressed air further confirm that, once thermal energy is added to the gas stream, accessible carrier gases can provide sufficient thermo-kinetic energy for gas-driven delamination.

Another major experimental finding was that post-processing controls the usable recovered output as strongly as the exfoliation step itself. Re-dispersion and repeated centrifugation of the sediment showed that a significant fraction of exfoliated nanosheets remains trapped in the sediment cake after the first centrifugation step. Therefore, sediment should not be considered waste, but a recoverable intermediate. For compressed-air CFE products, repeated recovery increased the

measured concentration of h-BN from approximately 0.21 to 0.53 $g \cdot L^{-1}$, Graphene from approximately 0.16 to 0.43 $g \cdot L^{-1}$, and MoS_2 from approximately 0.14 to 0.34 $g \cdot L^{-1}$ after five recovery cycles. This finding shifted the process interpretation from single-pass concentration measurement to total recoverable nanosheet output.

The MoS_2 centrifugation results further showed that the CFE-produced dispersion contains a distribution of exfoliated nanosheets with different sizes and thicknesses. At 1500 rpm, the largest recovered fraction was obtained, with a concentration of approximately 1.65 $g \cdot L^{-1}$, corresponding to about 52.5% of the total recovered MoS_2 across the three centrifugation conditions. This fraction had an average lateral length of 286 ± 22 nm and an estimated thickness of 23 ± 2 layers. At 3000 rpm, the recovered concentration decreased to approximately 1.0 $g \cdot L^{-1}$, corresponding to about 31.8% of the total recovered material, while the average lateral length decreased to 173 ± 18 nm and the estimated thickness decreased to 17 ± 1 layers. At 4500 rpm, the recovered concentration further decreased to approximately 0.49 $g \cdot L^{-1}$, corresponding to about 15.6% of the total, and the recovered nanosheets became smaller and thinner, with an average lateral length of 132 ± 13 nm and an estimated thickness of 13 ± 1 layers. Therefore, the centrifugation results do not simply show higher or lower recovery, they reveal that CFE produces a polydisperse MoS_2 product composed of a dominant larger/thicker nanosheet fraction and progressively smaller/thinner refined fractions at higher centrifugation speeds.

The starting particle size study also showed that smaller MoS_2 precursor particles strongly improved recovered concentration under the same CFE and recovery conditions. After five recovery cycles at a fixed centrifugation speed of 1500 rpm, the recovered concentration increased from approximately 0.29 $g \cdot L^{-1}$ for 12.5 μm starting MoS_2 to 0.77 $g \cdot L^{-1}$ for 4.5 μm MoS_2 and 1.38 $g \cdot L^{-1}$ for 1.5 μm MoS_2. Using the 200 mL collection volume, these values correspond to recovered masses of approximately 58 mg, 154 mg, and 276 mg, respectively. Therefore, the 1.5 μm starting powder produced about 4.8 times higher recovered concentration than the 12.5 μm powder and about 1.8 times higher than the 4.5 μm powder. However, the final nanosheet dimensions remained relatively similar across the three precursor sizes: the average lateral sizes were 280 ± 23 nm, 325 ± 47 nm, and 289 ± 13 nm, while the estimated layer numbers were 22 ± 2.1, 24 ± 2.3, and 23 ± 2.2 for the 12.5 μm, 4.5 μm, and 1.5 μm starting powders, respectively. This indicates that smaller starting particles mainly improve entrainment, acceleration, and recovered output, while the final

nanosheet size and thickness are controlled more strongly by the CFE flow condition and the fixed centrifugation/recovery protocol. Based on this finding, controlled short-time pre-milling or mild ball milling of the precursor powder could be considered as a future process-improvement strategy to reduce feed-particle size before CFE and increase recovered yield.

For Graphene, re-exfoliation of recovered sediment provided another route for increasing total material utilization. Freeze-drying and reprocessing the Graphene sediment increased the recovered concentration across repeated cycles, and the cumulative recovered mass reached approximately 316 mg from a 1 g feed basis, corresponding to approximately 31.6% recovery. This result is important because it shows that the CFE process can be integrated with recycling loops to increase overall yield without requiring all material to be exfoliated in a single pass. From a scale-up perspective, this finding supports the future development of continuous feeding, sediment recycling, and continuous recovery systems.

The final characterization chapter confirmed that the improved experimental output was not achieved by severely damaging or chemically destroying the starting materials. TEM, STEM, and HRTEM images showed that CFE produced laterally extended nanosheets. Graphene, h-BN, and MoS_2 retained sheet-like morphologies rather than being reduced only to pulverized fragments. HRTEM lattice features further supported the preservation of local crystalline order after CFE. Therefore, the microscopy results confirmed that the optimized process induces delamination while retaining the nanosheet character of the materials.

XPS analysis showed that CFE introduces moderate surface and edge modification, but the dominant chemical bonding frameworks of the materials remain preserved. Graphene remained dominated by graphitic carbon, although the increased defect-related and oxygen-containing components indicated the formation of additional edges and moderate surface functionalization. h-BN remained dominated by B–N and N–B bonding, confirming preservation of the boron nitride framework, while air processing introduced more oxygen-containing surface species than helium. MoS_2 remained dominated by Mo–S and sulfide bonding, with only minor oxidation and no clear evidence of a major metallic 1T-MoS_2 transformation. These results show that CFE is chemically milder than many liquid or chemically assisted exfoliation methods, although gas choice can influence the degree of surface oxidation.

Raman spectroscopy provided complementary evidence for structural preservation and exfoliation. For Graphene, the retained G and 2D bands confirmed that the graphitic framework was preserved, while the D band and broadened 2D response indicated few-layer Graphene with edge-related disorder rather than fully amorphous carbon. For h-BN, the characteristic E_2g vibrational mode remained clear after exfoliation, confirming retention of the h-BN lattice. For MoS_2, the E_2g^1 and A_1g modes remained well defined, and the reduced peak separation compared with bulk MoS_2 supported thickness reduction toward few-layer MoS_2. Together, the Raman and XPS results confirmed that CFE can reduce layer number and generate nanosheet-rich products without causing severe amorphization or major phase conversion.

Overall, the thesis establishes CFE as a scalable and tunable gas-driven exfoliation platform for 2D nanomaterials. The continuum model identified the critical process variables, the atomistic simulations explained how these variables control molecular-scale energy transfer, the energy-based analysis quantified how they reduce exfoliation barriers, the experimental work demonstrated how heating and recovery improve output using practical gases, and the characterization results confirmed that the optimized products retain the structural and chemical identity of Graphene, h-BN, and MoS_2. The central conclusion is that heated CFE operates through a coupled thermo-kinetic delamination mechanism in which high-speed gas expansion, aerodynamic shear, pressure-driven collision frequency, thermal activation, precursor entrainment, and post-processing recovery collectively determine the final nanosheet output. This integrated understanding provides the scientific basis for the future development of continuous, multi-nozzle, and application-oriented CFE systems.

The future directions described below are based on the main limitations identified in the present study, manual precursor loading, short-burst operation, batch centrifugation-based recovery, limited continuous concentration capability, and the need for application-level validation. Addressing these limitations would move CFE from a validated laboratory-scale process toward a continuous and scalable production platform.

8.3 Current Limitations of the Present Study

Although this thesis establishes heated CFE as a promising gas-driven route for producing multiple two-dimensional nanomaterials, the present work should be interpreted as a mechanistic and

laboratory-scale validation rather than a finished industrial process. Several limitations remain and define the next stage of development.

First, the current CFE system relies on manual precursor loading. This limits process continuity, makes powder feeding less uniform, and restricts the ability to maintain a steady particle concentration in the carrier gas. Since CFE performance depends strongly on particle entrainment and gas–particle interaction, future systems require controlled and continuous precursor feeding.

Second, the present experiments use short-burst operation and batch collection. This configuration is effective for mechanism validation and parameter optimization, but it does not yet represent a fully continuous production process. Continuous operation will require stable feeding, controlled gas delivery, repeatable nozzle performance, and integrated downstream recovery.

Third, the current recovery pathway still depends heavily on centrifugation, sediment re-dispersion, and repeated post-processing cycles. These steps are useful for studying recovery and fractionation, but they can become bottlenecks for scale-up. The MoS_2 centrifugation and Graphene sediment re-exfoliation results showed that recovery strongly influences measured concentration, meaning that the process output cannot be evaluated only from the gas-phase exfoliation event.

Fourth, application validation remains limited. This thesis demonstrates material production, recovery enhancement, and structural and chemical preservation, but it does not yet evaluate the performance of CFE-produced nanosheets in end-use systems such as cementitious composites, polymer nanocomposites, protective coatings, thermal-management materials, or tribological systems. Application-specific testing is therefore required to determine whether the observed nanosheet characteristics translate into measurable performance benefits.

Finally, the economic and engineering feasibility of CFE at industrial scale has not yet been fully established. The results show that nitrogen and compressed air can become practical carrier gases when combined with gas preheating, but continuous feeding, multi-nozzle operation, energy consumption, nozzle durability, powder handling, filtration, solvent recovery, and quality control must still be developed before CFE can be considered an industrial production platform.

The future-work directions below are therefore not independent ideas; each directly addresses one of the limitations identified above. Together, they define the engineering path required to move

CFE from a validated laboratory process toward a continuous, scalable, and application-oriented production platform.

8.4 Future Work Connected to Current Limitations

The results of this thesis demonstrate that CFE is a promising gas-driven route for producing 2D nanomaterials through high-pressure expansion, particle acceleration, and intense aerodynamic forces. The computational and experimental findings establish the feasibility of CFE for exfoliating layered materials such as Graphene, h-BN, and MoS_2 while preserving their main structural and chemical characteristics. However, the present system still represents an early-stage laboratory platform, where precursor loading, product recovery, and throughput remain limited by manual operation and batch-based post-processing. Therefore, the next stage of CFE development should focus on transforming the method from a validated experimental process into a continuous, scalable, and controllable production platform.

Future development should prioritize engineering improvements that directly address the current limitations of feeding, throughput, yield, and recovery. Automated precursor feeding inspired by the cold spray coating process could enable controlled powder delivery into the high-pressure gas stream, while parallelized multi-nozzle architectures could increase production rate without sacrificing the optimized local flow conditions responsible for exfoliation. In addition, wet-assisted feeding may further enhance yield by improving precursor dispersion and reducing agglomeration or restacking during collection. Finally, integrating continuous recovery methods such as tangential flow filtration could reduce dependence on centrifugation and make downstream separation more compatible with continuous operation. Together, these directions provide a practical pathway for advancing CFE toward a more robust and scalable manufacturing technology for 2D nanomaterials.

8.4.1 Automated Precursor Feeding

One of the most important future developments for CFE is the design of an automated precursor-feeding system. In the present experimental configuration, the precursor powder is weighed and loaded into a high-pressure stainless-steel entrainment chamber before each run, after which the pressurized carrier gas fluidizes the powder and drives the gas–particle suspension through the

nozzle restriction. While this approach is suitable for controlled laboratory experiments, it limits process continuity, makes the powder feed rate difficult to quantify, and restricts the ability to operate CFE as a steady or semi-continuous production process. Therefore, a future CFE system should incorporate a controlled powder-feeding module that can deliver graphite, h-BN, MoS_2, or other layered precursors into the high-pressure gas stream at a defined and reproducible mass flow rate. This would allow the powder-to-gas ratio to become a controllable processing parameter rather than a fixed initial loading condition. The need for this development follows directly from the current CFE apparatus, which relies on a high-pressure gas source, gas heating section, powder entrainment chamber, nozzle/orifice restriction, and liquid collection vessel.

Cold spray coating provides a useful engineering model for this type of feeding system because it also requires controlled injection of solid powder particles into a high-velocity gas stream. In cold spray, powder particles are carried by a separate gas stream and injected either into the nozzle entrance or into a lower-pressure region downstream of the nozzle entrance, where they are accelerated by the main gas flow. High-pressure cold spray systems require a powder feeder capable of operating under elevated pressure, while low-pressure systems inject powder downstream after partial gas expansion [159]. Cold spray literature also emphasizes that the process depends on the coupling between pressurized gas expansion, nozzle geometry, powder injection location, and particle acceleration [160]. These design principles are directly relevant to CFE, although the objective is different: in cold spray, particle acceleration is used for coating deposition, whereas in CFE, particle acceleration, shear, and gas–particle interactions are used to promote delamination of layered materials.

A possible future CFE feeding design could include a pressurized powder hopper connected to the main gas line through a metered carrier-gas branch. The powder reservoir could be equipped with a vibration-assisted or screw-assisted metering mechanism to prevent powder bridging and to maintain a stable feed rate. A pressure-equalization line would be required to prevent backflow from the main high-pressure gas stream into the powder feeder, since cold spray systems similarly require careful pressure balancing between the feeder and the working gas line [161]. The powder could then be injected upstream of the nozzle, where residence time and gas–particle mixing are higher, or at a downstream injection point, where clogging may be reduced but acceleration time may be shorter. This design choice should be evaluated experimentally because the powder

injection location affects particle heating, residence time, acceleration history, and gas–particle interaction intensity [161].

For CFE, the preferred design would likely be a high-pressure, cold-spray-inspired powder feeder rather than a simple gravity-fed hopper. This would allow the precursor to be introduced continuously without depressurizing the system between runs. The feeder should include: (i) a sealed powder reservoir rated for the operating pressure, (ii) a carrier-gas inlet for powder fluidization, (iii) a metering element such as a rotating disk, auger, or vibratory feeder, (iv) a pressure-balanced injection line, (v) anti-backflow protection, and (vi) a removable cleaning section to address clogging by fine layered powders. Such a system would make it possible to study the effect of real-time feed rate on exfoliation yield, particle entrainment, nozzle stability, and final nanosheet concentration. Ultimately, automated feeding would represent a key step in transforming CFE from a burst-based laboratory process into a continuous gas-phase exfoliation platform. A conceptual automated precursor-feeding configuration for future continuous CFE operation is shown in ***Figure 8.1***.

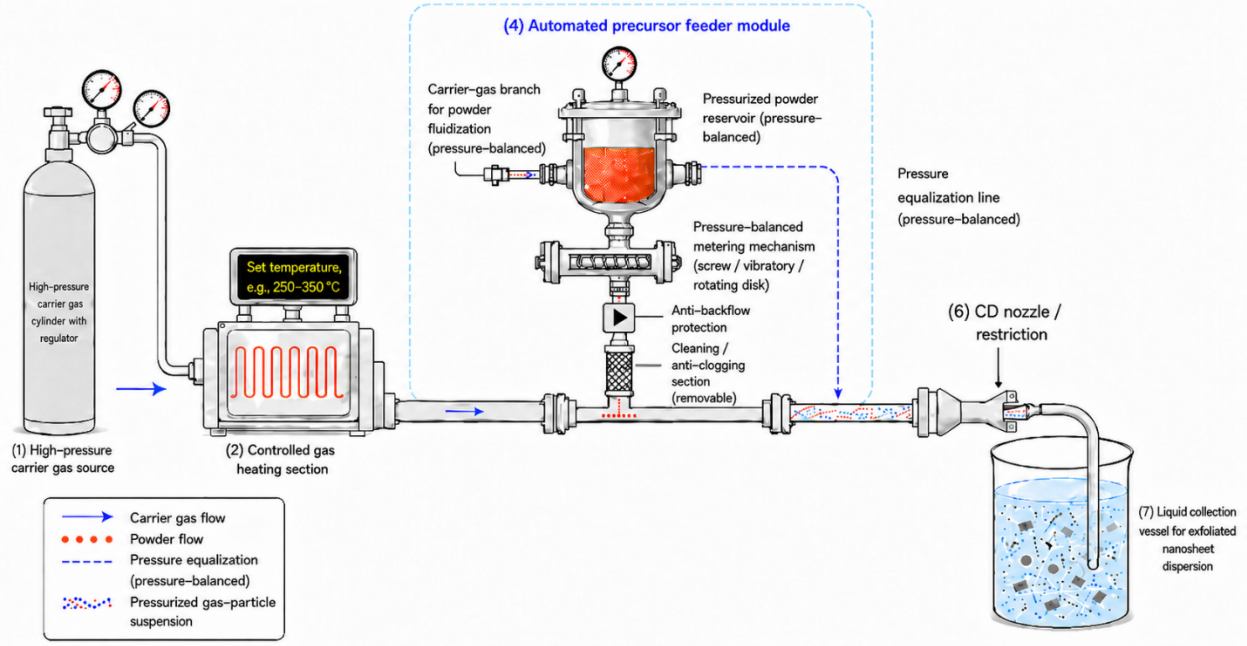

Figure 8.1*: Conceptual schematic of an automated precursor-feeding system for continuous CFE operation.*

8.4.2 Parallelized Multi-Nozzle CFE Architecture for Throughput Enhancement

A second important future direction is the development of a parallelized multi-nozzle CFE architecture to increase production throughput while preserving the local exfoliation conditions established in the present work. In the current CFE process, exfoliation depends strongly on the local gas–particle interaction inside the nozzle, where high-pressure gas expansion generates rapid acceleration, aerodynamic shear, particle–gas momentum transfer, and intense flow gradients. Therefore, simply increasing the size of a single nozzle may not be the most reliable scale-up strategy, because a larger nozzle could change the local velocity field, residence time, shear distribution, and particle acceleration history. Instead, a more controlled approach would be to operate several optimized CFE nozzles in parallel, allowing the total production rate to increase while each individual nozzle maintains the flow conditions already validated experimentally. This approach is consistent with the optimized CFE findings in Chapter 6, where the process performance was linked to pressure, gas heating, particle entrainment, and high-shear flow through the nozzle.

This strategy is conceptually similar to the numbering-up approach used in microreactor and microchannel technologies. In these systems, scale-up is often achieved not by making one channel much larger, but by operating many small channels in parallel so that each channel preserves the transport conditions responsible for the desired process performance. Reviews of micro- and millireactor scale-up identify numbering-up as one of the major scale-up strategies, alongside sizing-up and combined approaches [162]. Similarly, multi-channel reactor studies emphasize that numbering-up allows findings from a single optimized channel to be transferred toward industrial devices only when flow, heat, and reaction conditions remain similar across the parallel channels [163]. For CFE, this analogy is useful because the exfoliation mechanism is highly dependent on local flow conditions; therefore, preserving nozzle-level physics while multiplying the number of nozzles is likely more reliable than redesigning the entire process around a single larger restriction.

A future parallelized CFE system could consist of a high-pressure gas manifold feeding multiple identical nozzle cartridges, each supplied with a controlled fraction of the precursor–gas suspension. The automated feeder described in the previous section could distribute the precursor either into a common upstream manifold or into separate feeder branches connected to each nozzle.

The outlet jets could then discharge into a shared collection chamber or into independent collection vessels for comparison and quality control. However, this design would require careful control of flow distribution across all nozzles. Previous studies on multi-channel systems show that flow maldistribution is a major challenge in numbering-up, because non-uniform flow can broaden residence-time distribution and reduce consistency between channels [163]. This is especially important for CFE, where even small differences in pressure drop, powder loading, or nozzle blockage could cause one nozzle to dominate the flow while another becomes underfed or clogged. Therefore, the key engineering challenge for a multi-nozzle CFE system would be uniform gas–powder distribution. The manifold should be designed so that each nozzle experiences a comparable pressure drop, feed concentration, and gas velocity. Studies on compact parallel channels and multi-nozzle arrays show that geometry strongly affects flow uniformity, and that inlet diameter, channel diameter, channel length, spacing, and area ratio can be used to guide more uniform distribution between nozzles [164, 165]. For CFE, similar principles could be applied by using symmetric manifolds, matched nozzle cartridges, calibrated flow restrictors, and pressure sensors upstream of each branch. A modular design would also allow individual nozzles to be isolated, cleaned, or replaced without shutting down the entire system.

Overall, parallelization provides a practical pathway for increasing CFE throughput while maintaining the scientific basis of the optimized single-nozzle process. Rather than treating scale-up as a simple increase in nozzle size, future work should investigate a modular multi-nozzle architecture in which each nozzle acts as a repeatable exfoliation unit. This would allow the production rate to scale with the number of operating nozzles while preserving the high-shear, high-velocity gas expansion conditions required for delamination. Such a design would represent an important step toward transforming CFE from a laboratory-scale exfoliation method into a scalable continuous production platform for 2D nanomaterials.

8.4.3 Moisture- and Agent-Conditioned Precursor Feeding for Yield Enhancement

A further future direction for improving CFE yield is moisture-conditioned precursor feeding, in which the layered precursor powder is exposed to a controlled, small amount of water before introduction into the CFE feeder. Low concentrations of selected additives may also be used to modify particle cohesion, interlayer accessibility, or powder flowability. Unlike conventional

liquid-phase exfoliation, this approach would not introduce a continuous liquid stream, slurry, or inline water injection into the nozzle. Instead, water would serve only as a pre-conditioning agent to alter the physical state of the powder before gas-driven processing. The precursor would remain a feedable damp powder, while exfoliation would continue to be driven primarily by high-pressure gas expansion, particle acceleration, aerodynamic forces, and particle–particle or particle–wall interactions within the CFE restriction.

The motivation for this concept comes from newer hydrodynamic-assisted and mechanically assisted exfoliation methods, where exfoliation efficiency is improved by combining layered particles with controlled pressure drop, flow restriction, shear, collision, cavitation, or intermediate force-transfer mechanisms. For example, Zhang et al. demonstrated a hydrodynamic-assisted exfoliation method using a needle valve, where a graphite suspension passed through a narrow valve gap that generated cavitation, velocity gradients, normal forces, and shear forces [166]. Although the proposed CFE approach would not pump a liquid suspension through the nozzle, the key transferable principle is that particle-containing flow through a narrow restriction can promote exfoliation through intense local stresses, shear, and collisions.

For future CFE experiments, the simplest implementation would be to pre-mix graphite, h-BN, MoS_2, or other layered powders with a controlled small amount of DI water, IPA, or DI water/IPA mixture before loading them into the automated powder feeder. The moisture content should be low enough that the powder remains flowable and does not form a slurry, paste, or sticky agglomerate. The purpose would be to reduce dry powder cohesion, improve precursor dispersion, decrease dusting, reduce bridging inside the feeder, and increase the fraction of particles that are uniformly entrained into the high-pressure gas stream. During passage through the heated gas line and nozzle, part of the surface moisture may evaporate, while the pre-conditioned powder morphology may still improve gas–particle contact and reduce the tendency for large dry agglomerates to bypass the most effective exfoliation zone.

A further extension of this strategy would be to incorporate removable assisting agents during the moisture-conditioning step. Inorganic salts such as NaCl or $CuCl_2$ could be mixed with the layered precursor using a small amount of water or water/alcohol mixture, followed by partial drying until the feedstock remains powder-like. This idea is supported by salt-assisted exfoliation, where graphite and inorganic salts were mixed in water, dried, and then exfoliated into few-layer

Graphene sheets [167]. In the context of CFE, such agents could act as temporary spacers between layered particles, reduce face-to-face restacking, and increase local particle–particle contacts during high-speed gas acceleration. After exfoliation, the salts could be removed by washing, centrifugation, or future continuous recovery methods such as tangential flow filtration.

Other removable force-transfer agents could also be explored. Intermediate-assisted grinding exfoliation has shown that micro-particles can act as force intermediates, converting applied mechanical forces into localized shear forces for exfoliating layered materials such as h-BN, graphite, black phosphorus, and transition metal dichalcogenides [168]. For CFE, this concept could be adapted by blending small amounts of removable solid additives with pre-moisturized graphite, h-BN, or MoS_2 before feeding. These additives would not be intended to chemically functionalize the nanosheets; instead, they would serve as temporary processing aids to improve powder separation, local collisions, and shear transfer inside the gas–particle stream.

This future study should compare fully dry precursor feeding, moisture-conditioned feeding, salt-assisted moisture conditioning, and intermediate-assisted conditioning under identical CFE operating conditions. The main variables would include solvent type, moisture content, additive type, additive-to-precursor ratio, mixing protocol, resting or partial-drying time, powder flowability, clogging tendency, feed stability, recovered nanosheet concentration, sediment fraction, and final material purity. Excessive moisture or additive loading must be avoided because it could increase sticking, promote nozzle clogging, damp particle acceleration, contaminate the product, or reduce the gas-driven shear mechanism that distinguishes CFE from liquid-based exfoliation. If optimized carefully, moisture- and agent-conditioned feeding could provide a simple and practical route to improve powder entrainment and yield while preserving the central advantage of CFE as a rapid, high-pressure, gas-driven exfoliation process.

8.4.4 Continuous Recovery and Concentration Using Tangential Flow Filtration

Another important future direction is the integration of tangential flow filtration (TFF), also known as cross-flow filtration (CFF), as a continuous recovery and concentration method for CFE-produced nanosheets. In the present work, post-exfoliation recovery relied mainly on centrifugation, where larger unexfoliated or partially exfoliated particles sediment while the exfoliated nanosheets remain in the supernatant. However, Chapter 6 showed that this separation

is not perfectly selective: exfoliated nanosheets can become trapped inside the sediment cake, requiring repeated re-dispersion and re-centrifugation to recover additional material and increase the usable concentration of the product. Therefore, although centrifugation is effective at the laboratory scale, it becomes a limiting step for future continuous CFE operation because it is batch-based, time-consuming, and can underestimate the actual nanosheet production.

TFF provides a promising alternative because the suspension flows tangentially across the membrane surface rather than directly into it. This cross-flow motion helps reduce filter-cake formation and allows the retained material to continue circulating in the retentate stream, making the process more compatible with continuous operation than conventional dead-end filtration or repeated centrifugation. Recent work on solution-exfoliated 2D materials has introduced CFF as a centrifuge-free processing method for Graphene separation, showing that it can improve separation throughput by two orders of magnitude compared with centrifugation-based processing [169]. Similarly, recent studies on 2D-material inks have emphasized that conventional batch centrifugation hinders scalable manufacturing and that CFF can provide a continuous-flow route for separating and concentrating 2D nanosheets [170].

For future CFE development, TFF could be used in two complementary ways. First, it could replace or reduce centrifugation by continuously separating larger unexfoliated particles from smaller exfoliated nanosheets after collection. In this configuration, the CFE outlet dispersion would be directed into a TFF module, where the desired nanosheet fraction could be collected while larger particles are retained or recycled. Second, TFF could be used to increase the concentration of the recovered nanosheet dispersion by removing excess solvent through the permeate while retaining the nanosheets in the retentate. This is especially important because many downstream applications, such as printable inks, coatings, composites, and membrane fabrication, require concentrated dispersions rather than dilute post-exfoliation suspensions. Recent ceramic CFF work demonstrated an integrated separation and concentration system in which cross-flow microfiltration removed poorly exfoliated graphite, followed by cross-flow ultrafiltration to concentrate Graphene nanosheets into printable ink formulations [170].

A future CFE–TFF processing train could therefore consist of three linked steps: CFE exfoliation, continuous size-based separation, and retentate concentration. After the CFE jet is collected in solvent, the dispersion could first pass through a coarse cross-flow microfiltration stage to remove

large unexfoliated particles or agglomerates. The nanosheet-rich stream could then enter a second ultrafiltration stage, where solvent is removed and the nanosheet concentration is increased. The retained larger particles from the first stage could potentially be re-dispersed and returned to the CFE feeder for additional processing, while the concentrated nanosheet dispersion from the second stage could be collected directly for characterization or application testing. This design would reduce reliance on repeated centrifugation cycles and make the downstream recovery step more compatible with the continuous feeding and multi-nozzle scale-up strategies described in the previous sections.

The main design variables for this future study would include membrane pore size or molecular weight cutoff, membrane material, cross-flow velocity, transmembrane pressure, feed concentration, solvent composition, and fouling behavior. Porous ceramic membranes may be especially attractive for CFE because recent work showed that ceramic CFF membranes can tolerate higher nanosheet concentrations and flow rates than polymer membranes without compromising separation efficiency. However, the membrane must be selected carefully so that exfoliated nanosheets are not lost through the permeate or trapped irreversibly on the membrane surface. Overall, integrating TFF with CFE would directly address two major bottlenecks of the current recovery workflow: it could skip or minimize centrifugation and increase final nanosheet concentration in a continuous, scalable manner. The proposed tangential-flow-filtration-based recovery and concentration concept is shown schematically in ***Figure 8.2***.

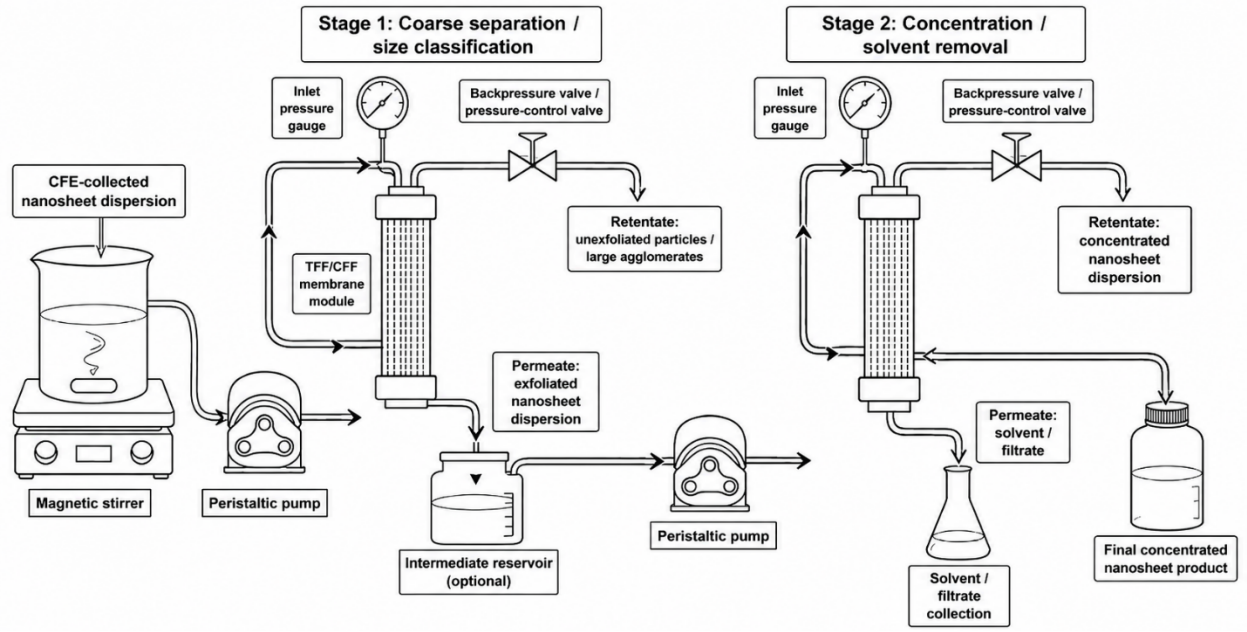

***Figure 8.2**: Conceptual schematic of tangential flow filtration for future CFE product recovery and concentration.*

8.4.5 Expansion of CFE toward MXenes and Other Emerging 2D Materials

The present thesis demonstrated that the optimized CFE process can be extended beyond a single precursor by applying the heated operating window to Graphene, h-BN, and MoS_2. This result suggests that CFE has potential as a broader gas-driven exfoliation platform for layered materials with different bonding, density, particle morphology, and surface chemistry. Future work should therefore investigate whether the same high-pressure expansion, particle acceleration, and aerodynamic shear mechanisms can be applied to additional families of two-dimensional materials. Expanding the material library would help determine whether CFE is limited to conventional van der Waals solids or whether it can be adapted for more chemically complex layered systems.

One particularly important class for future investigation is MXenes, which are two-dimensional transition-metal carbides, nitrides, or carbonitrides commonly produced from layered MAX-phase precursors. The first MXene, Ti_3C_2, was produced by selective etching of Ti_3AlC_2, opening a pathway to a large family of conductive 2D materials with attractive properties for energy storage, electromagnetic interference shielding, sensors, catalysis, and membrane applications [39].

However, MXenes also present several difficulties that make them more challenging than Graphene, h-BN, or MoS_2. Their synthesis typically requires chemical etching to remove the A-layer from the MAX phase, followed by intercalation and delamination to separate multilayer MXene stacks into few-layer or single-layer sheets. Established $Ti_3C_2T_x$ synthesis protocols emphasize that etchant chemistry, delamination route, washing conditions, flake size, and surface terminations strongly affect the final MXene quality [171]. Therefore, CFE should not initially be proposed as a complete replacement for MXene synthesis from MAX phases. A more realistic future direction is to use CFE as a post-etching physical delamination or secondary exfoliation step for already etched multilayer MXenes.

The main difficulty in applying CFE to MXenes is their chemical sensitivity. MXenes contain surface terminations such as –O, –OH, –F, or –Cl depending on the etching route, and these terminations strongly influence conductivity, hydrophilicity, interlayer spacing, and stability [171]. In addition, many MXenes, especially $Ti_3C_2T_x$, are susceptible to oxidation during processing and storage. Oxidation can occur in air, water, and colloidal dispersions, with aqueous environments often accelerating degradation compared with solid or composite states [172]. This creates a major challenge for CFE because the present system uses a liquid collection medium after gas-phase exfoliation. For MXenes, future experiments may require oxygen-limited processing, inert carrier gases, degassed solvents, low-temperature collection, short residence time in water, or solvent systems that delay oxidation. The collection and recovery steps would therefore need to be designed specifically for MXenes rather than directly copied from Graphene or h-BN processing.

Another difficulty is that MXenes are not simply weakly bonded neutral van der Waals solids. Their interlayer spacing, surface charge, hydration state, and intercalated ions can strongly affect how the sheets separate. This means the CFE conditions that work for h-BN, graphite, and MoS_2 may not directly translate to MXenes. Excessive gas-particle collisions could reduce lateral flake size or damage already delaminated sheets, while insufficient gas-particle interaction may fail to separate multilayer stacks. Future MXene-CFE work should therefore begin with multilayer $Ti_3C_2T_x$ as a model system and compare CFE-treated samples with conventionally delaminated MXene controls. The key characterization methods should include XPS to monitor surface

terminations and oxidation, Raman spectroscopy to detect structural changes, and XRD to track interlayer spacing.

Beyond MXenes, future studies should also explore additional transition-metal dichalcogenides such as WS_2, WSe_2, and $MoSe_2$, because these materials share layered structures with MoS_2 but differ in density, interlayer bonding, band structure, and oxidation behavior. These materials would help test whether CFE can be generalized across the broader TMD family rather than only MoS_2. Other candidates could include graphitic carbon nitride, layered double hydroxides, layered oxides, and black phosphorus. However, these materials should be introduced gradually because each presents different processing risks. For example, black phosphorus is highly sensitive to oxygen and moisture, while layered oxides and hydroxides may undergo surface chemical changes during collection or drying. Therefore, future expansion of CFE should follow a material-specific validation pathway rather than assuming one universal condition will work for all layered solids.

Overall, extending CFE toward MXenes and other emerging 2D materials would be an important step in determining the broader scientific and technological value of the process. MXenes are especially attractive because of their high conductivity, surface functionality, and relevance to energy, shielding, and membrane applications, but they also represent a more difficult test case due to oxidation sensitivity, surface termination chemistry, and complex delamination requirements. If CFE can be adapted to physically delaminate multilayer MXenes while preserving their surface chemistry and conductivity, it would significantly strengthen the case for CFE as a flexible platform for producing advanced 2D materials beyond Graphene, h-BN, and MoS_2.

8.4.6 Application-Oriented Demonstration in Composite System

A final future direction should focus on demonstrating CFE-produced nanosheets in application spaces where single-layer purity is not required, but where scalable production, acceptable nanosheet quality, low cost, and good dispersion are more important. Many practical composite applications do not require perfectly monolayer Graphene or atomically uniform 2D sheets. Instead, they can benefit from few-layer Graphene, Graphene nanoplatelets, exfoliated h-BN, or MoS_2 nanosheets, provided that the fillers have sufficient aspect ratio, surface area, structural integrity, and compatibility with the host matrix. This makes composite reinforcement a strong

application match for CFE, because the process is designed to produce exfoliated layered materials through rapid gas-driven mechanical forces rather than slow monolayer-isolation methods.

Concrete and cementitious composites are especially suitable as a first demonstration platform. Cement-based materials are high-volume, cost-sensitive, and performance-driven, so they do not require electronic-grade monolayer Graphene. Instead, the desired function is usually improved load transfer, crack bridging, pore refinement, hydration control, durability, or electrical conductivity for self-sensing. Graphene-enhanced concrete has been widely investigated because small additions of Graphene-family materials can improve mechanical and durability-related properties; a recent review notes that Graphene-infused concrete has been studied for strength, durability, economic viability, and sustainability, with reported improvements at low filler contents depending on Graphene type, dosage, and dispersion quality [173]. Studies on Graphene nanoplatelet cement composites also show that GNPs can improve compressive/flexural performance and reduce electrical resistivity by forming conductive networks within the cement matrix [174].

This application is well aligned with the expected output of CFE. Unlike electronic devices, where monolayer control, defect density, and atomic-scale cleanliness are often critical, concrete reinforcement can tolerate few-layer or multilayer nanosheets if they are produced consistently and can be dispersed effectively. In fact, Graphene nanoplatelets are already used as practical Graphene substitutes in composite applications because they are more accessible, lower-cost, and more scalable than monolayer Graphene while still providing high aspect ratio, electrical conductivity, and mechanical reinforcement capability [175]. Therefore, CFE-produced Graphene could be evaluated as cement additives.

A practical demonstration study could begin with CFE-produced Graphene or few-layer Graphene added to cement paste, mortar, or concrete at low dosages, for example 0.01–0.20 wt.% by cement mass. The CFE product should be compared against three controls: plain cementitious material, unprocessed graphite precursor, and a commercial Graphene nanoplatelet additive. The key performance metrics should include workability, compressive strength, flexural strength, electrical resistivity, water absorption, porosity, crack propagation, and durability indicators such as chloride penetration or freeze–thaw resistance. If the CFE material forms a partial conductive network, self-sensing behavior could also be tested by measuring resistivity changes under cyclic loading. This

direction is supported by previous studies showing that GNP–cement composites can exhibit piezoresistive behavior and can be used for structural health-monitoring concepts [176]. In one reported study, GNP–cement composites showed increased load-carrying capacity and failure strain compared with the control sample, and the composite was also evaluated for crack monitoring in a reinforced concrete beam [177].

Corrosion-protective nanocomposite coatings for offshore steel structures and oil-platform infrastructure represent another promising application area for CFE-produced few-layer 2D materials. In this application, perfect monolayer purity is not required; instead, the nanosheets mainly act as barrier fillers within epoxy or polymer coatings by increasing the diffusion pathway for water, oxygen, chloride ions, and other aggressive species. Graphene-family fillers have been widely studied for anticorrosion composite coatings, including epoxy-based coatings on steel, and reviews identify oil/gas pipelines among relevant industrial application areas. However, Graphene must be used carefully because its electrical conductivity can promote galvanic corrosion if conductive pathways contact exposed metal [178]. For this reason, CFE-produced h-BN nanosheets may be especially attractive, because h-BN can improve barrier performance while remaining electrically insulating. Ordered BN/epoxy nanocomposite coatings have also been shown to improve anticorrosion performance by creating more tortuous diffusion pathways for corrosive species [179].

A third application direction should focus specifically on CFE-produced MoS_2 nanosheets for lubricating additives, self-lubricating polymer composites, and wear-resistant coatings. This application is well matched to CFE because tribological performance does not require perfect monolayer MoS_2; few-layer or multilayer nanosheets can still provide useful low-friction behavior due to their layered structure and weak interlayer sliding. MoS_2 is already widely studied as a solid lubricant and friction-reducing additive in oils, greases, polymer composites, and protective coatings, where its lamellar structure can reduce shear resistance and support the formation of lubricating transfer films during sliding contact [180].

Overall, application-oriented validation should become an important part of future CFE development. Concrete and cementitious composites would be especially valuable as an initial demonstration because they connect CFE to a high-volume industrial market where scalable, low-cost, few-layer materials may be more useful than small quantities of pristine monolayers.

Concrete or cementitious composite, Corrosion-protective coatings, and MoS_2-based tribological systems would further demonstrate that CFE-produced nanosheets can be matched to applications according to material function. If CFE-produced nanosheets can improve composite-scale performance in these systems, it would strengthen the case for CFE as a practical production platform for application-ready 2D materials.

8.5 Final Remarks

This thesis set out to address one of the central barriers limiting the practical use of two-dimensional nanomaterials: the difficulty of producing nanosheet-rich materials at useful quantities while maintaining acceptable structural and chemical quality. Graphene, h-BN, MoS_2, and related layered materials have already shown exceptional promise, but their translation into industrial systems depends on production methods that are scalable, controllable, cost-aware, and compatible with downstream applications. The work presented here demonstrates that CFE can contribute to this challenge by using high-pressure gas expansion, particle acceleration, aerodynamic shear, and thermal activation to drive the delamination of layered precursor materials.
The most important contribution of this thesis is the development of a mechanistic understanding of CFE across multiple length scales. The continuum analysis identified the flow regions and process variables that control particle acceleration and mechanical work transfer. The atomistic simulations showed how gas velocity, pressure, temperature, and gas identity influence nanoscale layer motion, energy transfer, and interlayer weakening. The energy-based analysis then connected these effects to exfoliation pathways by showing how sliding and peeling barriers are modified under gas-flow conditions. Together, these modelling results establish that CFE is not simply a pressure-discharge or shock-driven process. Instead, it is a coupled thermo-kinetic exfoliation mechanism in which gas velocity, collision frequency, aerodynamic shear, thermal energy, and exposed nanosheet geometry collectively determine the probability of successful delamination.
The experimental results provide the practical validation of this mechanism. Gas preheating was shown to be a critical modification because it allowed nitrogen and compressed air to become effective carrier gases despite their lower velocities compared with helium. This is significant for scale-up because nitrogen and air are more accessible and economically practical than helium. The optimized heated CFE condition produced measurable nanosheet concentrations for h-BN,

Graphene, and MoS_2, confirming that the process can be extended across insulating, conductive, and semiconducting layered materials. The recovery studies further showed that the measured output of CFE depends not only on the exfoliation event itself, but also on how the exfoliated nanosheets are collected, separated, and recovered. Sediment re-dispersion, centrifugation fractionation, precursor size control, and Graphene sediment re-exfoliation all demonstrated that CFE output can be improved by treating the process as an integrated production-and-recovery system rather than a single-pass experiment.

Equally important, the characterization results show that improved recovery was not obtained at the cost of severe material degradation. Electron microscopy confirmed that the products retained sheet-like nanosheet morphologies with preserved lattice features. XPS showed that the dominant bonding structures of Graphene, h-BN, and MoS_2 remained intact, although some gas-dependent surface and edge modification occurred. Raman spectroscopy confirmed preservation of the characteristic structural fingerprints of each material, including graphitic features in Graphene, the E_2g mode of h-BN, and the predominantly 2H-MoS_2 vibrational signature. These results support the conclusion that CFE is a mechanically effective but chemically moderate exfoliation route.

At the same time, this thesis also makes clear that CFE is not yet a finished industrial process. The current laboratory system still depends on manual powder loading, batch collection, centrifugation-based recovery, and short-burst operation. These limitations define the next stage of development. Automated precursor feeding, multi-nozzle parallelization, moisture- or agent-conditioned powder preparation, tangential flow filtration, and sediment recycling should be developed to transform CFE from a validated laboratory method into a continuous and scalable production platform. Future work should also expand the material library beyond Graphene, h-BN, and MoS_2 and should test CFE-produced nanosheets in application-oriented systems such as cementitious composites, corrosion-protective coatings, polymer nanocomposites, thermal-management materials, and MoS_2-based tribological systems.

Overall, this thesis demonstrates that CFE has strong potential as a flexible gas-driven platform for producing application-relevant 2D nanomaterials. Its value lies not only in producing nanosheets, but in offering a new processing framework where compressible-flow physics, thermal activation, particle entrainment, and recovery design can be tuned together. By connecting

mechanism, optimization, and material quality, this work provides a foundation for the next generation of scalable, cleaner, and more practical 2D nanomaterial production technologies.

References

[1] K. S. Novoselov, A. K. Geim, S. V. Morozov, D. Jiang, Y. Zhang, S. V. Dubonos, I. V. Grigorieva and A. A. Firsov, "Electric Field Effect in Atomically Thin Carbon Films," *Science,* vol. 306, no. 5696, p. 666–669, 2004.

[2] A. H. Castro Neto, F. Guinea, N. M. R. Peres, K. S. Novoselov and A. K. Geim, "The electronic properties of graphene," *Reviews of Modern Physics,* vol. 81, no. 1, p. 109–162, 2009.

[3] C. Lee, X. Wei, J. W. Kysar and J. Hone, "Measurement of the Elastic Properties and Intrinsic Strength of Monolayer Graphene," *Science,* vol. 321, no. 5887, p. 385–388, 2008.

[4] A. A. Balandin, S. Ghosh, W. Bao, I. Calizo, D. Teweldebrhan, F. Miao and C. N. Lau, "Superior Thermal Conductivity of Single-Layer Graphene," *Nano Letters,* vol. 8, no. 3, p. 902–907, 2008.

[5] W. Ren, P. Bøggild, J. Redwing, K. S. Novoselov, L. Sun, Y. Qi, K. Jia, Z. Liu, O. Burton, J. Alexander-Webber, S. Hofmann, Y. Cao, Y. Long, Q.-H. Yang, D. Li, S. H. Choi, K. K. Kim, Y. H. Lee, M. Li, Q. Huang, Y. Gogotsi, N. Clark, A. Carl, R. Gorbachev, T. Olsen, J. Rosen, K. S. Thygesen, D. K. Efetov, B. S. Jessen, M. Yankowitz, J. Barrier, R. K. Kumar, F. H. Koppens, H. Deng, X. Li, S. Dai, D. N. Basov, X. Wang, S. Das, X. Duan, Z. Yu, M. Borsch, A. C. Ferrari, R. Huber, M. Kira, F. Xia, X. Wang, Z.-S. Wu, X. Feng, P. Simon, H.-M. Cheng, B. Liu, Y. Xie, W. Jin, R. R. Nair, Y. Xu, Q. Zhang, A. K. Katiyar, J.-H. Ahn, I. Aharonovich, M. C. Hersam, S. Roche, Q. Hua, G. Shen, T. Ren, H.-B. Zhang, C. M. Koo, N. Koratkar, V. Pellegrini, R. J. Young, B. Qu, M. Lemme and A. J. Pollard, "The 2D materials roadmap," *2D Materials,* vol. 13, no. 2, p. 021501, 2026.

[6] R. Bian, C. Li, Q. Liu, G. Cao, Q. Fu, P. Meng, J. Zhou, F. Liu and Z. Liu, "Recent progress in the synthesis of novel two-dimensional van der Waals materials," *National Science Review,* vol. 9, no. 5, p. nwab164, 2022.

[7] M. Yi and Z. Shen, "A review on mechanical exfoliation for the scalable production of graphene," *Journal of Materials Chemistry A,* vol. 3, no. 22, p. 11700–11715, 2015.

[8] G. R. Bhimanapati, Z. Lin, V. Meunier, Y. Jung, J. Cha, S. Das, D. Xiao, Y. Son, M. S. Strano, V. R. Cooper, L. Liang, S. G. Louie, E. Ringe, W. Zhou, S. S. Kim, R. R. Naik, B. G. Sumpter, H. Terrones, F. Xia, Y. Wang, J. Zhu, D. Akinwande, N. Alem, J. A. Schuller, R. E. Schaak, M. Terrones and J. A. Robinson, "Recent Advances in Two-Dimensional Materials beyond Graphene," *ACS Nano,* vol. 9, no. 12, p. 11509–11539, 2015.

[9] M. A. Islam, P. Serles, B. Kumral, P. G. Demingos, T. Qureshi, A. Meiyazhagan, A. B. Puthirath, M. S. B. Abdullah, S. R. Faysal, P. M. Ajayan, D. Panesar, C. V. Singh and T. Filleter, "Exfoliation mechanisms of 2D materials and their applications," *Applied Physics Reviews,* vol. 9, no. 4, p. 041301, 2022.

[10] L. Li, Y. Yu, G. J. Ye, Q. Ge, X. Ou, H. Wu, D. Feng, X. H. Chen and Y. Zhang, "Black phosphorus field-effect transistors," *Nature Nanotechnology,* vol. 9, no. 5, p. 372–377, 2014.

[11] K. F. Mak, C. Lee, J. Hone, J. Shan and T. F. Heinz, "Atomically Thin MoS2: A New Direct-Gap Semiconductor," *Physical Review Letters,* vol. 105, no. 13, p. 136805, 2010.

[12] M. Chhowalla, H. S. Shin, G. Eda, L.-J. Li, K. P. Loh and H. Zhang, "The chemistry of two-dimensional layered transition metal dichalcogenide nanosheets," *Nature Chemistry,* vol. 5, no. 4, p. 263–275, 2013.

[13] C. R. Dean, A. F. Young, I. Meric, C. Lee, L. Wang, S. Sorgenfrei, K. Watanabe, T. Taniguchi, P. Kim, K. L. Shepard and J. Hone, "Boron nitride substrates for high-quality graphene electronics," *Nature Nanotechnology,* vol. 5, no. 10, p. 722–726, 2010.

[14] M. Naguib, V. N. Mochalin, M. W. Barsoum and Y. Gogotsi, "25th Anniversary Article: MXenes: A New Family of Two-Dimensional Materials," *Advanced Materials,* vol. 26, no. 7, p. 992–1005, 2014.

[15] J. N. Coleman, M. Lotya, A. O'Neill, S. D. Bergin, P. J. King, U. Khan, K. Young, A. Gaucher, S. De, R. J. Smith, I. V. Shvets, S. K. Arora, G. Stanton, H.-Y. Kim, K. Lee, G. T. Kim, G. S. Duesberg, T. Hallam, J. J. Boland, J. J. Wang, J. F. Donegan, J. C. Grunlan, G. Moriarty, A. Shmeliov, R. J. Nicholls, J. M. Perkins, E. M. Grieveson, K. Theuwissen, D. W. McComb, P. D. Nellist and V. Nicolosi, "Two-Dimensional Nanosheets Produced by Liquid Exfoliation of Layered Materials," *Science,* vol. 331, no. 6017, p. 568–571, 2011.

[16] C. Backes, B. M. Szydłowska, A. Harvey, S. Yuan, V. Vega-Mayoral, B. R. Davies, P.-l. Zhao, D. Hanlon, E. J. G. Santos, M. I. Katsnelson, W. J. Blau, C. Gadermaier and J. N. Coleman, "Production of Highly Monolayer Enriched Dispersions of Liquid-Exfoliated Nanosheets by Liquid Cascade Centrifugation," *ACS Nano,* vol. 10, no. 1, p. 1589–1601, 2016.

[17] K. R. Paton, E. Varrla, C. Backes, R. J. Smith, U. Khan, A. O'Neill, C. Boland, M. Lotya, O. M. Istrate, P. King, T. Higgins, S. Barwich, P. May, P. Puczkarski, I. Ahmed, M. Moebius, H. Pettersson, E. Long, J. Coelho, S. E. O'Brien, E. K. McGuire, B. M. Sanchez, G. S. Duesberg, N. McEvoy, T. J. Pennycook, C. Downing, A. Crossley, V. Nicolosi and J. N. Coleman, "Scalable production of large quantities of defect-free few-layer graphene by shear exfoliation in liquids," *Nature Materials,* vol. 13, no. 6, p. 624–630, 2014.

[18] R. Rizvi, E. P. Nguyen, M. D. Kowal, W. H. Mak, S. Rasel, M. A. Islam, A. Abdelaal, A. S. Joshi, S. Zekriardehani, M. R. Coleman and R. B. Kaner, "High-Throughput Continuous Production of Shear-Exfoliated 2D Layered Materials using Compressible Flows," *Advanced Materials,* vol. 30, no. 30, p. 1800200, 2018.

[19] R. C. Sinclair, J. L. Suter and P. V. Coveney, "Graphene–Graphene Interactions: Friction, Superlubricity, and Exfoliation," *Advanced Materials,* vol. 30, no. 13, p. 1705791, 2018.

[20] Y. Zhu, S. Murali, W. Cai, X. Li, J. W. Suk, J. R. Potts and R. S. Ruoff, "Graphene and Graphene Oxide: Synthesis, Properties, and Applications," *Advanced Materials,* vol. 22, no. 35, p. 3906–3924, 2010.

[21] A. Chaves, J. G. Azadani, H. Alsalman, D. R. da Costa, R. Frisenda, A. J. Chaves, S. H. Song, Y. D. Kim, D. He, J. Zhou, A. Castellanos-Gomez, F. M. Peeters, Z. Liu, C. L. Hinkle, S.-H. Oh, P. D. Ye, S. J. Koester, Y. H. Lee, P. Avouris, X. Wang and T. Low, "Bandgap engineering of two-dimensional semiconductor materials," *npj 2D Materials and Applications,* vol. 4, p. 29, 2020.

[22] A. A. Iqbal, N. Sakib, A. K. M. P. Iqbal and D. M. Nuruzzaman, "Graphene-based nanocomposites and their fabrication, mechanical properties and applications," *Materialia,* vol. 12, p. 100815, 2020.

[23] E. V. Castro, K. S. Novoselov, S. V. Morozov, N. M. R. Peres, J. M. B. L. dos Santos, J. Nilsson, F. Guinea, A. K. Geim and A. H. C. Neto, "Biased Bilayer Graphene: Semiconductor with a Gap Tunable by the Electric Field Effect," *Physical Review Letters,* vol. 99, no. 21, p. 216802, 2007.

[24] R. R. Nair, P. Blake, A. N. Grigorenko, K. S. Novoselov, T. J. Booth, T. Stauber, N. M. R. Peres and A. K. Geim, "Fine Structure Constant Defines Visual Transparency of Graphene," *Science,* vol. 320, no. 5881, p. 1308–1308, 2008.

[25] V. Georgakilas, M. Otyepka, A. B. Bourlinos, V. Chandra, N. Kim, K. C. Kemp, P. Hobza, R. Zboril and K. S. Kim, "Functionalization of Graphene: Covalent and Non-Covalent Approaches, Derivatives and Applications," *Chemical Reviews,* vol. 112, no. 11, p. 6156–6214, 2012.

[26] F. Schedin, A. K. Geim, S. V. Morozov, E. W. Hill, P. Blake, M. I. Katsnelson and K. S. Novoselov, "Detection of individual gas molecules adsorbed on graphene," *Nature Materials,* vol. 6, no. 9, p. 652–655, 2007.

[27] M. Acerce, D. Voiry and M. Chhowalla, "Metallic 1T phase MoS2 nanosheets as supercapacitor electrode materials," *Nature Nanotechnology,* vol. 10, no. 4, p. 313–318, 2015.

[28] D. Voiry, A. Mohite and M. Chhowalla, "Phase engineering of transition metal dichalcogenides," *Chemical Society Reviews,* vol. 44, no. 9, p. 2702–2712, 2015.

[29] A. Splendiani, L. Sun, Y. Zhang, T. Li, J. Kim, C.-Y. Chim, G. Galli and F. Wang, "Emerging Photoluminescence in Monolayer MoS2," *Nano Letters,* vol. 10, no. 4, p. 1271–1275, 2010.

[30] H. Zeng, J. Dai, W. Yao, D. Xiao and X. Cui, "Valley polarization in MoS2 monolayers by optical pumping," *Nature Nanotechnology,* vol. 7, no. 8, p. 490–493, 2012.

[31] B. Radisavljevic, A. Radenovic, J. Brivio, V. Giacometti and A. Kis, "Single-layer MoS2 transistors," *Nature Nanotechnology,* vol. 6, no. 3, p. 147–150, 2011.

[32] D. Voiry, M. Salehi, R. Silva, T. Fujita, M. Chen, T. Asefa, V. B. Shenoy, G. Eda and M. Chhowalla, "Conducting MoS2 Nanosheets as Catalysts for Hydrogen Evolution Reaction," *Nano Letters,* vol. 13, no. 12, p. 6222–6227, 2013.

[33] J. D. Caldwell, A. V. Kretinin, Y. Chen, V. Giannini, M. M. Fogler, Y. Francescato, C. T. Ellis, J. G. Tischler, C. R. Woods, A. J. Giles, M. Hong, K. Watanabe, T. Taniguchi, S. A. Maier and K. S. Novoselov, "Sub-diffractional volume-confined polaritons in the natural hyperbolic material hexagonal boron nitride," *Nature Communications,* vol. 5, no. 1, p. 5221, 2014.

[34] M. Salavati, A. Mojahedin and A. H. N. Shirazi, "Mechanical responses of pristine and defective hexagonal boron-nitride nanosheets: A molecular dynamics investigation," *Frontiers of Structural and Civil Engineering,* vol. 14, no. 3, p. 623–631, 2020.

[35] K. Watanabe, T. Taniguchi and H. Kanda, "Direct-bandgap properties and evidence for ultraviolet lasing of hexagonal boron nitride single crystal," *Nature Materials,* vol. 3, no. 6, p. 404–409, 2004.

[36] A. Gupta, T. Sakthivel and S. Seal, "Recent development in 2D materials beyond graphene," *Progress in Materials Science,* vol. 73, p. 44–126, 2015.

[37] C. Gautam and S. Chelliah, "Methods of hexagonal boron nitride exfoliation and its functionalization: covalent and non-covalent approaches," *RSC Advances,* vol. 11, no. 50, p. 31284–31327, 2021.

[38] A. VahidMohammadi, J. Rosen and Y. Gogotsi, "The world of two-dimensional carbides and nitrides (MXenes)," *Science,* vol. 372, no. 6547, p. eabf1581, 2021.

[39] M. Naguib, M. Kurtoglu, V. Presser, J. Lu, J. Niu, M. Heon, L. Hultman, Y. Gogotsi and M. W. Barsoum, "Two-Dimensional Nanocrystals Produced by Exfoliation of Ti3AlC2," *Advanced Materials,* vol. 23, no. 37, p. 4248–4253, 2011.

[40] H. Liu, A. T. Neal, Z. Zhu, Z. Luo, X. Xu, D. Tománek and P. D. Ye, "Phosphorene: An Unexplored 2D Semiconductor with a High Hole Mobility," *ACS Nano,* vol. 8, no. 4, p. 4033–4041, 2014.

[41] P. Vogt, P. De Padova, C. Quaresima, J. Avila, E. Frantzeskakis, M. C. Asensio, A. Resta, B. Ealet and G. Le Lay, "Silicene: Compelling Experimental Evidence for Graphenelike Two-Dimensional Silicon," *Physical Review Letters,* vol. 108, no. 15, p. 155501, 2012.

[42] Z. Ni, Q. Liu, K. Tang, J. Zheng, J. Zhou, R. Qin, Z. Gao, D. Yu and J. Lu, "Tunable Bandgap in Silicene and Germanene," *Nano Letters,* vol. 12, no. 1, p. 113–118, 2012.

[43] M. Losurdo, M. M. Giangregorio, P. Capezzuto and G. Bruno, "Graphene CVD growth on copper and nickel: role of hydrogen in kinetics and structure," *Physical Chemistry Chemical Physics,* vol. 13, no. 46, p. 20836, 2011.

[44] Y. Hernandez, V. Nicolosi, M. Lotya, F. M. Blighe, Z. Sun, S. De, I. T. McGovern, B. Holland, M. Byrne, Y. K. Gun'Ko, J. J. Boland, P. Niraj, G. Duesberg, S. Krishnamurthy, R. Goodhue, J. Hutchison, V. Scardaci, A. C. Ferrari and J. N. Coleman, "High-yield production of graphene by liquid-phase exfoliation of graphite," *Nature Nanotechnology,* vol. 3, no. 9, p. 563–568, 2008.

[45] Y. Saito, K. Shin, K. Terayama, S. Desai, M. Onga, Y. Nakagawa, Y. M. Itahashi, Y. Iwasa, M. Yamada and K. Tsuda, "Deep-learning-based quality filtering of

mechanically exfoliated 2D crystals," *npj Computational Materials,* vol. 5, no. 1, p. 124, 2019.

[46] M. Cutini, L. Maschio and P. Ugliengo, "Exfoliation Energy of Layered Materials by DFT-D: Beware of Dispersion!," *Journal of Chemical Theory and Computation,* vol. 16, no. 8, p. 5244–5252, 2020.

[47] Z. Wan and Q.-D. Wang, "Machine Learning Prediction of the Exfoliation Energies of Two-Dimension Materials via Data-Driven Approach," *The Journal of Physical Chemistry Letters,* vol. 12, no. 46, p. 11470–11475, 2021.

[48] J. N. Israelachvili, Intermolecular and Surface Forces, 3 ed., Academic Press, 2011.

[49] D. Pacilé, J. C. Meyer, Ç. Ö. Girit and A. Zettl, "The two-dimensional phase of boron nitride: Few-atomic-layer sheets and suspended membranes," *Applied Physics Letters,* vol. 92, no. 13, p. 133107, 2008.

[50] D. J. Late, B. Liu, H. S. S. R. Matte, V. P. Dravid and C. N. R. Rao, "Hysteresis in Single-Layer MoS2 Field Effect Transistors," *ACS Nano,* vol. 6, no. 6, p. 5635–5641, 2012.

[51] Y. Huang, E. Sutter, N. N. Shi, J. Zheng, T. Yang, D. Englund, H.-J. Gao and P. Sutter, "Reliable Exfoliation of Large-Area High-Quality Flakes of Graphene and Other Two-Dimensional Materials," *ACS Nano,* vol. 9, no. 11, p. 10612–10620, 2015.

[52] F. Bonaccorso, A. Lombardo, T. Hasan, Z. Sun, L. Colombo and A. C. Ferrari, "Production and processing of graphene and 2d crystals," *Materials Today,* vol. 15, no. 12, p. 564–589, 2012.

[53] Y. Huang, Y.-H. Pan, R. Yang, L.-H. Bao, L. Meng, H.-L. Luo, Y.-Q. Cai, G.-D. Liu, W.-J. Zhao, Z. Zhou, L.-M. Wu, Z.-L. Zhu, M. Huang, L.-W. Liu, L. Liu, P. Cheng, K.-H. Wu, S.-B. Tian, C.-Z. Gu, Y.-G. Shi, Y.-F. Guo, Z. G. Cheng, J.-P. Hu, L. Zhao, G.-H. Yang, E. Sutter, P. Sutter, Y.-L. Wang, W. Ji, X.-J. Zhou and H.-J. Gao, "Universal mechanical exfoliation of large-area 2D crystals," *Nature Communications,* vol. 11, no. 1, p. 2453, 2020.

[54] A. Castellanos-Gomez, M. Poot, G. A. Steele, H. S. J. van der Zant, N. Agraït and G. Rubio-Bollinger, "Elastic Properties of Freely Suspended MoS2 Nanosheets," *Advanced Materials,* vol. 24, no. 6, p. 772–775, 2012.

[55] C. Cao, M. Daly, C. V. Singh, Y. Sun and T. Filleter, "High strength measurement of monolayer graphene oxide," *Carbon,* vol. 81, p. 497–504, 2015.

[56] D. Lee, B. Lee, K. H. Park, H. J. Ryu, S. Jeon and S. H. Hong, "Scalable Exfoliation Process for Highly Soluble Boron Nitride Nanoplatelets by Hydroxide-Assisted Ball Milling," *Nano Letters,* vol. 15, no. 2, p. 1238–1244, 2015.

[57] Z. Mohanta, H. S. Atreya and C. Srivastava, "Correlation between defect density in mechanically milled graphite and total oxygen content of graphene oxide produced from oxidizing the milled graphite," *Scientific Reports,* vol. 8, no. 1, p. 15773, 2018.

[58] A. Ambrosi, X. Chia, Z. Sofer and M. Pumera, "Enhancement of electrochemical and catalytic properties of MoS2 through ball-milling," *Electrochemistry Communications,* vol. 54, p. 36–40, 2015.

[59] Y. Arao, R. Kuwahara, K. Ohno, J. Tanks, K. Aida, M. Kubouchi and S.-i. Takeda, "Mass production of low-boiling point solvent- and water-soluble graphene by simple salt-assisted ball milling," *Nanoscale Advances,* vol. 1, no. 12, p. 4955–4964, 2019.

[60] L. H. Li, Y. Chen, G. Behan, H. Zhang, M. Petravic and A. M. Glushenkov, "Large-scale mechanical peeling of boron nitride nanosheets by low-energy ball milling," *Journal of Materials Chemistry,* vol. 21, no. 32, p. 11862, 2011.

[61] J. Xia, L. Liu, J. Xie, H. Yan, Y. Yuan, M. Chen, C. Huang, Y. Zhang, S. Nie and X. Wang, "Layer-by-layered SnS2/graphene hybrid nanosheets via ball-milling as promising anode materials for lithium ion batteries," *Electrochimica Acta,* vol. 269, p. 452–461, 2018.

[62] N. Khossossi, D. Singh, A. Ainane and R. Ahuja, "Recent progress of defect chemistry on 2D materials for advanced battery anodes," *Chemistry – An Asian Journal,* vol. 15, no. 21, p. 3390–3404, 2020.

[63] Deepika, L. H. Li, A. M. Glushenkov, S. K. Hait, P. Hodgson and Y. Chen, "High-Efficient Production of Boron Nitride Nanosheets via an Optimized Ball Milling Process for Lubrication in Oil," *Scientific Reports,* vol. 4, no. 1, p. 7288, 2014.

[64] C. Lin, L. Yang, L. Ouyang, J. Liu, H. Wang and M. Zhu, "A new method for few-layer graphene preparation via plasma-assisted ball milling," *Journal of Alloys and Compounds,* vol. 728, p. 578–584, 2017.

[65] H. Ji, S. Hu, Z. Jiang, S. Shi, W. Hou and G. Yang, "Directly scalable preparation of sandwiched MoS2/graphene nanocomposites via ball-milling with excellent electrochemical energy storage performance," *Electrochimica Acta,* vol. 299, p. 143–151, 2019.

[66] F. Najafi, G. Wang, S. Mukherjee, T. Cui, T. Filleter and C. V. Singh, "Toughening of graphene-based polymer nanocomposites via tuning chemical functionalization," *Composites Science and Technology,* vol. 194, p. 108140, 2020.

[67] A. Amiri, M. Naraghi, G. Ahmadi, M. Soleymaniha and M. Shanbedi, "A review on liquid-phase exfoliation for scalable production of pure graphene, wrinkled, crumpled and functionalized graphene and challenges," *FlatChem,* vol. 8, p. 40–71, 2018.

[68] Y. Hernandez, M. Lotya, D. Rickard, S. D. Bergin and J. N. Coleman, "Measurement of Multicomponent Solubility Parameters for Graphene Facilitates Solvent Discovery," *Langmuir,* vol. 26, no. 5, p. 3208–3213, 2010.

[69] C. E. Hamilton, J. R. Lomeda, Z. Sun, J. M. Tour and A. R. Barron, "High-Yield Organic Dispersions of Unfunctionalized Graphene," *Nano Letters,* vol. 9, no. 10, p. 3460–3462, 2009.

[70] A. Arifuzzaman, A. A. Khan, A. F. Ismail, M. Z. Alam and I. I. Yaacob, "Effect of Exfoliated Graphene Defects on Thermal Conductivity of Water Based Graphene

Nanofluids," *International Journal of Applied Engineering Research,* vol. 13, no. 7, p. 4871–4877, 2018.

[71] A. V. Tyurnina, I. Tzanakis, J. Morton, J. Mi, K. Porfyrakis, B. M. Maciejewska, N. Grobert and D. G. Eskin, "Ultrasonic exfoliation of graphene in water: A key parameter study," *Carbon,* vol. 168, p. 737–747, 2020.

[72] S. M. Notley, "Highly Concentrated Aqueous Suspensions of Graphene through Ultrasonic Exfoliation with Continuous Surfactant Addition," *Langmuir,* vol. 28, no. 40, p. 14110–14113, 2012.

[73] R. J. Smith, P. J. King, M. Lotya, C. Wirtz, U. Khan, S. De, A. O'Neill, G. S. Duesberg, J. C. Grunlan, G. Moriarty, J. Chen, J. Wang, A. I. Minett, V. Nicolosi and J. N. Coleman, "Large-scale exfoliation of inorganic layered compounds in aqueous surfactant solutions," *Advanced Materials,* vol. 23, no. 34, p. 3944–3948, 2011.

[74] Z. Baig, O. Mamat, M. Mustapha, A. Mumtaz, K. S. Munir and M. Sarfraz, "Investigation of tip sonication effects on structural quality of graphene nanoplatelets (GNPs) for superior solvent dispersion," *Ultrasonics Sonochemistry,* vol. 45, p. 133–149, 2018.

[75] J. A. Morton, M. Khavari, L. Qin, B. M. Maciejewska, A. V. Tyurnina, N. Grobert, D. G. Eskin, J. Mi, K. Porfyrakis, P. Prentice and I. Tzanakis, "New insights into sono-exfoliation mechanisms of graphite: In situ high-speed imaging studies and acoustic measurements," *Materials Today,* vol. 49, p. 10–22, 2021.

[76] R. Narayan and S. O. Kim, "Surfactant mediated liquid phase exfoliation of graphene," *Nano Convergence,* vol. 2, no. 1, p. 20, 2015.

[77] Q.-B. Wang, J.-Z. Yin, Q.-Q. Xu and J.-T. Zhi, "Insightful Understanding of Shear-Assisted Supercritical CO2 Exfoliation for Fabricating Graphene Nanosheets through the Combination of Kinetics and Process Parameters," *Industrial & Engineering Chemistry Research,* vol. 59, no. 23, p. 10967–10975, 2020.

[78] L. Liu, Z. Shen, M. Yi, X. Zhang and S. Ma, "A green, rapid and size-controlled production of high-quality graphene sheets by hydrodynamic forces," *RSC Adv.,* vol. 4, no. 69, p. 36464–36470, 2014.

[79] T. S. Tran, S. J. Park, S. S. Yoo, T.-R. Lee and T. Kim, "High shear-induced exfoliation of graphite into high quality graphene by Taylor–Couette flow," *RSC Advances,* vol. 6, no. 15, p. 12003–12008, 2016.

[80] S. Bellani, E. Petroni, A. E. Del Rio Castillo, N. Curreli, B. Martín-García, R. Oropesa-Nuñez, M. Prato and F. Bonaccorso, "Scalable Production of Graphene Inks via Wet-Jet Milling Exfoliation for Screen-Printed Micro-Supercapacitors," *Advanced Functional Materials,* vol. 29, no. 14, p. 1807659, 2019.

[81] N. Liu, P. Kim, J. H. Kim, J. H. Ye, S. Kim and C. J. Lee, "Large-Area Atomically Thin MoS2 Nanosheets Prepared Using Electrochemical Exfoliation," *ACS Nano,* vol. 8, no. 7, p. 6902–6910, 2014.

[82] K. Parvez, Z.-S. Wu, R. Li, X. Liu, R. Graf, X. Feng and K. Müllen, "Exfoliation of Graphite into Graphene in Aqueous Solutions of Inorganic Salts," *Journal of the American Chemical Society,* vol. 136, no. 16, p. 6083–6091, 2014.

[83] A. Ambrosi and M. Pumera, "Electrochemically Exfoliated Graphene and Graphene Oxide for Energy Storage and Electrochemistry Applications," *Chemistry – A European Journal,* vol. 22, no. 1, p. 153–159, 2016.

[84] S. Yang, S. Brüller, Z.-S. Wu, Z. Liu, K. Parvez, R. Dong, F. Richard, P. Samorì, X. Feng and K. Müllen, "Organic Radical-Assisted Electrochemical Exfoliation for the Scalable Production of High-Quality Graphene," *Journal of the American Chemical Society,* vol. 137, no. 43, p. 13927–13932, 2015.

[85] E. T. Bjerglund, M. E. P. Kristensen, S. Stambula, G. A. Botton, S. U. Pedersen and K. Daasbjerg, "Efficient Graphene Production by Combined Bipolar Electrochemical Intercalation and High-Shear Exfoliation," *ACS Omega,* vol. 2, no. 10, p. 6492–6499, 2017.

[86] A. J. Cooper, N. R. Wilson, I. A. Kinloch and R. A. Dryfe, "Single stage electrochemical exfoliation method for the production of few-layer graphene via intercalation of tetraalkylammonium cations," *Carbon,* vol. 66, p. 340–350, 2014.

[87] Y. Fang, X. Li, J. Li, C. Yao, H. Y. Hoh, X. Hai, J. Lu and C. Su, "Janus electrochemical exfoliation of two-dimensional materials," *Journal of Materials Chemistry A,* vol. 7, no. 45, p. 25691–25711, 2019.

[88] Y. Tang, X. Zhang, P. Choi, R. Manica, Q. Liu and Z. Xu, "Single-Molecule MoS2–Polymer Interaction and Efficient Aqueous Exfoliation of MoS2 into Single Layer," *The Journal of Physical Chemistry C,* vol. 122, no. 15, p. 8262–8269, 2018.

[89] K. Wang, B. Zheng, M. Shrestha, T. Schuelke and Q.-H. Fan, "Magnetically enhanced plasma exfoliation of polyaniline-modified graphene for flexible solid-state supercapacitors," *Energy Storage Materials,* vol. 14, p. 230–237, 2018.

[90] X. Zhu, J. Yang, X. She, Y. Song, J. Qian, Y. Wang, H. Xu, H. Li and Q. Yan, "Rapid synthesis of ultrathin 2D materials through liquid-nitrogen and microwave treatments," *Journal of Materials Chemistry A,* vol. 7, no. 10, p. 5209–5213, 2019.

[91] J. D. Anderson Jr., Modern Compressible Flow: With Historical Perspective, 4 ed., McGraw-Hill Education, 2021.

[92] B. R. Munson, D. F. Young and T. H. Okiishi, Fundamentals of Fluid Mechanics, 3 ed., New York: John Wiley & Sons, 1998.

[93] T. N. Tsironi, S. M. Chatzidakis and N. G. Stoforos, "The future of polyethylene terephthalate bottles: Challenges and sustainability," *Packaging Technology and Science,* vol. 35, no. 4, p. 317–325, 2022.

[94] C. Calcagno, C. Mariani, S. Teixeira and R. Mauler, "The effect of organic modifier of the clay on morphology and crystallization properties of PET nanocomposites," *Polymer,* vol. 48, no. 4, p. 966–974, 2007.

[95] S. Xie, O. M. Istrate, P. May, S. Barwich, A. P. Bell, U. Khan and J. N. Coleman, "Boron nitride nanosheets as barrier enhancing fillers in melt processed composites," *Nanoscale,* vol. 7, no. 10, p. 4443–4450, 2015.

[96] E. E. Michaelides, M. Sommerfeld and B. van Wachem, Multiphase Flows with Droplets and Particles, Third Edition, CRC Press, 2022.

[97] M. Parmar, A. Haselbacher and S. Balachandar, "Equation of motion for a sphere in non-uniform compressible flows," *Journal of Fluid Mechanics,* vol. 699, p. 352–375, 2012.

[98] E. Loth, "Compressibility and Rarefaction Effects on Drag of a Spherical Particle," *AIAA Journal,* vol. 46, no. 9, p. 2219–2228, 2008.

[99] M. B. Giles, "Analysis of the accuracy of shock-capturing in the steady quasi-1D Euler equations," Oxford University Computing Laboratory, 1995.

[100] M. F. Islam, S. Arabha, R. Hixon and R. Rizvi, "Compressible Flow Exfoliation of Two-Dimensional Nanomaterials: Insights Into Layer Separation Informed by Gas Dynamics," *Advanced Engineering Materials,* vol. 28, no. 6, p. e202502168, 2026.

[101] D. Stanescu and W. Habashi, "2N-Storage Low Dissipation and Dispersion Runge-Kutta Schemes for Computational Acoustics," *Journal of Computational Physics,* vol. 143, no. 2, p. 674–681, 1998.

[102] P. Hess, "Bonding, structure, and mechanical stability of 2D materials: the predictive power of the periodic table," *Nanoscale Horizons,* vol. 6, no. 11, p. 856–892, 2021.

[103] Y. Guo, C. Liu, Q. Yin, C. Wei, S. Lin, T. B. Hoffman, Y. Zhao, J. H. Edgar, Q. Chen, S. P. Lau, J. Dai, H. Yao, H.-S. P. Wong and Y. Chai, "Distinctive in-Plane Cleavage Behaviors of Two-Dimensional Layered Materials," *ACS Nano,* vol. 10, no. 9, p. 8980–8988, 2016.

[104] X. Tian, Y. Li, Z. Chen, Q. Li, L. Hou, J. Wu, Y. Tang and Y. Li, "Shear-Assisted Production of Few-Layer Boron Nitride Nanosheets by Supercritical CO2 Exfoliation and Its Use for Thermally Conductive Epoxy Composites," *Scientific Reports,* vol. 7, no. 1, p. 17794, 2017.

[105] Y. Lin, T. V. Williams and J. W. Connell, "Soluble, Exfoliated Hexagonal Boron Nitride Nanosheets," *The Journal of Physical Chemistry Letters,* vol. 1, no. 1, p. 277–283, 2010.

[106] W. Wang, S. Dai, X. Li, J. Yang, D. J. Srolovitz and Q. Zheng, "Measurement of the cleavage energy of graphite," *Nature Communications,* vol. 6, no. 1, p. 7853, 2015.

[107] T. Björkman, A. Gulans, A. V. Krasheninnikov and R. M. Nieminen, "van der Waals Bonding in Layered Compounds from Advanced Density-Functional First-Principles Calculations," *Physical Review Letters,* vol. 108, no. 23, p. 235502, 2012.

[108] Y. Li, W. Zhang, B. Guo and D. Datta, "Interlayer shear of nanomaterials: Graphene–graphene, boron nitride–boron nitride and graphene–boron nitride," *Acta Mechanica Solida Sinica,* vol. 30, no. 3, p. 234–240, 2017.

[109] T. K. Mukhopadhyay and A. Datta, "Deciphering the Role of Solvents in the Liquid Phase Exfoliation of Hexagonal Boron Nitride: A Molecular Dynamics Simulation Study," *The Journal of Physical Chemistry C,* vol. 121, no. 1, p. 811–822, 2017.

[110] G. Kamath and G. A. Baker, "Are ionic liquids suitable media for boron nitride exfoliation and dispersion? Insight via molecular dynamics," *RSC Advances,* vol. 3, no. 22, p. 8197, 2013.

[111] S. Plimpton, "Fast Parallel Algorithms for Short-Range Molecular Dynamics," *Journal of Computational Physics,* vol. 117, no. 1, p. 1–19, 1995.

[112] T. C. O'Connor, J. Andzelm and M. O. Robbins, "AIREBO-M: A reactive model for hydrocarbons at extreme pressures," *The Journal of Chemical Physics,* vol. 142, no. 2, p. 024903, 2015.

[113] C.-J. Shih, S. Lin, M. S. Strano and D. Blankschtein, "Understanding the Stabilization of Liquid-Phase-Exfoliated Graphene in Polar Solvents: Molecular Dynamics Simulations and Kinetic Theory of Colloid Aggregation," *Journal of the American Chemical Society,* vol. 132, no. 41, p. 14638–14648, 2010.

[114] L. Verlet, "Computer "Experiments" on Classical Fluids. I. Thermodynamical Properties of Lennard-Jones Molecules," *Physical Review,* vol. 159, no. 1, p. 98–103, 1967.

[115] W. G. Hoover, "Canonical dynamics: Equilibrium phase-space distributions," *Physical Review A,* vol. 31, no. 3, p. 1695–1697, 1985.

[116] S. Ahmed, S. Arabha, R. I. Gonzalez and R. Rizvi, "Interactions of Gas Particles with Graphene during High-Throughput Compressible Flow Exfoliation: A Molecular Dynamics Simulations Study," *The Journal of Physical Chemistry C,* vol. 126, no. 22, p. 9378–9385, 2022.

[117] S. J. Stuart, A. B. Tutein and J. A. Harrison, "A reactive potential for hydrocarbons with intermolecular interactions," *The Journal of Chemical Physics,* vol. 112, no. 14, p. 6472–6486, 2000.

[118] H. Au, "Molecular dynamics simulation of nanoporous graphene for selective gas separation," Massachusetts Institute of Technology, 2012.

[119] M. R. B. Shahadat, S. Ahmed and A. K. M. M. Morshed, "A molecular dynamics study of thermal transport in nanoparticle doped Argon like solid," *AIP Conference Proceedings,* vol. 1754, p. 050021, 2016.

[120] W. L. Jorgensen, D. S. Maxwell and J. Tirado-Rives, "Development and Testing of the OPLS All-Atom Force Field on Conformational Energetics and Properties of Organic Liquids," *Journal of the American Chemical Society,* vol. 118, no. 45, p. 11225–11236, 1996.

[121] H. A. Lorentz, "Ueber die Anwendung des Satzes vom Virial in der kinetischen Theorie der Gase," *Annalen der Physik,* vol. 248, no. 1, p. 127–136, 1881.

[122] E. Ganz, A. B. Ganz, L.-M. Yang and M. Dornfeld, "The initial stages of melting of graphene between 4000 K and 6000 K," *Physical Chemistry Chemical Physics,* vol. 19, no. 5, p. 3756–3762, 2017.

[123] D. F. Young, B. R. Munson, T. H. Okiishi and W. W. Huebsch, A Brief Introduction to Fluid Mechanics, 5 ed., John Wiley & Sons, 2010.

[124] L. Li, J. Xu, G. Li, X. Jia, Y. Li, F. Yang, L. Zhang, C. Xu, J. Gao, Y. Liu and Z. Fang, "Preparation of graphene nanosheets by shear-assisted supercritical CO2 exfoliation," *Chemical Engineering Journal,* vol. 284, p. 78–84, 2016.

[125] Y. Tao, Z. Li, Q. Han, C. Sun, Y. Zhang and Y. Chen, "Theory of aerodynamic heating from molecular collision analysis," *Physics Letters A,* vol. 384, no. 4, p. 126098, 2020.

[126] E. Shahini, K. Shankar and T. Tang, "Liquid-phase exfoliation of graphitic carbon nitrides studied by molecular dynamics simulation," *Journal of Colloid and Interface Science,* vol. 630, p. 900–910, 2023.

[127] S. Arabha, C. Jian, R. Hixon and R. Rizvi, "Free-Energy Mapping of Gas-Assisted Exfoliation Pathways for Graphene under Compressible Flow: Implications for High-Volume Nanocomposite Applications," *ACS Applied Nano Materials,* vol. 9, no. 19, p. 9092–9104, 2026.

[128] B. Isralewitz, M. Gao and K. Schulten, "Steered molecular dynamics and mechanical functions of proteins," *Current Opinion in Structural Biology,* vol. 11, no. 2, p. 224–230, 2001.

[129] D. P. Tran, K. Takemura, K. Kuwata and A. Kitao, "Protein–Ligand Dissociation Simulated by Parallel Cascade Selection Molecular Dynamics," *Journal of Chemical Theory and Computation,* vol. 14, no. 1, p. 404–417, 2018.

[130] A. Gotzias, "Binding Free Energy Calculations of Bilayer Graphenes Using Molecular Dynamics," *Journal of Chemical Information and Modeling,* vol. 61, no. 3, p. 1164–1171, 2021.

[131] T. Stoltenhoff, H. Kreye and H. Richter, "An Analysis of the Cold Spray Process and Its Coatings," *Journal of Thermal Spray Technology,* vol. 11, no. 4, p. 542–550, 2002.

[132] R. Dykhuizen and M. Smith, "Gas Dynamic Principles of Cold Spray," *Journal of Thermal Spray Technology,* vol. 7, no. 2, p. 205–212, 1998.

[133] U. Halim, C. R. Zheng, Y. Chen, Z. Lin, S. Jiang, R. Cheng, Y. Huang and X. Duan, "A rational design of cosolvent exfoliation of layered materials by directly probing liquid–solid interaction," *Nature Communications,* vol. 4, no. 1, p. 2213, 2013.

[134] J. H. Jung, C.-H. Park and J. Ihm, "A Rigorous Method of Calculating Exfoliation Energies from First Principles," *Nano Letters,* vol. 18, no. 5, p. 2759–2765, 2018.

[135] Z. Fang, X. Li, W. Shi, Z. Li, Y. Guo, Q. Chen, L. Peng and X. Wei, "Interlayer Binding Energy of Hexagonal MoS2 as Determined by an In Situ Peeling-to-Fracture Method," *The Journal of Physical Chemistry C,* vol. 124, no. 42, p. 23419–23425, 2020.

[136] M. Singh, D. Bianco, J. Adam, A. Capaccio, S. Clemente, M. R. Del Sorbo, C. Feoli, J. Kaur, C. Nappi, M. Panico, G. Rusciano, M. Rossi, A. Sasso, M. Valadan,

A. Cuocolo, E. Battista, P. A. Netti and C. Altucci, "Gamma rays impact on 2D-MoS2 in water solution," *Scientific Reports,* vol. 14, no. 1, p. 22130, 2024.

[137] P. Hoffmann, N. Fainer, M. Kosinova, O. Baake and W. Ensinger, "Compilation on Synthesis, Characterization and Properties of Silicon and Boron Carbonitride Films," in *Silicon Carbide - Materials, Processing and Applications in Electronic Devices*, M. Mukherjee, Ed., Rijeka, InTech, 2011, p. 487–546.

[138] K. S. Rountree, S. A. Shah, C. B. Sweeney, F. Irin and M. J. Green, "Graphene reflux: improving the yield of liquid-exfoliated nanosheets through repeated separation techniques," *Nanotechnology,* vol. 27, no. 50, p. 505601, 2016.

[139] V. Ravichandran and E. Varrla, "Sustainable high-yield h-BN nanosheet production by liquid exfoliation for thermal interface materials," *RSC Applied Interfaces,* vol. 2, no. 2, p. 534–549, 2025.

[140] P. Ni, M. Dieng, J.-C. Vanel, I. Florea, F. Z. Bouanis and A. Yassar, "Liquid Shear Exfoliation of MoS2: Preparation, Characterization, and NO2-Sensing Properties," *Nanomaterials,* vol. 13, no. 18, p. 2502, 2023.

[141] A. Ciesielski and P. Samorì, "Graphene via sonication assisted liquid-phase exfoliation," *Chemical Society Reviews,* vol. 43, no. 1, p. 381–398, 2014.

[142] T. R. Gengenbach, G. H. Major, M. R. Linford and C. D. Easton, "Practical guides for x-ray photoelectron spectroscopy (XPS): Interpreting the carbon 1s spectrum," *Journal of Vacuum Science & Technology A: Vacuum, Surfaces, and Films,* vol. 39, no. 1, p. 013204, 2021.

[143] M. Baker, R. Gilmore, C. Lenardi and W. Gissler, "XPS investigation of preferential sputtering of S from MoS2 and determination of MoSx stoichiometry from Mo and S peak positions," *Applied Surface Science,* vol. 150, no. 1-4, p. 255–262, 1999.

[144] A. D. Marinov, A. J. Clancy, C. A. Howard and P. L. Cullen, "XPS Peak-Fitting of 2H MoS2 , 1T MoS2 , and MoS2-X Nanosheets in MoS2 Powders and Battery Electrodes After Ar+ Ion Depth-Profiling," *ACS Applied Nano Materials,* vol. 9, no. 2, p. 1183–1194, 2026.

[145] R. Egerton, Physical Principles of Electron Microscopy: An Introduction to TEM, SEM, and AEM, 2 ed., Cham: Springer International Publishing, 2016.

[146] J. Köster, A. Storm, T. E. Gorelik, M. J. Mohn, F. Port, M. R. Gonçalves and U. Kaiser, "Evaluation of TEM methods for their signature of the number of layers in mono- and few-layer TMDs as exemplified by MoS2 and MoTe2," *Micron,* vol. 160, p. 103303, 2022.

[147] J. H. Warner, M. H. Rümmeli, T. Gemming, B. Büchner and G. A. D. Briggs, "Direct Imaging of Rotational Stacking Faults in Few Layer Graphene," *Nano Letters,* vol. 9, no. 1, p. 102–106, 2009.

[148] A. C. Ferrari, J. C. Meyer, V. Scardaci, C. Casiraghi, M. Lazzeri, F. Mauri, S. Piscanec, D. Jiang, K. S. Novoselov, S. Roth and A. K. Geim, "Raman Spectrum of Graphene and Graphene Layers," *Physical Review Letters,* vol. 97, no. 18, p. 187401, 2006.

[149] A. C. Ferrari and D. M. Basko, "Raman spectroscopy as a versatile tool for studying the properties of graphene," *Nature Nanotechnology,* vol. 8, no. 4, p. 235–246, 2013.

[150] L. G. Cançado, A. Jorio, E. H. M. Ferreira, F. Stavale, C. A. Achete, R. B. Capaz, M. V. O. Moutinho, A. Lombardo, T. S. Kulmala and A. C. Ferrari, "Quantifying Defects in Graphene via Raman Spectroscopy at Different Excitation Energies," *Nano Letters,* vol. 11, no. 8, p. 3190–3196, 2011.

[151] C. Lee, H. Yan, L. E. Brus, T. F. Heinz, J. Hone and S. Ryu, "Anomalous Lattice Vibrations of Single- and Few-Layer MoS2," *ACS Nano,* vol. 4, no. 5, p. 2695–2700, 2010.

[152] R. V. Gorbachev, I. Riaz, R. R. Nair, R. Jalil, L. Britnell, B. D. Belle, E. W. Hill, K. S. Novoselov, K. Watanabe, T. Taniguchi, A. K. Geim and P. Blake, "Hunting for Monolayer Boron Nitride: Optical and Raman Signatures," *Small,* vol. 7, no. 4, p. 465–468, 2011.

[153] Q. Cai, D. Scullion, A. Falin, K. Watanabe, T. Taniguchi, Y. Chen, E. J. G. Santos and L. H. Li, "Raman signature and phonon dispersion of atomically thin boron nitride," *Nanoscale,* vol. 9, no. 9, p. 3059–3067, 2017.

[154] G. Greczynski and L. Hultman, "A step-by-step guide to perform x-ray photoelectron spectroscopy," *Journal of Applied Physics,* vol. 132, no. 1, p. 011101, 2022.

[155] A. D. Marinov, L. Bravo Priegue, A. R. Shah, T. S. Miller, C. A. Howard, G. Hinds, P. R. Shearing, P. L. Cullen and D. J. L. Brett, "Ex Situ Characterization of 1T/2H MoS2 and Their Carbon Composites for Energy Applications, a Review," *ACS Nano,* vol. 17, no. 6, p. 5163–5186, 2023.

[156] S. Vasi, S. V. Giofrè, S. Perathoner, D. Mallamace, S. Abate and U. Wanderlingh, "X-ray Characterizations of Exfoliated MoS2 Produced by Microwave-Assisted Liquid-Phase Exfoliation," *Materials,* vol. 17, no. 16, p. 3887, 2024.

[157] C. Backes, K. R. Paton, D. Hanlon, S. Yuan, M. I. Katsnelson, J. Houston, R. J. Smith, D. McCloskey, J. F. Donegan and J. N. Coleman, "Spectroscopic metrics allow in situ measurement of mean size and thickness of liquid-exfoliated few-layer graphene nanosheets," *Nanoscale,* vol. 8, no. 7, p. 4311–4323, 2016.

[158] A. Griffin, A. Harvey, B. Cunningham, D. Scullion, T. Tian, C.-J. Shih, M. Gruening, J. F. Donegan, E. J. G. Santos, C. Backes and J. N. Coleman, "Spectroscopic Size and Thickness Metrics for Liquid-Exfoliated h-BN," *Chemistry of Materials,* vol. 30, no. 6, p. 1998–2005, 2018.

[159] V. K. Champagne Jr., O. C. Ozdemir and A. Nardi, Eds., Practical Cold Spray, 1 ed., Cham: Springer International Publishing, 2021.

[160] W. Sun, X. Chu, H. Lan, R. Huang, J. Huang, Y. Xie, J. Huang and G. Huang, "Current Implementation Status of Cold Spray Technology: A Short Review," *Journal of Thermal Spray Technology,* vol. 31, no. 4, p. 848–865, 2022.

[161] A. Sova, S. Grigoriev, A. Kochetkova and I. Smurov, "Influence of powder injection point position on efficiency of powder preheating in cold spray: Numerical study," *Surface and Coatings Technology,* vol. 242, p. 226–231, 2014.

[162] Z. Dong, Z. Wen, F. Zhao, S. Kuhn and T. Noël, "Scale-up of micro- and milli-reactors: An overview of strategies, design principles and applications," *Chemical Engineering Science: X,* vol. 10, p. 100097, 2021.

[163] M. Saber, J. Commenge and L. Falk, "Microreactor numbering-up in multi-scale networks for industrial-scale applications: Impact of flow maldistribution on the reactor performances," *Chemical Engineering Science,* vol. 65, no. 1, p. 372–379, 2010.

[164] W. Guo, Q. Wang, X. Wei, N. Jin, Y. Chen, X. Chen and Y. Zhao, "Characteristics of numbering-up and flow distribution of multi-channel microreactor with 2-D constructal inlet distributors," *Chemical Engineering Science,* vol. 299, p. 120495, 2024.

[165] Z. Wang, S. Wu, Y. Liu, J. Zhang, Y. Chen, Z. Qin, J. Su, C. Sun and H. You, "Researching and Predicting the Flow Distribution of Herschel-Bulkley Fluids in Compact Parallel Channels," *Applied Sciences,* vol. 13, no. 5, p. 2802, 2023.

[166] Z. Zhang, H. Jin, C. Wu and J. Ji, "Efficient Production of High-Quality Few-Layer Graphene Using a Simple Hydrodynamic-Assisted Exfoliation Method," *Nanoscale Research Letters,* vol. 13, no. 1, p. 416, 2018.

[167] L. Niu, M. Li, X. Tao, Z. Xie, X. Zhou, A. P. A. Raju, R. J. Young and Z. Zheng, "Salt-assisted direct exfoliation of graphite into high-quality, large-size, few-layer graphene sheets," *Nanoscale,* vol. 5, no. 16, p. 7202, 2013.

[168] C. Zhang, J. Tan, Y. Pan, X. Cai, X. Zou, H.-M. Cheng and B. Liu, "Mass production of 2D materials by intermediate-assisted grinding exfoliation," *National Science Review,* vol. 7, no. 2, p. 324–332, 2020.

[169] J. R. Downing, S. Diaz-Arauzo, L. E. Chaney, D. Tsai, J. Hui, J. T. Seo, D. R. Cohen, M. Dango, J. Zhang, N. X. Williams, J. H. Qian, J. B. Dunn and M. C. Hersam, "Centrifuge-Free Separation of Solution-Exfoliated 2D Nanosheets via Cross-Flow Filtration," *Advanced Materials,* vol. 35, no. 24, p. 2212042, 2023.

[170] S. Diaz-Arauzo, J. R. Downing, D. Tsai, J. Trost, J. Hui, K. Donahue, N. Antonopoulos, L. E. Chaney, J. B. Dunn and M. C. Hersam, "Ultrahigh-throughput cross-flow filtration of solution-processed 2D materials enabled by porous ceramic membranes," *Materials Horizons,* vol. 11, no. 23, p. 5960–5971, 2024.

[171] M. Alhabeb, K. Maleski, B. Anasori, P. Lelyukh, L. Clark, S. Sin and Y. Gogotsi, "Guidelines for Synthesis and Processing of Two-Dimensional Titanium Carbide (Ti3C2Tx MXene)," *Chemistry of Materials,* vol. 29, no. 18, p. 7633–7644, 2017.

[172] T. Habib, X. Zhao, S. A. Shah, Y. Chen, W. Sun, H. An, J. L. Lutkenhaus, M. Radovic and M. J. Green, "Oxidation stability of Ti3C2Tx MXene nanosheets in solvents and composite films," *npj 2D Materials and Applications,* vol. 3, no. 1, p. 8, 2019.

[173] A. H. Alateah, "Graphene concrete: Recent advances in production methods, performance properties, environmental impact and economic viability," *Case Studies in Construction Materials,* vol. 19, p. e02653, 2023.

[174] A. I. Patrinou, E. Tziviloglou, A. Varoutoglou, E. P. Favvas, A. C. Mitropoulos, G. Z. Kyzas and Z. S. Metaxa, "Cement Composites with Graphene Nanoplatelets and Recycled Milled Carbon Fibers Dispersed in Air Nanobubble Water," *Nanomaterials,* vol. 12, no. 16, p. 2786, 2022.

[175] A. Zotti, S. Zuppolini, A. Borriello and M. Zarrelli, "Polymer nanocomposites based on Graphite Nanoplatelets and amphiphilic graphene platelets," *Composites Part B: Engineering,* vol. 246, p. 110223, 2022.

[176] Z. Ge, J. Qin, R. Sun, Y. Guan, H. Zhang and Z. Wang, "The Effect of the Addition of Graphene Nanoplatelets on the Selected Properties of Cementitious Composites," *Frontiers in Built Environment,* vol. 7, p. 673346, 2021.

[177] S. Rehman, Z. Ibrahim, S. Memon, M. Javed and R. Khushnood, "A Sustainable Graphene Based Cement Composite," *Sustainability,* vol. 9, no. 7, p. 1229, 2017.

[178] Z. Yang, J. Che, Z. Zhang, L. Yu, M. Hu, W. Sun, W. Gao, J. Fan, L. Wang and G. Liu, "High-efficiency graphene/epoxy composite coatings with outstanding thermal conductive and anti-corrosion performance," *Composites Part A: Applied Science and Manufacturing,* vol. 181, p. 108152, 2024.

[179] M. Cui, S. Ren, S. Qin, Q. Xue, H. Zhao and L. Wang, "Non-covalent functionalized hexagonal boron nitride nanoplatelets to improve corrosion and wear resistance of epoxy coatings," *RSC Advances,* vol. 7, no. 70, p. 44043–44053, 2017.

[180] Z. Lu, Q. Lin, Z. Cao, W. Li, J. Gong, Y. Wang, K. Hu and X. Hu, "MoS2 Nanomaterials as Lubricant Additives: A Review," *Lubricants,* vol. 11, no. 12, p. 527, 2023.

[181] L. Guardia, M. Fernández-Merino, J. Paredes, P. Solís-Fernández, S. Villar-Rodil, A. Martínez-Alonso and J. Tascón, "High-throughput production of pristine graphene in an aqueous dispersion assisted by non-ionic surfactants," *Carbon,* vol. 49, no. 5, p. 1653–1662, 2011.